ABSTRACT

Title of Dissertation:	Catalysts Development for Non-oxidative Methane Upgrading Towards Hydrocarbons and Hydrogen Production
	Zixiao Liu, Doctor of Philosophy, 2024
Dissertation directed by:	Professor, Dongxia Liu, Chemical and Biomolecular Engineering, University of Delaware

Methane, the main constituent of natural gas and biogas is deemed to be an alternative source to replace crude oil in the production of chemicals and fuel. Non-oxidative methane conversion enables methane coupling or splitting to produce hydrogen and more significant hydrocarbons, but catalyst deactivation has been a challenge in past research. This dissertation addresses catalyst deactivation issues in non-oxidative methane conversion by inventing novel catalyst systems.

For direct non-oxidative methane coupling, a pathway for methane upgrading into hydrogen, olefin, and aromatic products, the silica-supported catalysts were synthesized by flame fusion of a mixture of quartz silica and metal silicate precursors. Compared to the cristobalite silica-supported catalysts reported previously, vitreous silica-supported catalysts have disordered Si-O bonds and structural defects, enabling

better metal dispersion and more vital metal-support interaction. The as-prepared vitreous silica-supported iron catalyst had a shorter induction period in methane activation and lower coke yield. The increase in iron concentration elongated the catalyst induction period and promoted aromatics and coke formation. Among different transition metal catalysts, the cobalt supported by vitreous silica had the best methane conversion, hydrocarbon product yield, and catalyst stability.

For catalytic methane pyrolysis, a pathway producing COx-free hydrogen and valuable carbon product, a siliceous zeolite-supported cobalt catalyst was invented. In comparison to the methane pyrolysis catalysts in literature, the siliceous zeolite support in the invented catalyst has limited Brönsted acidity and increased mesoporosity, which limited the acid-catalyzed deactivation mechanism and facilitated the mass transport, and thus significantly increased the catalyst lifetime. The cobalt sites change the cluster sizes and coordination structures with the loading concentrations in the zeolite support, which leads to carbon products with different properties.

CATALYST DEVELOPMENT FOR NON-OXIDATIVE METHANE UPGRADING TOWARDS HYDROCARBONS AND HYDROGEN PRODUCTION

by

Zixiao Liu

Dissertation submitted to the Faculty of the Graduate School of the
University of Maryland, College Park, in partial fulfillment
of the requirements for the degree of
Doctor of Philosophy
2024

Advisory Committee:
Professor Dongxia Liu, Chair
Professor Ashwani K. Gupta (Deans's Representative)
Professor Mohamad Al-Sheikhly
Professor Chen Zhang
Professor Yifei Mo

© Copyright by

Zixiao Liu

2024

Dedication

To my supporting and loving parents, Dr. Xiaofeng Wang and Kang Liu.

Acknowledgments

Firstly, I'd like to begin by extending my deepest gratitude and love to my parents, Dr. Xiaofeng Wang and Kang Liu. In my eyes, they are unparalleled, embodying strength and resilience to navigate through life's most challenging moments. Their guidance has been the beacon lighting for my path to success, instilling values that have shaped who I am. Their unwavering support and understanding, especially at life's critical junctures, are something I cherish deeply. I offer them my heartfelt thanks and wish them continued happiness and well-being.

To begin with, I am profoundly thankful to my advisor, Professor Dongxia Liu, for her understanding, consideration, and responsibility. As a distinguished woman in academia and science, Professor Liu has offered me unwavering support and expertly guided my philosophical approach to research throughout my five years of graduate study. Her meticulous, hands-on guidance in developing experiments, mastering craftsmanship in scientific techniques, addressing problems, and identifying significant research topics and directions has been an invaluable lesson to me. These experiences extend far beyond completing this thesis and will benefit me significantly in my future endeavors. Professor Liu's exemplary moral standards and professionalism as a leading scientist have profoundly shaped my values and career aspirations. It is with immense pride that I regard myself as her student.

I am immensely grateful to my wonderful lab mates and friends, Dr. Sichao Cheng, Dr. Junyan Zhang, Dr. Yuan Zhang, and Dr. Emily Schulman. The memories

of our time spent collaborating, supporting one another, and sharing in the camaraderie of our lab will stay with me forever. I also owe a debt of gratitude to Ali Kamali, Akash Wanty, and Antara Bowhwik for their assistance and friendship during my transition to the University of Delaware (UDEL). Further, I extend my thanks to Dr. Evan P. Jahram from NIST, Dr. Yuying Shu from W.R. Grace, Dr. Dionisios G. Vlachos (UDEL), and the many talented graduate students from both UDEL and UMD with whom I had the privilege to collaborate. Working alongside such skilled individuals has been an honor and a profound learning experience.

I want to thank our supportive assistants from UDEL and UMD, such as Megan Argoe (UDEL) and Rachel Katz (UMD). I sincerely thank Adaire N. Parker, Dr. Ichiro Takeuchi, and all other academic program advisors who provided me with valuable guidance. I would also like to thank Dr. Lei Zhang, Dr. Liangzhu Zhu, Dr. Taylor D. Sparks, and Dr. Anil V. Virkar for their long-term friendship and mentorship before I advanced to graduate study.

I extend my heartfelt gratitude to my dear fiancée, Cara Wang, whose excellence, understanding, and easy-going nature make her the wonderful woman I am eager to spend the rest of my life with. I am also deeply thankful to my friends and cat for their unwavering support and companionship. I wish them all the best in their life, hoping for success and happiness in all their endeavors.

Table of Contents

Dedication ii

Acknowledgments iii

Table of Contents v

List of Tables xi

List of Figures xii

List of Abbreviations xviii

Chapter 1: Introduction 1

1.1 Motivation of Methane Upgrading 1

1.2 Conventional Use of Methane as Feedstock: A Brief History 4

1.3 Abundance of Methane 5

1.4 Strategies of Methane Upgrading for Net-zero Emission 8

1.4.2. In-direct Methane Upgrade to Alcohol and Hydrocarbons 13

1.4.3. Direct, Methane Upgrading to Hydrocarbons 15

1.4.4. Direct, Non-oxidative Upgrading Methane Towards Hydrocarbons and Hydrogen 17

1.5 Direct, Non-oxidative Methane Upgrading: Reaction Overview 19

1.6 Catalysts Development for Non-oxidative Methane Upgrading 22

1.6.1 Early Development of Catalysts and Methane Activation 22

1.6.2 Supported-Nanostructured Catalysts for Methane Upgrading Towards Hydrogen 24

1.6.**3** Unconventional Liquid Phase Catalysts for Methane Upgrading Towards Hydrogen 25
1.6.4 Early Catalysts Development for NMC 26
1.6.5 Zeolite-Supported Mo Catalysts for Methane Upgrading Towards Hydrocarbons 27
1.6.6 Singel-atom Catalysts for Methane Upgrading Towards Hydrocarbons 28
1.7 Challenges for Non-Oxidative Methane Upgrading 32
1.8 Dissertation Objective and Overview 37
Chapter 2: Develop Vitreous Silica Supported Fe/SiO2 Catalyst for Direct, Non-oxidative Methane Coupling Towards Hydrocarbons Production 39
2.1 Abstract 39
2.2 Introduction 40
2.3 Experimental Methods 43
2.3.1 Materials 43
2.3.2 Prepare Flame Fused, Vitreous Silica-supported Fe/SiO_2 Catalysts 43
2.3.3 Catalyst Characterization 44
2.3.4 Catalyst Test Under NMC Conditions 45
2.3.5 Analysis of Spent Catalysts 47
2.4 Results and Discussion 47
2.4.1 Fe/SiO_2 Catalysts with Different Silica Polymorph Supports. 47
2.4.1.1 Physicochemical Properties of as-prepared Fe/SiO_2 Catalysts 47
2.4.1.2 Methane Activation over Fe/SiO_2 Catalysts 55
2.4.1.3 Analysis of Spent Fe/SiO_2 Catalysts 60

2.4.2 Vitreous Silica-supported Fe/SiO_2 Catalysts: Effect of Fe Concentrations... 62

2.4.2.1 Physicochemical Properties of the High Fe Loading Fe/SiO_2-v Catalysts. 62

2.4.2.2 Methane Activation Study over Fe/SiO_2-v with Different Loading 66

2.4.2.3 Analyses of spent Fe/SiO_2-v catalysts with different Fe concentrations 70

2.5 Summary 71

Chapter 3: Experimental Screening Vitreous Silica Supported M/SiO_2 (M = Mn, Fe, Co, Ni, and Cu) Catalysts under Direct, Non-oxidative Conversion of Methane. 73

3.1 Abstract 73

3.2 Introduction 74

3.3 Experimental Methods 77

3.3.1 Materials 77

3.3.2 Catalyst Preparation 77

3.3.3 Catalysts Characterization 78

3.3.4 Catalytic reaction test 79

3.3.5 Analysis of spent catalyst 80

3.3.6 X-ray absorption fine structure measurements 80

3.4 Results and Discussion 83

3.4.1 Physicochemical properties of M/SiO_2-v catalysts 83

3.4.1.1 Morphology and composition of M/SiO_2-v catalysts 83

3.4.1.2 Bonding environments in M/SiO_2-v catalysts 84

3.4.1.3 Reducibility of metal species in M/SiO_2-v catalysts 87

3.4.1.4 Oxidation states of metal species in M/SiO_2-v catalysts 88

3.4.2 NMC reaction over M/SiO_2-V catalysts 93

3.4.2.1 Methane activation in the initial reaction stage 93
3.4.2.2 Methane conversion and product selectivity over M/SiO2-v catalysts 95
3.4.3 Coking species in spent M/SiO_2-v catalysts 97
3.4.4 Evolution of metal species in M/SiO_2-v catalysts in NMC reaction 99
3.4.5 Correlation between catalyst type and NMC performance 109
3.5 Summary 111
Chapter 4: Direct, Non-oxidative Conversion of Methane over Fe/SiO_2 Catalytic Wall Reactor 112
4.1 Abstract 112
4.2 Introduction 113
4.3 Experimental method 116
4.3.1 Materials 116
4.3.2 Catalyst synthesis and CWR fabrication 116
4.3.4 Catalytic reaction test 117
4.3.5 Analysis of spent CWR 118
4.4 Result and Discussion 120
4.4.1 Physicochemical properties of Fe/SiO_2-CWRs 120
4.4.2 Catalytic performance of CWR 121
4.4.3 Analysis and Characterization of spent Fe/SiO_2-CWR 124
4.5 Summary 129
Chapter 5: Robust Siliceous Zeolite Supported Cobalt Catalyst for Non-oxidative Methane Decomposition Towards Hydrogen and Cabon Nanotube Production 131
5.1 Abstract 131

5.2 Introduction 132
5.3 Experimental Methods 136
5.3.1 Materials 136
5.3.2 Catalyst synthesis 136
5.3.3 Catalysts Characterization 137
5.3.4 Catalysis test 138
5.3.5 Spent catalyst analysis 139
5.4 Results and discussion 140
5.4.1 Physiochemical properties of Co/DeAl-BEA catalysts 140
5.4.2 Coordination structure of Co-particles in Co-DeAl-BEA catalysts 143
5.4.3 Reducibility of Co-particles in Co-DeAl-BEA catalysts 144
5.4.4 Catalytic performance of Co-DeAl-BEA in methane decomposition 145
5.4.5 Spent catalysts characterization and analysis. 149
5.5. Summary 157
Chapter 6. Conclusions, Limitations, Recommendations, and Contributions 159
6.1. Conclusions of the Thesis Study 159
6.2. Limitations and Recommendations 162
6.2.1 Distinct the Surface Reaction and Gas Phase Reactions for Fe/SiO_2 System 162
6.2.2. Innovation in Catalysts Development for NMC with Control Environment 162
6.2.3. Requires More Processing Stimulation and Reaction Engineering Studies 163

6.2.4. Tailoring Catalyst Configuration for NMD and Discovering Spent Catalyst Utilizations 164
6.3. Contributions 164
Achievements 165
Published Work 165
Working Papers 165
Bibliography 167

List of Tables

Table 1.1. Application of syngas as feedstock to downstream products based on different H_2/CO ratio[45]. 13

Table 2.1. Fe Concentration in the prepared Fe/SiO_2 catalysts 49

Table 3.1. Metal concentration in the prepared M/SiO2-v catalysts. 84

Table 3.2. EXAFS fitting results for the selected catalysts. Uncertainties correspond to one standard error. 100

Table 3.3. K-edge XANES fitting with results of linear combination for species types and fractions for Co, Ni, and Fe/SiO_2-v catalysts. 102

Table 5.1. Actual Co loading determined by ICP-OES. 141

List of Figures

Figure 1.1. The energy network adopted hydrogen as a future renewable energy source, incorporating methane upgrading strategies (the original energy network design was proposed in the literature[24]). 9

Figure 1.2. Thermodynamic data of typical non-oxidative methane conversions to carbon, hydrogen, ethylene, and aromatics. (A) Gibbs free energy of non-oxidative methane reactions as a function of temperatures (Data adapted from NIST Chemistry Web Book[81]), (B) Equilibrium conversion of non-oxidative methane coupling reactions (cited from literature[80]). 20

Figure 2.1. Schematics of quartz reactor (A) and inside view of reactor position in the furnace as well as measured temperature profile (B) used in the NMC reaction. 46

Figure 2.2. The characterization data of 0.1 wt.% Fe/SiO_2-V and 0.1 wt.% Fe/SiO_2-C catalysts: (A) XRD patterns, (B) Raman spectra, (C) DR UV-vis spectra, and (D) H_2-TPR profiles. The characterization data for quartz support are included for comparison purpose. 49

Figure 2.3. Images of catalysts prepared in the experiments: (A) 0.1wt.% Fe/SiO_2-C, (B) 0.1wt.% Fe/SiO_2-V, (C) 0.5wt.% Fe/SiO_2-V, and 1.5wt.% Fe/SiO_2-V. 50

Figure 2.4. N_2 adsorption/desorption isotherms of 0.1wt.% Fe/SiO_2-C (A) and 0.1wt.% Fe/SiO_2-V (B) catalysts. 51

Figure 2.5. XPS spectra of survey scan (A), Si 2p (B), O 1s (C), and Fe 2p (D) of 0.1 wt.% Fe/SiO_2-V and 0.1 wt.% Fe/SiO_2-C catalysts. 55

Figure 2.6. Methane activation over 0.1wt% Fe/SiO_2-C (A) and 0.1 wt.% Fe/SiO_2-V (B) versus TOS tracked by a MS instrument. (C) and (D) show MS signals at TOS of <100s in (A) and (B), respectively. (NMC conditions: 1273 K, WHSV=3200 h^{-1}, 81.04 kPa CH_4, Ar used as internal standard)..... 57

Figure 2.7. Methane conversion as function of TOS (A), and hydrocarbon product formation rates versus TOS over 0.1 wt.% Fe/SiO_2-C (B), 0.1 wt.% Fe/SiO_2-V (C), the quartz blank (D). (NMC conditions: 1273 K, WHSV=3200 h^{-1}, 81.04 kPa CH_4, Ar used as internal standard)..... 59

Figure 2.8. TGA data (A) and TPO profile of CO_2 (B), and CO (C) of spent 0.1 wt.% Fe/SiO_2-C and 0.1 wt.% Fe/SiO_2-V catalysts. (NMC conditions: 1273 K, WHSV=3200 h^{-1}, 81.04 kPa CH_4, Ar used as internal standard, TOS of 5 h)..... 62

Figure 2.9. Characterization data of 0.5 wt.% and 1.5 wt.% Fe/SiO_2-V catalysts: (A) XRD patterns, (B) Raman spectra, (C) DR UV-vis spectra, and (D) H_2-TPR profiles. The characterization data for 0.1wt% Fe/SiO_2-V are included for comparison purposes. 65

Figure 2.10. XPS spectra of Fe 2p (A), Si 2p (B), and O 1s (C) of 0.5 wt.% and 1.5 wt.% Fe/SiO2-V catalysts. The characterization data for 0.1 wt.% Fe/SiO_2-V are included for comparison purpose..... 66

Figure 2.11. Methane activation over 0.5wt% (A) and 1.5wt% (B) Fe/SiO_2-V versus TOS tracked by a MS instrument. (C) and (D) show MS signals at TOS of <140 s in (A) and (B), respectively. (NMC conditions: 1273K, WHSV=3200 h^{-1}, 81.04 kPa CH4, Ar used as internal standard)..... 68

Figure 2.12. Methane conversion as function of TOS for 0.50 and 1.50 wt. % Fe/SiO_2-V (A) and hydrocarbon product formation rates versus TOS over 0.50 wt. % Fe/SiO_2-V (B) and 1.50 wt. % Fe/SiO_2-V (C) catalysts. (NMC conditions: 1273K, WHSV=3200 h_{-1}, 83.04 kPa CH4, Ar used as internal standard)..... 69

Figure 2.13. TGA data (A) and TPR profile of CO_2 (B) and CO (C) of spent 0.50 wt. % Fe/SiO_2-V and 1.50 wt. % Fe/SiO_2-V catalysts, the present of 0.1 wt. % Fe/SiO_2-V as comparison purpose. (NMC conditions: 1273K, WHSV=3200 h^{-1}, 83.04 kPa CH_4, Ar used as internal standard, TOS of 5 h)..... 71

Figure 3.1. Picture of fresh Mn/SiO2-v (A), Fe/SiO2-v (B), Co/SiO2-v (C), Ni/SiO2-v (D), and Cu/SiO2-v (E) catalysts. 84

Figure 3.2. Basic properties of fresh M/SiO_2-v (M = Mn, Fe, Co, Ni, and Cu) catalysts characterized by (A) XRD, (B) Raman spectra, (C) UV-vis DRS spectra, and (D) H2-TPR profile. 86

Figure 3.3. XPS spectra (A-E) and NEXAFS spectra (F-J) for fresh M/SiO2-v catalysts (M =Mn (A) and (F), Fe (B) and (G), Co (C) and (H), Ni (D) and (I), and Cu (E) and (J)). Reference oxides serve as empirical standards in NEXAFS spectra in (F)-(J). 92

Figure 3.4. XPS survey scan (A), and high-resolution scan of Si 2p (B), O 1s (C), and C1s, (D) for M/SiO_2-v catalysts. 93

Figure 3.5. Species revolution as a function of TOS in methane activation over M/SiO_2-v Mn (A), Fe (B), Co (C), Ni (D), and Cu (E) monitored by a MS. (NMC Condition: 1273 K, WHSV = 6400 h^{-1}, 81.4 kPa, Ar as internal standard)..... 95

Figure 3.6. Catalytic performance of M/SiO_2-v catalysts in NMC reaction: (A) methane reaction rate, (B) C_2 formation rate, (C) aromatics formation rate, and (D) coke formation rate. (NMC Condition: 1273 K, WHSV = 6400 h^{-1}, 81.4 kPa, Ar as internal standard) 96

Figure 3.7. CO_2 formation rate (A), CO formation rate (B), and O2 consumption rate (C) in TPO profile of spent M/SiO_2-v catalysts after 5 hours of NMC reaction. TPO profiles measured for spent catalysts as CO_2 formation rate (A), CO formation rate (B), and O_2 consumption rate (C), TPO peak temperature as effect of catalysts (D). 99

Figure 3.8. XANES and EXAFS spectra for fresh and activated M/SiO_2-v catalysts (M =Mn, Fe, Co, Ni, and Cu) for Mn (A-B), Fe (C-D), Co (E-F), Ni (G-H), and Cu (I-J)..... 105

Figure 3.9. XANE Spectra with the fitted curve for Fe/SiO_2-v (A), Co/SiO_2-v (B), Ni/SiO_2-v (C-D) to determine the catalyst site status. K-edge Fourier-transformed EXAFS spectra with the fitted curve for Mn (F-G), Co (H), and Cu/SiO_2-v (I) as the demonstration of the short-range coordination status of these catalyst sites. 106

Figure 3.10. Fourier transform (left panel) and Morlet Wavelet transform (right panel) for the k^2-weighted Co K-edge EXAFS signals for fresh Co/SiO_2-v (A), and metallic Co (B)..... 107

Figure 3.11. Thermal dynamic stability of metal silicate precursors described by their formation energies and melting/decomposition temperature of metal precursors. (Data were extracted from reference[298-307]) 109

Figure 4.1. Scheme of catalytic wall reactor testing aperture. 118

Figure 4.2. Picture of as-prepared Fe/SiO_2-CWR (A), and microstructure of as-prepared Fe/SiO_2-CWR in cross section view (B), and surface of Fe/SiO_2-CWR catalytic wall (C). 121

Figure 4.3. Methane conversion and species selectivity as a function of temperature for Fe/SiO2-CWRs (A), and species formation rate versus temperature (B), selectivity and methane conversion of CWR operated under 1273 K for 140 hours (C), and species formation rate of CWR operated under 1273 K for 140 hours. (NMC Condition: 1073-1273 K, 67.55 kPa, Ar as internal standard). 123

Figure 4.4. Catalytic performance of Fe/SiO_2-CWR tested between 1073-1373 K under different flow rates conditions. 4 mL/min CH_4 + 2 mL/min Ar (A), 2 mL/min CH_4 + 2 mL/min Ar (B), 2 mL/min CH_4 + 1 mL/min Ar (C). 124

Figure 4.5. Microstructure and morphology of carbon product formed in spent Fe/SiO_2-CWR under typical NMC reaction for 140 hours. (NMC condition: 1273 K, 67.55 kPa, Ar as internal standard). 126

Figure 4.6. Property of carbon product from spent Fe/SiO_2-CWR by Raman spectroscopy (A), and weight loss profile by TGA. 127

Figure 4.7. TPO profile of CO_2 (A), CO (B), and O_2 of spent Fe/SiO_2-CWR under NMC condition for 140 hours. (TPO conditions: 20 mg spent catalyst, 10 K/min under flow rate of 50 mL/min 10 % O_2/Ar). 129

Figure 5.1 Fundamental physiochemically properties of as-prepared Co catalysts characterized by XRD (A), zoomed in XRD peak in 5-10° 2theta (B), zoomed in XRD peak in 20-25° 2theta (C), N_2 isotherm of Co-DeAl-BEA catalysts (D), N_2 isotherm of Co-BEA-300 and Co-SBA-300 (E). 143

Figure 5.2 Coordination environment and status of Co catalysts sites characterized by UV-vis DRS (A), and H_2-TPR profile of Co-DeAl-BEA catalysts. 144
Figure 5.3. Catalytic performance of Co-DeAl-BEA under NMD conditions demonstrated methane conversion (A), H_2 formation rate (B), long term stability (C), and reaction activation energy measured from 723 K to 823 K (D). (NMD reaction conditions: 0.375 g catalyst, 773 K, WHSV=6400 h^{-1}, 10 mL/min 50 % CH_4 balanced in Ar as internal standard). 148
Figure 5.4. Microstructure and morphology of spent Co-DeAl-BEA catalysts after 8 hours of NMD. SEM images of CNTs distributions (A), (D), (G), (J), and (M), TEM image of CNTs morphology (B-C), (E-F), (H-I), (K-L), and (N-O). 154
Figure 5.5 Spent catalysts analysis after 8 hours NMD reaction at 773 K by TGA (A), and TPO profile of CO_2 evolution signal (B), CO evolution signal (C), and O_2 consumption signal (D). 157

List of Abbreviations

ATR	Auto thermal reforming
BEA	Zeolite BEA
CNSs	Carbon nanospheres
CNTs	Carbon nanotubes
C_2H_2	Acetylene
C_2H_4	Ethylene
C_2H_6	Ethane
CO	Carbon monoxide
CO_2	Carbon dioxide
C_6H_6	Benzene
C_7H_8	Toluene
$C_{10}H_8$	Naphthalene
CAR	Catalytic wall reactor
CU	Carbon utilization efficiency
DI	Deionized
DeAl-BEA	Dealuminated zeolite BEA
DOE	U.S. Department of Energy
DR UV-vis	Diffuse reflectance UV-vis spectroscopy
DRM	Dry reforming of methane
EIS	Electrochemical impedance spectroscopy
EXAFS	Extended X-ray absorption fine structure
FID	Flame ionization detector
FT	Fischer Tropsch
FWHM	Full width at half maximum
GC	Gas Chromatography
H_2	Hydrogen
H_2-TPR	Hydrogen-temperature programmed reduction
HDPE	High-density polyethylene
ICP-OES	Inductively coupled plasma-optical emission spectrometry
ktoe	Kilotonnes of oil equivalent
MS	Mass spectroscopy
MWCNT	Multiwall carbon nanotube
NEXAFS	Near-edge X-ray absorption fine structure
NMC	Non-oxidative methane coupling
NMD	Non-oxidative methane decomposition
NSLS-II	National Synchrotron Light Source II
OCM	Oxidative coupling of methane

PFY	Partial fluorescence yield
POM	Partial oxidization of methane
POX	Partial oxidization
ppm	Parts per million
SACs	Singel-atom catalysts
SBA-15	Santa Barbara Amorphous-15 silica
SEM	Scanning electron microscope
SMR	Steam methane reforming
TCD	Thermal conductivity detector
tcf	Trillion cubic feet
TEM	Transmission electron microscopy
TEY	Total electron yield
TGA	Thermogravimetric analysis
TOS	Time on stream
TPO	Temperature-programmed oxidation
VLS	Vapor-liquid-solid
WGS	Water-gas shift
XAFS	X-ray absorption fine structure
XANES	X-ray absorption near-edge structure
XPS	X-ray photoelectron spectroscopy
XRD	X-ray powder diffraction

Chapter 1: Introduction

1.1 Motivation of Methane Upgrading

The advancement of human civilization over the past two centuries has led to the production and release of massive amounts of greenhouse gases into the atmosphere, significantly affecting the environment. A key contributor is carbon dioxide (CO_2). According to the Global Monitoring Laboratory's annual report, atmosphere CO_2 concentration has already reached a dangerous level of 421 parts per million (ppm) by the end of 2023[1]. The growth has been 50% since the Industrial Revolution in the 1800s, primarily due to the reliance on fossil fuels for industrial operations, urban heating, and transportation. The elevated levels of CO_2 in the atmosphere contribute to a host of complex environmental problems, including global warming[2], which in turn threatens our climate, oceans, and ecosystems[3-5]. Immediate action is required to reduce CO_2 emissions. In response to this urgent need, the concept of a net-zero economy has been proposed, aiming to significantly reduce CO_2 emissions and ultimately achieve a balance where the amount of CO_2 emitted is equal to the amount removed from the atmosphere. This strategy involves all human activities, including transportation, energy production, and industrial processes. Achieving net-zero emissions has become a critical development strategy for numerous countries, including the United States, Germany, and China. Currently, efforts are being made worldwide to advance towards this goal through developing essential technologies,

formulating new energy policies, and designing innovative energy frameworks to support the objective of net-zero emissions.

To achieve future net-zero emissions for human activities, there is an essential push towards developing technologies that seek CO_2 reduction in the comprehensive energy chain, from energy production to supply, storage, and recycling. Among them, the most effective way to reduce CO_2 emissions is adopting carbon-free, renewable energy sources to replace conventional fuels but also aim to capture and convert current CO_2 emissions into valuable hydrocarbons, thereby fostering a sustainable carbon cycling economy. In the various non-fossil fuel-based energies under development, hydrogen energy emerges as a leading candidate to propel the world towards net-zero emissions. Because of its abundance, clean, renewable, and higher heat combustion value than conventional fossil fuels, hydrogen stands out as an ideal candidate for powering future transportation, industrial, and residential needs. Deploying hydrogen fuel cells, which convert hydrogen into electricity with high efficiency and energy density under moderate conditions, is critical in energy networks to achieve net-zero emissions[6, 7].

Although hydrogen is a rich element in the earth, relying on current technologies to produce large amounts of hydrogen as a renewable fuel is not feasible. At present, hydrogen is primarily extracted from reforming processes with high energy penalties and creates significant CO_2 emissions, contradicting the goals of net-zero emissions. The recently proposed variety of innovative technologies, such as photocatalysis and electrolysis of water, presents a cleaner alternative. Still, it is limited by its high equipment costs, materials costs, and substantial power requirements. The

source must be abundant, and processing costs must remain low as the prerequisite to enable large, affordable hydrogen to become available. To avoid CO_2 emissions, if carbon-containing raw materials are used, it is essential to consolidate the carbon to liquid or solid form when processing the energy or powder. Based on these ideas, non-oxidative methane upgrading is a promising strategy to separate hydrogen and carbon without CO_2 emissions. It could produce hydrogen at a cost that supports net-zero emission goals if scaled up with profits. This method promises a cleaner way to utilize methane and aligns with the transition toward cleaner fuel options.

Beyond hydrogen production, non-oxidative upgrading methane to hydrocarbons is also an option for fully utilizing carbon resources while addressing the growing demand for petroleum chemicals amidst expanding human activities and economies. Daily, vast quantities of petroleum chemicals like gasoline, diesel, paraffin, aromatics, lubricating oil, and heavy oils are refined, serving many human needs across transportation, packaging, pharmaceuticals, defense, and construction sectors. With petroleum being a non-renewable resource at risk of depletion based on current consumption rates and given the high energy input and greenhouse gas emissions associated with petroleum refinement, there is an urgent need to develop alternative, emission-free chemical processing methods. Adopting non-oxidative conditions for methane upgrading into hydrocarbons represents a promising technology that meets the demands for future chemical production and adheres to net-zero emission principles.

1.2 Conventional Use of Methane as Feedstock: A Brief History

Natural gas, recognized early in history, was initially used in Europe during the early 1800s as a source of light and residential heating[8]. Its transformation into a critical industrial feedstock began with the development of steam reforming of methane in the 1930s[9]. This period marked the preference for natural gas over coal for steam reforming, mainly due to the established natural gas pipeline infrastructure and the introduction of catalysts that significantly enhanced the conversion of methane to syngas (a mixture of hydrogen and carbon monoxide, with a small amount of carbon dioxide). Syngas are a useful fuel and essential feedstock for metallurgy, the petroleum industry, and ammonia synthesis, which enhances the steam methane reforming (SMR) as a critical industrial process. By 2020, global hydrogen production reached 87 million tons, with the SMR process accounting for over 68 % of this output[10]. Today's SMR technology is sophisticated and designed to produce syngas with precise compositions at competitive costs—approximately \$1.2 to \$3.0 per kilogram, excluding CO_2 capture[11].

Beyond hydrogen production, the conversion of syngas into more valuable chemicals became feasible in the 1920s, with processes developed for synthesizing methanol and long-chain hydrocarbons. Germany launched the world's first commercial-scale syngas-to-methanol plant in 1923[12]. The later advances in materials, reactor designs, and catalysts enabled more efficient syngas to methanol processes developed in the 1970s[12]. By 2018, the global capacity of over 90 plants reached 110 million tons[13], becoming the dominant methanol production process. The Fischer-Tropsch (FT) process, developed in the late 1920s, provided a path to convert syngas

into valuable hydrocarbons like diesel, wax, and gasoline[14]. During World War II, Nazi Germany used the FT process to manufacture synthetic fuels, generating roughly 130,000 barrels between 1939 and 1945. This production largely met the demand for traditional chemicals, gasoline, and wax, especially when access to petroleum resources was constrained[15]. Modern FT processes operated by most major oil companies, including Sasol and Shell, established methane to be used in higher-valued hydrocarbons, which is extremely promising for regions with limited petroleum resources.

Although the current methane used as feedstock is well-developed and dominates the current hydrogen production, the critical disadvantages of current methane utilization cannot be ignored, such as low efficiency, high energy penalty, complexity reactions, and high CO_2 emissions, which could limit its development when the cost of CO_2 capturing is accounted for. Addressing these disadvantages and aligning them with the net-zero emission goal requires methane utilization with a much simpler process path, high carbon utilization, and CO_2 emission-free, which is still under development.

1.3 Abundance of Methane

The critical element of methane upgrading to hydrogen, hydrocarbons, and value-added chemicals depends on the base reserves of methane availability and the price. Notably, Earth's subsurface is rich in natural gas, the presence of both conventional non-associated and associated gases, which constitute the primary sources of natural gas extraction today, located beneath geological seals[16]. However, it is

essential to recognize that these conventional reserves account for a small segment of the overall natural gas endowment and have been extracted. In contrast, the non-conventional gas reserves, comprising tight sand gas, gas-rich shale, and coalbed methane, are collectively estimated to contain between 1503 and 2500 trillion cubic feet (tcf)[17] but have not yet been extracted due to requiring advanced drilling technology. Additionally, the reserves of methane hydrates are believed to encompass an extraordinary volume ranging from 100,000 to 1,000,000,000 tcf[17]. These hydrates are primarily situated in continental margins beneath oceans and within permafrost sandstone, where the current extraction has not yet been realized due to the significant technological challenges involved[17]. The exploration and utilization of unconventional gas reserves stand at the forefront of strategic development within the natural gas sector. The shift towards these reserves heralds a significant phase in diversifying and expanding global energy resources, contingent upon overcoming the technical hurdles associated with their extraction in the next 100 years. This paradigm shift underscores the imperative for continuous innovation in drilling and extraction technologies aimed at unlocking the vast potential of unconventional gas to meet burgeoning energy demands.

The exploration and development of unconventional natural gas resources, including shale and tight gas, have seen significant advancements over the past few decades. An important breakthrough in drilling technologies in the United States has set the stage for shale gas to become the dominant gas source since 2020, occupying approximately 50 % of overall gas production[18]. The projections demonstrated increasing nearly 120 tcf of total gas production by 2050, where ¾ comes from shale

gas. This provides sufficient evidence for future natural as abundant, low-cost feedstocks.

Beyond traditional extraction methods, natural gas can also be sourced from sustainable practices, such as converting landfill waste, food waste, and wastewater into biogas and digestates through anaerobic digestion processes[19, 20]. This technique is exceptionally viable in rural areas for converting agricultural and animal waste into biogas. Predominantly composed of methane, biogas emerges as a renewable energy source that can significantly lower the costs associated with energy production and supply while simultaneously reducing greenhouse gas emissions. The potential of biogas as a renewable energy source is underscored by estimates projecting its growth to 32 kilotons of oil equivalent (ktoe) per year by 2022, an 88% increase from 2012[21]. Europe and Asia lead in biogas production, with the United States also showing a steady rise in production capabilities. The potential for expanding the biogas market in the United States is particularly notable, given the country's large-scale, technologically integrated agricultural and farming sectors, which can efficiently minimize the costs of collecting organic waste for biogas production, expect to expand 3-5 % of total natural gas market[22]. In summary, the prospects for the future utilization of natural gas, both from conventional drilling and sustainable biogas production, appear promising. The ability to harness methane from diverse sources enables methane to be an affordable, abundant, well-dispersed location, suitable feedstock for clean hydrogen and value-added hydrocarbon production.

1.4 Strategies of Methane Upgrading for Net-zero Emission

Methane used as feedstock for upgrading to hydrogen and hydrocarbons is a promising reaction to create value-added chemicals and hydrogen. As previously introduced, the increasing demand for renewable, green hydrogen as the primary power source can be expected worldwide to reduce CO_2 emissions. Meanwhile, petroleum, as a non-renewable resource, faces risks of depletion. Therefore, looking for alternative ways of processing petroleum chemicals without emission means significant net-zero emission development. The methane upgrading to value-added hydrocarbons could be incorporated into the renewable hydrogen economy to fulfill necessary needs and indirectly reduce CO_2 emissions, as demonstrated in **Figure 1.1**[23]. The general picture shows that methane upgrading is primarily used for hydrogen and value-added hydrocarbon production, with unconventional techniques such as solar, wind, nuclear, and geothermal as the auxiliary. The hydrogen upgraded from methane can be directly used as a fuel cell for power generation for the energy network and transportation fuel. To achieve this, it is necessary to understand and analyze the methane upgrading technologies. This section provides a systematic overview of the currently developed technologies for methane upgrading, including indirect and direct methane upgrading. The contrast of these technologies will be discussed as part of this dissertation design.

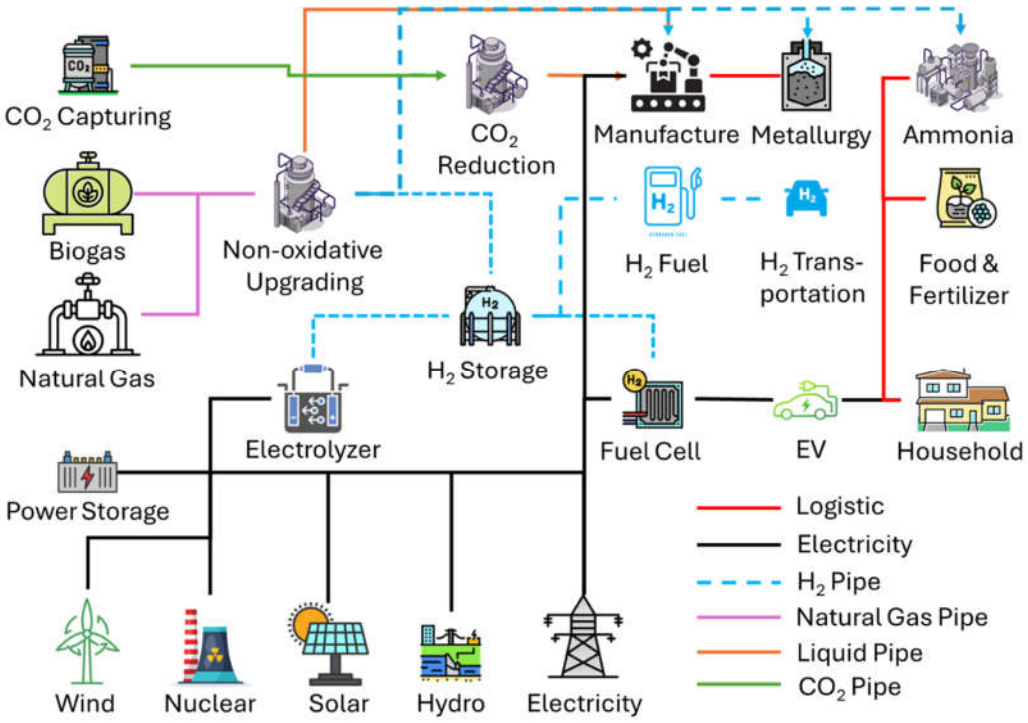

Figure 1.1. The energy network adopted hydrogen as a future renewable energy source, incorporating methane upgrading strategies (the original energy network design was proposed in the literature[23]).

1.4.1. Indirect Methane Upgrading to Hydrogen

Methane as the feedstock can be upgraded to syngas (carbon monoxide and hydrogen), the process known as SMR can be expressed as below[24]:

$$CH_{4(g)} + H_2O_{(g)} \leftrightarrow CO_{(g)} + 3H_{2(g)} \quad \Delta H_f^\circ = +206.17\ kJ/mol \qquad (1.1)$$

Hydrogen can be furtherly extracted from the syngas by water gas shift reaction with greenhouse emission:

$$CO_{(g)} + H_2O_{(g)} \leftrightarrow CO_{2(g)} + H_{2(g)} \quad \Delta H_f^\circ = -41\ kJ/mol \qquad (1.2)$$

Due to the reaction in **eq. 1.1** is highly endothermic and requires external thermal energy to drive the reaction. Typically, commercial SMR is driven by another

combustion reaction with heat recovering from the fuel gas convection to reach higher efficiency and maintain profitability; the process is also known as auto thermal reforming (ATR). The typical SMR is performed at 973-1173 K under 20-40 bar pressure to avoid coking on the catalysts[25]. Using catalysts such as supported single or bimetallic Co[26], Fe[26], Ni, and Ru[27] can effectively promote the reaction by activating the C-H bonds and boosting the reaction kinetic. The reaction mechanism undergoes a surface catalysis route: methane absorbs over the catalyst surface to weaken the C-H bonds. It is uncleaned by the surface adsorbed OH or O sites to form hydrogen and CO. The rate determination is the adsorption of methane, which means the main challenge is still methane activation. The CO_2 was also generated in the side reaction by continuous reforming of CO with the stream, which was often used to adjust the H_2/CO ratio, as an essential parameter of syngas determines its further applications. The overall SMR can reach a high hydrogen yield efficiency of around 74 % with an estimated cost of $ 1.8 per kg of hydrogen[28]. This process is currently the most popular hydrogen acquisition method because of its low capital cost. However, the drawback of SMR is that the reaction towards hydrogen will be harmful to the environment in the long term due to the significant CO_2 emissions as carbon footprint, which contradicts the goal of net zero emission[29]. The future SMR could use biomethane, a renewable energy that effectively reduces greenhouse gas emissions. However, the overall process still cannot avoid CO_2 emissions. When CO_2 emission price increases, traditional SMR will no longer be more profitable in addition to emission-free technologies. The hope is to combine CO_2 capturing technology with SMR to reduce CO_2 emissions and convert to more value-added fuel.

Alternative way such as dry reforming of methane (DRM) was proposed to produce syngas using CO_2 to reform methane via the below equation[30]:

$$CH_{4(g)} + CO_{2_{(g)}} \leftrightarrow 2CO_{(g)} + 2H_{2(g)} \ \Delta H_f^\circ = +247.3 \text{ kJ/mol} \quad (\mathbf{1.3})$$

Ideally, the CO_2 can be reduced to valuable hydrocarbons. This more endothermic reaction than SMR requires a high operating temperature above 973 K[31] to reach profitable methane conversion and avoid coke formation. The major challenge remaining in the DRM is the coking caused by the boundary reaction over the catalyst, which typically has a low CO_2 removal rate and causes rapid coke formation[32]. Because of this, DRM is still on the trip of extensive adoption, but the small-scaled has been established since the 1990s[33]. DRM currently uses two processes: CALCOR[34] and SPARG[35]. The CALCOR process pursues maximum CO production, which is feasible to avoid coke thermodynamically[36]. Thus, the product typically has a low H_2/CO ratio and can be purified to nearly 99 % CO after CO_2, H_2, and H_2O recovery[34]. In the SPARG process, a sulfur poisoning strategy was used to prevent coking on catalysts by sacrificing reaction rate and overall activity. Both CALCOR and SPARG were developed to overcome the coke formation. The high CO production remains a small market; hence, the DRM is not ideal for producing hydrogen. The future direction of DRM is aimed at a more broadly applicable process with a more comprehensive understanding of coke formation to assist catalyst design.

To improve the energy efficiency of syngas production, partial oxidization of methane (POM) was proposed with better energy efficiency operated under less intense condition (773 - 1173 K) for syngas synthesis[37-39], the reaction can be express as following:

$$CH_{4(g)} + \frac{1}{2}O_{2(g)} \leftrightarrow CO_{(g)} + 2H_{2(g)} \ \Delta H_f^\circ = -36\ kJ/mol \quad (\mathbf{1.4})$$

The overall reaction is exothermic with energetic benefits, which makes the POM more competitive than SMR in modern industry. The reaction uses oxygen to cleave the C-H bond, and the water-gas shift reaction formed the CO and H_2 as the secondary reforming since oxygen is a much more potent oxidizer than CO_2 and H_2O. In commercial-scale POM, a reaction at high temperatures is required to pursue a high yield of syngas and hydrogen, but this might jeopardize the activity of catalysts. Therefore, in some commercial-scale facilities, POM was operated under high temperatures and pressurized conditions without catalysts, known as partial oxidization (POX)[40].

Given the high operating temperature of POX[37], ATR can be designed with SMR and POX incorporated to reach thermal neutrality, which requires no external heat to achieve high efficiency. This enables ATR to generate syngas cost-effectively, making ATR promising and attractive in the industry[41]. However, the challenges remain in the ATR, such as harsh reaction conditions and the cost of equipment, raising the high capital costs in the current ATR process (based on the unit hydrogen cost)[42]. ATRs are expected to be more cost-effective than SMRs when an extensive CO_2 capture system can be incorporated to convert CO_2 into value-added syngas and fuel[43], where the future SMR economy will depend on the cost of CO_2 capturing[11]. When the CO_2 capturing cost increases, ATR will become more competitive than conventional SMR to reach near-neutralized CO_2 emission. In European countries, ATR will become the leading new blue hydrogen production route, combining CO_2 emission reductions in the next few years.

1.4.2. In-direct Methane Upgrade to Alcohol and Hydrocarbons

Syngas from the in-direct methane conversion, such as SMR, POM, POX, and ATR, can further convert to hydrocarbons and alcohols via the FT process and syngas reduction. A suitable H2/CO ratio is required for the specific process to govern the formation of different products. The dominated hydrocarbons can be adjusted since the SMR and different reforming processes produce syngas with different H2/CO ratios. Here, a product range of syngas as feedstock for FT and syngas reduction is shown in **Table 1.1.** below, indicating the methane upgrading to alcohol, hydrocarbons, and hydrogen-based on specific H_2/CO ratio[44].

Table 1.1. Application of syngas as feedstock to downstream products based on different H_2/CO ratio[44].

Feedstock	H_2/CO	Process	Downstream	Further Downstream
Syngas	≤ 1	Ethanol	Ethanol	Variety of industrials
	~ 2	Methanol Conversion	DME	Gasoline
			Ethylene,	Polymers materials,
			Acetic Acid	Ketene, acetic ester,
			Methyl acetate	Acetic anhydride, fine
			Formaldehyde	Resin, polymers,
	≥ 2	Fischer-Tropsch	Wax	Variety of industrials
			Diesel-Kerosene	Fuel
			Gasoline	Fuel
			Naphtha	Ethylene, reforming,
	≥ 50	Hydrogen	Hydrogen	Refinery, metallurgy,
			Power	Gas turbine, fuel cell

Methanol is the most considerable downstream alcohol from syngas. The process typically requires a 2:1 H_2/CO ratio for methanol formation and follows the stereochemistry of syngas from SMR. As for the reduction of CO by H_2, the reaction

was carried out under 5-20 MPa at 423-523 K over supported Cu and Zn-based catalysts[38, 45]. The general reaction can be expressed as below[46]:

$$CO_{(g)} + 2H_{2(g)} \leftrightarrow CH_3OH_{(g)} \ \Delta H_f^\circ = -90.7\ kJ/mol \quad (\mathbf{1.5})$$

Methanol produced from syngas is the essential precursor for higher-valued downstream products, such as formaldehyde, plastic, and fibers. The current methanol production has reached 110 million metric tons annually[47], and it is estimated to increase the market size to fossil level in the next 10 years[48]. The low cost of natural gas and future syngas technology enables methanol obtained from syngas to become the most popular process adopted by industries to obtain methanol. However, the conventional method is not emission-free. The estimate shows that approximately 97-110 g CO_2 eq/MJ carbon footprint was obtained for most state-of-the-art alcohol production from natural gas[49]. Hence, an alternative method to produce methanol with a CO_2 emission-free or CO_2-neutralized path is needed, such as CO_2 capturing combined CO_2 reduction to the technique, which is still under development.

For the indirect methane conversion to higher hydrocarbons, the FT process requires syngas with higher (≥ 2) H_2/CO as the essential process used to convert syngas to olefins. The below (unbalanced) reaction can express the general reaction of FT:

$$2(n+1)H_{2\,(g)} + n\,CO_{(g)} \rightarrow C_nH_{(2n+2)} + n\,H_2O_{(g)} \quad (\mathbf{1.6})$$

The FT process is typically carried out over Fe[14], Co[14, 50-52], and Ru-based catalysts[14, 53] under high pressure (20-40 bar) to promote the reaction and make the process profitable. The typical products from FT highly overlap with the chemicals from petroleum refinement, with even less sulfur contamination, including light olefins, low-sulfur diesel, gasoline, synthetic wax, and aromatics[54]. The H_2/CO ratio

plays a vital role in determining the length of hydrocarbon yield. For example, in the case of high-temperature FT at 573- 623 K, C_1-C_{15} hydrocarbons and olefins can be obtained using a low H_2/CO ratio (<< 2). In low-temperature FT conditions at 473 - 523 K, a board range of hydrocarbons C_1-C_{100} can be obtained with a high H_2/CO ratio (1.75-2) feed[55]. Therefore, the FT process can be a significant means to the region with limited petroleum resources. In terms of efficiency, although the FT process produces hydrocarbons, the efficiency of carbon utilization remains low, around 50 %[56, 57]. This means a high carbon footprint remains for FT, with considerable carbon emitted as CO_2. The modern commercial-scale FT facilitated has already developed several successful plants by major oil companies. The future FT process will expand the feedstock capability, such as biomass and CO_2 to reduce the total carbon footprint.

1.4.3. Direct, Methane Upgrading to Hydrocarbons

Direct methane upgrading was proposed as the competitive process to substitute the conventional, multiple steps involved in methane upgrading to hydrocarbons. Direct methane conversion undergoes a single step converting methane to hydrogen or hydrocarbons. However, the reaction faces a few challenges, such as the high stability of methane and efficient catalysts. Given the high stability of methane, the direct approach using oxygen to active C-H bond was attempted at the beginning of 1980s[58, 59], known as the direct, oxidative coupling of methane (OCM) reactions, which can be expressed as below equations:

$$2CH_{4\,(g)} + \frac{1}{2}O_{2\,(g)} \rightarrow C_2H_{6(g)} + H_2O_{(g)}\ \Delta H_f^\circ = -177\ \text{kJ/mol} \qquad (\mathbf{1.7})$$

$$C_2H_{6\,(g)} + \frac{1}{2}O_{2\,(g)} \rightarrow C_2H_{4(g)} + H_2O_{(g)}\ \Delta H_f^\circ = -150\ \text{kJ/mol} \qquad (\mathbf{1.8})$$

The process is attractive because of its single step to yield light olefins, which is much simplified than conventional processes such as FT and petroleum cracking. The reaction is exothermic in thermodynamics but limited by the kinetic, which requires efficient catalysts. Typical catalysts used for OCM includes supported oxides such as: Mn-$NaWO_4/SiO_2$[60], PbO/Al_2O_3, and $La_{0.8}Sr_{0.2}Ga_{0.8}Mg_{0.2}O_{3-\delta}$[61]. The perovskite oxide catalysts have recently become attractive for OCM due to the high structural defects that favor methane activation[62], oxygen transports[62], and its distinguished thermal stability[62]. To reduce the coke formation, the reaction conditions were carried out under high temperature (973-1173 K) and pressure (up to 250 kPa); however, this required high thermal stability of catalysts and reactor[63]. Another challenge regarding OCM is that the C2 formation undergoes a gas-phase radical reaction route, where side reactions are hard to avoid. Methane radicals are active species that react with H_2O in the gas phase and can jeopardize the C_2 by forming CO_2, which is impossible to prevent because forming CO_2 is more favorable in thermodynamics[64]. Although evidence shows CO_2 could increase the selectivity of C_2[65], the total conversion is decreasing with the side reaction promotion. Besides, water can reform the C_2 to contribute to the formation of CO. The reaction system undergoes combined surface and gas phase routes[66], and suppressing the side reactions in OCM is challenging. The progress of commercial-scale OCM is still under development. The current OCM can reach 40-50 % methane conversion[67] with 60-70 % C_2 olefins selectivity[68-70], which produces C_2 higher than conventional process[63, 71]. Despite catalyst design, technical challenges such as reactor design and process optimization make commercial-scaled OCM profitable. The possible strategies can be applied to

reduce the effect of side reactions and promote the hydrocarbon formation for OCM, such as designing efficient catalysts to produce dissociated oxygen, using a membrane reactor to deliver oxygen ions, removing CO_2 and C_2 products to shift the reaction[63, 72] to make the overall process become profitable.

1.4.4. Direct, Non-oxidative Upgrading Methane Towards Hydrocarbons and Hydrogen

Methane can be directly coupled to various hydrocarbons via a non-oxidative methane coupling reaction (NMC). The absence of oxygen enables an overall emission-free process, potentially reaching 100 % of carbon utilization. NMC produces a variety of essential hydrocarbon products such as C_2 olefines (Acetylene, ethylene, and ethane), aromatics (benzene, toluene, and naphthalene), and hydrogen, which is a promising path for these essential hydrocarbons acquisition alternative to the conventional petroleum chemicals. The reaction can be generally expressed via the several equations shown as below:

$$2CH_{4\,(g)} \rightarrow C_2H_{4(g)} + H_{2(g)}\ \Delta H_f^\circ = +202.2\ \text{kJ/mol} \quad (1.9)$$

$$6CH_{4\,(g)} \rightarrow C_6H_{6(l)} + 9H_{2(g)}\ \Delta H_f^\circ = +498.2\ \text{kJ/mol} \quad (1.10)$$

$$10CH_{4\,(g)} \rightarrow C_{10}H_{8(s)} + 16H_{2(g)}\ \Delta H_f^\circ = +825.7\ \text{kJ/mol} \quad (1.11)$$

The product selectivity can be towards differently depends on the reaction condition and catalysts. However, the reactions are highly endothermic in thermodynamically and limited by kinetic, which requires considerable energy impute and effective catalyst to promote the reaction, respectively. Consequently, challenges

have emerged such as spontaneous coking[73, 74], catalyst sintering[75], and high cost of equipment which significantly drag down the commercial scaled NMC development. Although the challenges regarding NMC has not yet been fully resolved, the promising features of NMC have never been shaded. NMC will become attractive in small-medium onsite processes to produce hydrocarbons for the regions with high cost of petroleum chemicals. The NMC could be more attractive than the conventional methane upgrading process when emissions cost will be accounted[76]. The one-step reaction of NMC is also an advantage over conventional processes. These competitive features of NMC enable it to become the most promising and attractive topic in research and commercial interests.

Methane can be decomposed to hydrogen and solid carbon under non-oxidative methane decomposition (NMD) process, which has recently received intensive attention due to the growing need for hydrogen for future renewable energy to meet zero-emission. Methane is the ideal feedstock with abundant reserve, affordable price, and high hydrogen content. The ultra-pure, CO_X-free hydrogen, and solid carbon can be produced via the following reaction without greenhouse emission[77]:

$$CH_{4\,(g)} \rightarrow C_{(s)} + 2H_{2(g)}\ \Delta H^{\circ}_{f} = +75\ \mathrm{kJ/mol} \quad (1.12)$$

The reaction is endothermic which requires energy input to drive. Under the promotion of catalysts such as supported Ni catalysts, the reaction temperature can rapidly decrease as low as 773 K[77]. However, the reaction faced the critical challenge of catalyst deactivation, which inhibited commercial-scale methane decomposition. The technological-economic evaluation of NMD exhibited a promising future in that NMD can be profitable and suitable to produce hydrogen on a small/medium industrial

scale[78]. However, the current price of hydrogen from NMD is still higher than that of SMR. To make NMD profitable, conducting necessary studies and resolving technical issues in catalysis and reaction engineering are required before the commercial-scale development of NMD[76]. In the meantime, carbon as a by-product can also contribute to NMD profits. The different morphology/structure of carbon can be obtained depending on the reaction conditions. The NMD will become more economical and profitable when valued carbon products such as carbon nanotubes (CNTs) can be produced, which have the potential for the carbon materials market.

1.5 Direct, Non-oxidative Methane Upgrading: Reaction Overview

The abundance of methane with grown shale gas mining in the next 30-50 years is expected to support low-price methane as a hydrogen and hydrocarbon production feedstock under non-oxidative conditions with CO_2 emission-free. Both reactions for methane upgrade to hydrogen or hydrocarbons are endothermic and unfavorable in thermodynamics, which requires intensive energy input, shown in **Figure 1.2 A** and reaction **equation 1.9-1.11**. From the thermodynamics data, the formation of hydrocarbons to reach equilibrium requires extremely high temperatures beyond 1200 K, where the methane decomposition to carbon reaches zero Gibbs free energy much faster, around lower 1000 K to spontaneous. This demonstrated that coke formation is more thermodynamically favorable than forming hydrocarbons, which can be a significant challenge that needs to be addressed when moving toward hydrocarbon formation. The calculation also shows the maximum allowance of thermodynamic

equilibrium for methane upgraded to hydrocarbons, typically smaller than hydrogen, in **Figure 1.2 (B)**[79].

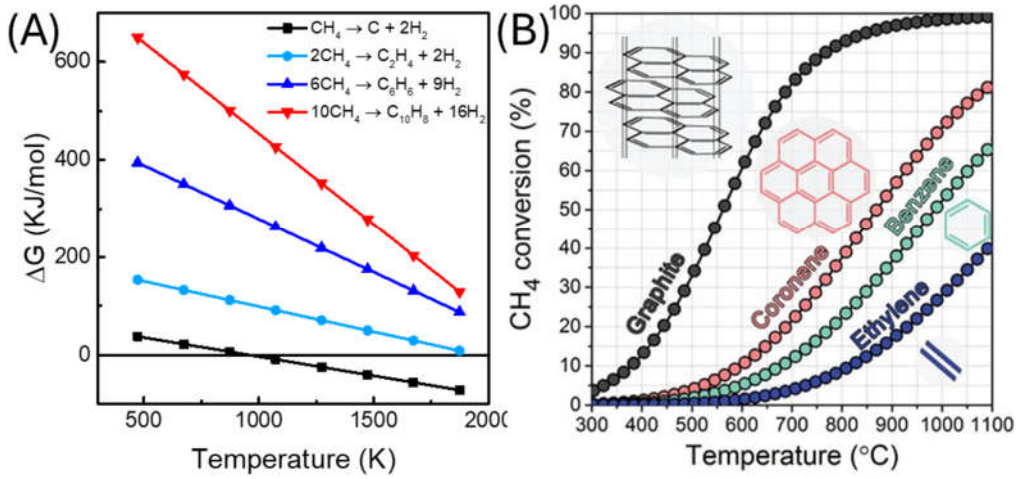

Figure 1.2. Thermodynamic data of typical non-oxidative methane conversions to carbon, hydrogen, ethylene, and aromatics. (A) Gibbs free energy of non-oxidative methane reactions as a function of temperatures (Data adapted from NIST Chemistry Web Book[80]), (B) Equilibrium conversion of non-oxidative methane coupling reactions (cited from literature[79]).

Besides the thermodynamic limitations, the reaction is an equilibrium-limited reaction. As the reaction equations described in **equations 1.9-1.12.**, the overall volume is expanding towards forming value-added hydrocarbons and hydrogen. Pressuring the system will result in a reaction backward from the equilibrium condition, thus reducing the total conversion. The equilibrium conversion of methane to hydrocarbons drops if the system is pressurized, the reaction will fall into a much lower equilibrium conversion and take very long to reach actual conversion[81]. To address the dilemma of

reaction suppressed by equilibrium limitation, previous studies have pointed out that if hydrogen as the byproduct can be removed via a hydrogen-permeable reactor, the reaction can be further shifted to break the limitation of equilibrium. Attempts have been made to use perovskite oxides such as Eu-doped $SrCeO_3$ as the hydrogen permeable membrane to demonstrate shifted equilibrium to elevate hydrocarbon yield successfully[82-85].

The direct, one-step NMC reaction to hydrocarbons is much simpler than the conventional gas-to-liquid (GTL) process. It can be foreseen that the NMC can significantly reduce the cost of operation and maintain a conventional process. The goal is converting methane into useful hydrocarbons, making neither coke nor CO_2. The carbon utilization efficiency for NMC can be evaluated as the selectivity of hydrocarbons, compared with the conventional GTL as below:

Carbon utilization (CU) efficiency of NMC:

$$\eta_{CU-NMC} = Hydrocarbons\ selectivity\ (C-atom\ basis) = 99\ \%\ ^{86} \quad \textbf{(1.13)}$$

Carbon utilization efficiency [87] of GTL:

$$\eta_{CU-GTL} = \frac{Converted\ Hydrocarbons\ (C-atom\ basis)}{Total\ Feeded\ CO} = 60\ \% \quad \textbf{(1.14)}$$

Kinetic limitation is another critical challenge to NMC. Without catalysts present, the formation of hydrocarbons typically requires a much higher temperature beyond 1500 K with a very minimum methane conversion. Applying an effective catalyst can significantly reduce the reaction temperature and boost the reaction rate by creating a catalytic path; the detailed discussion is available in the subsequent section and chapters 2 and 3.

Regarding methane upgrading to hydrogen and carbon, the reaction also faces challenges in thermodynamics, as described in section 1.4.4. The reaction has hydrogen formation enthalpy (+75 kJ/mol), which requires high energy impute but much less than NMC. The energy efficiency of the methane upgrade to hydrogen (~ 51 %) is much smaller than conventional SMR (~ 89 %) due to no CO_2 emission[76]. Similar to NMC, the reaction is also equilibrium limited due to the formation of hydrogen causing the pressure build-up, which depresses the truth equilibrium conversion[76, 88]. When pressure builds up, the equilibrium conversion will shift to lower due to the reaction reversal, where the hydrogen starts reforming the carbon back to methane. This can significantly limit the formation of hydrogen. Although the methane decomposition to hydrogen and carbon is more favorable than NMC, the reaction is also limited by kinetic as the high stability of methane requires high energy impute to active C-H bond. A suitable catalyst can significantly reduce the reaction temperature by reconfiguring the reaction path with much lower activation energy and rapidly improving the reaction rate. The detailed discussion will be continued in section 1.7 and further chapters.

1.6 Catalysts Development for Non-oxidative Methane Upgrading

1.6.1 Early Development of Catalysts and Methane Activation

The origin of non-oxidative methane upgrading can be traced to the early thermal decomposition of methane without catalysts. Bone et al. first demonstrated the thermal decomposition of methane to obtain unsaturated hydrocarbons, hydrogen, and

coke in Berlin porcelain tubes up to 1273 K[89]. Due to the absence of a catalyst, the reaction received a low selectivity of hydrocarbon yield. Similar results were observed by Jones using thermal treatment to decompose methane in a quartz reactor, and a trace amount of olefins was obtained[90]. Such low conversion and selectivity can be attributed to the absence of a catalyst, and Kassel agreed that it's impossible to reach equilibrium without catalysts[91]. Besides the conventional thermally non-catalytic methane upgrading, Jones first reported that platinum wire electric sparking could decompose methane but received a very minimum higher hydrocarbon yield of less than 10 %[90]. Storch reported that a carbon filament lamp was designed to decompose methane from temperatures ranging from 1730-1973 K, which can effectively form C_2 hydrocarbons, thus reducing the coke selectivity. Although the non-catalytic methane upgrading is inappropriate for reaction promotion toward reasonable conversion with valuable product selectivity, these early findings in non-catalytic methane decomposition have inspired the route of converting methane into higher hydrocarbons[92, 93].

Back to the early studies of the thermal decomposition of methane. Bone et al. first reported the effect of surface packing materials in the reactor that can promote methane decomposition at relatively lower temperatures [89]. A similar phenomenon was also discovered in Slater's study that different materials such as quartz, magnesia, silica bulbs, graphite, silica carbide, iron, and copper were investigated as the surface for methane decomposition[94]. The results show that Fe, C, and silica carbide received higher methane activation than other materials. Since then, metals have become possible candidates for methane activation. In 1927, Yamaguti reported that reduced Ni from NiO has a remarkable activity to decompose methane toward hydrogen and

carbon between 873 -1273 K with methane conversion up to 18 %[95]. Holliday et al. verified that the Ni catalyst can significantly boost reaction toward equilibrium in methane decomposition[96]. The extraordinary performance of Ni catalyst was also recognized by Cantelo[97]. These early studies have demonstrated the promising performance of catalysts to boost methane decomposition to hydrogen and carbon but cannot move toward hydrocarbons significantly. However, Ni-based catalysts received intensive attention as successful catalysts for upgrading methane to hydrogen.

1.6.2 Supported-Nanostructured Catalysts for Methane Upgrading Towards Hydrogen

The catalyst development in the early study focused on bulk metal oxide and metals; the insufficient activity remains due to the inhomogeneous distribution of sites, insufficient surface area, and particle size. New catalysts prepared by dispersing the transition metal nanoparticles and clusters on specific supporting material can effectively overcome the above issues in bulk-form catalysts. Ni-based catalysts are the most popular studied for methane decomposition toward hydrogen due to their favorable methane activation[98-109]. These catalysts primarily have Ni active sites in nanoparticles or cluster forms distributed on the surface of supporting materials, which create suitable surfaces for methane adsorption with very low energy and favor dissociation of C-H bonds[110]. Other transitional metals such as Fe[107, 111-113], Co[107, 114-116], Pd[117-119], Pt[103, 120, 121] were investigated showing activity decomposition of methane. The supported nanostructured catalysts can significantly reduce the reaction temperature below 873 K[108, 109], form carbon nanotube with CO_2 free hydrogen by

following the typical tip[116, 122] and base grown mechanism based on Langmuir-Hinshelwood principle[123]. However, the major drawbacks in supported nanostructured catalysts, including deactivation caused by coking[124, 125], sites migrating[122], and sintering[126] at high temperatures, significantly limited its applications in commercial-scaled processing. To better understand the structure-properties-performance relationship, the effect of support[99, 114, 127], the effect of particle size[128, 129], and the effect of promotors[106, 130]were investigated, which can be further used to design robust, coking tolerance catalysts for methane decomposition.

1.6.3 Unconventional Liquid Phase Catalysts for Methane Upgrading Towards Hydrogen

To overcome the deactivation issues discussed in the supported nanostructured catalysts, the liquid phase systems were reported as effective catalysts and media to separate the carbon generated from methane decomposition. Serban reported Sn, Pb can be used to isolate the carbon generated from the methane decomposition[131]. Plevan and Geißler et al. evaluated the Sn system in a bubble column reactor and received active NMD performance[132, 133]. However, the methane conversion was low in the Sn and Pb system due to the Sn and Pb being less active for methane activation. Wang et al. proposed using liquid Mg as both catalyst and separation media and discovered Mg_3C_2 as reaction catalytic intermedia[134]. Upham et al. reported a Ni-Bi binary system for methane decomposition at 1338 K with much higher methane conversion up to 95 %[135]. The Ni-Bi system has atomic dispersed Ni, which is the extraordinary active catalyst for methane decomposition. This remarkable Ni-Bi system received attention

and further inspired many valuable works in the following, such as Ni-Sn[136, 137], Ni-Bi-Mo[138], and Cu-Bi[139] systems. Other than liquid systems were also investigated, such as: $MnCl_2$[140], $FeCl_2$[141], Ga[88] and Te[142]. The liquid phase catalysts also exhibited some disadvantages such as the Ni-Bi system having carbon contamination issues[143], catalyst deactivation[138], and metal evaporation[143], which is unacceptable to make profits. The molten salt system can largely suppress the evaporation, but the activity is much lower than the Ni-Bi system. Therefore, the technological challenges of liquid phase catalysts remain and must be addressed before they are scaled up commercially.

1.6.4 Early Catalysts Development for NMC

The catalyst developments for NMC were initiated from the same early study of methane decomposition discussed in section 1.6.1. The methane converted to higher value-added hydrocarbons is promising but unsuccessful due to a lack of effective catalysts. The bulk catalysts such as Pt[144], carbon filament[145, 146], silica[96], Ni[147], and Fe[94] reported from these early studies, did not observe promising performance due to insufficient surface area and low activity. To overcome the kinetic limitation, suppress the coke selectivity, and improve the overall activity, supported nanostructured catalysts were developed to significantly improve the methane activation performance by reducing process temperature. Nanostructured catalyst such as 6 %-Pt/SiO_2 was evaluated with active performance to produce higher hydrocarbons but received very low conversion after exposure to methane[148] at 523 K. To improve the overall hydrocarbon production and suppress coke formation, bi-metallic design of Pt-Sn[149], Pt-Bi[150], and Ni-P[151] demonstrated successfully of coke suppression and improvement

of hydrocarbons selectivity by tailoring the electronic structure of Pt and Ni. Other types of nanostructured catalysts were also reported such as GaN/Silica and Ga modified zeolite[152, 153] and tailoring the electronic structure of catalysts by bi-metallic design gains valuable inside of methane activation under non-oxidative conditions, however, did not significantly receive improvement due to insufficient conversion and high coking selectivity, which is not acceptable for commercialized development of NMC.

1.6.5 Zeolite-Supported Mo Catalysts for Methane Upgrading Towards Hydrocarbons

High-surface area and three-dimensional silica-aluminate framework zeolite are popular supporting materials for catalysis. In 1993, Wang et al. first reported zeolite-supported Mo/ZSM-5 catalyst exhibiting exclusive high aromatic selectivity at 973 K[154]. The success of Mo/ZSM-5 has become the state-of-art, most popular catalyst for NMC in the past few decades. Unlike other nanostructured catalysts, the ZSM-5 framework provides a satisfactory spatial effect for aromatics formation[155-157]. The studies have revealed two well-recognized mechanisms of aromatics formation over Mo/ZSM-5. First, Mo species were carburized to Mo_2C, dispersed Mo_2C_2, or MoC species after exposure to the methane, depending on the actual loading catalysts. In the hydrocarbon pool mechanism, the highly activated, unsaturated aromatics precursor C_xH_y intermediates were formed by dehydrogenation on the Mo_2C surface and inside the ZSM-5 channel. The unsaturated aromatics precursor C_xH_y can be reformed by hydrogen to yield aromatics[158]. In the bifunctional mechanism, the Mo speices firstly

cleave the C-H bond and convert methane to C_2 as intermediates, then the C_2 was dehydrogenated at the Brønsted acid sites of ZSM-5 to form aromatics[159]. The Brønsted acid sites in zeolite are unique features to improve the dispersing of the Mo site and provide oligomerization opportunities, which can be adjusted with suitable Si/Al ratio and type of structure. Based on this, the Mo/ZSM-5 structure can be tailorized with different proprotors[160, 161], Si/Al ratio[162], and active sites[163] to enable selectivity shifts and activity improvements. These investigations also expanded to other catalysts such as Zn[164, 165], Fe[157, 166], Ga, and W[155, 167] which exhibited active NMC performance. Although Mo/ZSM-5 is the active catalyst for NMC which has been intensively studied. The drawbacks remain on Mo/ZSM-5 were still not fully addressed. Coking formed inside the zeolite channel during NMC reaction can often block the contact of catalytic sites to methane, has significantly deactivated the NMC performance, and requires regeneration[158, 161, 168]. Besides, the high operating temperature also causes Mo site sintering[169], which irreversibly damages the catalysts. These drawbacks must be addressed before establishing a commercial NMC process using the Mo/ZSM-5 catalyst.

1.6.6 Singel-atom Catalysts for Methane Upgrading Towards Hydrocarbons

Singel-atom catalysts (SACs) are atomically dispersed supported catalysts recently become attractive in catalysis engineering due to their unique design and extraordinary catalytic performance. The atomic dispersing of SACs can effectively utilize the catalyst, thus significantly reducing the metal loading and cost in catalysts.

Noble metals such as Ru, Rh, Pd, and Pt could be produced with SAC configuration to withstand even better performance at less cost. However, atomic dispersing is metastable in thermodynamics, which tends to agglomerate to nanoclusters or particles. Because the agglomerate of a single site is typically irreversible and highly coordinated, strong bonding of the active center to the support is typically used to maintain dispersing and immobilizing the atomic active center. Xie et al.[170] reported SACs $Pt_1@CeO_2$ exhibiting active NMC performance with 75 % hydrocarbon selectivity in 14.4 % methane conversion at 1248 K. The high stability of SAC $Pt_1@CeO_2$ can be attributed to its unique synthesis method via the crystallization of CeO_2 with $PtCl_4$ precursor under hydrothermal conditions. The metal-organic synthesis method successfully built robust SACs on different surfaces. Soulivong et al. innovated a single atom Ta supported by silica as an active center for NMC exhibiting high selectivity of C_2 (>98%) with 0.5 % methane conversion at 748 K[171]. The catalyst has a unique configuration as $((\equiv SiO)_2Ta{-}H)$ prepared by wet chemistry metal-organic synthesis, as the method to secure single dispersed Ta atoms. Similar methods were adopted in silica-supported Fe single site for NMC reported by Šot et al.[172]. The direct wet impregnation method has also been used to synthesize SACs Mo/MCM-22, where Mo can also exist as the isolated site in porous silica/zeolite[173, 174]. These SACs can effectively activate methane, but the performance is low and unacceptable for commercial-scaled NMC.

Despite the wet-chemistry prepared SCAs, a remarkable SAC developed by Guo et al. using fame fusion of Fe_2SiO_4 with silica to confine single atom Fe catalyst (denoted as $Fe©SiO_2$), which exhibited highly high performance in NMC with 45 %

methane conversion at 1373 K without coking[86]. Fe©SiO_2 is a promising candidate combining high performance and low coke selectivity as the current state-of-the-art SAC for NMC. It has unique Fe single atoms confined by the silica lattice, created by flame fusion of Fe_2SiO_4. The Fe coordinated to the support has high strength with a low surface area of support, resulting in reduced coke formation and high methane activation. The mechanism of NMC over Fe©SiO_2 was disclosed with the co-existence of multiple complex processes. Firstly, $FeSiC_2$©SiO_2 carburized from fresh state FeO_3©SiO_2 by activating, verified as the actual active center for methane activation[86, 175]. A radical process was reported as a possible mechanism involving surface catalytic reaction and gas phase. For C_2 formation, Liu et al. proposed a surface activation path of methane activation via absorption followed by dissociation of C-H over $FeSiC_2$©SiO_2[176]. The critical step inside is to activate methyl on $FeSiC_2$©$SiO_{2,\ which}$ can couple the carbon atom on $FeSiC_2$©SiO_2 to form C_2 and restore by reforming CH_4 molecules. The mechanism can successfully explain the activation of the C-H bond but is insufficient to explain the formation of lavishing compounds. Kim et al. proposed that the $FeSiC_2$©SiO_2 active methane undergoes synergic surface catalytic path and gas phase path[177]. In the surface reaction path, methane firstly absorbed to $FeSiC_2$©SiO_2 center and dissociated the C-H bond. The following formation of C_2 was assisted by CH_3 radicals reforming. In the gas phase path, the role of the active center involving many radicals such as methyl, ethyl, and hydrogen radicals is essential for hydrocarbon formation and regenerating the catalytic sites, which has been reported by many literatures[178-180]. Regarding the aromatic formation, Puente‐Urbina et al. reported a gas phase path starting from ethylene as the precursor via dehydrogenation and

coupling to higher unsaturated hydrocarbons[181]. The key finding by detecting the C_3-C_5 intermediates is highly correlated to aromatics formation. Postma et al. studied the effect of C_2 co-feeding. They discovered that co-feeding improves the formation of aromatics and elevates the overall methane conversion by the gas phase process [178, 182]. Overall, the combined surface catalytic and gas phase reaction seems to be a general feature for SACs in NMC reactions. Besides the reaction mechanism, Fe-based SACs were incorporated with reactor design to promote hydrocarbon formation, such as catalytic wall reactor and membrane reactor. The results indicate the robustness of the Fe-based SACs-coated catalytic wall reactor; even when coke formation occurs, the reaction does not exhibit deactivation[183, 184]. The membrane can effectively shift equilibrium forward over the catalyst and drive the formation of hydrocarbons[82-85]. Except for the experimental efforts, processing design, and reaction optimization were also studied using computational methods and provided valuable guidance to design NMC to receive profits[185-187]. The catalyst development on Fe-based SACs was also investigated. Han et. al. reported cristobalite-supported Fe SACs prepared via furnace fusion and studied the effect of bi-metallic by incorporating Co, Ni, Pd, and Pt with Fe/SiO_2 and received promotional effect[188, 189]. More than experimental evidence, computational catalyst design provides inside guidance for future catalyst design by DFT simulation[190] and screening[191]. These results have systematically contributed to gaining new understanding of NMC over Fe-based SACs, which can be used as enlightenment for the further NMC process design.

1.7 Challenges for Non-Oxidative Methane Upgrading

Following the goal of net zero-emission, the growth value of processing hydrogen and valuable hydrocarbon without greenhouse emissions can be anticipated. To become commercially profitable, the overall process of methane upgrading needs to produce hydrogen and hydrocarbons at a much lower cost of production. Blue hydrogen still holds the most competitive price, around $ 1.8-3 per kg. The methane price in March of 2024 was $ 1.752 mmbtu[192], equivalent to $ 1.97/kg hydrogen, but still higher than the conventional SMR. There are two possible factors for NMD to become profitable: when the cost of CO_2 emission is included and the carbon market rises[76]. If NMD can be developed with yields of high-valued, advanced nanocarbon materials such as carbon nanotubes or fibers, it should make NMD more competitive.

Based on the process simulation[185], the NMC to value-added hydrocarbons process requires less than 20 % coke formation and an overall methane conversion more significant than 25 % to achieve profitability with the distribution of 26.8 % ethylene, 22.9 % benzene, plus 20.2 % naphthalene. The investigation indicates that low-cost and high-performance catalyst development is essential for the NMC to become profitable. To meet these requirements, the following challenges need to be resolved.

1) Limitation by Reaction Kinetic and Pressure Effect

The critical challenge in methane upgrading is the kinetic of methane activation. Based on the previous discussion, the high symmetry of methane molecules requires a very high temperature (> 1500 K) to active methane without presenting catalysts.

Without a catalyst, the reaction reached equilibrium conditions as the final dehydrogenation and jeopardized the formation of hydrocarbons. **Figure 1.2** demonstrates the thermodynamic equilibrium of methane converted to hydrocarbons and carbons without presenting a catalyst. A conflict of increasing overall methane conversion by rising temperature will spontaneously allow coke formation, thus attenuating the selectivity of hydrocarbon. This is because, at higher temperatures, the gas phase reaction is more dominated. Under the gas-phase condition, increasing the temperature does not help the hydrocarbon selectivity increase. The conversion increases result in the hydrogen partial pressure, which could neutralize the important intermediates, causing the C2 product to decrease, but the aromatics increased[193]. Therefore, a necessary catalyst is required to produce hydrocarbons and suppress the kinetic limitation by turning selectivity to specific products, regulating gas phase reactions, and significantly reducing the reaction temperature.

2) Challenges of Low Robustness and Coking in Catalyst Development

Developing a suitable catalyst is needed besides the kinetic challenges remaining in non-oxidative methane upgrading. Several issues remain from the previous discussion of catalyst development status for non-oxidative methane upgrading. Coking is the most critical issue to deactivation and needs to be addressed immediately. For non-oxidative methane converts to hydrocarbons, conventional Mo/ZSM-5 and nano-structured catalysts cannot satisfy the current demands due to their low coking tolerance and rapid deactivation during reaction conditions. This is because the coke deposition can create diffusion limitation between catalytic sites to

the methane, making catalysts out of function. Typically, coke deposition cannot be removed uncles under an oxidative environment, which is unsuitable for commercial-scaled processing. The only hope to minimize the coke formation is to understand the nature of the coke formation mechanism and develop a suitable catalyst combined with low coke selectivity and high coke tolerance without sacrificing its performance. To begin with, this requires the catalyst to have high activity, rationally dispersed catalytic sites such as SACs, and a support that does not favor coking. For methane upgrading to hydrogen and solid carbon, coking is an even more severe problem that harms the catalysts, such as conventional supported metal catalysts deactivated by a coking-caused diffusion barrier, as discussed above. The recently developed non-conventional catalysts, such as liquid metal catalysts, also face deactivation issues caused by coking. Although the liquid metal does not wet with the carbon, a tiny portion of carbon can still dissolve into the liquid metal, which can cause deactivation and be extremely hard to remove. A similar problem also existed in the molten salt system, which has no such way to resolve. A possible solution can be created by creating a surface reaction catalyst with a high carbon transfer ability that directionally guides carbon accumulation.

Besides the coking, the high-temperature condition of methane upgrading is another crucial challenge to the catalyst that must be durable under elevated temperature conditions. Because thermodynamics requires methane activation, the NMC and NMD must be operated at high temperatures. Conventional zeolite-supported nano-catalysts cannot tolerate temperatures above 1073 K due to their instability of structure[194-196]. Typically, there are two types of instability: structural collapse and catalytic site migration. For structure collapse, such as zeolite-type

support, becomes unstable under high temperatures. This has limited the application of zeolite catalysts for high-temperature NMC. Regarding the catalytic site migration, the high temperature can severely jeopardize the catalytic sites, resulting in sintering[197, 198], evaporation[199], and phase separation[200], which can be ascribed to the quantum size effect[128, 201, 202] of nano or atomic-scaled objects. For example, the melting temperature of a 4.3 nm nickel nanoparticle is approximately 1200 K[203], where the bulk nickel is 1726 K. Therefore, the sized-dependent physical and chemical properties could be endangered when reaction temperatures range from 800-1200 K. These catalytic site migrations are often irreversible, causing the catalysts to be permanently malfunction or deactivated. To go against these catalyst failures under high temperatures, it is necessary to develop catalysts with robust structures and establish stable bounding between catalytic sites with the supports. Possible strategies could be selecting thermally stable catalyst support, applying chemical or physical treatment, and using synthesis techniques to enhance the bonding between catalysts to the support. This is especially meaningful to the progress of non-oxidative methane upgrading.

3) Engineering Challenges for Non-oxidative Methane Upgrading

The remaining engineering challenge in the commercial development of non-oxidative methane upgrading is improving overall efficiency. Thermal management is the most essential engineering control strategy, so the goal is to maximize heat efficiency. With the high-temperature demand for NMC, improving heat transfer to the methane becomes the most critical challenge. In the conventional fixed bed reactor, the heating profile goes by convection from the heating element to the reactor wall,

followed by convection from the wall to the catalyst bed. However, utilizing a catalytic wall reactor design could improve the heat transfer efficiency and reduce the convection by bridging continuous conduction-dominated heat transfers, so the heat transfer gradient from the heating source to the catalyst can be significantly reduced[184]. In the meantime, the reaction efficiency can be improved by preheating the recent gas, as demonstrated in some previous study[180]. The coupling of the NMC or NMD with the methane oxidization to an autothermal reactor will also contribute to reaching high thermal efficiency. To move forward with these designs, necessary studies, and tests are required to prove ideas, estimate the overall cost, and optimize the process condition if applicable, which has not been fully discovered.

Besides thermal management challenges, engineering strategies have not been fully understood to boost the production reaction rate to reach a sufficiently high level, as the guarantee for the overall process maintains profits. Necessary engineering designs have not been investigated, such as reactor space, contact time, and temperature profile related to the reaction. These results are critical to pursuing a commercial-scaled process. The carbon product removal strategies also need to be considered. Since the coking cannot be suppressed entirely, the high-valued coke (carbon nanomaterials) must be retrieved. The process of retrieving carbon from spent catalyst needs to be studied to establish a complete production line for non-oxidative methane upgrading. Several fundamental works have proposed method address the above challenges for methane upgrade to hydrogen[135, 142], where the NMC remain under development.

1.8 Dissertation Objective and Overview

Techniques of non-oxidative methane upgrading to hydrogen, hydrocarbons, and advanced carbon materials are promising strategies for zero-emission goals. The technologies can satisfy the gigantic need for hydrogen for power generation via fuel cells, chemicals, and materials using less expensive, renewable, and non-fossil sources, which can establish a robust, self-sufficient economy ecosystem. Two core technologies, NMC and NMD are still facing several critical challenges, as discussed in the ed in above sections. To address these challenges, this dissertation focused catalyst to understand how structure and different catalytic elements affect the performance of NMC and NMD, plus providing catalytic solutions while solutions with considering how to produce value-added coke.

In this dissertation, chapter 2 reported the development of a flamed fused vitreous silica-supported Fe catalyst for NMC with low coking selectivity and high coking tolerance. The flame fusion enables rapid phase change of silica, which can create sufficient structural defects to confine Fe sites and maintain isolated dispersion. The vitreous silica is a superior support than cristobalite due to less coking and exhibiting no degradation even if a small amount of coke was formed. This successful development of catalyst can be used for continuous NMC reaction.

Chapter 3 investigated Mn, Fe, Co, Ni, and Cu transitional metal catalysts using a vitreous silica support platform to screen suitable alternative catalysts for NMC. The study revealed that variation of NMC activity resulted from different structures, which were determined by flame fusion and correlated to the inside fundamental properties of these transitional metals.

Chapter 4 introduced a novel catalytic wall reactor that demonstrated high methane conversion under NMC conditions. This reactor can be used to produce valuable hydrocarbons, hydrogen, and carbon nanospheres.

Chapter 5 described a newly developed robust zeolite support Co catalyst for catalytic methane decomposition. By posttreatment, such as dealumination, zeolite BEA can maintain its original framework structure but gain abundant defects, which can be utilized to increase the confinement of Co atoms or nanoparticles. The design catalyst targeted low-temperature NMD, process hydrogen, and utilizable CNTs.

Chapter 2: Develop Vitreous Silica Supported Fe/SiO2 Catalyst for Direct, Non-oxidative Methane Coupling Towards Hydrocarbons Production

This chapter is adapted from Liu, Zixiao, Sichao Cheng, Emily Schulman, Weiqi Chen, Dionisios G. Vlachos, Yuying Shu, Dat T. Tran, and Dongxia Liu. "Direct non-oxidative methane coupling on vitreous silica-supported iron catalysts." Catalysis Today 416 (2023): 113873.

2.1 Abstract

In advancing direct NMC as a promising route for converting methane into valuable olefins and aromatics, the role of silica-supported iron catalysts, specifically Fe/SiO_2, has not yet been discovered. This study delves into the largely unexplored territory of how the structural property of silica supports the influence of catalyst behavior and NMC performance by introducing a novel catalyst, Fe/SiO_2-v, created through the flame fusion of quartz silica and fayalite. The investigation reveals that vitreous silica supports, characterized by their disordered Si-O bonds and structural defects, facilitate improved iron dispersion and stronger metal-support interaction compared to the traditional crystalline cristobalite supports. This leads to a notable decrease in the induction period for methane activation and reduced coke formation during NMC. Moreover, an increase in iron content within the Fe/SiO_2-v catalysts is observed to extend the induction period while also enhancing aromatic and coke

production, with the coke generated by the spent Fe/SiO_2-v catalyst showing a more uniform composition than that from cristobalite-supported iron catalysts. This highlights the potential benefits of employing vitreous silica as a support material in developing more efficient iron-based NMC catalysts.

2.2 Introduction

Direct NMC is one of the approaches to convert methane into chemicals such as ethylene (C_2H_4), benzene (C_6H_6), and naphthalene ($C_{10}H_8$), which combined are referred to as C_2+ hydrocarbons, and hydrogen (H_2). In the absence of oxygen (O_2), fully or partially oxidized by-products (e.g., carbon dioxide (CO_2), carbon monoxide (CO), and water (H_2O)) do not exist, both carbon and hydrogen in methane in the NMC can approach high carbon utilization efficiency.

The earliest studies for direct NMC demonstrated non-catalytic thermal decomposition in closed batch reactors towards hydrogen and carbon products [89, 96, 204]. High temperature (e.g., >1473 K) and sizeable heated surface area are essential to reach high methane conversions. C_2+ hydrocarbons from methane production in NMC were mainly studied in flow reactors at medium-high temperatures (e.g., ~1273 K) in catalysts with mixed surface and gas-phase reactions[94, 205-208]. Therefore, the role of catalysts is insignificant due to rapid gas-phase radical chemistry in the studied temperature conditions. Considerable efforts have been devoted to catalyst development for catalytic NMC reactions at relatively low-temperature conditions (e.g., ~1023K) in the past decades[83, 86, 154, 209]. Bulk metal, metal oxide, boron nitride, zeolite-supported metal, metal oxide-supported metal, etc. catalysts have been widely

studied[210, 211]. The molybdenum/zeolite (e.g., Mo/ZSM-5) has been the most extensively studied catalyst[156, 157, 168, 212]. Although a substantial enhancement of the hydrocarbon product selectivity has been realized in NMC over the Mo/ZSM-5 catalyst compared to non-catalytic methane pyrolysis, methane conversion is relatively low (e.g., ~16% at 1023 K), and the catalyst has speedy deactivation. The iron/silica (Fe/SiO_2, Fe species embedded in SiO_2 matrix) is a catalyst actively studied in recent years[86, 178, 188]. Compared to the Mo/ZSM-5 catalyst, the Fe/SiO_2 enables NMC at higher temperatures (e.g., ~1273 K), produces C_2+ hydrocarbons, and minimizes coking when proper temperature and space velocity are selected.

Following the potential of Fe/SiO_2 catalysts in the NMC chemistry, studies for fundamental insight into the type of active site[172, 175, 213], and reaction mechanism [176, 177, 179, 181] of this catalyst system have been actively pursued. The engineering of reactors to manipulate the mixed surface-gas phase chemistry to optimize the C_2+ hydrocarbon production and minimize coke formation has also been investigated [84, 178, 180, 183, 184]. In all these studies, it should be noted that the Fe/SiO_2 catalyst was prepared from a mixture of quartz and fayalite in a melt-fusing process at 1973 K in a heating furnace[82, 85, 188]. The silica support in the as-fused catalysts has a crystalline cristobalite polymorph. Compared with other silica supports, such as zeolite or amorphous silica synthesized from low-temperature processes in the Fe-containing catalyst analogues[86, 188], the cristobalite-supported iron catalysts had a higher resistance to structural sintering and coke deposition. As the most abundant metal oxide in the earth's thrust, silica has multiple polymorphs. Studies have shown that all the polymorphs have different Si-O bond lengths, angles, ordering, etc., which determine different

physicochemical properties[214]. However, the studies for Fe/SiO_2 catalysts have not explored other silica support polymorphs except for cristobalite in the open literature that we can locate.

Here, we aimed to prepare the Fe/SiO_2 catalysts supported by amorphous vitreous silica and study their physicochemical properties and catalytic performance in the NMC reactions. The quartz silica was used as the precursor material of vitreous silica. The catalysts were prepared by flame fusion of quartz support and fayalite particles using an oxyhydrogen torch. The phase transformation under high temperature distorts the Si-O bonding structure and creates structural defects in the vitrified silica in comparison to the crystalline silica polymorphs, which is expected to influence the iron habitation environment in the as-developed catalysts and the consequent NMC performances. The as-prepared Fe/SiO_2-v catalyst was studied by elemental composition analysis, N_2 adsorption/desorption isotherm, X-ray powder diffraction (XRD), Raman spectrometry, X-ray photoelectron spectroscopy (XPS), diffuse reflectance UV-vis spectroscopy (DR UV-vis) and hydrogen-temperature programmed reduction (H_2-TPR) collectively. The catalyst activation and steady-state performance in the NMC were studied and compared to those of the cristobalite-supported Fe/SiO_2 catalyst. The effects of the iron content in the Fe/SiO_2-v were also studied. The spent catalysts were analyzed by thermogravimetric analysis and temperature-programmed oxidation (TPO) to understand coke properties.

2.3 Experimental Methods

2.3.1 Materials

High-purity, low Fe containing silica powder (Quartz phase, 0.4 ppm Fe, IOTA-4, Sibelco, Inc) and fayalite (Fe_2SiO_4) were used as precursors for synthesizing the vitreous silica-supported iron (Fe/SiO_2-v) catalysts. A sol-gel method first reported by DeAngelis, Michael T., et al. was adopted to synthesize the Fe_2SiO_4 [215], with the purity verified by XRD. Nitric acid (HNO_3, ACS grade) was purchased from Fisher Scientific. Deionized water used by the experiment was supplied by Milli-Q® EQ 7008/16 ultrapure water system.

2.3.2 Prepare Flame Fused, Vitreous Silica-supported Fe/SiO_2 Catalysts

Fe/SiO_2-v catalysts were prepared by the following procedures: 10.00 g silica (Quartz phase, IOTA-4, Seblco Group) mixed with a certain amount of Fe_2SiO_4 material in a 125 mL Nalgene® high-density polyethylene (HDPE) bottle, followed by a well-mixing in a jar mill for 24 h. The mixture was then pressed to a pellet under five metric tons in a stainless-steel die (28.6 mm in diameter, Carver, P/N:2090-0). The pellet was placed on the top of an alumina insulation block and fused by an oxy-hydrogen flame to form a glassy ingot. The apparatus used for flame fusion is demonstrated in Figure. The ingot was then crushed into pieces and sieved to 40-80 mesh particle size range by the ASTM standard mesh set. The as-sieved Fe/SiO_2-v particles were suspended in 1.0 M HNO_3 solution (the weight ratio of catalyst to HNO_3 solution = 1:10) under rigorous magnetic stirring at ambient temperature for 3 h.

Subsequently, the particles were collected by centrifugation, washed with deionized water three times, and dried at 343 K overnight. Finally, the Fe/SiO_2-v sample was calcined in dry air (100 mL min-1, Airgas) by raising the furnace temperature from 298 K to 823 K at a ramp rate of 5 K min^{-1} and kept for 4 h at 823K. After cooling to room temperature, the sample was transferred into a glass vial and kept in a desiccator for further characterization and catalysis tests.

To study the effects of iron concentration in the catalysts, FeSiO_2-v samples with nominal iron loadings of 0.10 wt. %, 0.50 wt. % and 1.50 wt. % were prepared. For comparison purposes, the cristobalite-supported iron catalyst (denotated as Fe/SiO_2-c) containing 0.10 wt.% iron was prepared following the same procedure as the Fe/SiO_2-v catalyst, except that the sample was fused in a high-temperature furnace (SentroTech, ST-1800-121216) at 1973 K under ambient air for 6 h.

2.3.3 Catalyst Characterization

XRD pattern of catalysts and Fa_2SiO_4 were measured on a Bruker® D8 diffractometer using the Cu-Kα radiation. The scan was performed with a step size of 0.02 degrees and a step time of 3 s. The iron content in the catalyst was determined by the inductively coupled plasma-optical emission spectrometry (ICP-OES). Raman spectra were collected at room temperature using HJY LabRam ARAMIS Raman spectrometer under 532 nm wavelength, 600 grid/mm gathering size, and calibrated at 520 cm-1 using an intrinsic silicon wafer standard. X-ray photoelectron spectroscopy (XPS) data were measured using a Kratos Axis 165 spectrometer with Al monochromatic X-ray source. N_2 isotherms were measured at 77 K using an Autosorb-

iQ analyzer (by Quantachrome Instruments). Before the measurement, samples were evacuated overnight at 573 K under 1 mmHg pressure. DR UV-vis spectra were obtained using an Ocean Optics USB2000 + spectrometer equipped with an IS200-4 integrating sphere detector.

Temperature programed reduction of under H_2 gas (H_2-TPR) for the fresh Fe/SiO_2 catalysts were carried out by the Quantachrome Autosorb-iQ analyzer equipped with a thermal conductivity detector (TCD). The sample was thermally treated under N_2 gas flow (40 mL min-1, Research grade, Airgas) at 823 K for 4 h before the measurement. After cooling to 323 K, the gas was switched to 5 % H_2/N_2 (40 mL/min). The catalyst sample was then heated to 1223 K with a 10 K/min ramp rate and dwelled for 10 min at the final temperature. An inline liquid nitrogen cold trap was used to condense water vapor generated during the experiment to avoid TCD signal interference.

2.3.4 Catalyst Test Under NMC Conditions

The NMC reaction was conducted in a straight tubular packed-bed quartz reactor with a scheme shown in **Figure 2.1 A**. In each experiment, the catalyst sample (0.375 g) in the reactor was placed in a vertical tube furnace aperture (**Figure 2.1 B**), heated from room temperature to 1273 K under a flowing N_2 (50 mL min^{-1}, UHP grade, Airgas) at a ramping rate of 10 K min^{-1}. The tube furnace has a sufficient isotherm zone that enables the catalyst bed's uniformly distributed temperature profile. After reaching the set temperature, methane (Research grade, Airgas) flow at 16 mL min^{-1} mixed with Ar gas (internal standard) at 4 mL min^{-1} was introduced into the reactor. The catalyst

temperature was measured using a K-type thermocouple whose tip was placed at the middle position of the catalyst bed on the external surface of the quartz reactor. The reaction effluents were analyzed using a gas chromatograph (Agilent 7890A) containing a methyl-siloxane capillary column (HP-1, 50.0 m × 320 μm × 0.52 μm) connected to a flame ionization detector (FID) and a packed column (ShinCarbon ST Columns, 80/100 mesh, 1.83 m) configured to a TCD. Methane activation on the catalyst in the initial stage of the reaction was monitored by mass spectroscopy (MS, Prima BT, ThermoFisher Scientific). Before reaching the MS equipment, the product effluents flowed through a dry ice/acetone cold trap to condense out the aromatic products to prevent blockage of gas lines in the MS system by aromatics products.

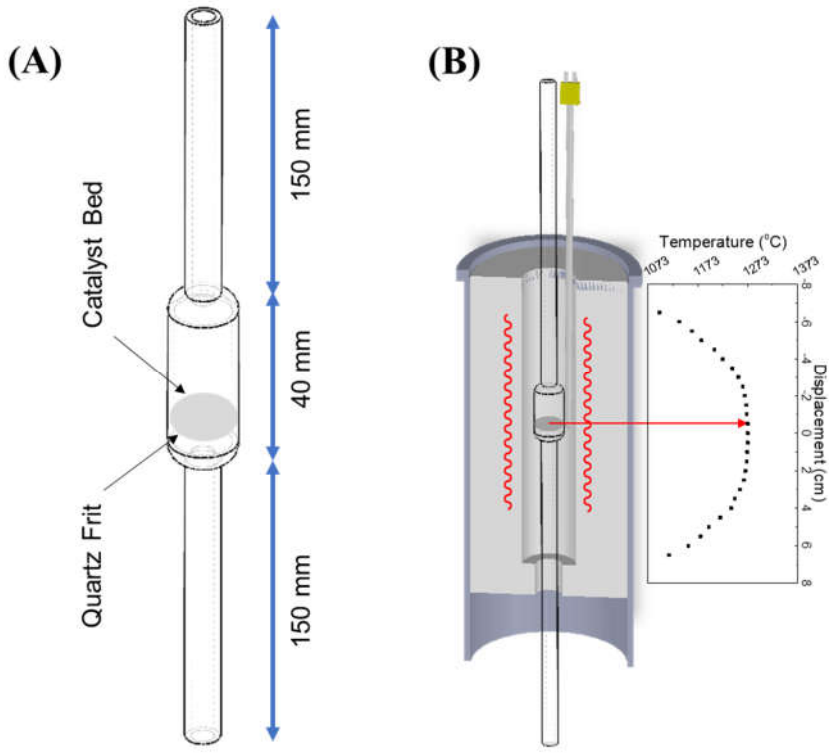

Figure 2.1. Schematics of quartz reactor (A) and inside view of reactor position in the furnace as well as measured temperature profile (B) used in the NMC reaction.

2.3.5 Analysis of Spent Catalysts

The coke quantity in the spent catalysts was determined by the thermogravimetric analysis (TGA, Shimadzu, TA-50) method. Typically, 0.05 g of spent catalyst was exposed to 50 mL min^{-1} flowing air (Research grade, Airgas) and ramped from room temperature to 1273 K with a 10 K min^{-1} rate. The weight loss resulting from the combustion of coke on the catalyst was recorded. The coke nature of the spent catalyst was examined using the TPO. The spent catalyst was placed inside a quartz cell, immobilized by quartz wool, and then set in a temperature-controlled furnace. The temperature was monitored by a K-type thermocouple attached to the outer wall of the quartz sample cell. The furnace was ramped to 1123 K at a ramp rate of 10 K min^{-1} under a flowing Ar (45 mL min^{-1}, ultrapure, Airgas) and O_2 (5 mL min^{-1}, ultrapure, Airgas) atmosphere. The O_2, CO_2, and CO profiles were monitored using the same mass spectrometer in the catalytic NMC reaction experiments.

2.4 Results and Discussion

2.4.1 Fe/SiO_2 Catalysts with Different Silica Polymorph Supports.

2.4.1.1 Physicochemical Properties of as-prepared Fe/SiO_2 Catalysts

To study the effect of silica support in the catalysts, Fe/SiO_2-c and Fe/SiO_2-v containing 0.1 wt.% nominal iron loading were studied comparatively. Firstly, XRD was used to determine the phase and structure. The sharp diffraction peaks in the XRD pattern (**Figure 2.2 (A)**) confirm the existence of a cristobalite support phase in the Fe/SiO_2-c catalyst, consistent with the Fe/SiO_2 catalysts prepared by fusing at 1973 K

in a heating furnace in previous reports. The Fe/SiO_2-v, however, only has a broad peak centered at 2 theta (2θ) goniometer equals to 21.75°, indicating the presence of amorphous silica phase for the catalyst prepared by the oxyhydrogen flame fusing. Both samples have distinct XRD patterns from the quartz, the precursor Fe_2SiO_4 for both Fe/SiO_2-c and Fe/SiO_2-v catalysts. The actual iron contents in both catalysts are 0.102 and 0.097 wt.%, respectively, close to the nominal loadings used in the catalyst preparation (**Table 2.1**). The photographs of both samples (**Figures 2.3 (A-B)**) show that Fe/SiO_2-V is transparent, while Fe/SiO_2-C exhibits a pale-yellow, translucent color. The N_2 adsorption/desorption isotherms (**Figures 2.4 (A-B)**) show that both catalyst samples have identical but low surface areas, i.e., ~0.30 m^2 g^{-1}.

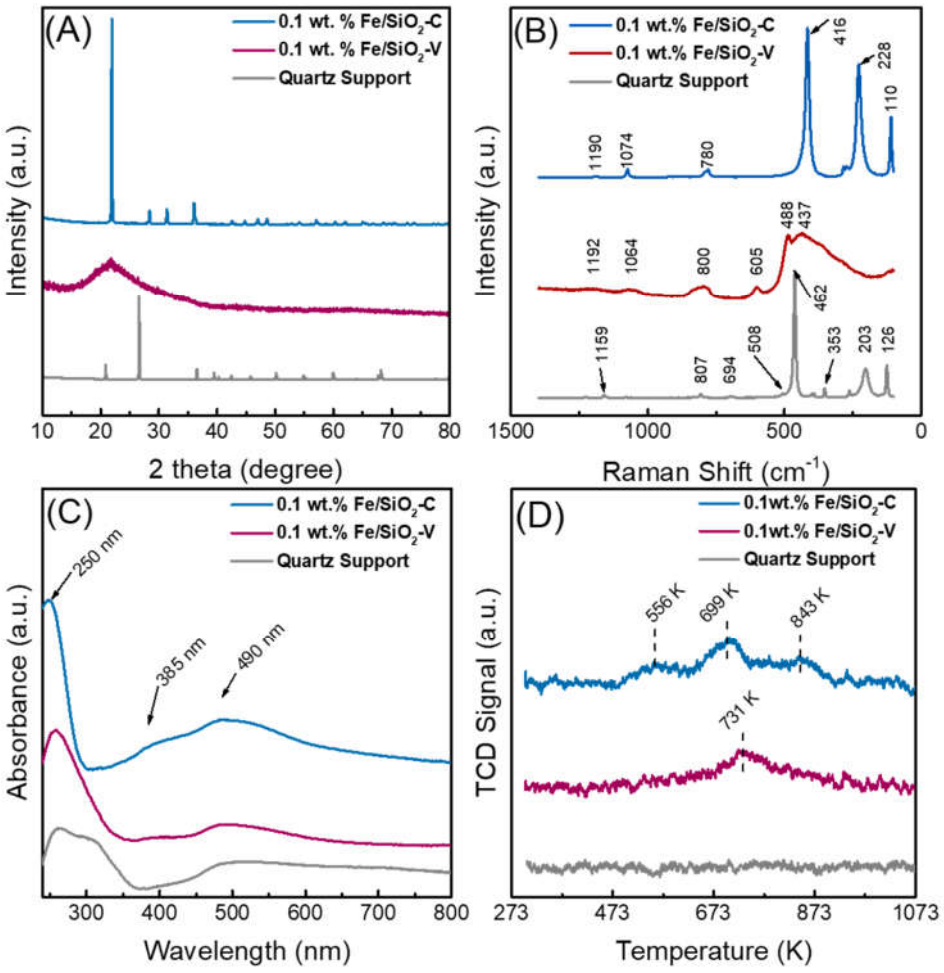

Figure 2.2. The characterization data of 0.1 wt.% Fe/SiO_2-V and 0.1 wt.% Fe/SiO_2-C catalysts: (A) XRD patterns, (B) Raman spectra, (C) DR UV-vis spectra, and (D) H_2-TPR profiles. The characterization data for quartz support are included for comparison purpose.

Table 2.1. Fe Concentration in the prepared Fe/SiO_2 catalysts

Catalyst	Quartz	0.10 wt.%	0.10 wt.%	0.50 wt.%	1.50 wt.%
Nominal Loading	0.000	0.100	0.100	0.500	1.500

Actual Loading	0.003	0.102	0.097	0.460	1.290

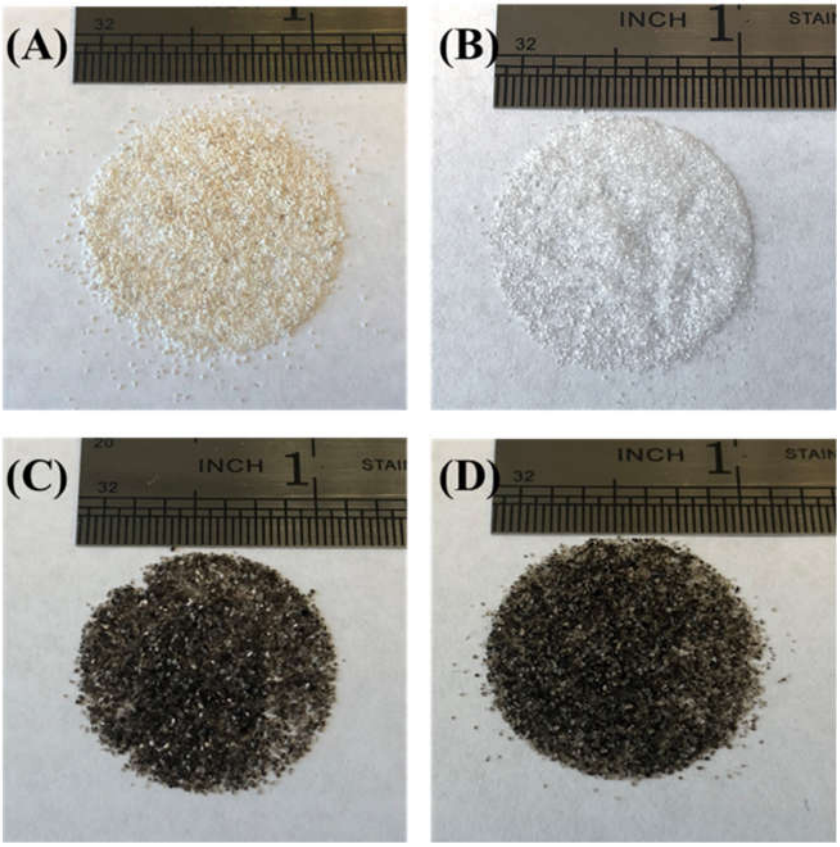

Figure 2.3. Images of catalysts prepared in the experiments: (A) 0.1wt.% Fe/SiO_2-C, (B) 0.1wt.% Fe/SiO_2-V, (C) 0.5wt.% Fe/SiO_2-V, and 1.5wt.% Fe/SiO_2-V.

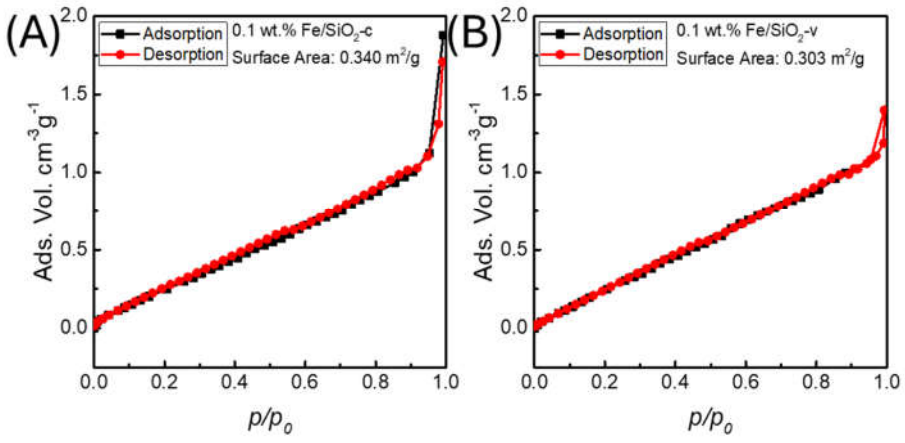

Figure 2.4. N_2 adsorption/desorption isotherms of 0.1wt.% Fe/SiO_2-C (A) and 0.1wt.% Fe/SiO_2-V (B) catalysts.

The silica bonding environment in the quartz support (before the high-temperature treatment process), Fe/SiO_2-v, and Fe/SiO_2-c catalysts were revealed by Raman spectroscopy. As shown in **Figure 2.2 (B)**, all the spectra contain three frequency regions of > 700 cm^{-1}, 500-350 cm^{-1}, and < 350 cm^{-1}, which are assigned to the vibrational modes of Si-O stretching, Si-O-Si symmetric stretching and bending, and O-Si-O bending and torsional/twisting vibrations, respectively. A close examination of these spectra shows that these three silica polymorphs have different band shapes and positions. Both quartz support and cristobalite (i.e., support in the Fe/SiO_2-c sample) have symmetric and sharp Raman bands, especially for the one belonging to the Si-O-Si symmetric stretching and bending vibrations. The band positions for the same type of vibration modes in these two crystalline silica samples are different, which is caused by the bond lengths and angles and short-range connectivity of the bond network in different silica polymorphs. For the amorphous

vitreous silica in the Fe/SiO_2-v sample, the bands in the Raman spectrum are broad and asymmetric. For example, the Si-O-Si symmetric stretching and bending vibrations exhibit an intense broadband at 437 cm^{-1} and a shoulder at 488 cm^{-1}. The changes in the band shape and shifts of the band positions in the Fe/SiO_2-v catalysts correspond to the defects present in the structure, which results in wide variations of bridging Si-O-Si bond lengths and angles. It should be noted that no band related to iron-based structures was detected in Raman spectra in **Figure 2.2 (B)**, which should be due to the low iron loadings in both Fe/SiO_2 samples.

The DR UV-Vis spectra in **Figure 2.2 (C)** show the coordination environments of iron species in the catalysts. The iron concentration in the quartz support is very low, so the absorption peaks are weak. The presence of iron in the silica support leads to intense UV-vis absorptions in both Fe/SiO_2-c and Fe/SiO_2-v catalysts. The Fe/SiO_2-c has three bands centered at ~250 nm, ~385 nm and ~490 nm, which can be assigned to the isolated ionic iron species, small iron oxide $(FeO)_n$ oligonuclear clusters, and iron oxide nanoparticles, in sequence. The strong intensity of the band at ~250 nm and broad band at ~490 nm indicates co-existence of isolated iron species and iron oxide nanoparticles in the Fe/SiO_2-c catalyst. The Fe/SiO_2-v catalyst also has three absorption bands at the similar wavelengths to those of the Fe/SiO_2-c sample. The bands assigned to the small iron oxide $(FeO)_n$ oligonuclear clusters and iron oxide nanoparticles, however, are much weaker. This result indicates that the majority of iron stays as isolated species in the Fe/SiO_2-v sample. The better dispersion of iron in the vitreous silica should be related to the diverse Si and O bond lengths and angles in the defective amorphous support.

The H_2-TPR profiles in **Figure 2.2 (D)** show the reducibility of iron species and the interaction between the metal and support in the Fe/SiO_2-v and Fe/SiO_2-c samples. The quartz support does not show any detectable reduction peaks due to its low iron content. The H_2-TPR profile of Fe/SiO_2-c catalyst has three reduction peaks: a weak one at 556 K, a strong peak at 699 K and a weak one at 843 K, in sequence. In agreement with previous reports, the first peak at the lower temperature can be related to the reduction of Fe_2O_3 to Fe_3O_4, the second peak at the middle-temperature range can be attributed to the reduction of Fe_3O_4 to FeO, whereas the third peak at higher temperature can be caused by the reduction of FeO to metallic iron. The strong peak at 699 K and weak peaks at the other two temperature ranges suggest that the majority of iron species are not fully oxidized in the Fe/SiO_2-c catalyst. The H_2-TPR profile of Fe/SiO_2-V sample is relatively simple, only showing a predominant peak at 731 K. This peak can be attributed to the reduction of Fe_3O_4 to FeO species. The peak position is about 32 K higher than that of the Fe/SiO_2-c catalyst. These results hint that the Fe/SiO_2-v catalyst prepared by the flame-fusing method has more uniform ion oxidation states. The oxidation degree is lower, and the interaction between the iron and the silica support is possibly stronger than those of the Fe/SiO_2-c catalyst. The longer fusing time in the preparation of the Fe/SiO_2-c catalyst in the static air might contribute to the higher oxidation degree of iron species in the resulting catalyst. On the contrary, it only took 25 s at the flame temperature to prepare the Fe/SiO_2-v catalyst in the oxyhydrogen flame fusing approach. Such a short processing time mitigates the solid-state migration, and thus could contribute to better Fe dispersion.

The bonding environment of elements in the Fe/SiO_2-v and Fe/SiO_2-c catalysts were studied by the XPS spectra. **Figure 2.5 (A)** shows that the survey scan only detected Si, O, and C elements, confirming the absence of other metal contaminants in the as-prepared catalysts. The carbon peak is attributed to adventitious carbon present on the catalyst surface. The iron concentration is too low to detect in the XPS spectra. This is further confirmed by the absence of peaks in the Fe 2p line shown in **Figure 2.5 (B)**. **Figure 10(C)** presents the XPS spectra of Si 2p in both Fe/SiO_2-v and Fe/SiO_2-c samples. The shape of the Si 2p line is less symmetric in Fe/SiO_2-v than that of Fe/SiO_2-c. The position of this peak shifts slightly to lower binding energy in the Fe/SiO_2-v sample, which should be caused by the disordered defective Si-O bonding structure in the amorphous vitreous silica support. The XPS spectra of O 1s in **Figure 2.5 (D)** show that the Fe/SiO_2-v exhibits a less asymmetric peak than that of the Fe/SiO_2-c sample. The O 1s peak can be deconvoluted into two peaks located at 532.7 and 533.2 eV, which can be assigned to the Si-O-Si and Si-O-H bonds, respectively. The results from the XPS data further show diverse Si-O bonding environments in the vitreous silica support than the crystalline cristobalite polymorph.

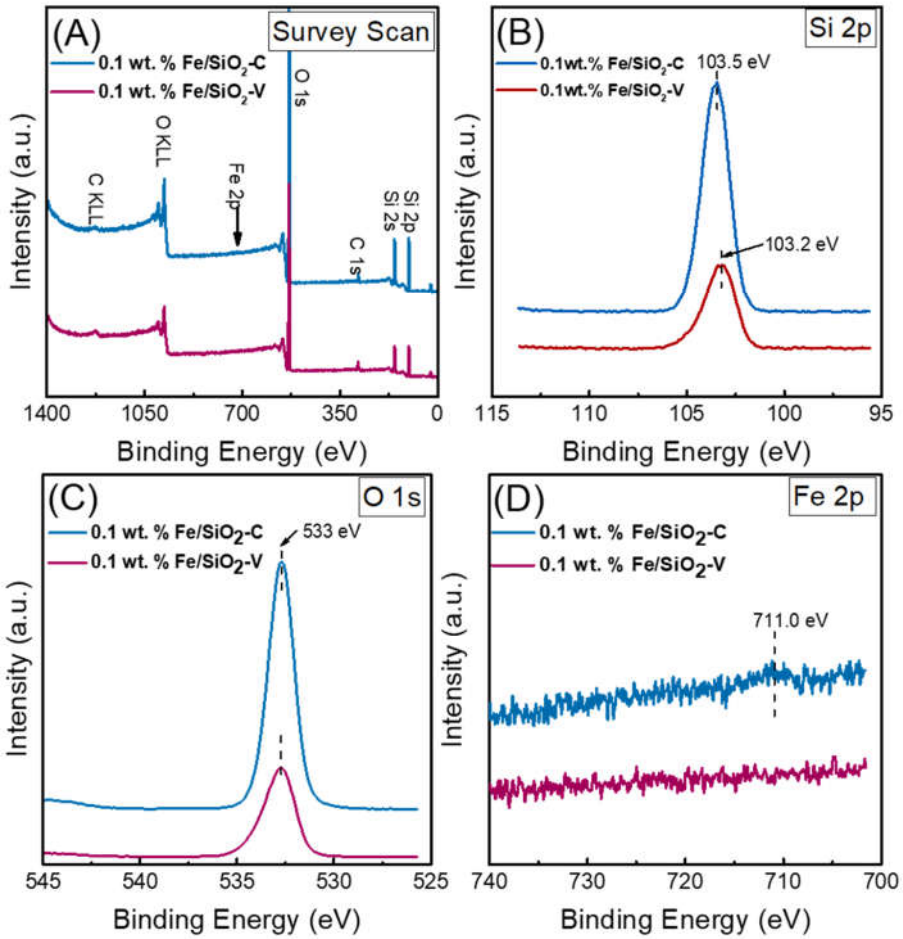

Figure 2.5. XPS spectra of survey scan (A), Si 2p (B), O 1s (C), and Fe 2p (D) of 0.1 wt.% Fe/SiO_2-V and 0.1 wt.% Fe/SiO_2-C catalysts.

2.4.1.2 Methane Activation over Fe/SiO_2 Catalysts

Methane activation over the Fe/SiO_2 catalysts in the initial stage of the NMC reaction was tracked by the mass-to-charge ratio (m/z) signals in the mass spectrometry. As shown in **Figures 2.6 (A)-(B)**, the methane reactant (m/z = 16) was

first detected in the effluent stream. Following the methane event, hydrogen (m/z = 2) signal was clearly observed. The signals belonging to acetylene (m/z = 26), ethylene (m/z = 28), and ethane (m/z = 30) then appeared, although the intensity of the ethane signal was much weaker compared to the other C_2 hydrocarbons. The time required to reach stable m/z signals in NMC over the Fe/SiO_2-c catalyst is ~250 s (**Figure 2.6 (A)**), 135 s later than that of Fe/SiO_2-v catalyst (**Figure 2.6 (B)**). This suggests that the Fe/SiO_2-V catalyst prepared by the flame fusion process has a shorter induction period, which should be consistent with its more uniform iron species in the support, as evidenced in Section 2.4.1.1 above.

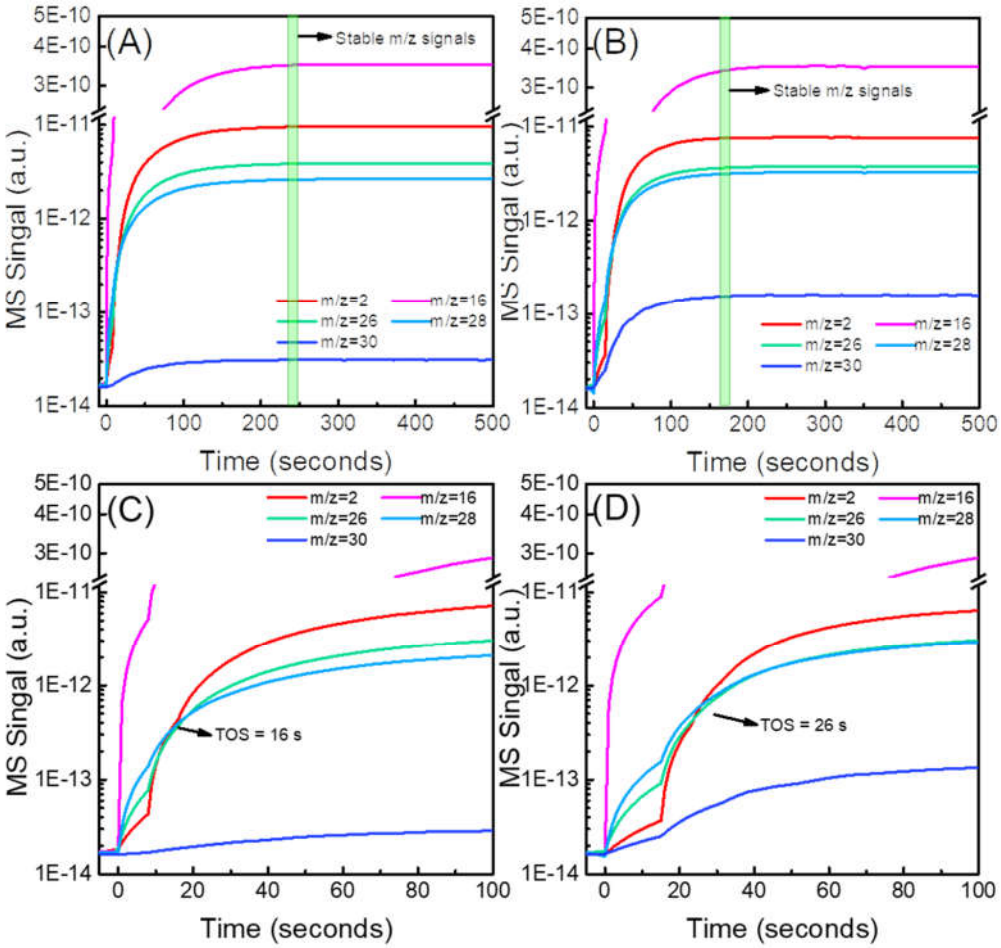

Figure 2.6. Methane activation over 0.1wt% Fe/SiO_2-C (A) and 0.1 wt.% Fe/SiO_2-V (B) versus TOS tracked by a MS instrument. (C) and (D) show MS signals at TOS of <100s in (A) and (B), respectively. (NMC conditions: 1273 K, WHSV=3200 h^{-1}, 81.04 kPa CH_4, Ar used as internal standard)

To better understand the events at the very beginning of catalyst activation, we zoomed in on the time-on-stream (TOS) of 100 s in the NMC on both Fe/SiO_2-v and Fe/SiO_2-c catalysts, and the data shown in **Figures 2.6 (C)-(D)**, accordingly. Right after the methane signal evolution, the ethylene (m/z=28) and acetylene (m/z=26) were

detected, ahead of hydrogen (m/z=2) signal, in both catalysts. After TOS of 16 s in Fe/SiO_2-c (**Figure 2.6 C**) and 26 s in Fe/SiO_2-v catalyst (**Figure 2.6 D**), when the hydrogen signal surpassed those of ethylene and acetylene compounds. The suppression of hydrogen production in the very initial stage of the methane activation should be caused by the catalyst reduction since the catalyst was only exposed to the Ar gas in the pretreatment stage. The co-existence of iron species in different coordination environments in Fe/SiO_2-c, as evidenced by the DR UV-vis spectra in **Figure 2.2 (C)**, could contribute to the faster H_2 signal surpassing over the C_2 signals, but a longer induction period to reach stable product signals was needed. On the contrary, the relatively more uniform dispersed iron species in the Fe/SiO_2-v catalyst led to a longer period of active site reduction, indicated the longer TOS before the H_2 signal surpassed the hydrocarbon products, but the catalyst can reach stable NMC reaction stage more quickly (**Figure 2.6 (B)**) once the iron species were all activated in the initial stage.

To test the catalyst performance after the induction period, methane conversions and hydrocarbon formation rates on both Fe/SiO_2-c and Fe/SiO_2-v catalysts were monitored continuously for a TOS of 5 hours. As shown in Figure 2.7 (A), after the catalyst induction period (i.e., TOS of ~2 h), both catalysts reached stable methane conversion and hydrocarbon formation. In particular, both catalysts had similar methane conversions of ~5.8%, much higher than the conversion (~1.0%) obtained in the blank test, in which the reactor was loaded with vitreous silica supported in the absence of iron species (**Figure 2.7 (A)**). The hydrocarbon product formation rates over both catalysts (**Figures 2.7 (B)-(C)**) are in the order of ethylene > benzene >

acetylene > ethane > toluene ~ naphthalene. The ethylene, benzene and acetylene production rates were higher in the Fe/SiO_2-v catalyst than these products in the Fe/SiO_2-v catalyst. The blank experiment (**Figure 2.7 (D)**) showed the formation of similar hydrocarbon products, but all of them had very low production rates compared to either Fe/SiO_2-v or Fe/SiO_2-c catalyst.

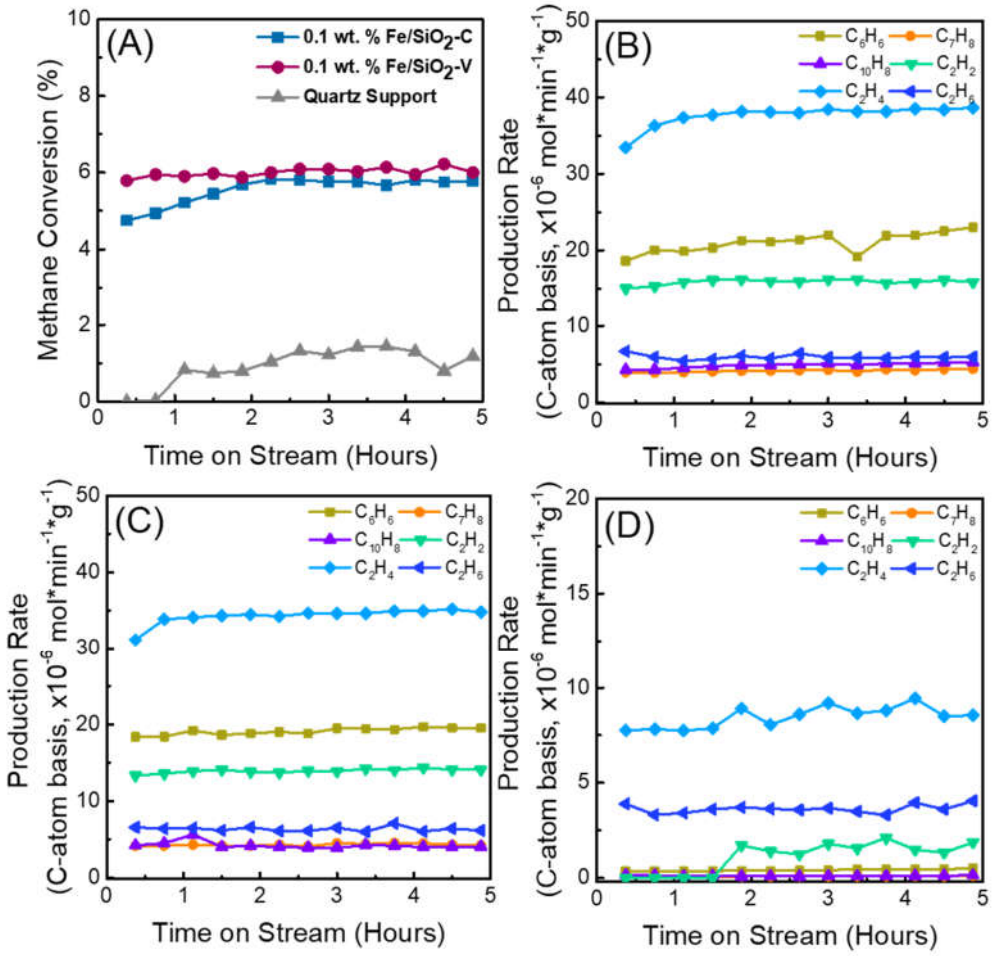

Figure 2.7. Methane conversion as function of TOS (A), and hydrocarbon product formation rates versus TOS over 0.1 wt.% Fe/SiO_2-C (B), 0.1 wt.% Fe/SiO_2-V (C), the

quartz blank (D). (NMC conditions: 1273 K, WHSV=3200 h^{-1}, 81.04 kPa CH_4, Ar used as internal standard)

2.4.1.3 Analysis of Spent Fe/SiO_2 Catalysts

The carbon deposits on the spent catalysts were quantified by the TGA measurements. Prior to this test, the as-prepared catalysts were tested in the NMC reaction for a TOS of 5 h, as described in Section 2.4.1.4 above. As shown in **Figure 2.8 (A)**, Fe/SiO_2-v catalyst contained 2.14 wt.% carbon deposition, while the Fe/SiO_2-c catalyst had 7.1 wt.% carbon deposit, ~3.4 times higher than that on Fe/SiO_2-v catalyst. The TGA data indicate that Fe/SiO_2-v has less tendency to coking than the crystalline cristobalite supported iron catalyst.

The properties of coke on the spent catalysts were studied by the TPO profiles. Figures 13(B)-(C) illustrate CO_2 and CO evolutions in the spent Fe/SiO_2-c and Fe/SiO_2-v catalysts. The CO_2 signal from the spent Fe/SiO_2-c catalyst (**Figure 2.8 (B)**) displayed a relatively broad peak, with an onset of ~721 K and completion at ~1112 K, a span of ~392 K. The peak temperature is centered at ~994 K, with two shoulder peaks on both sides of the peak temperature position. The shoulder peak at the lower temperature side is much stronger than the high temperature one. The CO_2 profile of the spent Fe/SiO_2-v catalyst has a similar shape to the Fe/SiO_2-c, but the onset and ending temperatures are higher and lower relatively. In addition, the peak temperature moved to a slightly high position (i.e., ~1005 K), and the high-temperature shoulder is much smaller. The CO profiles in **Figure 2.8 (C)** show the same features as those of CO_2 profiles of both spent catalysts. The CO_2 and CO evolution profiles can be deconvoluted into three

peaks at low-, medium- and high-temperature regions, which correspond to soft amorphous coke, polymeric aromatic carbon deposit, and ordered graphitic hard coke in sequence. Clearly, the dominant coke type in both spent catalysts is the polymeric aromatic carbon deposit, while the one on Fe/SiO_2-v needs a slightly higher temperature to remove. The spent Fe/SiO_2-c has more soft and hard cokes than the spent Fe/SiO_2-v catalyst. Overall, the coke type in the spent Fe/SiO_2-v catalyst is more uniform compared to the spent Fe/SiO_2-c catalyst.

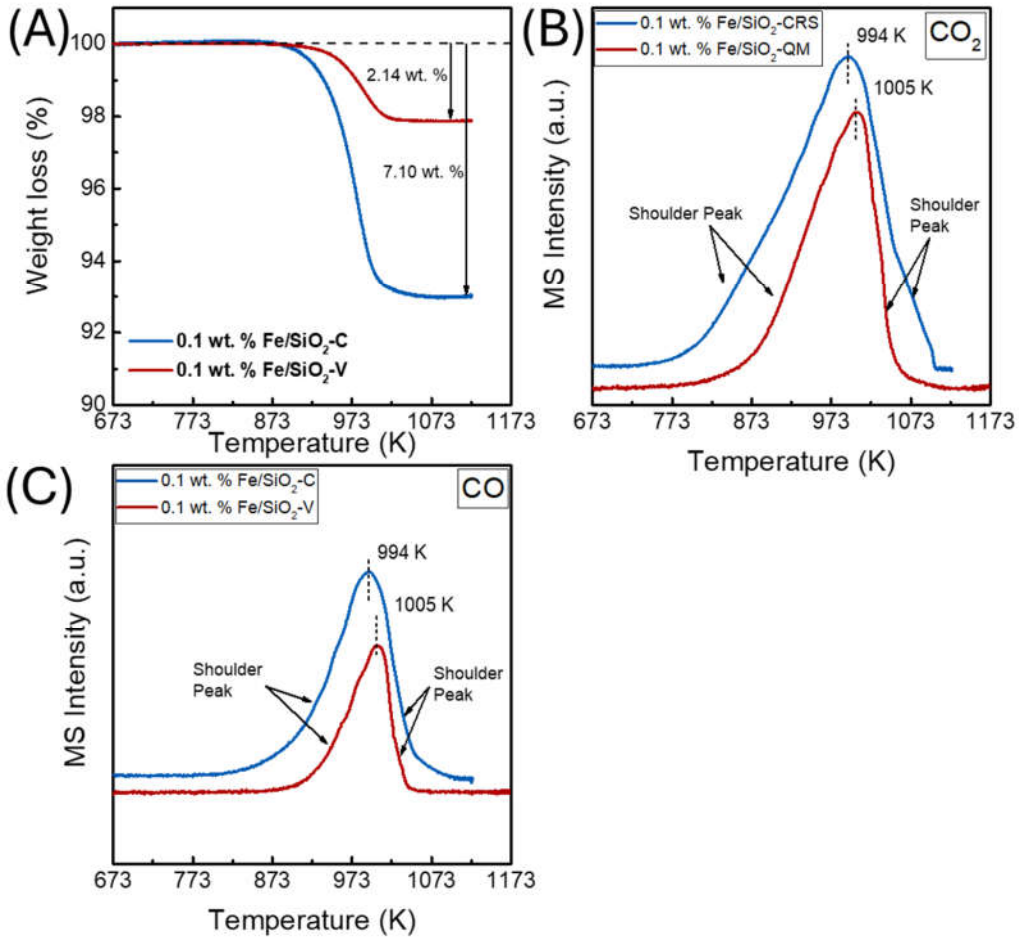

Figure 2.8. TGA data (A) and TPO profile of CO_2 (B), and CO (C) of spent 0.1 wt.% Fe/SiO_2-C and 0.1 wt.% Fe/SiO_2-V catalysts. (NMC conditions: 1273 K, WHSV=3200 h^{-1}, 81.04 kPa CH_4, Ar used as internal standard, TOS of 5 h)

2.4.2 Vitreous Silica-supported Fe/SiO_2 Catalysts: Effect of Fe Concentrations

2.4.2.1 Physicochemical Properties of the High Fe Loading Fe/SiO_2-v Catalysts

To examine the effects of iron content in the Fe/SiO_2-v catalysts on the NMC reaction, the vitreous silica supported iron catalysts with iron concentrations of 0.50 wt.% and 1.50 wt.% were studied. With increasing iron concentration, the Fe/SiO_2-V catalyst changed the color from transparent white (i.e., 0.1 wt.% in **Figure 2.3 (B)**) to grayish dark (0.50 wt.% and 1.50 wt.%, see **Figure 2.3 (C)-(D)**). The actual Fe concentrations of these two catalyst samples are slightly lower than the nominal loadings (**Table 2.1**) because the acid treatment could remove a sort of Fe species. The silica polymorph of these two catalysts was verified with the XRD measurements. As shown in **Figure 2.9 (A)**, similar to 0.1 wt.% Fe/SiO_2-V sample, both 0.50 wt.% and 1.50 wt.% Fe/SiO_2-V catalysts only have a broad peak around $2\theta = 21.89°$, suggesting the absence of silica crystallinity in the catalyst support. In addition, no peak associated with iron species was detected in the XRD patterns, suggesting better iron dispersion in these catalysts, even when the iron concentration was as high as 1.5 wt.%.

The Raman spectra of these catalysts were presented in **Figure 2.9 (B)**. The spectrum of 0.5 wt.% Fe/SiO_2-V shows the same vibrational bands to those of 0.1 wt.% Fe/SiO_2-V catalyst. For the 1.5 wt.% Fe/SiO_2-V sample, all the vibrational bands are similar to those in the other two catalysts in this figure, except for the band centered at 663 cm^{-1} which is assigned to the iron oxide species. The detection of vibrational band belonging to the iron species in the Raman spectra indicates that large iron oxide particles could form in the Fe/SiO_2-V catalysts when the iron loadings were high in the silica support.

The coordination environments of iron species in Fe/SiO_2-V catalysts with different iron loadings were characterized by the DR UV-vis spectra (**Figure 2.9 (C)**). Similar to the 0.1 wt.% Fe/SiO_2-V, the other two catalysts show three absorption peaks centered around ~262 nm, ~380 nm and ~480 nm, corresponding to the isolated ionic iron species, small iron oxide (FeO)n oligonuclear clusters, and iron oxide nanoparticles, respectively. With increasing iron concentration in the silica support, the peak intensity at 262 nm position decreases, while intensities of the other two peaks at higher wavelength positions increase. This indicates the increase in the quantity of aggregated iron species in the samples with high iron loadings, accompanied with a decline in the amount of isolated iron species. The H_2-TPR profiles in **Figure 2.9 (D)** shows broad and strong peaks in the Fe/SiO_2-V catalysts with higher iron concentrations. As discussed in Section 2.4.1.1. above, the peak at 556 K is related to the reduction of Fe_2O_3 to Fe_3O_4, the peak at 699 K can be attributed to the reduction of Fe_3O_4 to FeO, whereas the peak at 843 K can be caused by the reduction of FeO to metallic iron. The increase in iron loading in the vitreous silica support apparently

increased the aggregation sizes of iron species, which lead to the consecutive reduction steps in the H_2-TPR profiles. This also reflects the interaction between the iron sites and silica support becomes weaker since these iron species can be easily reduced to lower oxidization states.

Figures 2.10 (A)-(C) shows the XPS spectra of Fe 2p, Si 2p and O 1s, respectively, of the Fe/SiO_2-V catalysts with different iron concentrations. In comparison to 0.1 wt.% Fe/SiO_2-V sample, the peaks correlating to Fe^{3+} binding energie, which appear at ~701.7 eV and ~725.1 eV, are observed, although the signal-to-noise ratio is relatively high. In addition, one more peak around 707.4 eV was detected in the 0.5 wt.% and 1.5 wt.% samples, which is attributed to the reduced Fe species. The oxyhydrogen flame environment could be the reason that led to the formation of reduced iron species in the as-prepared catalysts, as it is known that the oxyhydrogen flame structure could create local reducing environment. The Si 2p scan in **Figure 2.10 (B)** shows that all three samples have nearly similar peak shape and position, suggesting a similar Si bonding environment. The O 1s scan in **Figure 2.10 (C)** shows the shoulder peak position (~531.5 eV) moves slightly to lower binding energies with increasing iron loading in the catalyst. This should be caused by the interaction between Fe-O bond and Si-O bond in the vitreous silica support.

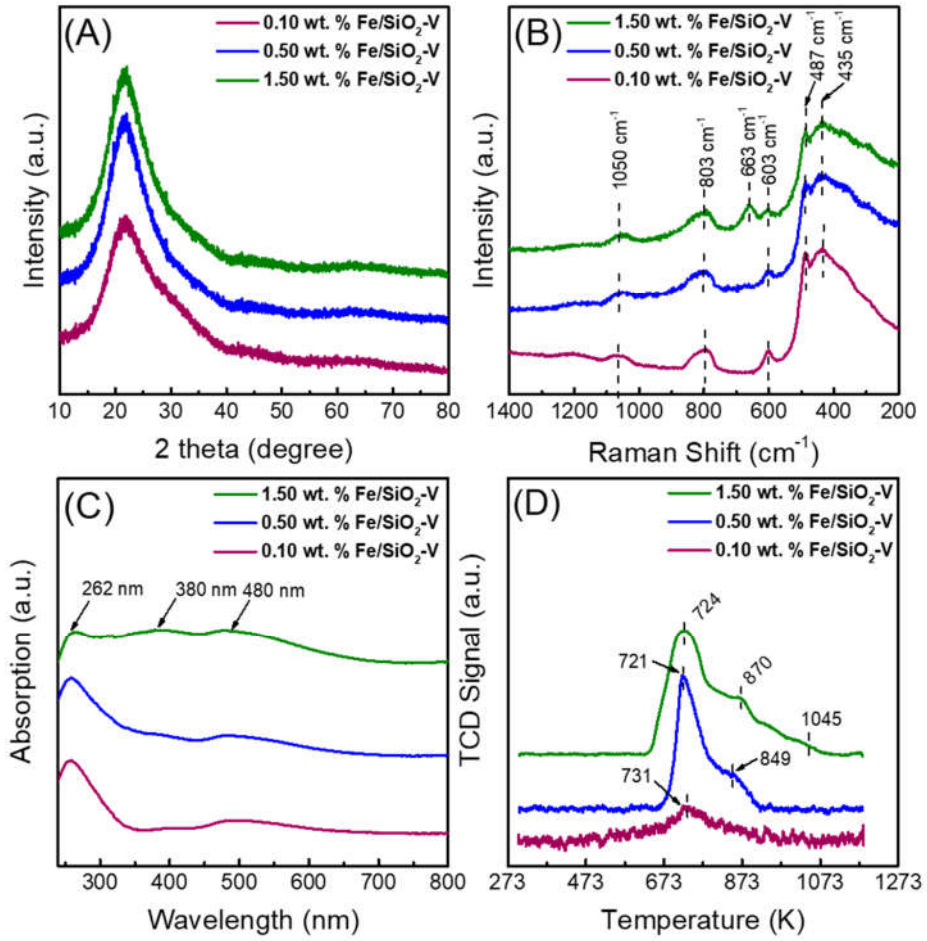

Figure 2.9. Characterization data of 0.5 wt.% and 1.5 wt.% Fe/SiO_2-V catalysts: (A) XRD patterns, (B) Raman spectra, (C) DR UV-vis spectra, and (D) H_2-TPR profiles. The characterization data for 0.1wt% Fe/SiO_2-V are included for comparison purposes.

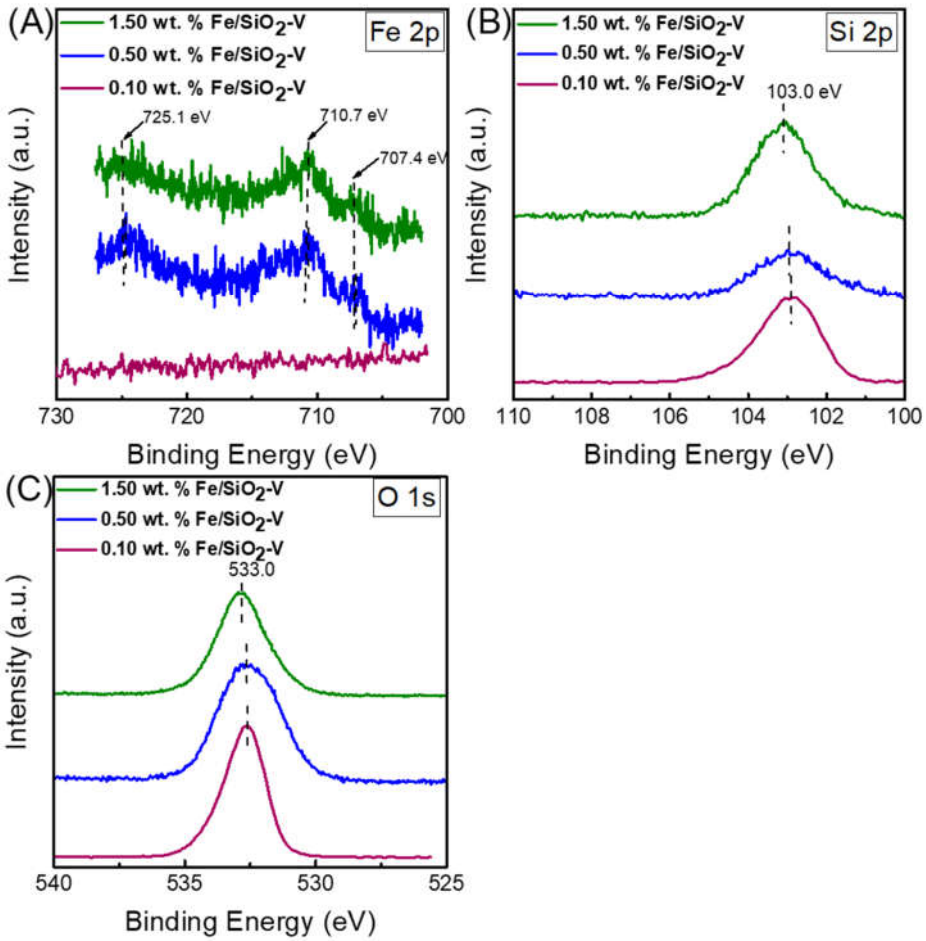

Figure 2.10. XPS spectra of Fe 2p (A), Si 2p (B), and O 1s (C) of 0.5 wt.% and 1.5 wt.% Fe/SiO2-V catalysts. The characterization data for 0.1 wt.% Fe/SiO_2-V are included for comparison purpose**.**

2.4.2.2 Methane Activation Study over Fe/SiO_2-v with Different Loading

The methane activation over the Fe/SiO_2-V catalysts with 0.5 wt.% and 1.5 wt.% iron concentrations were firstly monitored by the MS instrument. As shown in **Figures 2.11 (A)-(B),** the signal of m/z = 16, which should be attributed to the methane feed,

was firstly detected in the effluent stream. Right after the methane signal, the hydrogen (m/z = 2) signal were detected, followed by m/z = 26, m/z = 28 and m/z =30 signals that belong to the C_2 hydrocarbons. With increasing iron concentration in the catalyst, the product signals need a longer time to reach stability, as indicated a TOS of ~249 s in 0.5 wt.% Fe/SiO_2-v and 302 s in 1.5 wt.% Fe/SiO_2-v, in contrast to the TOS of 175 s in the 0.1 wt.% Fe/SiO_2-v (**Figure 2.11 (B)**). A close examination on the very initial stage of (i.e., within TOS of 140 s) catalyst activation was done by the zoomed in plots in **Figures 2.11 (C)-(D)**. Similar to 0.1 wt.% Fe/SiO_2-v, the hydrogen (m/z=2) production was suppressed in the very beginning, but it surpassed the C_2 product signals after a TOS of 12 s in 0.5 wt.% Fe/SiO_2-v and 16 s in 0.5 wt.% Fe/SiO_2-v catalysts. The higher iron concentration in the catalyst apparently needs to a longer time to reach stable NMC performance, while the catalyst requires a short time to start to function to the activating methane for hydrocarbons production.

The methane conversion and hydrocarbon product formation rates were measured for a TOS of 5 h. As shown in **Figure 2.12 (A)**, the 0.50 wt.% Fe/SiO_2-V catalyst had a methane conversion close to that of 0.1 wt.% Fe/SiO_2-v, but slightly higher than 1.50 wt.% Fe/SiO_2-v. The product formation rate in the 0.5 wt.% Fe/SiO_2-V catalyst follows the order of ethylene > naphthalene ~ benzene > acetylene > ethane ~ toluene (**Figure 2.12 (B)**). For the 0.5 wt. % Fe/SiO_2-V sample, the product formation rate is in the order of ethylene > naphthalene > benzene > acetylene > ethane ~ toluene (**Figure 2.12 (C)**). In both catalyst samples, the naphthalene formation rates were increased significantly than that of 0.1 wt. % Fe/SiO_2-v. The higher iron concentration in the catalyst seems to induce heavy aromatic formation in the NMC reaction.

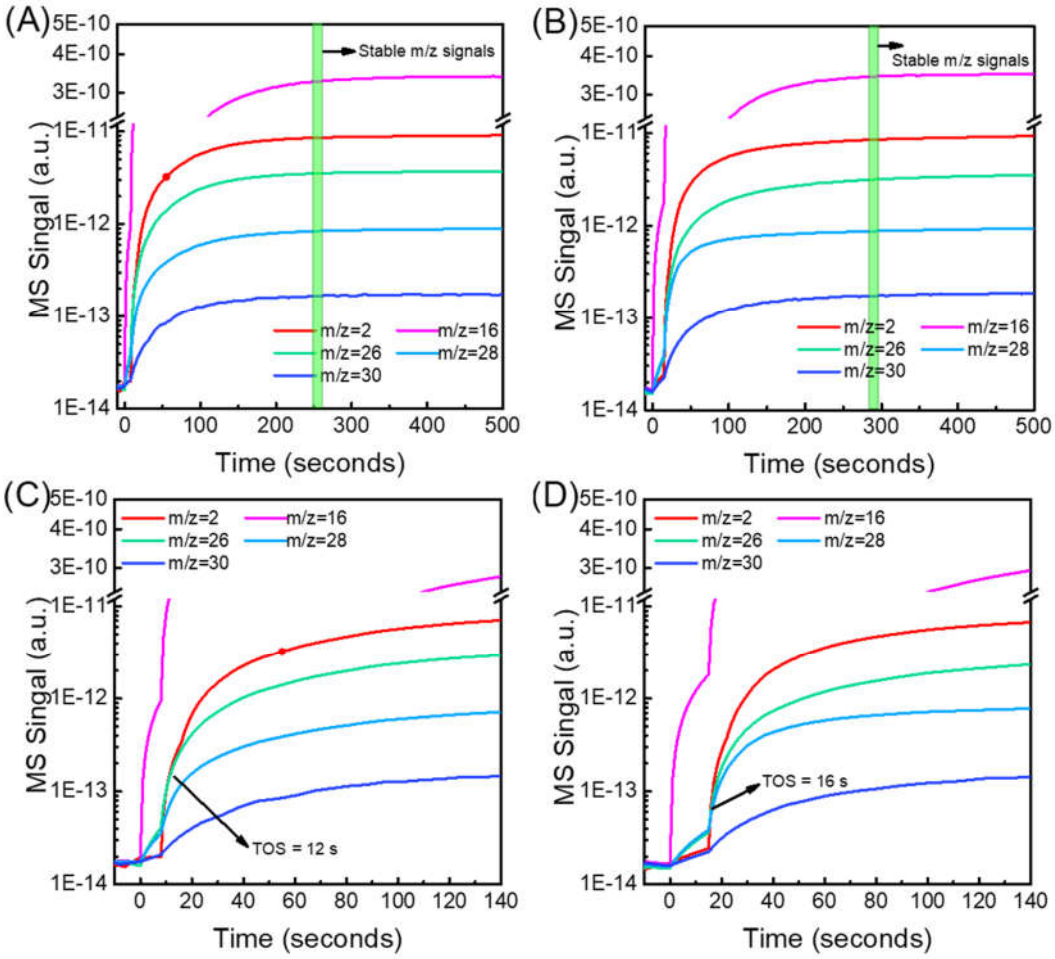

Figure 2.11. Methane activation over 0.5wt% (A) and 1.5wt% (B) Fe/SiO_2-V versus TOS tracked by a MS instrument. (C) and (D) show MS signals at TOS of <140 s in (A) and (B), respectively. (NMC conditions: 1273K, WHSV=3200 h^{-1}, 81.04 kPa CH4, Ar used as internal standard)

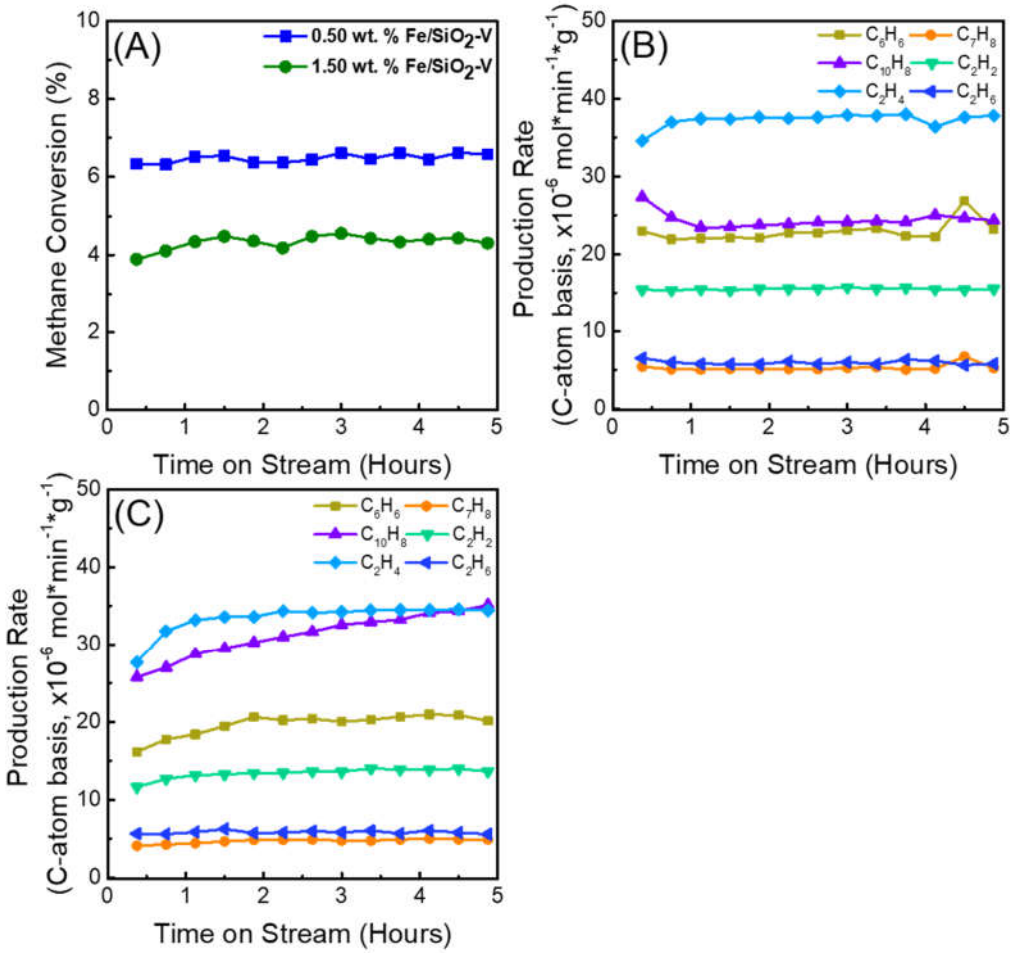

Figure 2.12. Methane conversion as function of TOS for 0.50 and 1.50 wt. % Fe/SiO_2-V (A) and hydrocarbon product formation rates versus TOS over 0.50 wt. % Fe/SiO_2-V (B) and 1.50 wt. % Fe/SiO_2-V (C) catalysts. (NMC conditions: 1273K, WHSV=3200 h^{-1}, 83.04 kPa CH4, Ar used as internal standard)

2.4.2.3 Analyses of spent Fe/SiO_2-v catalysts with different Fe concentrations

The coke quantities in the spent catalysts with higher iron concentrations were measured by the TGA instrument. As shown in **Figure 2.13 (A)**, the weight losses were 2.81 % and 3.14 % for 0.5 wt.% and 1.50 wt.% Fe/SiO_2-v, which are1.34 and 1.50 times higher than that of the 0.1 wt.% Fe/SiO_2-v catalyst. The coke formation increases with increasing iron concentration in the vitreous silica support. In addition, the onset of the coke combustion temperature decreases with iron concentration in the catalysts.

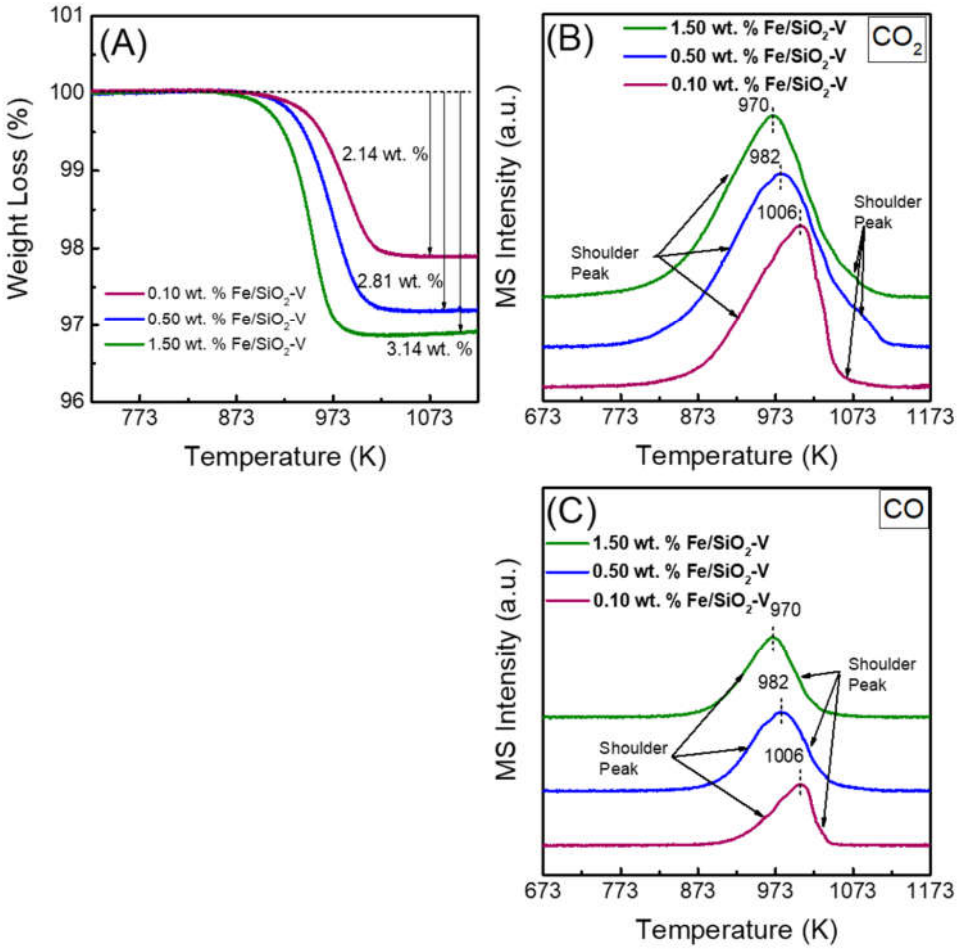

Figure 2.13. TGA data (A) and TPR profile of CO_2 (B) and CO (C) of spent 0.50 wt. % Fe/SiO_2-V and 1.50 wt. % Fe/SiO_2-V catalysts, the present of 0.1 wt. % Fe/SiO_2-V as comparison purpose. (NMC conditions: 1273K, WHSV=3200 h^{-1}, 83.04 kPa CH_4, Ar used as internal standard, TOS of 5 h)

The properties of the coke on the spent catalysts were further explored by the TPO measurement. **Figure 2.13 (B)-(C)** presents the CO_2 and CO evolution profiles of the spent catalysts with high iron loadings. The CO_2 evolution peak from the spent 0.5 wt.% Fe/SiO_2-v spans from ~733 K to near ~1123 K, with the peak maximum at 982 K and a small shoulder at 1073 K. The 1.5wt.% Fe/SiO_2-V catalyst has a broad CO_2 profile, spanning from the onset temperature of 673 K to the ending temperature of 1123 K. The peak maxima stay at 970 K, and no clear shoulder is observed in this spent catalyst. In comparison to that of 0.1wt.% Fe/SiO_2-v, the CO_2 evolution in the TPO measurement shifts to lower temperatures with increasing iron concentration in the catalysts. In addition, the peak shape becomes more symmetric. The CO profiles in **Figure 2.13 (C)** show the same trends as those of the CO_2 profiles. Overall, more soft coke was formed in the spent catalysts with higher iron loadings.

2.5 Summary

We developed vitreous silica-supported iron catalysts using flame fusion, involving a quartz and fayalite mixture and an oxyhydrogen torch. This method converted crystalline quartz silica into amorphous vitreous silica. The results from characterization revealed a disordered Si-O bonding and structural defects in the vitreous silica, promoting iron dispersion and strong iron-silica bonds. Compared to

crystallized cristobalite-supported Fe/SiO_2 catalysts, our vitreous silica-supported Fe/SiO_2 showed better performance in methane activation, with reduced coke deposit and a more uniform coke type. However, increasing iron content in the catalyst did not enhance methane conversion. Instead, it favored the production of benzene, naphthene, and coke, and lengthened the catalyst induction period.

Chapter 3: Experimental Screening Vitreous Silica Supported M/SiO_2 (M = Mn, Fe, Co, Ni, and Cu) Catalysts under Direct, Non-oxidative Conversion of Methane.

This chapter is adapted in part from Zixiao Liu, Charles J. Titus, Cherno Jaye, Daniel A. Fischer, Antara Bhowmick, Genwei Chen, Yuying Shu, Evan P. Jahrman, and Dongxia Liu, "Vitreous Silica Supported Metal Catalysts for Direct Non-oxidative Methane Coupling". Manuscrpit submitted to Chemical Engineering Journal. March, 2024

3.1 Abstract

Direct NMC transforms methane into valuable chemicals and hydrogen, which is a promising pathway to boost industrial decarbonization. The reaction, however, is challenged by high C-H bond activation temperature, catalyst coking, and low selectivity towards hydrocarbon products. Here we studied the efficacy of five vitreous silica supported 3d transition metal (Mn, Fe, Co, Ni, and Cu) catalysts (denoted as M/SiO_2-v) for NMC. These catalysts were prepared by flame fusion of mixtures of quartz and metal silicate precursors. The metal species in the as-synthesized catalysts were fully or partially oxidized, with their stability following the order of Mn > Fe ≈ Co > Ni > Cu in the NMC reaction. The Cu species has low methane reaction rate, due to the high adsorption and dissociation energies of methane. The Mn and Ni species have high methane reaction and coke formation rates, which is supported by easy

kinetics of methane deep dehydrogenation to carbon. In contrast, Fe and Co species showed the best hydrocarbon product selectivity. Particularly, the Co species emerged as the optimal catalyst for NMC, showcasing a balanced methane activation, hydrocarbon formation, and low coke yield. The relationship between the evolved metal species under reaction conditions and their NMC performance was discussed. The present study screens and provides effective catalyst formulations for NMC reactions.

3.2 Introduction

According to the US Department of Energy's industrial decarbonization roadmap[216], technological advances producing cost-effective clean energy and sustainable chemical feedstocks are crucial to reducing greenhouse gas emissions. Methane (CH_4), the main ingredient of natural gas, is anticipated to gain popularity as a cost-effective feedstock, courtesy of the vast reserves within the US, underpinning the supply of clean energy and valuable chemicals[217]. Presently, methane is primarily consumed by combustion for electrical power generation and syngas production, yet both processes yield significant amounts of greenhouse gas emissions[218, 219]. However, deliberate management and utilization of methane to produce clean energy and chemicals could become key strategies to boost industrial decarbonization and reduce global carbon footprints.

Direct NMC is one of the promising processes toward decarbonized clean energy and chemical production[220]. It transforms methane into olefins (e.g., ethylene (C_2H_4) and acetylene (C_2H_2)), aromatics (e.g., benzene (C_6H_6) and naphthalene

($C_{10}H_8$)), and hydrogen (H_2), without greenhouse gas emissions. The reaction, however, is challenged by high reaction temperature, low catalyst stability and low hydrocarbon selectivity. Zeolite supported metal catalyst (e.g., molybdenum/ZSM-5 (Mo/ZSM-5)) has been the most extensively studied NMC catalyst since 1993[154]. Substantial enhancement in hydrocarbon product selectivity and catalyst stability have been realized in NMC over the metal/zeolite catalysts in the past decades, but the reaction typically occurs < 1023 K due to catalyst stability and is limited by low CH_4 conversion (≈16% at 1023 K) and by fast catalyst deactivation (≤10 h) due to coke deposition[74, 221, 222]. The silica supported metal (e.g., Fe/SiO_2, Fe species confined in SiO_2 matrix) is a more recent NMC catalyst reported in 2014[86]. Compared to the metal/zeolite catalysts, this catalyst works at higher temperatures (e.g., ≈1273 K), produces higher hydrocarbon yields, and reduces coking when proper reaction conditions were selected.

The fundamental studies for the Fe/SiO_2 catalysts in the NMC chemistry have been focused on the elucidation of structures of the active sites[86, 175, 188] and methane reaction mechanisms[176, 178, 179, 181, 223]. The Fe/SiO_2 catalyst was reported to contain an iron atom coordinated by one Si and two C atoms and thus embedded within the SiO_2 matrix. The isolation of the iron atoms in the silica matrix through bonding to Si and C atoms achieves high selectivity toward hydrocarbons and reduces coke formation under high-temperature reaction conditions[86]. Additionally, it has been proposed that the reaction mechanism follows the activation of methane by dehydrogenation over Fe sites to generate $\cdot CH_3$ and $\cdot H$ radicals, which subsequently release from the catalyst surface and undergo a series of gas-phase reactions to form dehydrogenated and cyclized

products[223]. The engineering of reactors[85, 184] can manipulate the mixed surface-gas phase chemistry to optimize the C_{2+} hydrocarbon production and minimize coke formation.

The synthesis of M/SiO_2 catalysts for NMC has been focused on cristobalite supported iron species, which was formed by fusion in a high temperature furnace [188]. The effects of polymorphs of silica support and/or types of metal species in the M/SiO_2 catalysts on NMC have been explored recently. For example, silica dehydroxylated at 1353 K[172], porous SBA-15[224], ZSM-5[173, 225] and silica[86], as well as vitreous quartz[226] have been used as the metal supports for NMC. The high surface area from the porous silica support led to high coke formation[226]. The vitreous silica support that was prepared by a flame fusion method has disordered Si-O bonds and structural defects, enabling better iron dispersion and more vital metal-support interaction, and consequently a shorter induction period in methane activation and lower coke yield in NMC[226]. The metal type, including bi-metallic sites (e.g., Fe combined with Co, Ni, Pd, Pt)[189] or Co-, Ni-, Cu-, Mo-, and Ru-based nanocatalysts[224] have been prepared in M/SiO_2 catalysts for NMC. The alloying of Fe species in the bimetallic catalysts is reported to suppress coke formation, in contrast to catalysts comprising singular elements[189]. In tandem with experimental studies, computational endeavors have also yielded significant insights on effects of metal types in the silica support on NMC. For instance, He et al.[191] evaluated the potential of 25 transition metal candidates for inclusion in the silica-based catalyst and found that Mn, Fe, W, and Re exhibited elevated performance for methane activation, a key step in the NMC research. It should

be noted that the experimental screening of the catalyst formulations for the NMC reaction has been rarely explored.

This work aimed to experimentally screen the performance of vitreous silica supported transition metal catalysts for NMC. The catalyst was synthesized as the previous report[226] on the Fe/SiO_2-v catalyst. The 3d transition metals Mn, Fe, Co, Ni, and Cu were used in the M/SiO_2-v catalysts. The correlations between the NMC performance, catalyst structure, and physiochemical properties were investigated. The present study provides effective catalyst formulations and guides the future development of silica-based catalysts for the selective conversion of methane to higher hydrocarbons in NMC.

3.3 Experimental Methods

3.3.1 Materials

Metal silicates (M_2SiO_4, M = Mn, Fe, Co, Ni) and copper polysilicate ($CuSiO_3$) were used as M/SiO_2-v precursors and were synthesized via the sol-gel method described in previous publication[85, 215, 226]. Silica (quartz phase, IOTA-4, Sibelco Group, USA), nitric acid (HNO_3, ACS Grade, Fisher Chemical), and deionized (DI) water were used without extra purification.

3.3.2 Catalyst Preparation

For the preparation of the M/SiO_2-v catalyst, certain amount of Mn_2SiO_4, Fe_2SiO_4, Co_2SiO_4, Ni_2SiO_4, and $CuSiO_3$ precursor was mixed with 20.00 g of quartz into a 50 mL dense zirconia ceramic milling jar to ensure 0.5 wt. % of total metal

loading. Another 100 g of 6 mm zirconia milling media was added into the jar and followed by milling on the jar milling machine (755 RMV, US. Stoneware) for 24 h with 100 rpm speed. The grounded powder was pressed into a pellet in a carbon steel die under 5 metric tons of force. The pellet was fused by oxy-hydrogen flame to form a glassy ingot. A detailed procedure of catalyst processing after flame fusion, including grinding, sieving, and cleaning, was described in the previous publication [35].

3.3.3 Catalysts Characterization

The crystalline phase of the catalyst was measured via XRD by Bruker® D8 diffractometer under Cu-Kα radiation. The 0.02-degree step size and 3 s of step time were selected as scan parameters. The actual metal loading in the as-prepared catalysts was determined by Spectro Arcos II inductively coupled plasma-optical emission spectrometry (ICP-OES). Raman spectra of the catalysts were collected using a HJY LabRam ARAMIS Raman spectrometer with 532 nm wavelength, 600 grid/mm gathering size. The XPS data were measured using a Kratos Axis 165 spectrometer with a monochromatic Al X-ray source. DR UV-vis spectra of the catalysts were measured using the Cary 60 UV-vis spectrophotometer.

The temperature-programmed reduction (H_2-TPR) profiles of the catalysts were measured in the Quantachrome Autosorb-iQ system, which is equipped with a thermal conductivity detector (TCD) with a sampling frequency of 1 Hz. Before the measurement, the catalyst was pre-treated under N_2 gas flow (40 mL min^{-1}, Research grade, Airgas) at 823 K for 4 h. After cooling to 323 K, the gas was switched to 5 % H_2/N_2 (40 mL min^{-1}). The catalyst sample was then heated to 1223 K at a 10 K min^{-1}

ramp rate and kept at the final temperature for 10 min. An inline liquid nitrogen cold trap was equipped to remove moisture produced during the experiment to avoid possible interference with the TCD signal.

3.3.4 Catalytic reaction test

The NMC reaction was conducted in a straight-packed bed reactor made from fused quartz. Typically, a 0.375 g catalyst sample was placed in the reactor, heated from room temperature to 1273 K under 50 mL min^{-1} flowing of Ar (UHP grade, Airgas) with the ramping rate of 10 K min^{-1}. After reaching 1273 K, 16 mL min^{-1} methane (Research grade, Airgas) mixed with 4 mL min^{-1} Ar (as the internal standard) was introduced into the reactor. The temperature of the catalyst bed was monitored by using a K-type thermocouple. The reactor outlet was analyzed using a gas chromatograph (Agilent 7890A) equipped with a methyl-siloxane capillary column (HP-1, 50.0 m × 320 μm × 0.52 μm) configured to a flame ionization detector (FID) and a packed column (ShinCarbon ST Columns, 80/100 mesh, 1.83 m) configured to a TCD.

For methane activation in the initial stage of the reaction, the reactor outlet was monitored by mass spectroscopy (MS, Prima BT, ThermoFisher Scientific). Since the MS records the mass to charge ratio (m/z), the matrix deconvolution method was used to retrieve the actual species signal based on previous work [227]. To prevent blockage of gas lines in the MS system, an inline dry ice/acetone cold trap was used to condense liquid-phase hydrocarbon products.

3.3.5 Analysis of spent catalyst

The coke formation in the spent catalysts was determined by the TGA method by the Shimadzu TA-50 TGA system. Typically, around 20 mg of the spent catalyst was exposed to 50 mL min^{-1} flowing air (Breathing grade, Airgas) immobilized in a fused quartz sample cell and ramped from room temperature to 1273 K with a 10 K min^{-1} rate. The nature of coke formed on the spent catalyst was examined using the temperature-programmed oxidation (TPO) technique. The temperature was monitored by a K-type thermocouple attached to the outer wall of the quartz sample cell. The furnace was ramped from room temperature to 1123 K at a ramp rate of 10 K min^{-1} under a flowing Ar (45 mL min^{-1}, ultrapure, Airgas) and O_2 (5 mL min^{-1}, ultrapure, Airgas) atmosphere. The nature of coke was profiled by the temperature-dependent consumption or formation of O_2, CO_2, and CO species based on pervious study[226].

3.3.6 X-ray absorption fine structure measurements

Metal L-edge near-edge X-ray absorption fine structure (NEXAFS) spectra were taken at the microcalorimeter end station of the NIST SST-1 beamline, 7-ID-1, at the National Synchrotron Light Source II (NSLS-II). Powdered samples were prepared on conductive tape on top of an aluminum bar. Measurements were conducted under UHV conditions with a ring current of 400 mA. X-rays from an elliptically polarized undulator source were monochromatized with a 1200 l/mm plane grating monochromator with an exit slit of 25 μm, providing about 0.1 eV full width at half maximum (FWHM) energy resolution in a 1.5 x 1.5 mm spot on the sample. Spectra were recorded in Total Electron Yield mode (TEY) via drain current, and in Partial

Fluorescence Yield (PFY) mode via a Transition-Edge Sensor array with 1 eV FWHM resolution, operated as described by Lee et al. [228] Spectra were normalized by the beam intensity, as measured by the drain current from a gold mesh.

Hard X-ray measurements were performed on the NIST BMM beamline, 6-BM, at NSLS-II. A 3-pole wiggler delivered an unfocused beam tuned by a Si (111) monochromator across the K-edges of Mn, Fe, Co, Ni, and Cu. A series of oxides for each element were sourced from NSLS-II to serve as empirical standards. These standards were measured in transmission mode with a metallic foil of the corresponding element simultaneously measured downstream to verify the stability of the monochromator. Catalyst samples were measured in fluorescence mode with the powders spread between layers of polyimide tape. To facilitate proper pre-edge subtraction and post-edge normalization, each spectrum was collected from 200 eV below the corresponding edge to an energy above the edge corresponding to a photoelectron momentum of 15 $Å^{-1}$. Standard normalization procedures were applied in the Athena software package[229].

Speciation analyses were performed using the X-ray absorption near-edge structure (XANES) results. For all elements except Fe, this was accomplished by linear combination analysis. This entailed fitting a spectrum of interest to a linear combination of reference spectra using the statsmodels python library[230]. For the Co, Mn, and Cu *K*-edges, this was done to estimate the fraction of metallization occurring during reaction. Therefore, the spectra corresponding to the as-prepared M/SiO_2-v catalyst and the metal foil were selected as references. As significant metallization was found in the as-prepared Ni/SiO_2-v sample, it was deemed preferable to fit the Ni/SiO_2-v spectra to a

linear combination of NiO and Ni metal. For the Fe/SiO_2-v catalysts, assigning oxidation state distributions for oxides at the Fe *K*-edge requires detailed peak fitting[231, 232]. We fit the pre-edge of the as-prepared sample's spectrum according to procedures reported elsewhere [233]. First, the edge position of metallic Fe was set to 7110.75 eV, consistent with Kraft et al.[234] Two Gaussian features were used to accommodate the background shape and an additional two were assigned to the pre-edge features with their widths constrained to be equal. The fraction of Fe atoms present as Fe (III) was then estimated from the centroid position according to the calibration curve established by Wilke et al.[232] for a similar family of vitreous silica materials. This method was chosen in lieu of constructing a variogram due to the complex coordination environments that Fe is known to occupy in vitreous silica frameworks.

Extended X-ray absorption fine structure (EXAFS) fitting was performed to analyze the local atomic environment of several transition metals. First, a FEFF calculation was performed according to methods described elsewhere[235]. As first shell fits were desired, model structures were constructed by substituting transition metal and oxygen atoms into the structure of rock salt. The path corresponding to the first shell was then fit in real-space using the appropriate functions in the Larch library [236]. Fits varied four variables, the radial distance of the ligand (R), the coordination number (C.N.), the Debye-Waller factor (σ^2), and the change in the photoelectron energy shift needed to align theoretical calculations to the experimental edge position (ΔE_0). Varied k-weightings of k, k^2, and k^3 were incorporated to heighten the contrast between spectral effects caused by coordination number and disorder[237]. To enable the calculation of coordination numbers, the passive amplitude reduction factor was fixed

for each edge according to the value produced by a fit to an empirical standard after asserting chemical transferability.

3.4 Results and Discussion

3.4.1 Physicochemical properties of M/SiO_2-v catalysts

3.4.1.1 Morphology and composition of M/SiO_2-v catalysts

The morphology of as-prepared M/SiO_2-v catalysts is shown by photographs (**Figures 3.1 (A-E)**) in the Supporting Information. Due to the metal species incorporation, Mn- and Cu/SiO_2-v (**Figures 3.1 (A)** and **(E)**) are light yellow, Fe- and Ni/SiO_2-v (**Figures 3.1 (B)** and **(D)**) are grey, and Co/SiO_2-v (**Figure 3.1 (C)**) is blue. The particle sizes in all samples were in the range of 177 μm – 400 μm. The actual metal loadings in these catalysts are around 0.5 mass %, consistent with their nominal concentration (**Table 3.1**). The surface areas of these catalysts are ≈0.30 m^2 g^{-1}, determined by the N_2-isotherms and analysis method described in the previous work[226]. The XRD patterns (**Figure 3.2 (A)**) show the as-synthesized M/SiO_2-v catalysts have a broad peak at $2\theta \approx 20.94°$, suggesting the amorphous feature of vitreous silica support. The absence of any other obvious peaks suggests that the metal species is well dispersed in the silica support.

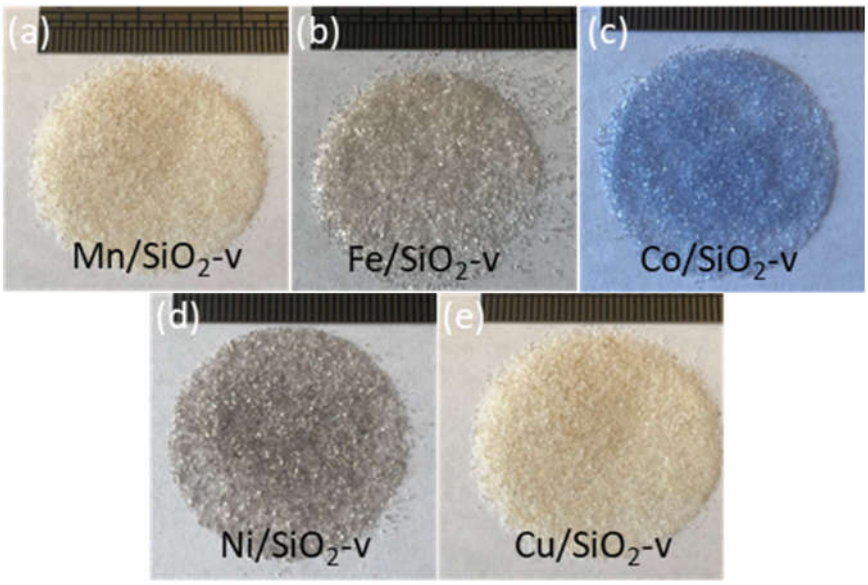

Figure 3.1. Picture of fresh Mn/SiO2-v (A), Fe/SiO2-v (B), Co/SiO2-v (C), Ni/SiO2-v (D), and Cu/SiO2-v (E) catalysts.

Table 3.1. Metal concentration in the prepared M/SiO2-v catalysts.

Catalysts	**Fresh Mn/SiO_2-v**	**Fresh Fe/SiO_2-v**	**Fresh Co/SiO_2-v**	**Fresh Ni/SiO_2-v**	**Fresh Cu/SiO_2-v**
Nominal	0.50	0.50	0.50	0.50	0.50
Actual	0.46	0.65	0.46	0.30	0.37

3.4.1.2 Bonding environments in M/SiO_2-v catalysts

The silica bonding environment in the M/SiO_2-v catalysts was probed by the Raman spectra (**Figure 3.2 (B)**). For all samples, the main band located at 442 cm^{-1} can be attributed to high membered (6 or more) Si-O ring structures, which is the key

characteristic band of amorphous silica[238, 239]. The bands at 492 cm^{-1} and 604 cm^{-1} refer to the 4 membered Si-O rings and 3 membered Si-O rings, respectively, indicative of amorphous silica with structural defects[238-240]. The band presenting at 800 cm^{-1} can be assigned to the vibrations in the random network of Si-O bonds[241], which further evidences the defects in the vitreous silica support. Another two bands at 1069 cm^{-1} and 1202 cm^{-1} are assigned to the asymmetric stretching of the bridging oxygen species[238, 242].

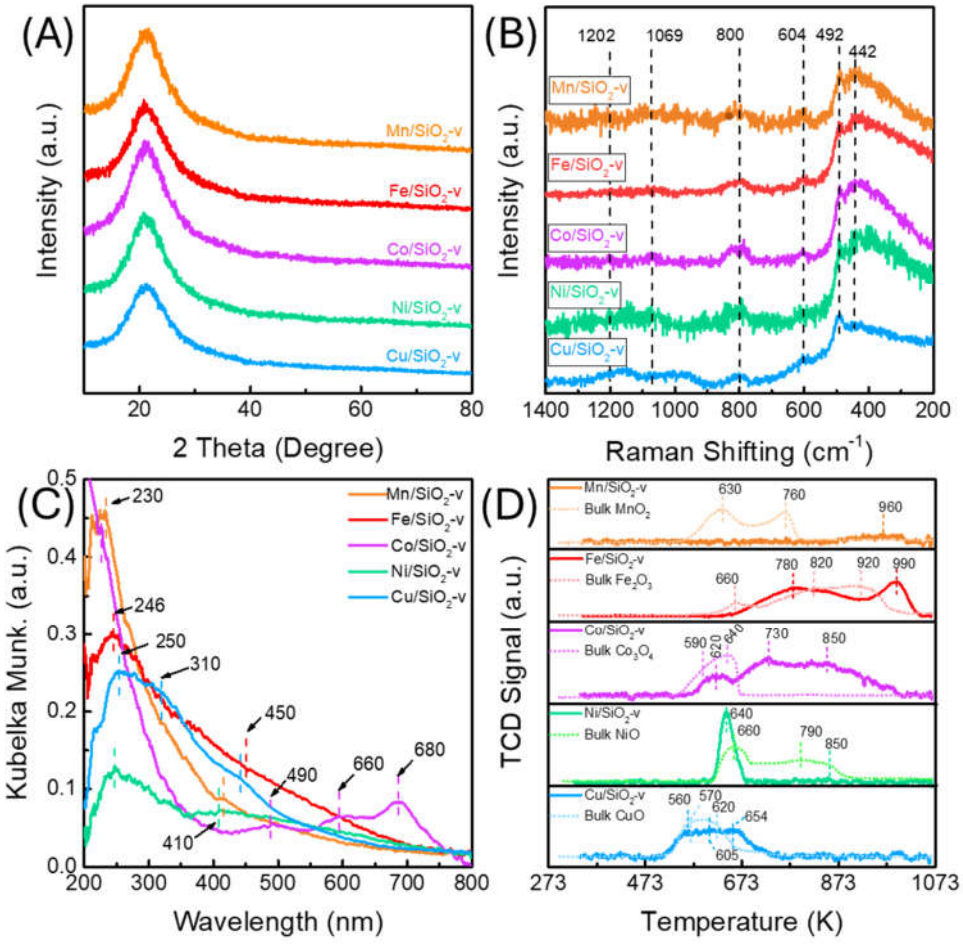

Figure 3.2. Basic properties of fresh M/SiO_2-v (M = Mn, Fe, Co, Ni, and Cu) catalysts characterized by (A) XRD, (B) Raman spectra, (C) UV-vis DRS spectra, and (D) H2-TPR profile.

The coordination environments of metal species in the M/SiO_2-v catalysts were studied by DR UV-vis spectra (**Figure 3.2 (C)**). The Mn/SiO_2-v has a very strong absorption band at ≈230 nm which can be assigned to the charge transfer involving Mn(II)-O(II) site in the silica matrix[243, 244]. A weak absorption band at ≈410 nm can be assigned to d–d transitions of octahedral Mn^{2+} ions[245]. Although the DR UV-vis absorption spectrum of Mn/SiO_2-v has a broad tail, no obvious absorption band extends beyond 500 nm, which suggests the majority of Mn species forms isolated sites[246]. The Fe/SiO_2-v sample contains a strong band at ≈250 nm and a broad tail without obvious absorption bands beyond 350 nm, which evidences isolated Fe sites are the primary species in the catalyst. The Ni- and Cu/SiO_2-v samples have the similar DR UV-vis spectroscopic features to those of Fe/SiO_2-v, except that there are a few absorption bands at higher wavelengths. For the Ni/SiO_2-v sample, the absorption bands at ≈250 nm and ≈410 nm can be assigned to charge transfer involving Ni (II)-O site and d-d transition of Ni-O-Ni site (II), respectively[247]. Similarly, the bands at ≈250 nm, 310 nm, and 450 nm are contributed by charge transfer of isolated Cu (I, II)-O, chain structure of Cu-O-Cu as Cu oxide cluster[248, 249], and tetrahedral nanoparticles of Cu (I, II), in sequence [250]. The appearance of bands at wavelength of > 300 nm suggests that these two samples contain more aggregated metal species [251-254]. The Co/SiO_2-v has the highest number of absorption bands, distributed at ≈230 nm, ≈500 nm, ≈600 nm and ≈690 nm in sequence. The band at ≈250 nm can be ascribed to Co (II) coordinated by

oxygen in the tetrahedral site[255], which is evidence of isolated Co sites in the silica lattice framework. The other three bands can be assigned to extra-framework Co (II) ions in the octahedral site at 600 nm and tetrahedral site at 683 nm, evidence of small clustering or nanoparticle formation[255, 256]. The very strong peak at ≈250 nm suggests the isolated Co (II) is dominant in the as-prepared Co/SiO_2-v catalyst. In summary, the DR UV-vis spectra suggest that Mn/SiO_2-v has the highest amount of isolated metal sites, while the other four samples have a mixed single metal sites and clusters.

3.4.1.3 Reducibility of metal species in M/SiO_2-v catalysts

The reducibility of the metal site and bond strength was probed by the H_2-TPR profiles (**Figure 3.2 (D)**). For comparison purpose, the H_2-TPR profiles of bulk MnO_2, Fe_2O_3, Co_3O_4, NiO, and CuO were measured and included. The Mn/SiO_2-v catalyst does not have obvious peaks except for the weak broad one at ≈960 K, while the bulk MnO_2 sample contains the reduction of Mn (IV) to Mn (III) at 632 K and Mn (III) to Mn (II) at 760 K, respectively[257]. The broad weak peak at ≈960 K in Mn/SiO_2-v could be assigned to the reduction of Mn (II) species. In combination with the DR UV-vis data above, it seems that Mn (II) is the dominant species in the Mn/SiO_2-v catalyst.

The H_2-TPR profile of Fe/SiO_2-v catalyst exhibited two peaks at 778 K and 993 K, which are assigned to reduction of Fe (II, III) to Fe (II) and Fe (II) to metallic Fe in sequence[258]. Compared with the reduction of Fe (III) to Fe (II, III) at 659 K in the H_2-TPR profile of bulk Fe_3O_4, Fe species predominately stayed as a mixed Fe (II, III) state in the Fe/SiO_2-v catalyst. The H_2-TPR profile of Co/SiO_2-v catalyst exhibits three reduction peaks at 620 K, 727 K, and 847 K, which can be ascribed to reduction of Co

(II) to Co (0), smaller Co (II) clusters to Co (0), and stronger Co-O-Si interaction based on previous studies[50, 51, 258]. The bulk Co_3O_4 only show a broad reduction peak centered at 641 K, which often lumps the reduction steps of Co (III) to Co (II) and Co (II) to metallic species together[258, 259]. The shifting of reduction peaks to high temperatures in the Co/SiO_2-v sample suggests the strong bonding between Co species and silica support. Similarly, the H_2-TPR profiles of Ni- and Cu/SiO_2-v catalysts have broader peaks than those of the bulk metal oxides. The extension of the reduction peaks to higher temperatures should be caused by the interaction between metal (Ni or Cu) species and the vitreous silica support. In comparison with the Mn-, Fe-, and Co/SiO_2-v catalysts, the existence of strong peaks associated with reduction of NiO and CuO bulk oxides in their H_2-TPR profiles indicates the existence of these species or weak interaction between the metal and silica support in these two samples.

3.4.1.4 Oxidation states of metal species in M/SiO_2-v catalysts

The oxidation states of metal sites in the M/SiO_2-v catalysts were studied by XPS (**Figures 3.3 (A-E)**) and NEXAFS (**Figures 3.3 (F-J)**) data. The Mn 2p XPS scan in Mn/SiO_2-v sample (**Figure 3.3 (A)**) have two peaks at binding energies of 642.0 eV and 654.0 eV, contributed by transitions from Mn $2p_{3/2}$ and Mn $2p_{1/2}$ states, which could nominally originate from the Mn (II) species [260, 261]. The proximity of binding energies from differing Mn oxidation states and Poisson noise, however, complicates a definite assignment at the exclusion of others. To support this assignment, the NEXAFS spectra corresponding to excitations from the same core states, Mn $2p_{3/2}$ and Mn $2p_{1/2}$, are presented in **Figure 3.3 (F)**. Notably, these spectra probe the dipole-allowed transitions

into the unoccupied density of states near the Fermi level, and thus provide a sensitive fingerprint of the local electronic structure. As a further contrast to XPS, the sample's NEXAFS spectrum was collected via partial fluorescence yield which, unlike the electron based XPS, is particularly well suited for studies of dilute metals in insulating materials. Here, a large characteristic resonance at 639.6 eV aligned well with that observed from the Mn (II) reference. Furthermore, the spectral shape agreed with previous reports for hydrated Mn (II) and Mn (II) coordinated to acetylacetonate [262, 263], confirming Mn (II) species were present.

The Fe 2p XPS scan in Fe/SiO_2-v sample (**Figure 3.3 (B)**) has peaks at 712.0 eV and 726.1 eV as the binding energy for Fe $2p_{3/2}$ and Fe $2p_{1/2}$. This should be attributed to the presence of mixed Fe species has (II, III) oxidation states [264, 265]. In particular, the broadness of the Fe $2p_{3/2}$ peak is suggestive of a mixture of the Fe (II) and Fe (III) oxides. Meanwhile, two low-intensity peaks located at binding energy 718.6 eV and 733.5 eV were found as satellite peaks affiliated with the Fe $2p_{3/2}$ and Fe $2p_{1/2}$ features belonging to the Fe (III) oxidation states [265]. More precisely, the NEXAFS spectrum of as-prepared Fe/SiO_2 in **Figure 3.3 (G)** shows two peaks at 708.6 eV and 710.0 eV which are close in energy but of significantly different intensities than peaks found with a Fe_2O_3 standard. Other researchers have attributed such peaks to Fe(II) and Fe(III) in silicates[266], thus the greater relative intensity of the peak at 708.6 eV suggests reduction of the catalyst and further evidences the presence of Fe (II, III) oxidation states.

The Co 2p XPS scan of Co/SiO_2-v (**Figure 3.3 (C)**) has two distinct peaks at binding energies of 780.6 eV, and 796.5 eV, which correspond to the Co $2p_{3/2}$ and Co

$2p_{1/2}$ states. These binding energies indicate the presence of Co (II) oxidation states[267, 268] in the catalyst sample. However, instead of pursuing rigorous fits of a spectrum dominated by Poisson noise, a clearer fingerprint of the chemistry can be obtained from the NEXAFS results. Specifically, the decline of Co (III) species is evidenced by the NEXAFS spectra in (**Figure 3.3 (H)**), where the as-prepared Co/SiO_2-v spectrum was well aligned with the CoO features at 777.5 eV to779.4 eV, and 793.7 eV. Notably, the Co/SiO_2-v spectrum did not exhibit the resonance at approximately 775 eV, which is often attributed to Co species in an octahedral coordination state [269]. The Ni/SiO_2-v in (**Figure 3.3 (D)**) shows XPS features at a binding energies of 854.8 eV for Ni $2p_{3/2}$ and 873.3 eV for Ni $2p_{1/2}$, which correspond to the Ni (II) species [270, 271]. Besides, two low-intensity peaks were found with binding energy at 862.4 eV and 881.8 eV, which were assigned to the satellite peaks affiliated with the Ni $2p_{3/2}$ and Ni $2p_{1/2}$ features [270-272]. The result was also supported by NEXAFS spectra in (**Figure 3.3 (I)**), as the Ni (II) presented in Ni/SiO_2-v, though the lower feature intensities may indicate the presence of Ni metal. This will be investigated further in the context of the K-edge XANES results.

The Cu/SiO_2-v exhibited its Cu $2p_{3/2}$ and Cu $2p_{1/2}$ peaks at binding energies of 933.2 eV and 953.5 eV that are contributed by Cu (I, II) species [45, 273]. Due to the low concentration resulting in an insufficient signal-to-noise ratio of the Cu 2p peaks, only qualitative statements can be made based on the XPS. Clearer evidence is provided by the NEXAFS spectra in (**Figure 3.3 (J)**). Note that Cu_2O features found at 929.6 eV and 949.5 eV are indicative of some surface oxidation as it is difficult to obtain a pristine Cu_2O reference [274]. Finally, the catalyst's spectrum exhibited multiple features

roughly aligned with those found in Cu_2O and CuO reference oxides. As the Cu(I) feature is of similar intensity to those of Cu_2O and the Cu (II) features are significantly less intense than those from CuO, it was determined that the catalyst contains a mixture of Cu(I) and a minor Cu (II) phase. It should be noted that the overall interpretations of the metal 2p XPS and NEXAFS features of the M/SiO_2-v catalysts agree with the DR UV-vis and H_2-TPR results discussed above.

The survey scan of vitreous silica catalysts in **Figures 3.4 (A-D)** found significant features for only Si, O, and C, and did not reveal any obvious contamination elements. In **Figure 3.4 (B)**, the Si 2p scan found all of the peaks to be symmetric with a binding energy near 704.4 eV, falling into the Si-O bonds in vitreous silica[275-277]. The O 1s scan in **Figure 3.4 (C)** shows all samples had the O 1s peak between 533.1 eV and 533.5 eV, corresponding to the typical Si-O-Si bonds in amorphous silica phase[226, 278-280]. The C 1s scan in **Figure 3.4 (D)** exhibited typical adventitious carbon with binding energy around 285.2 eV, which corresponds to C-C and C-H bonds[281-283]. Not surprisingly, the formation of adventitious carbon is due to the natural contamination of specimens which were prepared and treated under an ambient air environment.

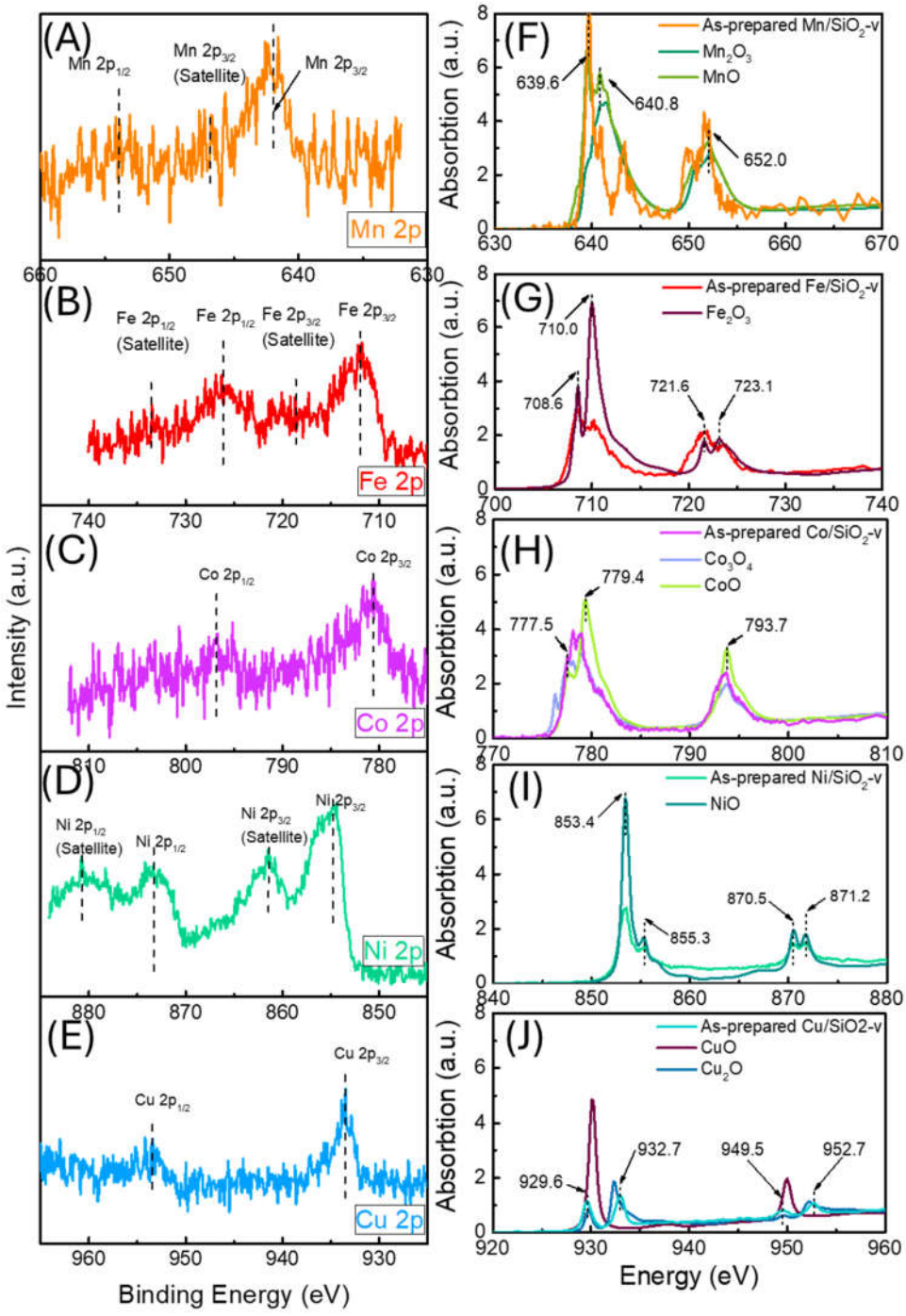

Figure 3.3. XPS spectra (A-E) and NEXAFS spectra (F-J) for fresh M/SiO2-v catalysts (M =Mn (A) and (F), Fe (B) and (G), Co (C) and (H), Ni (D) and (I), and Cu (E) and (J)). Reference oxides serve as empirical standards in NEXAFS spectra in (F)-(J).

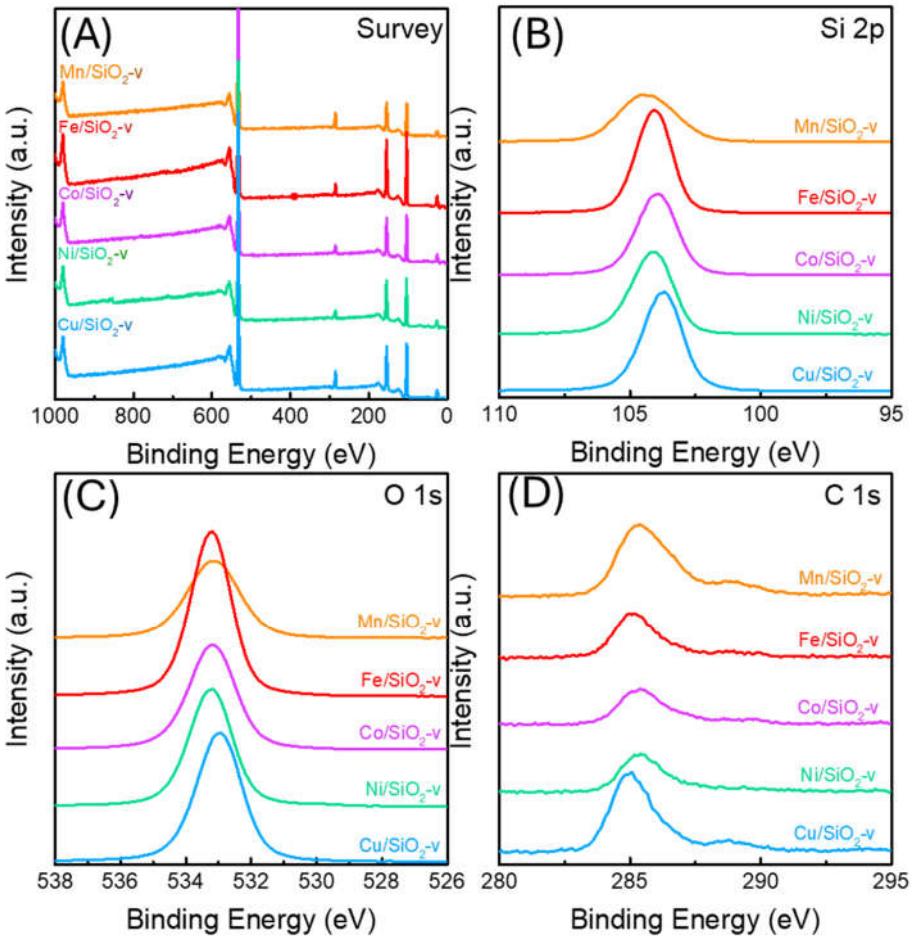

Figure 3.4. XPS survey scan (A), and high-resolution scan of Si 2p (B), O 1s (C), and C1s, (D) for M/SiO_2-v catalysts.

3.4.2 NMC reaction over M/SiO_2-V catalysts

3.4.2.1 Methane activation in the initial reaction stage

A mass spectrometer was used to track methane activation over the M/SiO_2-v catalysts during the early stages of the NMC reactions. Upon introduction of methane

into the M/SiO_2-v catalysts, H_2 product formed, and its signal increased proportionally with the CH_4 event (**Figures 3.5 (A-E)**). Within time on stream (TOS) < ≈20 s, C_2H_6 and C_2H_2 products appeared, followed by C_2H_4 and higher hydrocarbon species such as C_3H_8. With the progress of NMC reaction (e.g., TOS > ≈20 s), the signals of C_2 products increased and then reached plateau values at TOS of >≈150 s. The C_2H_4 signal increased significantly in the reaction period of TOS < ≈100 s. All the M/SiO_2-v catalysts show a similar trend in evolution of these product species versus the reaction time.

The fine differences in methane activation over these catalysts can be detected by a close examination of species evolution data (**Figures 3.5 (A-E)**). Firstly, the generation of H_2 over Mn- and Ni/SiO_2-v catalysts (**Figures 3.5 (A)** and **(D)**) was sooner than that of Fe-, Co- and Cu/SiO_2-v (**Figures 3.5 (B), (C)** and **(E)**) catalysts, suggesting the former two catalysts have stronger C-H scission capability. In contrast, Cu/SiO_2-v catalyst has the slowest hydrogen formation, which might be caused by the sinking of Cu sites into the silica surface that cannot provide suitable site for anchoring methyl groups[191]. Secondly, the formation of C_2H_2 product quantity over these catalysts followed the trend of Mn > Ni > Fe > Co > Cu, indicating Mn and Ni have the high activity for C_2H_2 formation. C_2H_2 has been reported to be the precursor of coke deposition[284], and thus it is expected that Mn- and Ni/SiO_2-v catalysts could have high coking rates. The last different feature is the formation of CO and CO_2 signals over these M/SiO_2-v catalysts. Ni-, Fe- and Cu/SiO_2-v (**Figures 3.5 (B), (D),** and **(E)**) have obvious CO and detectable CO_2 signals at TOS of ≤ 50 s, while these signals were very

weak in the Mn- and Co/SiO_2-v catalysts. The CO_x signals should be attributed to the reduction of metal species to the lower oxidation states. It seems that the as-prepared Mn and Co/SiO_2-v catalysts have more stable metal species than the other three catalysts that were formed in the flame fusion process.

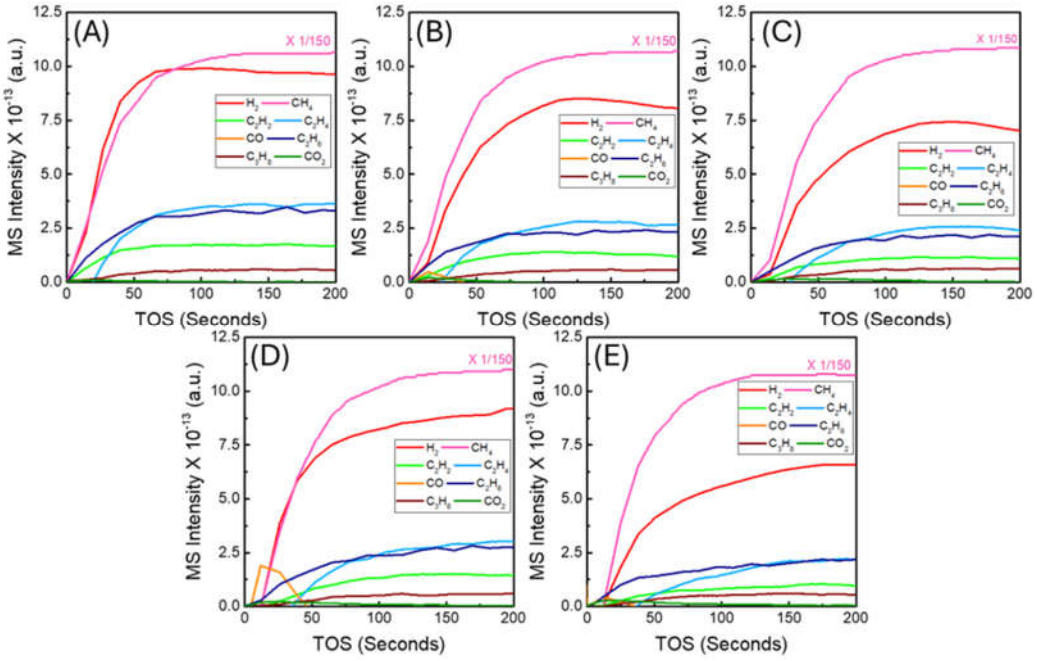

Figure 3.5. Species revolution as a function of TOS in methane activation over M/SiO_2-v Mn (A), Fe (B), Co (C), Ni (D), and Cu (E) monitored by a MS. (NMC Condition: 1273 K, WHSV = 6400 h^{-1}, 81.4 kPa, Ar as internal standard)

3.4.2.2 Methane conversion and product selectivity over M/SiO2-v catalysts

Methane reaction and product formation rates were measured in the NMC over the M/SiO_2-v catalysts with TOS of 5 h. After the induction period of TOS of ≈1 h, the NMC reaction reached stable performance. Averaged methane reaction and product formation rates were plotted against metal type for further analysis. In **Figure 3.6 (A)**,

Mn- and Ni/SiO_2-v have the highest methane reaction rates, followed by Co- and Fe/SiO_2-v catalysts, and then by the Cu/SiO_2-v catalyst. The low reaction rate over Cu species in the silica support agrees with previous computation work [191], showing that Cu is a poor methane activator due to an over-inflated geometry at the Cu site， causing the d_z^2 orbital to have electron distribution below the Fermi level and thus forming ineffective interaction with C-H bond.

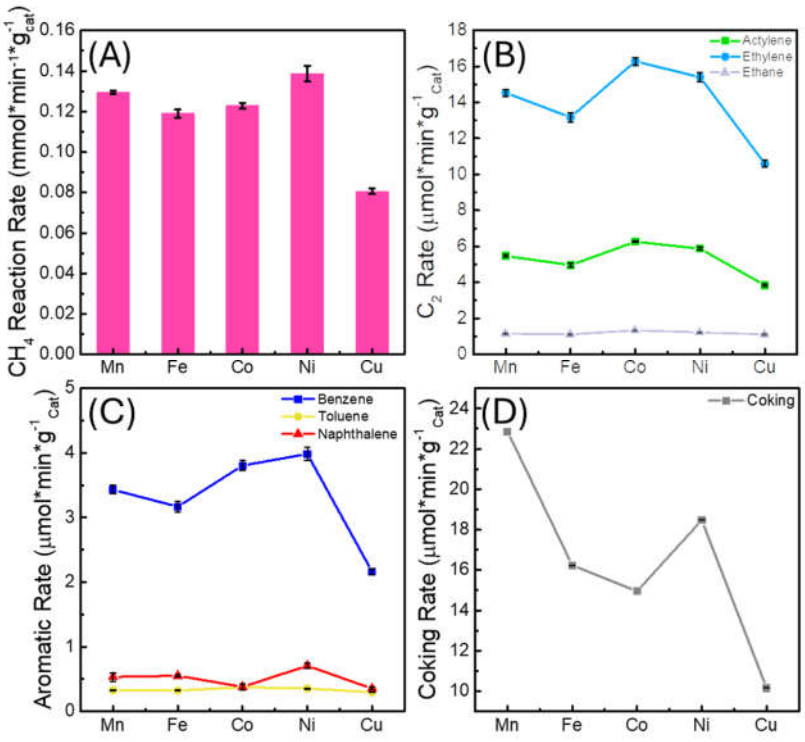

Figure 3.6. Catalytic performance of M/SiO_2-v catalysts in NMC reaction: (A) methane reaction rate, (B) C_2 formation rate, (C) aromatics formation rate, and (D) coke formation rate. (NMC Condition: 1273 K, WHSV = 6400 h^{-1}, 81.4 kPa, Ar as internal standard)

The dominant products from the NMC reactions are C_2 (i.e., ethane, ethylene, and acetylene) and aromatics (i.e., benzene, toluene, and naphthalene), in which ethylene and benzene are the dominant products (**Figures 3.6 (B-C)**). Among these five different NMC catalysts, Co- and Ni/SiO_2-v catalysts have the highest C_2 and aromatics formation rates, followed by Mn- and Fe/SiO_2-v catalysts. The Cu/SiO2-v has the lowest hydrocarbon product formation rate, which should be caused by its low methane reaction rates due to inferior methane activation on this catalyst. The coke formation rates (**Figure 3.6 (D)**), quantified by TGA measurement, follows the order of Mn > Ni > Fe > Co > Cu. Mn and Ni species exhibited high methane conversion with relatively lower hydrocarbon selectivity, which could be due to their high deeper dehydrogenation capability of forming carbon product[202, 285]. The Cu/SiO_2-v exhibited low methane conversion due to its resistance to methane activation. Overall, the Co/SiO_2-v catalyst demonstrated reasonably high methane reaction rate, hydrocarbon formation and low coking rates.

3.4.3 Coking species in spent M/SiO_2-v catalysts

The carbon deposits on the spent catalysts were probed by the O_2-TPO profiles after TOS of 5 h in the NMC reaction. **Figures 3.7 (A-C)** shows the CO_2, CO, and O_2 evolution profiles in the measurement. Two distinct differences among the five spent catalysts were observed. Firstly, the peak evolution temperatures follow the order of Co < Ni ≈ Fe < Mn ≈ Cu in the M/SiO_2-v catalysts. Secondly, the degree of asymmetry of the CO_2, CO and O_2 peaks increase in the trend of Mn ≈ Ni < Fe < Co < Cu. In particular, the combustion of spent Mn/SiO_2-v catalyst displayed relatively narrow and

slightly symmetric TPO profiles (**Figure 3.7 (A)**), with an onset of 896 K and completion occurring at 1127 K, a span of 231 K. The Co/SiO_2-v catalyst has a clear shoulder peak (centered at 897 K) at the low temperature region of the TPO profile. The tail on the lower temperature range (854 K) is relatively smooth. For Cu/SiO_2-v catalyst, there is a clear low temperature peak, which can be easily separated from the high temperature peak at 980 K.

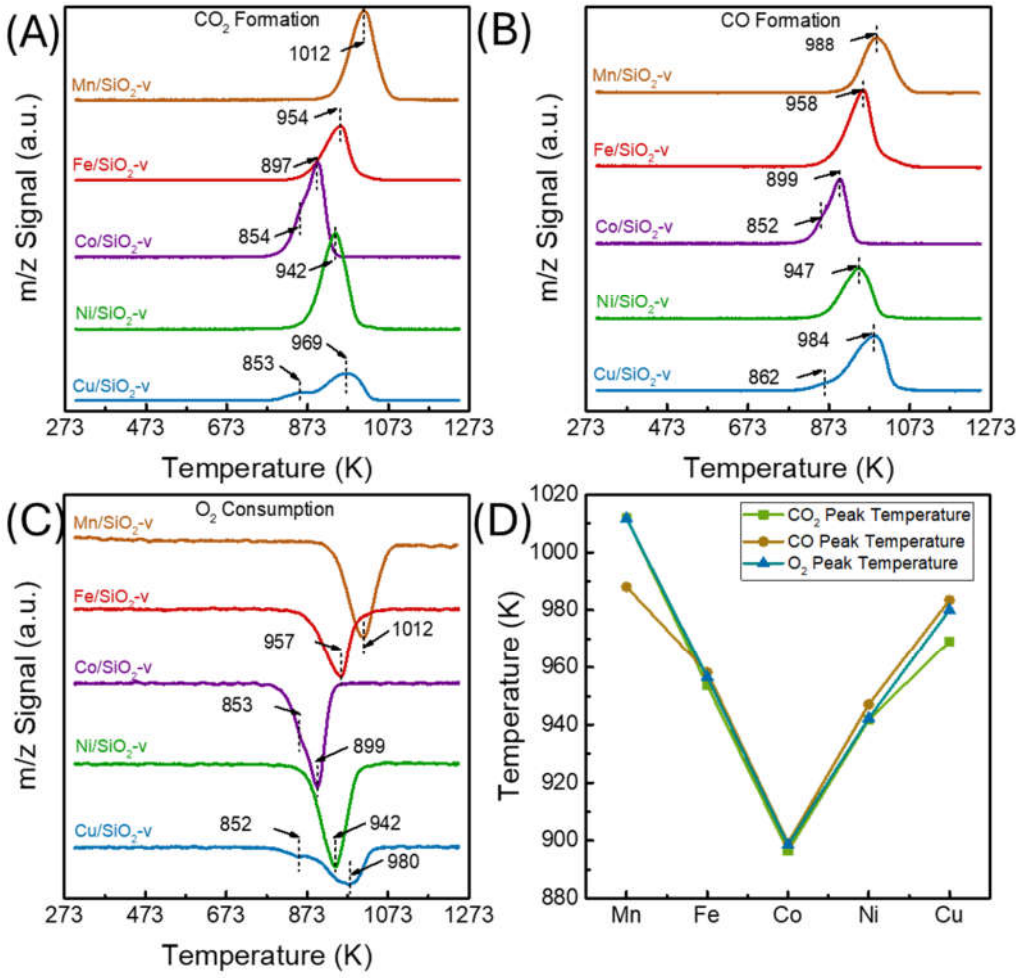

Figure 3.7. CO_2 formation rate (A), CO formation rate (B), and O2 consumption rate (C) in TPO profile of spent M/SiO_2-v catalysts after 5 hours of NMC reaction. TPO profiles measured for spent catalysts as CO_2 formation rate (A), CO formation rate (B), and O_2 consumption rate (C), TPO peak temperature as effect of catalysts (D).

The TPO peak temperatures reflect the types of coking species in the spent M/SiO_2-v catalysts. The TPO spectra for each spent catalyst can be deconvoluted into three peaks - low, medium, and high temperature peaks - as reported previously[226]. The low temperature peak can be ascribed to amorphous and oxidized "soft" coke, the medium temperature peak to polymeric aromatic carbon, and the high temperature peak to the ordered, graphitic "hard" coke. The formation of diverse carbon species in the NMC reaction has been observed in Mo/ZSM-5[221, 286, 287] and metal/sulfated zirconia catalysts[288-290] as well as in methane pyrolysis in the absence of any catalyst[291-294]. The Co/SiO_2-v catalyst has the highest amount of low temperature coke, which can be actively involved in the reaction. The Mn/SiO_2-v accumulated the hardest ordered graphitic coke. **Figure 3.7 (D)** shows the coke removal temperature exhibits a volcano shape with regards to the positions of these five transition metals in the periodic table.

3.4.4 Evolution of metal species in M/SiO_2-v catalysts in NMC reaction

To study effects of NMC reaction on the metal sites in the vitreous silica supported metal catalysts, X-ray absorption fine structure (XAFS) can be used to measure the local electronic and atomic structure of the transition metals in each catalyst, which includes their oxidation states and coordination environments before and after the NMC reaction activation. The procedure of catalyst activation under NMC

was carried out by exposing 0.375 g of as-prepared catalyst to NMC conditions for 15 mins, producing so called activated catalysts. In **Figure 3.8 (A)**, the Mn K-edge XANES spectra for the as-prepared Mn/SiO_2-v and activated Mn/SiO_2-v are nearly superimposed and exhibit edge positions in general alignment with MnO, suggesting Mn (II) is the predominant oxidation state of the Mn atoms in the catalysts. From the inset, the pre-edge features are also elevated in intensity relative to that of octahedral MnO, which indicates the Mn atoms may be in a site without inversion symmetry[295]. This result is supported by the corresponding EXAFS results shown in **Figure 3.8 (B)** and reported in **Table 3.2**, which demonstrate the Mn is approximately four-fold coordinated to oxygen, albeit slightly undercoordinated. Moreover, these results reveal almost no change of the coordination environment in as prepared and activated catalysts. The fitted results of Fourier-transformed EXAFS from (**Figures 3.8 (E and F)**) exhibit a single predominate peak at ≈1.595 Å (not phase corrected) for both as-prepared and activated Mn/SiO_2-v. The lack of significant peaks at higher radial distances suggests the Mn atoms are occupying disordered sites without long-range order, which is consistent with the Mn atoms dispersing on the vitreous silica matrix as opposed to forming metallic clusters.

Table 3.2. EXAFS fitting results for the selected catalysts. Uncertainties correspond to one standard error.

Sample	**Mn/SiO_2-v (Fresh)**		**Mn/SiO_2-v (Spent)**		**Co/SiO_2-v (Fresh)**		**Cu/SiO_2-v (Fresh)**	
Bond Type	Result	Stand. Err.	Result	Stand. Err.	Result	Stand. Err.	Result	Stand. Err.
	Mn-O		Mn-O		Co-O		Cu-O	
ΔE_0 (eV)	-3.46	0.13	-4.9	0.5	-5.4	0.3	-0.8	0.4

C.N.	3.60	0.05	3.88	0.19	4.08	0.10	1.93	0.06
R (Å)	2.082	0.001	2.073	0.005	1.979	0.002	1.850	0.003
σ^2 (Å^2)	0.0057	0.0002	0.0066	0.0007	0.0077	0.0004	0.0038	0.0005

The Fe K-edge XANES spectra of Fe/SiO_2-v are shown in **Figure 3.8 (C)**. The as-prepared Fe/SiO_2-v catalyst's edge position was found to be slightly higher in energy than the divalent references. This is consistent with the results of pre-edge peak fitting shown in Figure **3.9 (A)** which found the centroid to be at 7113 eV, according to the method of Wilke et al.[232]. This suggests that ≈ 36 % of the Fe atoms are Fe (III) while the remainder are Fe (II), see **Table 3.3**. This agrees with the earlier DR UV-vis, H_2-TPR, and XPS results, which found a combination of Fe (II, III) oxidation states. Notably, the reacted Fe/SiO_2-v XANES spectrum resembles fayalite (Fe_2SiO_4), suggesting the Fe atoms were reduced to Fe (II) and occupied an octahedral Fe-O environment very similar to fayalite. The corresponding Fourier-transformed EXAFS spectra are shown in **Figure 3.8 (D)**. Both the as-prepared and activated Fe/SiO_2-v catalyst spectra exhibit clear first and second shell peaks, indicating formation of Fe oxide nanoparticles or clusters over the vitreous silica support, which is consistent with the DR UV-vis and H_2-TPR results. Furthermore, the reacted catalyst's EXAFS spectrum bears considerable resemblance to fayalite. This again suggests a similar local structure in those two samples.

Co K-edge XANES spectra for Co/SiO_2-v are shown in **Figure 3.8 (E)**. The edge position of both the as-prepared and activated samples is well aligned with CoO, indicating the presence of the Co (II) oxidation state. However, the white line at 7725 eV reduces intensity upon reaction, while the pre-edge region around 7710 eV increases

in intensity. This can be explained by the corresponding Fourier-transformed EXAFS spectra in **Figure 3.8 (F)**. For the as-prepared catalyst, the Co/SiO_2-v exhibits a single predominate peak which can be assigned to four-fold coordination with oxygen, see **Table 3.2.** While there is some spectral weight in the second shell, a wavelet transform analysis present in **Figures 3.10 (A-B)** revealed that the peaks are due to scattering from a neighbor lower in atomic number than Co. Finally, the fitted Fourier-transformed EXAFS spectra in (**Figure 3.9 (G)**), no significant peaks were found after 3.5 Å (not phase corrected). These results indicate the formation of isolated Co species in the vitreous silica matrix rather than metal agglomeration. In contrast, the activated Co/SiO_2-v exhibits a second peak at a position roughly consistent with metallic Co from **Figure 3.8 (F)** and more intense than the second peak of the as-prepared catalyst's spectrum. Returning to the Co K-edge XANES results in (**Figure 3.8 (B)**), fitting the activated Co/SiO_2-v spectrum to a linear combination of the as-prepared catalysts and the metallic Co's spectra provided excellent agreement with the activated spectrum and revealed that ≈15 % of the Co atoms formed metallic particles during reaction, as presented in **Table 3.3**.

Table 3.3. K-edge XANES fitting with results of linear combination for species types and fractions for Co, Ni, and Fe/SiO_2-v catalysts.

Catalyst	Co/SiO_2-v Spent		Ni/SiO_2-v Fresh		Ni/SiO_2-v Spent		Fe/SiO_2-v Fresh	
Species Type	Co (II)	Co (0)	Ni (II)	Ni (0)	Ni (II)	Ni (0)	Fe (III)	Fe (II)
Species Fraction	0.85	0.15	0.18	0.82	-0.02	1.02	0.36	0.64

Stderr	0.002	0.002	0.004	0.004	0.004	0.005	0.050	0.050

The Ni K-edge XANES spectra in (**Figure 3.8(G)**) reveal strong similarities between both the as-prepared and activated Ni/SiO_2-v with the metallic Ni spectrum. These spectra indicate the presence of metallic Ni particles over the vitreous silica support. Notably, the as-prepared sample exhibited a white line at 8350 eV that was slightly more intense than Ni (0), suggesting some Ni (II), which NEXAFS also observed in **Figure 3.3 (I)**. Here, linear combination analysis revealed the as-prepared spectra is well-reproduced by a mixture of ≈18 % Ni (II) oxide and ≈82 % Ni metal; the fitting results are presented in **Figure 3.9 (C)** and **Table 3.2.** This demonstrates that some Ni (II) species are present in the as-prepared sample and then become completely reduced to metallic Ni during the reaction. Furthermore, the Ni K-edge Fourier-transformed EXAFS spectra in **Figure 3.8 (H)** further confirm the presence of metallic Ni in both the as-prepared and activated Ni/SiO_2-v catalysts.

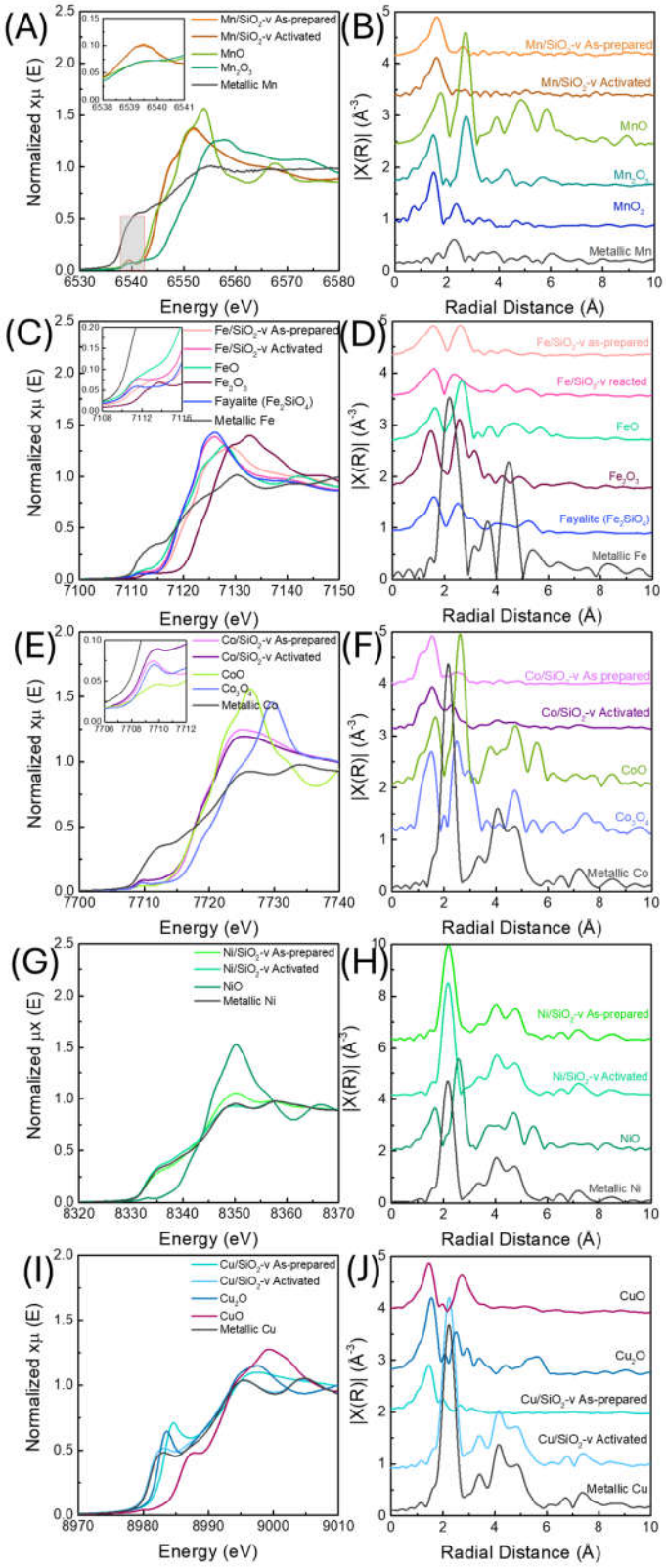
(A)
Normalized xμ (E)
Energy (eV)
Mn/SiO2-v As-prepared
Mn/SiO2-v Activated
MnO
Mn2O3
Metallic Mn
(B)
|X(R)| (Å-3)
Radial Distance (Å)
Mn/SiO2-v As-prepared
Mn/SiO2-v Activated
MnO
Mn2O3
MnO2
Metallic Mn
(C)
Normalized xμ (E)
Energy (eV)
Fe/SiO2-v As-prepared
Fe/SiO2-v Activated
FeO
Fe2O3
Fayalite (Fe2SiO4)
Metallic Fe
(D)
|X(R)| (Å-3)
Radial Distance (Å)
Fe/SiO2-v as-prepared
Fe/SiO2-v reacted
FeO
Fe2O3
Fayalite (Fe2SiO4)
Metallic Fe
(E)
Normalized xμ (E)
Energy (eV)
Co/SiO2-v As-prepared
Co/SiO2-v Activated
CoO
Co3O4
Metallic Co
(F)
|X(R)| (Å-3)
Radial Distance (Å)
Co/SiO2-v As prepared
Co/SiO2-v Activated
CoO
Co3O4
Metallic Co
(G)
Normalized μX (E)
Energy (eV)
Ni/SiO2-v As-prepared
Ni/SiO2-v Activated
NiO
Metallic Ni
(H)
|X(R)| (Å-3)
Radial Distance (Å)
Ni/SiO2-v As-prepared
Ni/SiO2-v Activated
NiO
Metallic Ni
(I)
Normalized xμ (E)
Energy (eV)
Cu/SiO2-v As-prepared
Cu/SiO2-v Activated
Cu2O
CuO
Metallic Cu
(J)
|X(R)| (Å-3)
Radial Distance (Å)
CuO
Cu2O
Cu/SiO2-v As-prepared
Cu/SiO2-v Activated
Metallic Cu

Figure 3.8. XANES and EXAFS spectra for fresh and activated M/SiO2-v catalysts (M =Mn, Fe, Co, Ni, and Cu) for Mn (A-B), Fe (C-D), Co (E-F), Ni (G-H), and Cu (I-J).

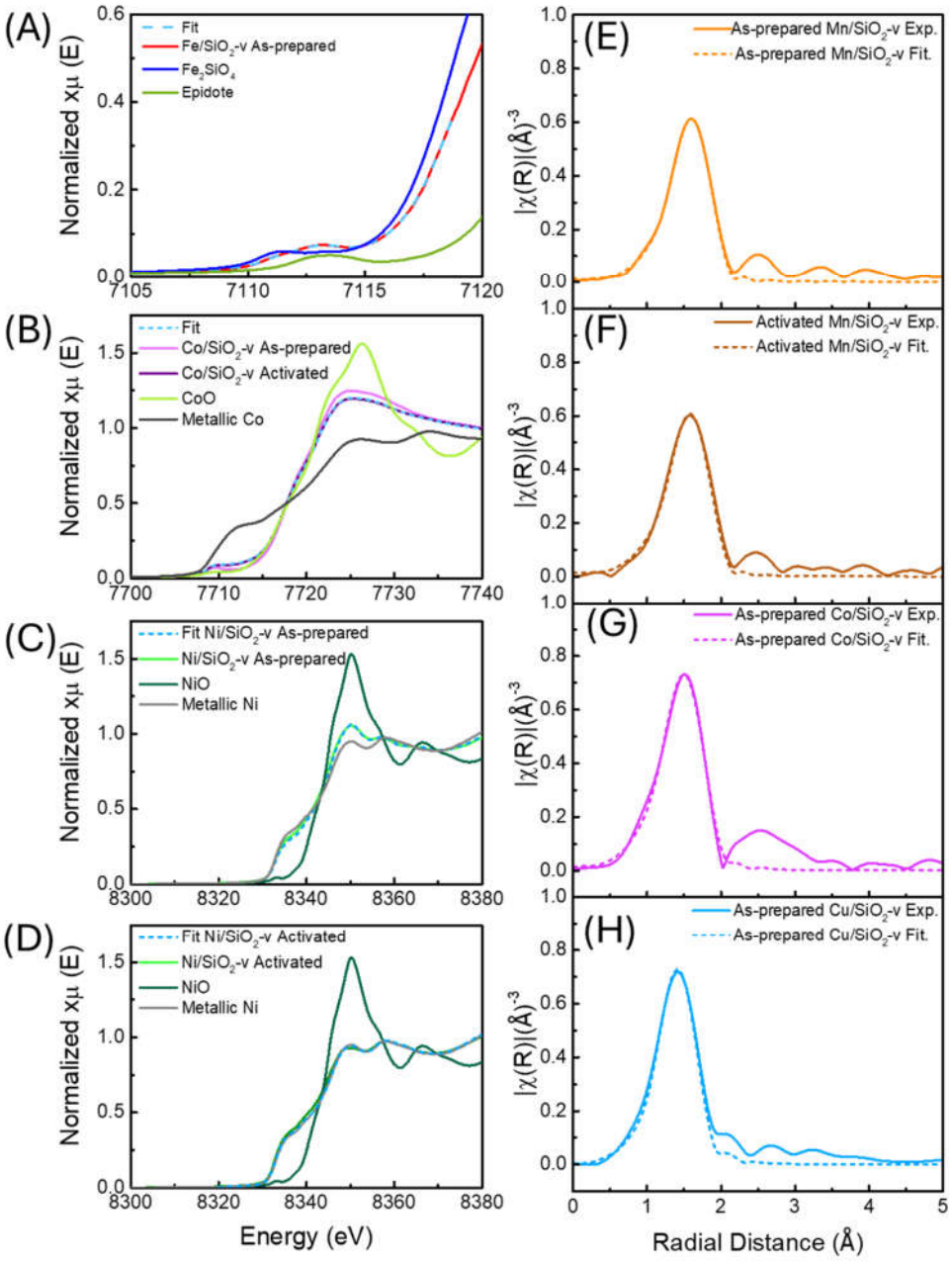

Figure 3.9. XANE Spectra with the fitted curve for Fe/SiO_2-v (A), Co/SiO_2-v (B), Ni/SiO_2-v (C-D) to determine the catalyst site status. K-edge Fourier-transformed EXAFS spectra with the fitted curve for Mn (F-G), Co (H), and Cu/SiO_2-v (I) as the demonstration of the short-range coordination status of these catalyst sites.

The Cu K-edge XANES spectra in **Figure 3.8 (I)** indicate Cu atoms in the as-prepared Cu/SiO_2-v catalyst are primarily found in a Cu (I) oxidation state. In particular, the shoulder feature at 8984 eV strongly indicates monovalent copper[296]. However, a slight chemical shift to higher energies suggests the Cu (I) oxidation state likely co-existed with Cu (II), consistent with NEXAFS results in Figure 2 (J). In contrast, the XANES spectra reveal Cu (0) species were formed in the spent Cu/SiO_2-v, as the spectra are well-aligned in the pre-edge and rising edge with metallic Cu. From the Fourier-transformed EXAFS spectra in **Figure 3.9 (H)**. A single predominate peak for Cu/SiO_2-v at 1.41 Å (not phase corrected) can be found. Fitting revealed the Cu atoms are two-fold coordinated, see **Table 3.3**, consistent with the peak exhibiting an intensity roughly identical to Cu_2O. The remaining features up to 4 Å resemble the Cu_2O and CuO spectra but lack significant intensity, perhaps indicating some small nanoparticles or clusters of Cu (I, II) over the Cu/SiO_2-v catalyst. Finally, the reacted Cu/SiO_2-v spectra exhibited significant overlap with the metallic Cu, meaning the Cu sites have been fully converted to metallic Cu, as can be verified from **Figures 3.8 (I)** and **(J)**.

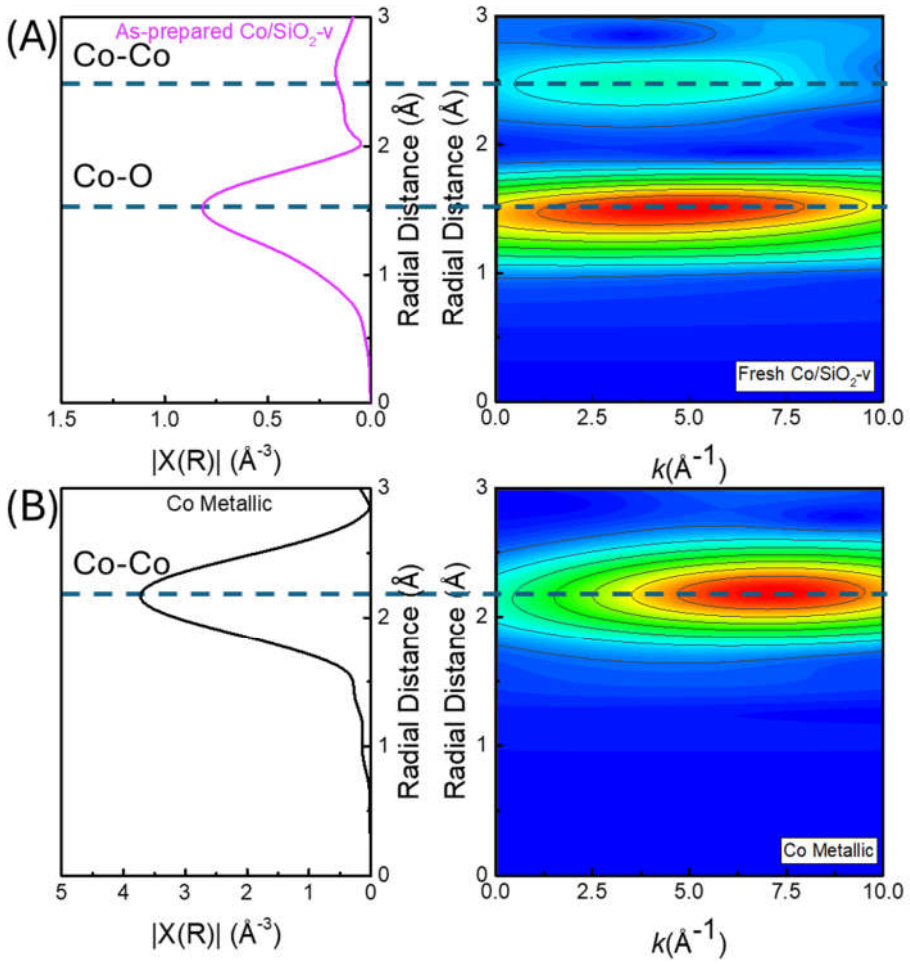

Figure 3.10. Fourier transform (left panel) and Morlet Wavelet transform (right panel) for the k²-weighted Co K-edge EXAFS signals for fresh Co/SiO_2-v (A), and metallic Co (B).

The XAFS data reveal that M/SiO_2-v catalysts have increasing fractions of metal sites and metal aggregation as the metal type change from Mn, Fe, Co, Ni to Cu. This behavior should result from their different solubility in the silica phase, as evaluated from the phase diagrams[297-300]. Flame fusion involves solid-state dissolution

reactions. A thermally stable metal silicate precursor is needed for the successful incorporation of metal sites into the silica matrix. **Figure 3.11** shows the thermal dynamic stability of silicate precursors. Although Mn, Fe, Co, Ni, and Cu have stable silicate compounds, the insufficient thermal stability results in the decomposition of Ni_2SiO_4 and $CuSiO_3$ to NiO + SiO_2[297] and CuO/Cu_2O + SiO_2[301, 302] at high-temperature conditions, while Mn, Fe, Co silicate are spinode compound that tend to melt before decomposition based on their phase diagrams[298-300]. The formation energy and melting/decomposition temperature can be used to indicate the degree of stability and metallic species evolution in the flame fusion process for preparation of M/SiO_2-v catalysts. The trend shows these five transition metals have a decreasing stability in term of their silicate compounds when moving to the right side in the periodic table[303-306]. This is why we observe a high fraction of reduced metal sites in the Cu- and Ni/SiO_2-v samples.

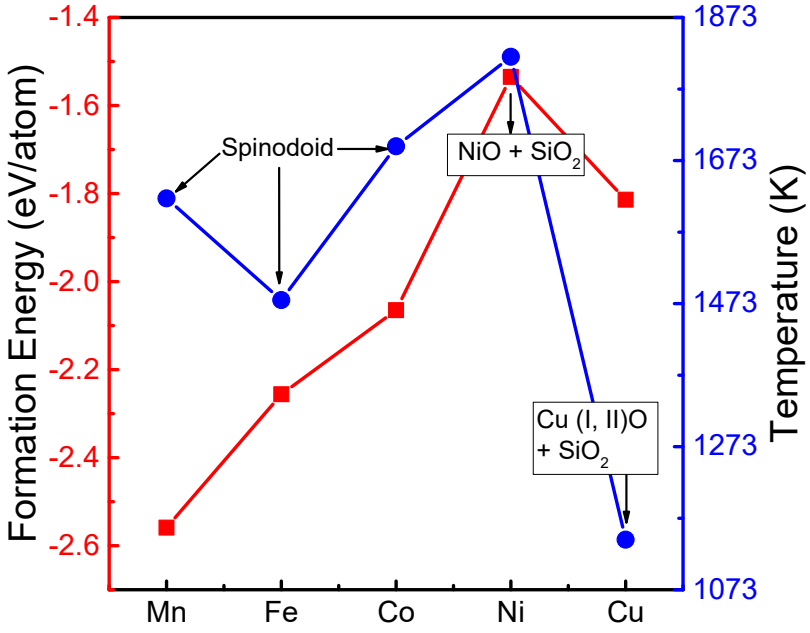

Figure 3.11. Thermal dynamic stability of metal silicate precursors described by their formation energies and melting/decomposition temperature of metal precursors. (Data were extracted from reference[297-306])

3.4.5 Correlation between catalyst type and NMC performance

The screening of metal type in silica matrix for NMC has been studied computationally by Chang and co-workers[191]. They replaced the Fe site in silica support with 25 different transition metals and examined their performance under the same activation conditions. The performance trends in terms of methane activation, ethylene formation and coke deposition across these transition metals have been explained by descriptors of the adsorption and dissociation energies of methane, the dissociation energy of second methane, and the deep dissociation of methylene generated from ethylene, respective. It was reported that Mn has a high adsorption energy and medium activation energy barrier for dissociation of the first C–H bond in methane, which is expected to give a high methane conversion rate. The dissociated methyl and hydrogen generated from scission of the first C-H bond prefer to be adsorbed at the Mn site and one carbon site of the active center in the Mn/SiO_2 catalyst. For coinage metals such as Cu, the atoms likely sink into the support surface and cannot provide a suitable site for anchoring methyl groups, which means Cu has a low methane activation rate. These computational findings are surprisingly consistent with our experimental observations for methane reaction rates over Mn- and Cu/SiO_2-v catalysts. In terms of the ethylene formation and coke deposition trends, He et al. did not screen all these transitional metal catalysts as was done for the C-H activation step in NMC. The performance

behavior of Co/SiO_2-v in NMC in our experimental tests, in terms of coke resistance, methane activation, hydrocarbon production, is the best. This finding was not noted in the computational efforts in literature. It should be pointed out the computational work has been focused on the active centers that are one metal atom coordinated with two carbon atoms and one silicon atom simulated on the (001) surface of β-SiO_2 through replacing the unit of SiO_3 by $FeSiC_2$[86, 177, 191]. As evidenced in our catalyst characterization data, the actual catalyst composition is far more heterogeneous in terms of the size and oxidation states of active centers in the vitreous silica matrix.

A descriptor for quantifying the site heterogeneity in M/SiO_2-v catalysts could be the fraction of metallic sites in the activated catalysts. The increase in the fraction of metallic sites indicates the migration and aggregation metal atoms in the catalysts to form dimers, clusters or nanoparticles, in comparison to the single metal sites in the silica matrix. The computational study[307] suggests that the active centers involving dual metal sites could lead to strong bonding to both methyl and hydrogen species upon dissociation of C-H bond in methane. This can lead to higher reaction rate, high temperature stability and coke resistance than single metal sites or clusters. Among the studied M/SiO_2-v catalysts (Section 3.4), the Co/SiO_2-v has a fraction of 15 % metallic Co (0) sites in the activated catalysts. In comparison to Mn/SiO_2-v that primarily contains Mn (II) single sites and Ni- and Cu/SiO_2-v catalysts that dominantly contain Ni (0) and Cu (0) sites, the Co/SiO_2-v has a higher tendency to form dimer or trimer Co (0) sites that could contribute to the high coke resistance and hydrocarbon yield in the NMC reactions.

3.5 Summary

In summary, we synthesized five vitreous silica-supported transition metal (i.e., Mn-, Fe-, Co-, Ni and Cu/SiO_2-v) catalysts and screened selected physiochemical properties and NMC reaction performance. Among the metal silicate precursors utilized in catalyst preparation, the thermal stability exhibits a decreasing trend from Mn to Cu in the periodic table. As a result, the as-prepared Mn/SiO_2-v primarily contains isolated Mn (II) sites, while Fe- and Co/SiO_2-v predominantly feature isolated Fe (II) and Co (II) sites alongside a small fraction of metal oxide nanoparticles. In contrast, Ni- and Cu/SiO_2-v have higher metal oxide components.

Upon catalyst activation in NMC, metal sites were generated through the reduction of their oxide forms in the fresh catalysts. The quantity of reduced metal sites increases from Mn to Cu in the catalysts. This site heterogeneity in the activated catalysts influenced the NMC performance. Moving through Mn-, Fe-, Co-, Ni- and Cu/SiO_2-v catalysts, Mn/SiO_2-v demonstrates the highest methane reaction rate and highest coke formation rate, whereas Cu/SiO_2-v exhibits the lowest methane reaction rate and coke formation rate. The Co/SiO_2-v catalyst emerges as the optimal candidate for NMC, excelling in methane reaction rate, hydrocarbon formation and coke resistance. It is noteworthy that the activated Co/SiO_2-v was determined to have ≈85% Co (II) and ≈15% metallic sites, likely forming small oligomers (i.e., Co-Co dimers) contributing to the observed performance. This work provides examples and guidance for the further development and optimization of NMC catalysts, contributing to the decarbonized production of clean energy and chemicals.

Chapter 4: Direct, Non-oxidative Conversion of Methane over Fe/SiO_2 Catalytic Wall Reactor

This chapter is adapted in part from Zixiao Liu, Sichao Cheng, Antara Bhowmick, Yuan Zhang, Dongxia Liu, "Vitreous Silica Supported Fe Catalytic Wall Reactor for Non-oxidative Conversion of Methane". Manuscrpit in Preparation

4.1 Abstract

Lattice-confined, single-atom Fe on silica is a recently developed highly active catalyst for direct, NMC with extraordinary performance and low coke selectivity. Rational design and utilize the catalyst in a catalytic wall reactor can reduce the use of catalysts, improve heat efficiency and reaction performance much more than the conventional fixed bed reactor. In this work, a vitreous silica-supported Fe catalyst was incorporated into a catalytic wall reactor (CWR) and demonstrated improved performance in NMC. At temperatures lower than 1273 K or higher space velocity conditions, the CWR demonstrated selectivity towards light olefins. When temperature increases above 1273 K, the reactor majorly produces aromatics and hydrogen. The overall reactor demonstrates stable catalytic performance without degradation, even if the coke was forming. The filter aperture in CWR can effectively collect active, high-purity, and uniformed carbon nanospheres as advanced carbon materials, which improves the overall process profitability.

4.2 Introduction

Towards net-zero emission requires zero carbon footprint for industrial, especially energy acquisitions. Due to the high carbon footprint, conventional energy process is not acceptable for net-zero emission economy. In the future net-zero emission economy, the abundant reserves of natural gas and new drilling technology could enable methane with more affordable price, which is an ideal feedstock to produce hydrogen and essential chemicals. Non-oxidative methane upgrading established an alternative path directly convert methane to value-added chemicals, such as hydrogen (H_2), acetylene (C_2H_2), ethylene (C_2H_4), and ethane (C_2H_6), benzene (C_6H_6), toluene (C_7H_8), and naphthalene ($C_{10}H_8$). The technology could reach very high caron utilization efficiency than conventional GTL processes, which is extraordinary promising to satisfy the demand of net-zero emissions.

Although non-oxidative methane upgrading is an attractive technology to net-zero emissions. However, the challenges remained in the technologies including thermodynamic and kinetic limitation, insufficient understanding of reaction mechanism, low activity of catalysts and requires reaction engineering. These inadequate has significantly inhibited commercial development of non-oxidative methane upgrading. The thermodynamic nature of non-oxidative methane upgrading, is not favorable for both hydrogen and hydrocarbons production, which require high temperature or products removal to shift equilibrium. The high stability of C-H bond in methane requires effective catalysts and suitable reaction conditions, which can significantly improve hydrocarbon selectivity and reduce the reaction temperatures. In

terms of catalysts development, conventional nanostructured, supported metal-based catalysts favors hydrogen + coke but exhibited low activity for hydrocarbons selectivity. The recently developed single atom catalysts exhibits much active performance and favors hydrocarbons selectivity. The state of art catalysts, a Fe single-site catalyst supported by silica (Fe©SiO_2) was developed by Guo and their co-works in 2014 which lattice confined Fe operating at high temperatures above 1273 K[308]. This catalyst can produce C_{2+} hydrocarbons, aromatics with the minimal amount of coke under the proper condition. Several critical studies has revealed the Fe©SiO_2 can active methane via surface reaction[86, 176, 177] form C_2 hydrocarbons (C_2H_6 and C_2H_4), which is the important precursors for aromatics (benzene, toluene, and naphthalene) via gas phase dehydrogenation reactions[181]. Besides, Fe site also initialed methane radicals, which is the key precursors for C_2 hydrocarbons[177]. Therefore, Fe©SiO_2 provides dual pathways for reaction via catalytic and gas phase reactions[177], which offers valuable information to catalysts developed, mechanism understanding, and future processing development.

Process simulation and reaction engineering are especially valuable to understanding the key factors in establishing commercial-scaled non-oxidative methane upgrading processes. To date, there rarely studies regarding process stimulations of non-oxidative methane upgrading and reaction engineering with essential information that to make the overall process profitable. Huang and the co-works evaluated the process, suggested overall conversion reaches > 25 % with coke formation less than 15 % to make process profitable [185, 186]. This demands catalysts with high activity and hydrocarbon selectivity, which the current Fe/SiO_2 can satisfy.

Since coke formation cannot be avoided entirely in a commercially scaled fixed bed reactor, there might be a risk of a coke-caused diffusion barrier with the continuous reaction for long-term operation. Of course, discontinuing the response to generate catalysts increases new costs for the processes. To reduce the frequency of reactor maintenance and avoid blockage caused by coking, a CWR is an effective solution. Developing a layer of catalyst bonded with the reactor can effectively reduce the coke blockage of the catalyst and reactor. Oh, and the co-workers developed a millisecond catalytic wall reactor for NMC, exhibiting the continuous reaction without deactivation, even if coke is formed [184]. On the other hand, the catalytic wall reactor is more efficient in thermal management than a conventional fix-bed reactor due to the catalysts bonding with the reactor having conductivity-dominated heat transfer, which is much more efficient than convection and radiation. In commercial development, a catalytic wall reactor is even promising to couple with another endothermic reaction to become an auto thermal reactor, especially for non-oxidative methane upgrading carried out at 1273 K[183, 184]. Given by this, in this study, we use the vitreous silica-supported Fe catalysts to develop a catalytic wall reactor and discover its possibilities under high conversion conditions. Here for the first time, we demonstrated the CWR with high methane conversion (up to 91%). The CWR exhibited dual function: Product hydrocarbons and hydrogen with nano carbon materials. Lower 1273 K, such CWR will undergo NMC reaction to produce hydrocarbons. When temperature elevated above 1273 K, the CWR functioned for NMD reaction to produce hydrogen, carbon, and aromatics. The developed CWR is robust without degradation in 140 hours of the continuous test. Such CWR is also a nanomaterial fabrication device that can produce

carbon nanospheres (CNSs) in the gas phase with roughly 150 nm diameter, which turns the low-valued coke into high-valued, advanced carbon materials. The characterization of CNSs exhibited a solid sphere with graphitic properties.

4.3 Experimental method

4.3.1 Materials

Quartz (99.99% purity, IOTA-4) purchased from Sibelco Inc was used as the catalyst support. The catalyst precursors (Fe_2SiO_4) were synthesized via a sol-gel method by following previous publications. Nitric acid (HNO_3, ACS grade) was purchased from Fisher Scientific. DI water was prepared from an ultrapure water system (Milli-Q® Direct, Millipore Sigma) with an electric resistance of 18.4 Ω at 298 K. The fused quartz tubing and quartz frit disks were purchased from the Technical Glass Products and cleaned by DI water before usage.

4.3.2 Catalyst synthesis and CWR fabrication

The synthesis of the M/SiO_2-v catalysts followed by pervious study [226]. The mixture was then pressed by packed in a 25 cm long, 12.7 mm diameter fused quartz tube and fused on the tube by a continuous oxy-hydrogen flame until the tube wall became bright white and slightly soft. A hollow catalyst wall tube was obtained by withdrawing the residual catalyst from the fused quartz tube after flame fusion. The as-fused catalyst wall tube was washed in an aqueous HNO_3 solution (1.0 mol L^{-1},) under rigorous magnetic stirring at ambient conditions for 3 h and followed by another three times DI water washing steps to remove residual acid, followed by drying at 343 K

overnight. A calcination step was carried out in a muffle box furnace at 823 K for 4 h under ambient conditions to remove the residual HNO_3. Finally, the catalytic wall reactor was obtained by welding the wall tube with other 12.7 mm to 6.35 mm adaptor, and a quartz frit in one end via the oxy-hydrogen flame and denoted as Fe/SiO_2-CWR.

4.3.3 Characterization

To determine the amount of catalyst loaded on the CWR, a conventional analytical balance (MS150DU, Mettler-Toledo) was used to measure the total weight difference of the quartz tube packed with the catalyst before flame fusion and after withdrawal of the unfused catalyst from the quartz tube. X-ray diffraction patterns were measured on a Bruker ® D8 diffractometer using Cu Kα radiation with a step size of 0.02 degrees. The microstructure of the Fe/SiO_2-CWR was visualized by a scanning electron microscope (SEM, GAIA 3, by TESCAN®). The Raman spectra were collected by using HJY LabRam ARAMIS Raman spectrometer, which was equipped with a 532 nm wavelength laser and calibrated at 520 cm^{-1} using a silicon wafer standard.

4.3.4 Catalytic reaction test

The as-prepared CWRs were tested on the apertures described in **Figure 4.1.** The temperature of the reactor was monitored by a thermal couple probe (Type K, Omega Engineering) attached to the outside of the CWR. Typically, a continuously flowing of 10 mL min^{-1} N_2 (UHP grade, Airgas) was introduced in the CWR firstly. Then, the CWR was heated by a program-controlled tube furnace (Model 3210, Applied Test System) from room temperature to the designated temperature with a 10

K min^{-1} ramping rate. After reaching the designated temperature, a reactant stream of 4 mL min^{-1} methane (Research grade, Airgas) and 2 mL min^{-1} Ar internal standard (UHP grade, Airgas) was induced to the CWR. The effluents of the reaction were continuously monitored by gas chromatography (GC, 6890 A, Agilent) which has equipped with a methyl-siloxane capillary column (HP-1, 50.0 m × 320 µm × 0.52 µm) configured to a flame ionization detector (FID), and a packed column (ShinCarbon ST Columns, 80/100 mesh, 1.83 m) configured to a TCD. An inline cold trap was set to trap the heavy hydrocarbons produced from the CWR, due to the condensation of heavy hydrocarbons could potentially block the sampling line.

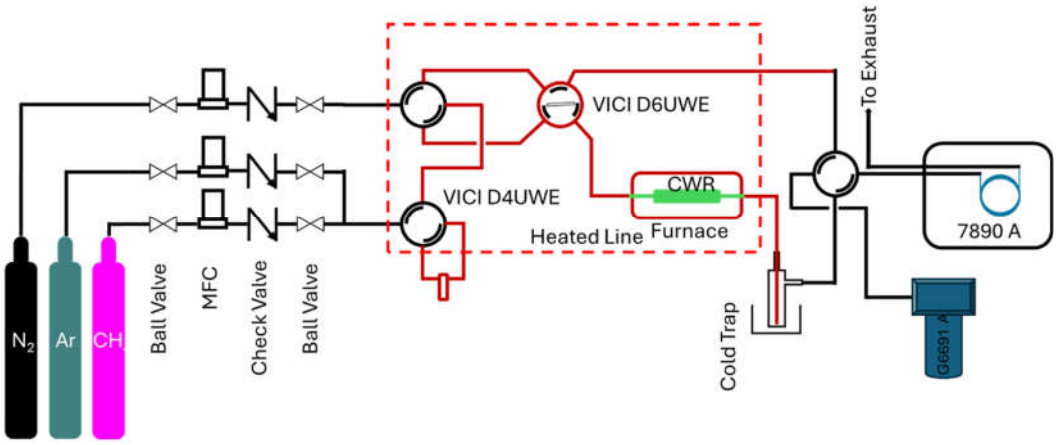

Figure 4.1. Scheme of catalytic wall reactor testing aperture.

4.3.5 Analysis of spent CWR

The reactor was measured weight change after reaction. The coke produced from the CWR can be retrieved by using a diamond saw to cut the reactor and collect powder liked coke materials. The morphology and microstructure of the advanced carbon were analyzed by SEM (GAIA 3, TESCAN®) and transmission electron

microscopy (TEM, JEOL-2100). The surface area of the advanced carbon was measured by N_2 isotherms method via the Quantachrome Autosorb-Qi automated gas sorption analyzer. The sample was pre-treated at 573 K under 1mm Hg pressure prior to the measurement. The electronic conductivity of the advanced carbon was examined via the electrochemical impedance spectroscopy (EIS) method carried by an impedance analyzer (1260 A, Solartron) at room temperature from 0.1 to 10^6 Hz frequency. The detailed procedure of electronic conductivity measurement and the experimental scheme were described in the supporting materials.

The nature of advanced carbon was determined by the thermogravimetric analysis (TGA, Shimadzu, TA-50) method, which typically uses 0.05 g sample exposed to 50 mL min^{-1} air (Medical grade, Airgas) flow and ramped from room temperature to 1123 K with 10 K min^{-1} rate. The TPO was also used to study the carbon nature. The carbon sample was placed in a tubular sample cell, immobilized by quartz wool, and then set in a temperature-controlled furnace. The temperature was monitored by a K-type thermocouple attached to the outer wall of the sample cell. The furnace was ramped to 1123 K at a ramp rate of 10 K min^{-1} under a flowing Ar (45 mL min^{-1}, ultrapure, Airgas) and O_2 (5 mL min^{-1}, ultrapure, Airgas) atmosphere. The O_2, CO_2, and CO streams were monitored by using the mass spectrometer (Prima-BT, ThermoFisher).

4.4 Result and Discussion

4.4.1 Physicochemical properties of Fe/SiO_2-CWRs

The fabricated Fe/SiO_2-CWR are configured with a 13.0 cm catalytic wall contains only 5.16 g catalyst with a loading density of 0.40 g cm^{-1} along the reactor tube demonstrated in **Figure 4.2 (A)**. The catalysts loading is significantly less than a conventional packed bed reactor. The microstructure images of the catalyst wall were shown in **Figures 4.2 (B)** and **(C)**, indicating a 300 µm uniform catalyst layer with 100 µm sized catalyst particles. The identical catalyst Fe/SiO_2-v were used, which should exhibit similar properties as in section 2.4 and 3.4. Apparently, the flame fusion did not completely melt the catalyst particles, but the partially fused with the fused quartz tube. Hint that catalysts are strongly bonded in the CWR.

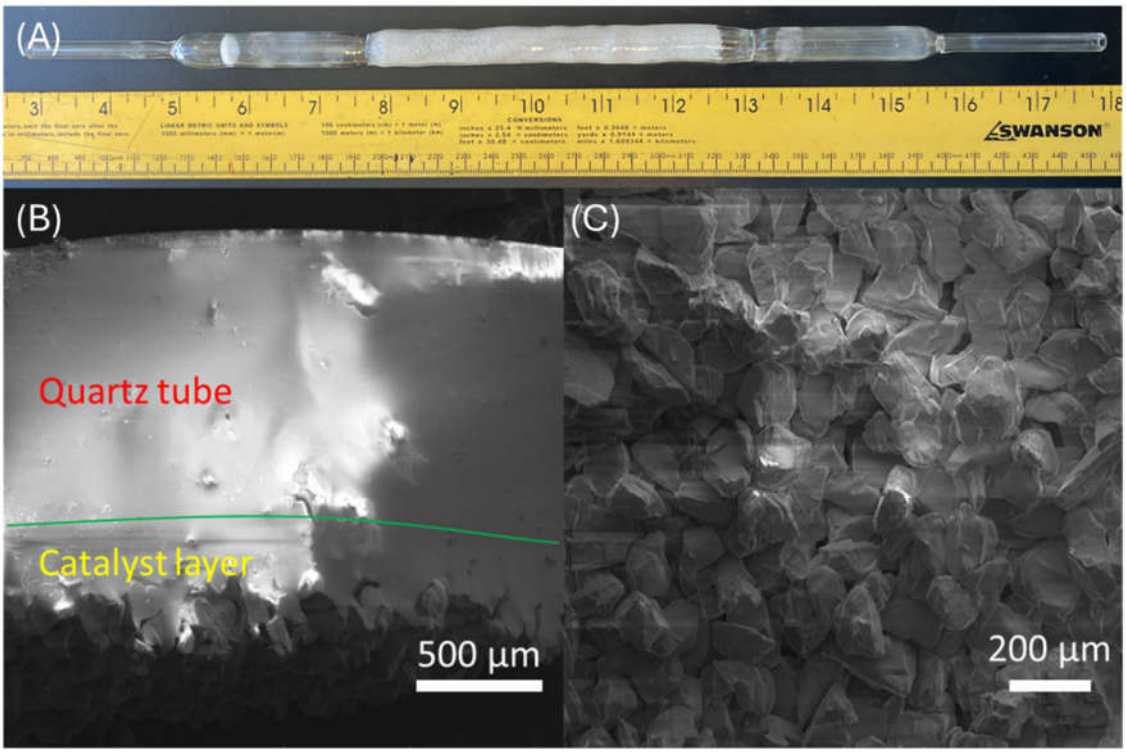

Figure 4.2. Picture of as-prepared Fe/SiO_2-CWR (A), and microstructure of as-prepared Fe/SiO_2-CWR in cross section view (B), and surface of Fe/SiO_2-CWR catalytic wall (C).

4.4.2 Catalytic performance of CWR

The performance of Fe/SiO_2-CWR was unrevealed by testing under NMC reactions from 1073- 1373 K, shown in **Figures 4.3 (A-D)**, Fe/SiO_2- CWRs have very low olefins selectivity, where the reaction is majority turns to methane cracking at 1373 K (**Figure 4.3 (A)**). When the temperature drops to 1273 K and towards 1073 K, the Fe/SiO_2-CWR has olefines selectivity increase but attenuated with the methane conversion. When the temperature finally reached 1073 K, the Fe/SiO_2-CWR only shows < 1 % methane conversion where the reaction is almost terminated. This demonstrated the necessary of reaction temperature for NMC require 1273 K to enable sufficient activity. The C_2 olefines exhibited attenuation of selectivity verse temperature, which can be explained by the thermodynamic instability of olefines at higher temperature which favors deactivation via gas phase reactions, results rapidly increasing of aromatics (**Figure 4.3 (B)**). A notable trend in **Figure 4.3 (B)** observing grown C_2H_6, as the evidence of gas phase reaction promotion by methyl radicals coupling[177, 181].

The fabricated Fe/SiO_2 also exhibited stable performance under typical NMC conditions for more than 140 hours without degradation (**Figures 4.3 (C-D)**). A notable selectivity change can be visible as the reduction of C_2 in (**Figure 4.3 D**), the C_2 olefines decreased rapidly in the first 20 hours. The C_6+ also observed a grown trend, a rapid

increasing of C_6+ in the first 20 hours. This selectivity change could be attributed to the carbon deposition to the catalyst surface has blocked the Fe catalytic site, resulting diffusion barrier to produce C_2 products. However, within the 140 hours of the test, the methane conversion did not have obvious drop, indicating even the coke formation cover the Fe catalyst, the carbon species might also contribute to the methane conversion. Evidence by the SEM image of spent Fe/SiO_2-CWR after 140 hours test under NMC condition, visible carbon coating layer with thickness can be observed. This indicating that to a point the diffusion barrier has been established and the conversion of methane relying on carbon as the active species, combined with the gas phase reaction.

Space velocity also a key factor governing selectivity of Fe/SiO_2-CWR under NMC conditions. In **Figures 4.4 (A)** and **(C)**, lower the flow rate to 2 mL/min CH_4 + 1 mL/min Ar resulting much higher C_6+ selectivity and slightly increasing of overall methane conversion, compared with the flow rate under 4 mL/min CH_4 + 2 mL/min Ar. This can be attributed to the lower flow rate enables better contact of methane to the catalysts, thus the overall conversion got increased. Regarding the C_6+ selectivity increasing can be attributed to the lower gas flow resulting higher chance for C_2 dehydrogenated to aromatics. The low hydrogen selectivity in **Figure 4.4 (C)** indicates the reaction shift its selectivity to aromatics. When increase the flow rate to 2 mL/min CH_4 + 2 mL/min Ar in **Figure 4.4 (B)**, the overall methane conversion remains almost same with **Figure 4.4 (C)**, but increased selectivity in C_2 and hydrogen. Slightly increase the velocity can reduce possibility of coke and aromatics formation, however, increases the C_6+ selectivity as well.

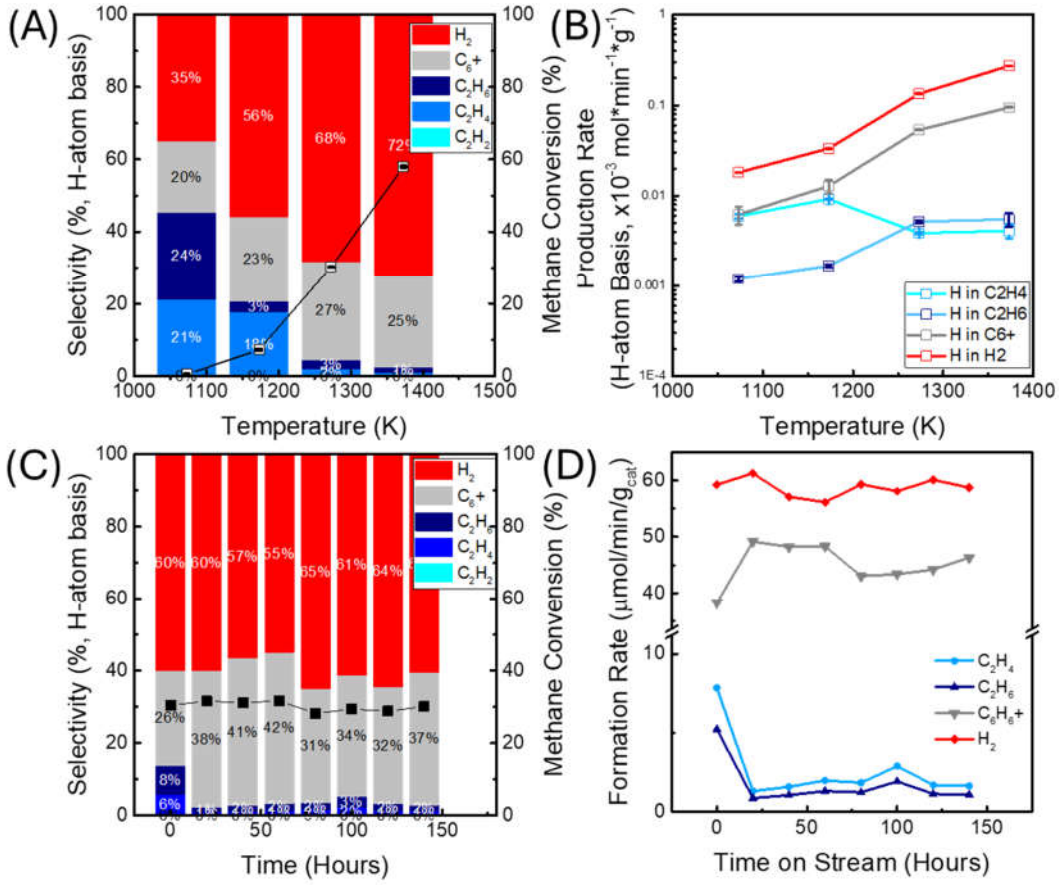

Figure 4.3. Methane conversion and species selectivity as a function of temperature for Fe/SiO2-CWRs (A), and species formation rate versus temperature (B), selectivity and methane conversion of CWR operated under 1273 K for 140 hours (C), and species formation rate of CWR operated under 1273 K for 140 hours. (NMC Condition: 1073-1273 K, 67.55 kPa, Ar as internal standard).

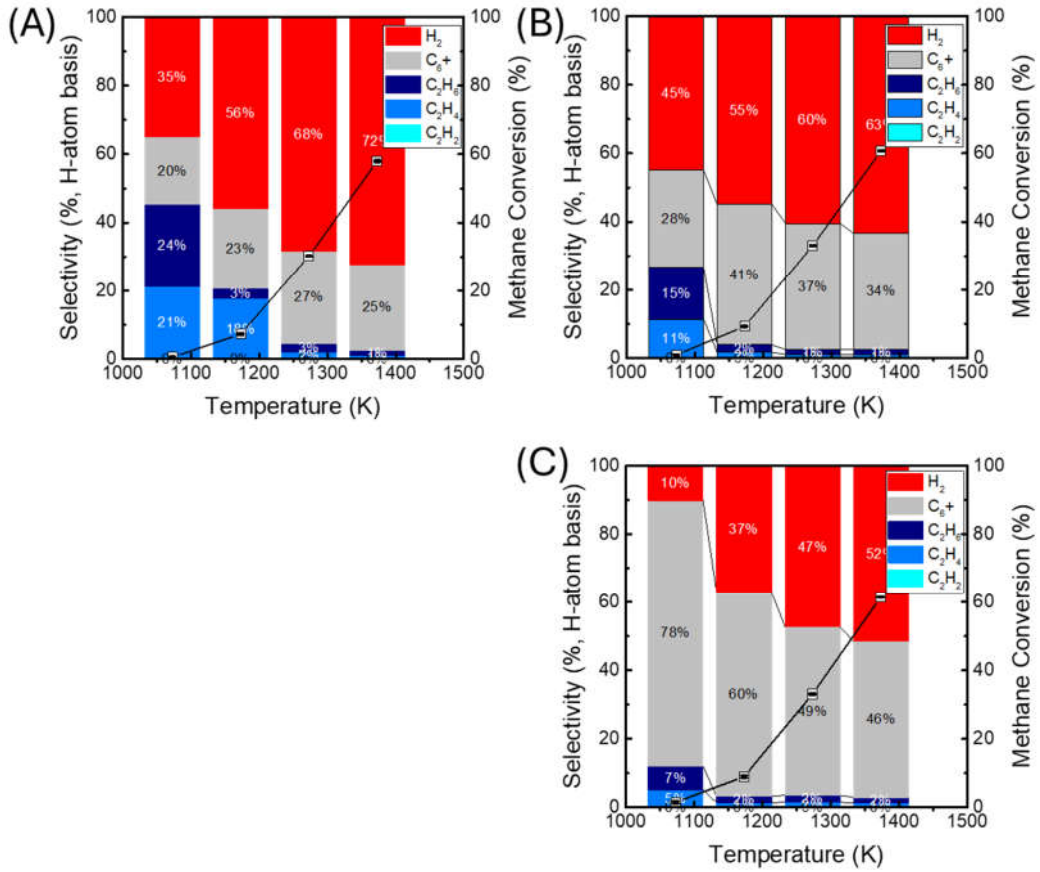

Figure 4.4. Catalytic performance of Fe/SiO_2-CWR tested between 1073-1373 K under different flow rates conditions. 4 mL/min CH_4 + 2 mL/min Ar (A), 2 mL/min CH_4 + 2 mL/min Ar (B), 2 mL/min CH_4 + 1 mL/min Ar (C).

4.4.3 Analysis and Characterization of spent Fe/SiO_2-CWR

Spent CWR was carefully cut to collect the coke from catalytic wall. A total of 5 different types of carbon were found and distributed in the different locations of the CWR. The carbon deposited on the catalyst wall was denoted as AC-1. A non-reflective

carbon with dendrite-liked morphology was found at the end of catalytic wall, denoted as AC-2. The spongy liked carbon collected at the quartz frit was denoted as AC-3. The microstructure images of AC 1-3 carbon were shown in **Figures 4.5 (A-C)**. From the outlet of the reactor, AC-3 shows nearly perfect spherical morphology with a diameter of 150-200 nm. The AC-2 has similar morphology to AC-3 with a much larger diameter around 1 μm, formed by stacking of the carbon layers described in a zoom out picture. The AC-1 carbon has 25-30 μm grain covered the entire catalyst surface, with a cross-section viewed microstructure shows the catalyst grain was completely covered by a thick layer of carbon, which evidenced that the selectivity change might because of this in **Figures 4.3 (C-D)**. AC-1 Carbon deposited at the end of the catalytic wall very similar to the AC-3, hint that methane decomposed to coke are likely produced in gas phase and fly to the end of reactor due to the AC-3 are small and fine nano particles can be careered in gas phase. The TEM images of AC-3 shown in **Figure 4.5 (D)** verified that AC-3 has as a solid core, polymer filler bonded, contains graphitic planes, amorphous carbon, crystallite edge, and silt-shaped cavity, which is identical to the result reported from the previous study[309, 310]. The zoomed-in view of AC-3 in **Figure 4.5 (D)** exhibited typical lattice fringes, which refers to the Π-bounded, stacked aromatic layers described in literature[310]. This explained the possible grown mechanism of AC-3 undergoes the grown source from gas phase active species and flying to the filter. The zoomed-out view of AC-3 in **Figure 4.5 (E)** demonstrated the AC-3 has 150 nm diameter, which is agreed with **Figure 4.5 (C)** and the results from pervious study[310].

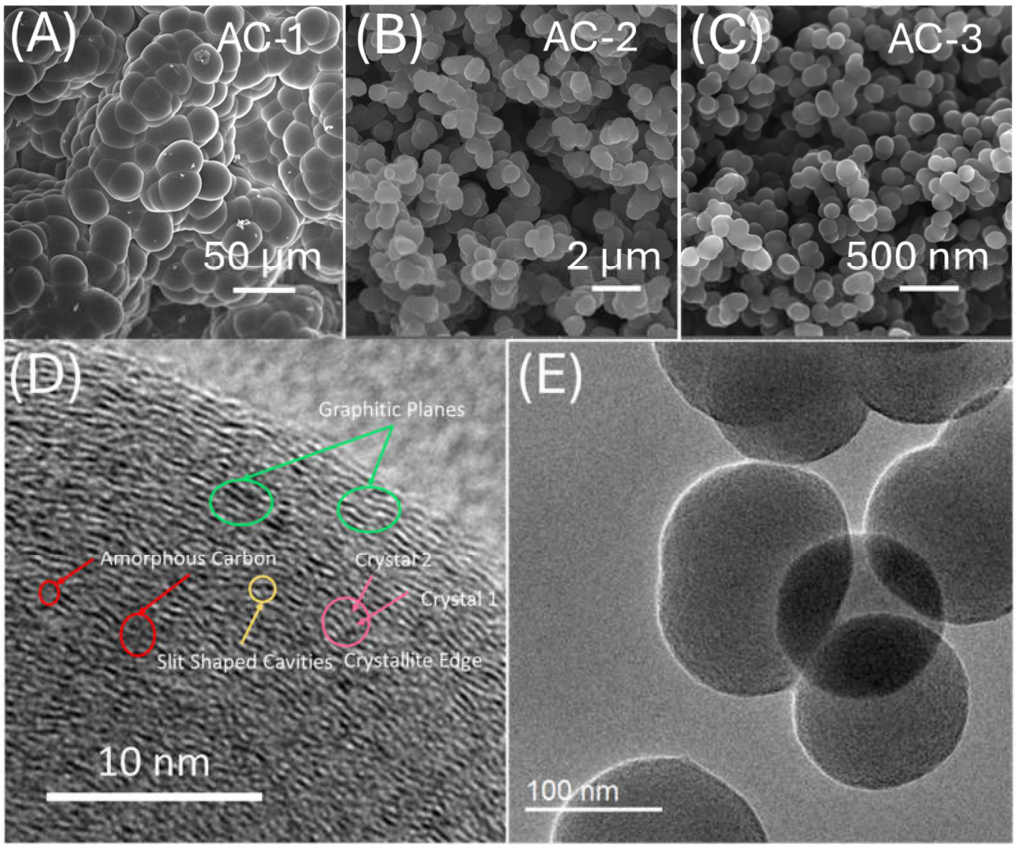

Figure 4.5. Microstructure and morphology of carbon product formed in spent Fe/SiO_2-CWR under typical NMC reaction for 140 hours. (NMC condition: 1273 K, 67.55 kPa, Ar as internal standard).

To understand the properties of AC1-3 formed in the CWR, Raman spectroscopy in **Figure 4.6 (A)** demonstrated D band at 1344.55 cm^{-1} and G band 1595.17 cm^{-1} for all AC 1-3 carbons. The G band at 1582 cm^{-1} refers to graphite, in the case of AC carbons shifted to higher band can be attributed to graphite nanocrystalline, evidenced by the pervious publication[311]. D band at 1358 cm^{-1} refers to the disordered feature of carbon, the lower shifting of D band in AC carbons to 1344.55 cm^{-1} generally refers to increasing of structural defects[312, 313]. The intensity ratio of D and G bands

were used to evaluate the defects[314]. By comparing the I(D)/I(G) listed in **Figure 4.6 (A)**, the AC-3 lowest I(D)/I(G) ration as 1.25, it means highly dense defect remaining in the structure. The AC-1 and 2 has slightly lower I(D)/I(G) ranged from 1.10-1.18, hint less defect than AC-3. Since these two carbons are primary from reactor zone, the dehydrogenization of methane could be a reaction to continuous supply carbon source to make up the defects, as pressing with less defects in AC-3.

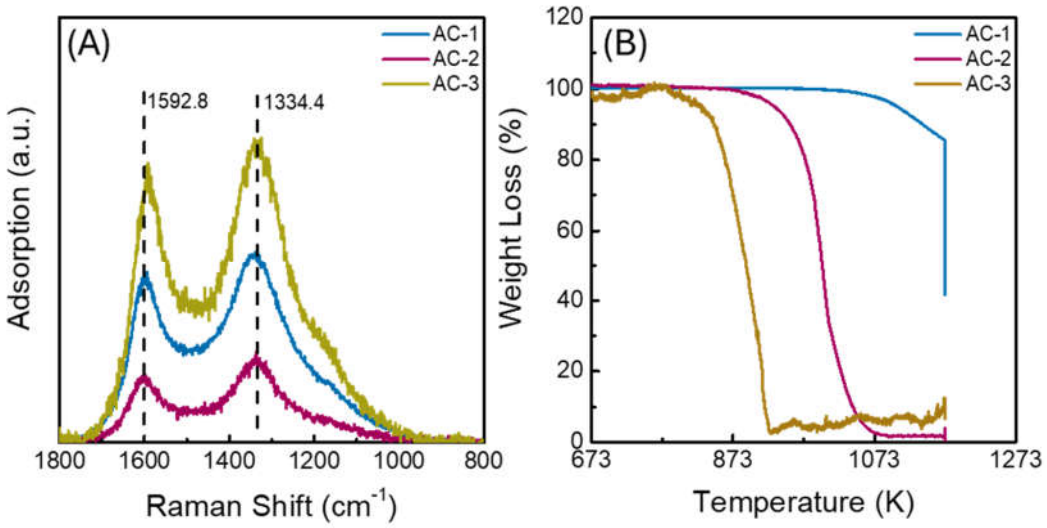

Figure 4.6. Property of carbon product from spent Fe/SiO_2-CWR by Raman spectroscopy (A), and weight loss profile by TGA.

The activity of AC carbons obtained from Fe/SiO_2-CWR was examined by TGA and presented in **Figure 4.6 (B).** In weight loss as a function of temperature profile of TGA shows weight lost percentage as AC-3≈AC-2>AC-1. The incompletion of weight loss in AC-1 due to AC-1 are sampling from the catalytic wall, with the residual weight corresponding to the actual catalyst. A notable difference of carbon activity can be examined by the weight loss staring temperature for the AC carbons. The AC-3 demonstrated very high activity than other carbons by its lowest temperature

of the weight loss as early as 778.10 K, followed by AC-2 (840.3 K), and AC-1 (979.8 K). This information reveals the high activity of AC-3, due to its lower particle size and intense defects evidenced in **Figure 4.6 (A)**. The TPO profile of AC carbons in **Figures 4.7 (A-C)** reveled more property information of AC1-3. The activity of AC carbons can be reflected from the peak position of CO_2, CO, and O_2 species. In Figure 36 (A), the AC-3, 2, and 1 has CO_2 peak temperature at 932.7 K, 1095.3 K, and 1130.1 K, respectively. The lower temperature of CO_2 revolution reflects less barrier of oxidation, hints higher activity than AC-1 and 2. The CO and O_2 evolution in **Figures 4.7 (B)** and **(C)** represent same trend and peak position corresponding to the CO_2 in **Figure 4.7 (A)**. The TPO profile can be deconvoluted to low, medium, and high-temperature peaks, which generally correspond to soft amorphous coke, polymeric aromatic deposition, and ordered graphitic hard coke. Back to **Figure 4.7 (A)**, the CO_2 and CO TPO profile exhibits an unsymmetric peak for AC-3 with a shoulder at 1066.7 K, indicating that AC-3 contains primarily soft, disordered carbons. For AC-2, the left shoulder peak presented at 986.7 K with the right shoulder peak at 1187 K, indicating the exist of much harder, graphitic, and ordered carbon. As for AC-1, the peak becomes more boarded with a left shoulder peak around 970 K, primarily composed of ordered, graphitic carbon. The O_2 signal in **Figure 4.7 (C)** shows much symmetrical peak with the degree of AC-3> AC>2 >AC-1, indicating more uniform of soft carbon in AC-3, and combined medium and hard carbon in both AC-1 and 2.

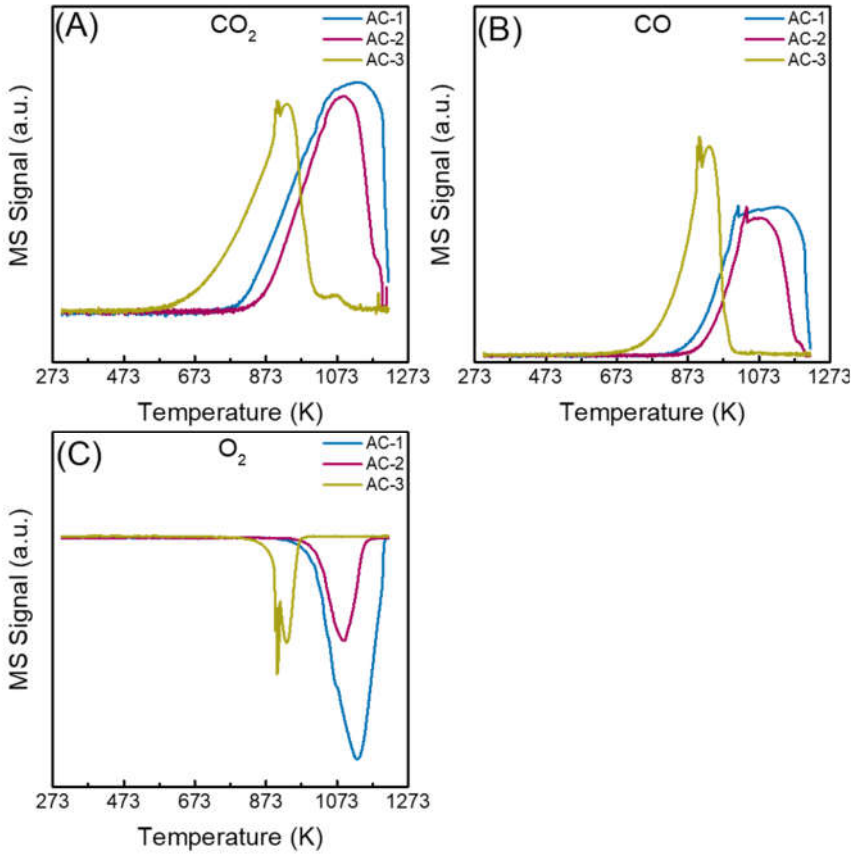

Figure 4.7. TPO profile of CO_2 (A), CO (B), and O_2 of spent Fe/SiO_2-CWR under NMC condition for 140 hours. (TPO conditions: 20 mg spent catalyst, 10 K/min under flow rate of 50 mL/min 10 % O_2/Ar).

4.5 Summary

The presented study has originated and demonstrated a dual function CWR for both NMC and NMD reactions. The Fe/SiO_2-CWR functioned by the catalyst initiate the reaction, then followed by a combination of catalytic and gas phase reaction collaboration. For NMC reaction, the CWR demonstrated better performance than conventional fixed bed reactor. At lower 1273 K with 7.27 % methane conversion and

45 % C_{2+} selectivity and 20 % C_{6+} selectivity. When temperature raised up to 1373 K, the CWR functioned for NMC reaction with 70 % + hydrogen selectivity and near 60 % conversion. The developed CWR demonstrated long lasting performance, high temperature tolerance, which can be furtherly manipulated with space velocity to control the reaction reaching suitable selectivity. Besides, the developed CWR is a nanofabricator can produce value added carbon nano spheres with uniform diameter of 150 nm, which can be easily collected as utilized. The obtained exhibited conductivity of 0.39 S/cm, similar with the carbon black used for fuel cell and advanced catalysis. The TPO, TGA analysis of carbon products generated from CWR shows the obtained is the most promising product by its very high activity.

Chapter 5: Robust Siliceous Zeolite Supported Cobalt Catalyst for Non-oxidative Methane Decomposition Towards Hydrogen and Cabon Nanotube Production

This chapter is adapted from: Zixiao Liu, Antara Bhowmick, Ali Kamali, Song Luo, Genwei Chen, Juyan Zhang, Yuying Shu, and Dongxia Liu. "Siliceous Zeolite Supported Cobalt Catalyst for Hydrogen and Cabon Nanotube Production from Non-oxidative Methane Decomposition", Manuscript in preparation, March 2024.

5.1 Abstract

Dealuminated zeolite-supported cobalt (i.e., Co-DeAl-BEA) catalysts were prepared and tested for non-oxidative methane (CH_4) decomposition to produce CO_x-free hydrogen (H_2) and carbon nanotube materials. In comparison to the zeolite BEA-supported cobalt (Co-BEA) catalyst, the Co/DeAl-BEA catalyst has limited Brönsted acid sites and increased mesoporosity, which limited the acid-catalyzed deactivation mechanism and facilitates the mass transport, and thus significantly increased the catalyst lifetime. The cobalt sites change their cluster size and coordination structure with their concentration in the zeolite support, which leads to different catalytic behaviors. The low Cobalt (Co) loading leads to isolated Co sites, which is insufficient to enable methane pyrolysis. The increase in Co concentration to 3 wt. %, led to methane dihydrogen reaching high activity with long-term stability without obvious degradation. The carbon product includes multiwall carbon nanotubes (MWCNTs)

demonstrated lavish, highly active, uniform multiwall carbon nanotubes majority grown with base grown mode, thanks to the dealumination in zeolite BEA can improve the Co catalysts stability and long-lasting lifetime.

5.2 Introduction

Consumption of energy is a daily necessity in the modern world, dramatically increasing along with the improvement in the quality of life and the increase in world population. The majority of energy required worldwide is created from the combustion of fossil fuels[315, 316]. Although these resources are essential to the world, the combustion of fossil fuels has resulted in increased health risks and global warming. Hydrogen technology has the potential to meet the energy needs of today's world and lessen the undesirable effects of energy consumption[317]. As the energy source, the burning of hydrogen (H_2) has no environmental impact apart from water as a byproduct. Compared to the conventionally used hydrocarbons, hydrogen exhibits higher energy yield. Thus, the use of hydrogen as an alternative fuel in the industrial, residential, and transportation sectors are desired since it has nearly zero emissions.

Currently, hydrogen is primarily produced from fossil fuels such as SMR, in which methane CH_4 and steam react over a catalyst to produce a mixture of H_2 and carbon dioxide CO_2[318, 319]. The process often consists of a series of operating units, such as a reformer followed by high-temperature and low-temperature water-gas shift WGS reactors, and equipment for H_2 separation and purification. Due to the endothermicity of SMR, the operating temperatures and pressures for reformers are in

the range between 1073 to 1273 K and 15 to 20 bar. The effluent stream contains a hydrogen-rich gas mixture with substantial CO content. The WGS reactors are used to convert CO into CO_2, so the outlet stream from the WGS reactor contains primary H_2 and CO_2, with a small amount of CO and CH_4 impurities. To obtain high-grade hydrogen, intensive separation and purification steps are needed. As part of the process, the formation of CO_2 products is unavoidable, and its release to the atmosphere causes the greenhouse effect and climate change.

As an alternative to hydrogen production from SMR, hydrogen can be produced from direct methane decomposition[320, 321]. Without an oxidant, CH_4 directly splits into hydrogen and solid carbon (C), as exemplified in equation **1.12**. Hydrogen produced in this pathway contains CO_x (i.e., CO and CO_2) free, which is the essential feedstock of hydrogen fuel cells. Previous research has studied the non-catalytic thermal decomposition of methane[322]. The structural symmetry and high C-H bond energy make CH_4 to be the most stable hydrocarbon. Thus, the non-catalytic methane decomposition requires a high temperature ($\geq$ 1473K) for C-H bond breakage to reach complete methane conversion[323-327].

Catalysts can facilitate C-H bond activation and lower reaction temperatures in methane decomposition. In catalytic methane decomposition, on the basis of experimental and theoretical studies[323-327], carbon[328-330], molten metals[88, 134-139, 143], salt[141], and transition metals[101, 107, 119, 130, 331-335] have been shown to be effective catalysts in enabling methane decomposition. In carbon catalysts, defects such as dislocations, low-coordination sites and vacancies are considered the main active sites. Disordered carbon such as activated carbon and carbon black are catalytically more

active than graphite or diamond structures. The catalytic activity of carbon catalysts is relatively low. High temperatures (~1073-1373K) are often required. Molten metals (e.g., Ni, Pb, Sn) and salts (e.g., KBr, NaCl) can activate methane at temperatures around 1273K. They are not very active catalysts either, but density differences between carbon and molten catalysts lead to carbon floats on the top of the liquid catalysts, avoiding the reactor blockage issue that occurs in other catalyst systems. The high operating temperature and reactor corrosion remain challenges for the applicability of this technology for methane decomposition on an industrial scale.

Transition metals (e.g., Ni, Fe, and Co) have partially filled "d_z" orbitals that can accept electrons from the C–H bonds of methane. They are the most active catalysts and can enable NMD at lower temperatures (e.g., ≤1023K). Specialty carbon products such as nanotubes or nanofibers are often formed in these catalysts. The widely believed mechanism for catalytic methane decomposition involves the chemisorption of CH_4 onto the catalyst surface followed by stepwise dissociation reactions resulting in elemental carbon and hydrogen[336, 337]. The formation of carbon nanotubes or fibers is well explained by the vapor-liquid-solid (VLS) model[338, 339]. The elemental carbon on the catalyst surface dissolves into the bulk of the catalyst particles giving rise to a liquid metastable carbide and diffuse within the particles driven by the temperature and/or concentration gradient. The solid carbon precipitates at the backside of the catalyst particles and forms carbon nanostructures. However, the transition metal-based catalysts suffer from quick deactivation caused by thermal sintering and encapsulation within formed carbon deposits.

The use of catalyst supports including silica, alumina, zeolite porous carbon, etc., has been shown to affect metal dispersion and catalytic performance in NMD[327]. In particular, zeolite-supported catalysts are little studied in NMD, but give the best results in the co-production of hydrogen and solid CNTs, better than most of metal oxide-supported catalysts. The ordered micropores and high surface areas of zeolites promote metal dispersion, resulting in higher catalytic activity, longer lifetime, and higher carbon accumulation. In literature, zeolites-supported metal catalysts were frequently studied such as the effect of structural promotors[340], the effect of activity promotors[341-344], the effect of Si/Al ratio[345], and the effect of metal particle size correlated to carbon nanotube formation[346]. Based on this literature, it concludes that zeolite-based support faces similar challenges as conventional oxides supported catalysts, such as coke-caused deactivation, catalyst site migration, and catalyst sintering effect, which requires establishing strong interaction of catalytic sites with the zeolite frameworks. Many zeolites contain an aluminate structure, which could be used as a strong structure promotor to enhance interaction between metal sites to the supports, but also causes the Brönsted acidity increase which much favors oligomerization reaction and coke deposition. As it is known that pure silica-based support does not have an aluminate site, but typically contains very limited surface area and microporosity. Here we report a robust zeolite-supported cobalt (i.e., Co-DeAl-BEA) catalyst for NMD reaction. In comparison with conventional BEA zeolite support, the DeAl-BEA has a very limited Brönsted acidity and an increase in surface area and mesoposority. The former property is expected to eliminate the coke deposition caused by acid chemistry in the zeolite pores and channels, and thus

removing one major catalyst deactivation mechanism. The creation of mesopores by dealumination created rich silanol chemistry that functions as a host for the cobalt particles. Therefore, a stable Co particle distribution in zeolite support is achieved to promote stable DMC chemistry. The Co-DeAl-BEA catalyst showed high catalyst performance and stability.

5.3 Experimental Methods

5.3.1 Materials

Commercial zeolite BEA (Product Number: 45874, Alfa-Aesar, ammonium-form, SiO_2/Al_2O_3 ratio of 38:1) was used as the precursor for preparing DeAl-BEA support. Cobalt nitrate hexahydrate ($Co(NO_3)_2{\cdot}6H_2O$, ACS reagent, Sigma-Aldrich) was used as the Co metal precursor. Nitric acid (HNO_3, 70% vol., Fisher Scientific) was used in the dealumination process. Deionized (DI) water (resistance 18.4 Ω-cm, at 298 K) was supplied from Milli-Q® EQ 7008/16 Ultrapure & Pure Water System. Santa Barbara Amorphous-15 silica (SBA-15) was used as the catalyst support for comparison purposes, which was purchased from ACS Materials.

5.3.2 Catalyst synthesis

To prepare the DeAl-BEA support, the as-purchased BEA zeolite was firstly treated at 823 K for 4 hours in a muffle furnace with 500 mL/min air flow (Medical grade, Airgas) to obtain the proton-form BEA (denoted as H-BEA) zeolite. For dealumination, a procedure reported previously was used[347]. Typically, 6.0 g of H-BEA

was suspended in 150 mL 70 vol. % concentrated HNO_3 in a PTFE bottle and thermally treated at 353 K for 16 hours in a silicone oil bath with vigorous stirring. The sample was collected by centrifugation and washed with DI water until the pH reached neutral. The sample was then dried in an oven at 343 K overnight and then calcined at 823 K for 4 hours in the muffle furnace with 500 mL/min air flow.

The loading of Co into DeAl-BEA was done via the wet impregnation method. For instance, to prepare 3.0 wt.% Co loading into the DeAl-BEA support (denoted as 3.0wt% Co-DeAl-BEA), 0.1527 g of $Co(NO_3)_2 \cdot 6H_2O$ was dissolved in 0.5 g of DI water in a glass vial, and the solution was added dropwise to 1.0 g DeAl-BEA with vigorously grounding in an agate mortar with a pestle. The mixture was dried at room temperature overnight and calcinated at 823 K for 4 hours with a 5 K/min ramp rate in a muffle furnace under 500 mL/min airflow. After calcination, the catalyst powder was placed in a 125 mL Nalgene ® HDPE bottle, rolling on with 125 rpm on a jar roller mill (755 RMV, U.S. Stoneware), then passed 40-80 mesh sieves to obtain a suitable round particle in the size range of 0.18-0.42 mm. The same procedure was also used to prepare other catalysts used in this study, such as 1.0 wt. %, 6.0 wt. % Co on DeAl-BEA support (denoted as Co-DeAl-BEA-100, 600 respectively), and 3.0 wt. % Co supported by H-BEA (Co-BEA-300) and SBA-15 (Co-SBA-300) for comparison purpose.

5.3.3 Catalysts Characterization

The XRD pattern of each catalyst sample was measured on a Bruker® D8 diffractometer using the Cu-Kα radiation. The scan was performed with a step size of

0.05 degrees and a step time of 5 s. The cobalt, aluminum, and silicon content in the catalyst were determined by inductively coupled plasma-optical emission spectrometry (ICP-OES, Spectro Arcos II). N_2 isotherms were measured at 77 K using an Autosorb-iQ analyzer (Quantachrome Instruments). Before the measurement, samples were evacuated overnight at 573 K under 1.0 mmHg pressure. Diffuse reflectance UV-vis (DR UV-vis) spectra were obtained using an Ocean Optics USB2000 + spectrometer equipped with an IS200-4 integrating sphere detector. The morphology of the catalyst was characterized by SEM (Zeiss Auriga 60 CrossBeam) and TEM (Zeiss Libra 120).

The H_2-TPR profile of the catalysts was carried out by the same Quantachrome Autosorb-IQ analyzer equipped with a TCD detector. The catalyst was pretreated under N_2 gas flow (40 mL/min, ultrahigh purity grade, Airgas) at 553 K for 4 hours. After cooling to 298 K, gas was switched to 5 % H_2/N_2 (40 mL/min) and ramped to 1223 K from room temperature with a 10 K/min rate dwelled for 10 min. An inline liquid nitrogen cold trap was equipped to remove moisture vapor produced throughout the experiment to prevent interference with the TCD signal.

5.3.4 Catalysis test

The catalytic performance tests for as-prepared catalyst samples were carried out in a tubular packed-bed reactor. 0.375 g of catalyst granular was placed in the reactor and reduced at 773 K for 2 hours under 5% H_2/N_2 (50 mL/min, Airgas) with the 5 K/min ramp rate. After pre-treatment, the feed was switched to a mixture gas flow (5 mL/min methane flow (Research grade, Airgas) and 5 mL/min Ar (UHP Grade, Airgas, use as internal standard)). The temperature of the catalyst bed was monitored

using a K-type thermocouple (TJ36-CAIN-14E-6, Omega Engineering) on the external surface of the quartz reactor. The reaction effluents were analyzed using a gas chromatograph (Agilent 7890A) equipped with a methyl-siloxane capillary column (HP-1, 50.0 m × 320 μm × 0.52 μm) configured to a FID and a packed column (ShinCarbon ST Columns, 80/100 mesh, 1.83 m) configured to TCD detector.

5.3.5 Spent catalyst analysis

The coke formation in the spent catalysts was determined by the TGA method carried out by the Shimadzu TA-50 TGA system. Typically, appromixly 20 mg of the spent catalyst was exposed to 50 mL min^{-1} flowing air (Medical grade, Airgas) and ramped from room temperature to 1073 K with a 10 K min^{-1} rate. The nature of coke formed on the spent catalyst was examined using the TPO experiment. Typically, 20 mg of spent catalyst sample was immobilized by quartz wool in a 12mm diameter U-shaped quartz sample cell and loaded in a temperature-controlled furnace with outlet monitored by a mass spectrometer under ion monitoring mode MS. The temperature was monitored by a K-type thermocouple attached to the outer wall of the quartz sample cell with temperature data recorded by a data logger (Type TC01, National Instruments) The furnace was ramped from room temperature to 1123 K at a ramp rate of 10 K min^{-1} under a flowing 50 mL min^{-1} 5 % O_2 balanced with Ar (ultrapure, Keen Gas) atmosphere. The nature of coke was profiled by the temperature-dependent consumption or formation of O_2, CO_2, and CO species based on pervious study[226].

5.4 Results and discussion

5.4.1 Physiochemical properties of Co/DeAl-BEA catalysts

The compositions of Co-DeAl-BEA catalyst and other control catalyst samples are shown in **Table 5.1**. The actual Co loadings are close to those nominal loadings, showing no metal loss in the sample preparation process. The Al content in the dealuminated DeAl-BEA support is low, with a Si/Al ratio of more than 4000 +, indicating the successful removal of Al element from the support, consistent with previous reports[347]. **Figures 5.1 (A-C)** shows the XRD patterns of H-BEA, DeAl-BEA and Co-DeAl-BEA catalyst samples. Major characteristic peaks at 2 θ = 7.87°, 13.36°, 14.55°, and 22.48° were detected, corresponding to the typical BEA polymorph structure[348]. The dealumination treatment did not cause significant crystalline structure change of the zeolite support. A right shift of all the XRD peaks can be visible in **Figures 5.1 (B-C)** for the DeAl-BEA sample was detected in comparison to the H-BEA zeolite, which means a decrease in d-spacing and unit-cell volume due to the removal of Al atoms[349]. Meanwhile, the crystallinity of DeAl-BEA slightly decreased, which can be visualized from the attenuation of the XRD peak intensity at 2θ of 7.86° and 22.48° in **Figures 5.1 (B-C)**. The loading of Co particles seems to restore the peak positions, as Co-DeAl-BEA samples demonstrated a left-shift of the XRD peaks compared to those in the DeAl-BEA sample. A tiny peak at 2θ = 36.42° corresponding to Co_3O_4 oxides was observed for only Co-SBA-300, indicating non-uniformed dispersing of Co particles. For other Co loaded samples, no obvious peaks were correlated to Co and Co oxide, indicating that Co-DeAl-BEA-100, Co-DeAl-BEA-300,

Co-DeAl-BEA-600 and Co-BEA-300 has uniform Co high dispersion of Co species in the catalysts.

Table 5.1. Actual Co loading determined by ICP-OES.

Sample Name	H-BEA	H-DeAl-BEA	Co-DeAl-BEA-100	Co-DeAl-BEA-300	Co-DeAl-BEA-600	Co-BEA-300	Co-SBA-300
Co Concentration (ppm)	0	0	9795	28806	55766	26982	28237
Al_2O_3 Concentration (%)	3.78	0.02	0.00	0.00	0.00	4.11	0.01
Si/Al Atomic Ratio	22.44	4406.53	+ ∞	+ ∞	+ ∞	19.98	8564.76

N_2 isotherm of the Co-DeAl-BEA sample demonstrated in Figures 5.1 (D-E) demonstrate the surface area (m^2/g) change before and after dealumination and cobalt loading. The dealumination process demonstrated the decreasing surface area of H-DeAl-BEA (465.51 m^2/g), compare with the H-BEA (514.11 m^2/g) in **Figure 5.1 (D)**. The decreasing of surface area can be attributed to the structural defects created by dealumination, as agreed by XRD data in **Figure 5.1 (A-C)**. Dealumination by removing Al-O_4 center can jeopardize the mesopore structure cause overall BET surface area reduced[350]. After loading with Co, the surface area slightly decreased to (354.9 m^2/g) for Co-DeAl-BEA-300 sample, indicating the Co species has filled the H-DeAl-BEA structures as agreed by XRD crystallinity recovering in **Figure 5.1 (A-C)**. Similarly, Co loading fill in mesoporous H-BEA to create partially blockage thus reduce the BET surface area, as demonstrated in **Figure 5.1 (B-C)**. An interesting result

shows that for SBA-15 and BEA support, Co species loading on the support only reduced surface area around 50 cm^3/STP , which can be attributed to Co dispersed at the surface of SBA-15 and H-BEA evidence by **Figures 5.1 (D) and (E)**. Since the absent of silanol cage in SBA-15 and H-BEA cannot withhold Co like H-DeAl-BEA. Other Co loaded samples exhibited decrease trend of surface area as Co loading increased, exhibited BET surface area Co-DeAl-BEA-100 >Co-DeAl-BEA-300 >Co-DeAl-BEA-600.

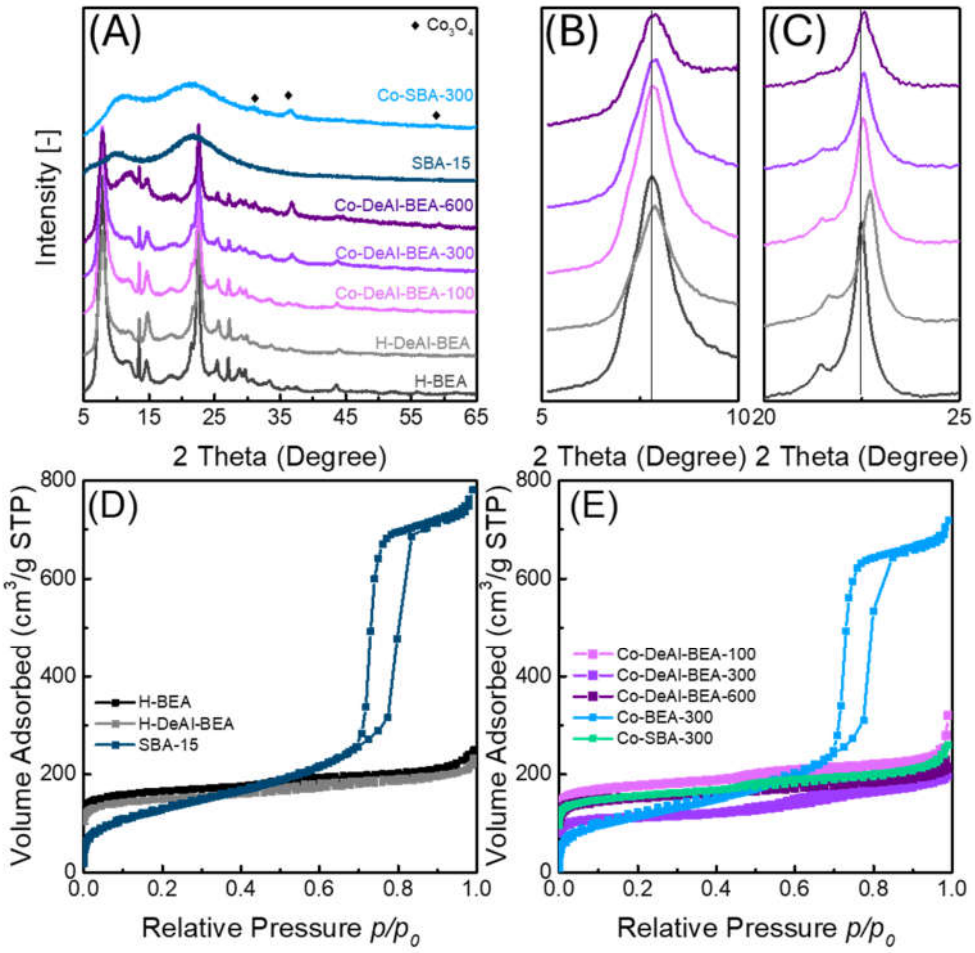

Figure 5.1 Fundamental physiochemically properties of as-prepared Co catalysts characterized by XRD (A), zoomed in XRD peak in 5-10° 2theta (B), zoomed in XRD peak in 20-25° 2theta (C), N_2 isotherm of Co-DeAl-BEA catalysts (D), N_2 isotherm of Co-BEA-300 and Co-SBA-300 (E).

5.4.2 Coordination structure of Co-particles in Co-DeAl-BEA catalysts

The Co species loaded on the DeAl-BEA support exhibited nanoparticle configured by Co_3O_4 evidenced by the DR UV-vis of Co-DABEA catalysts in **Figure 5.2 (A)**. The Co species were determined as surface Co_3O_4 nanoparticles for Co-DeAl-BEA -100, 300, and 600 samples due to three characteristics bands at 258.8, 447.1, and 720.6 nm, which agreed with the typical Co_3O_4 spinel structure[351-353]. The peak at 258.8 nm can be assigned to charge transferring of Co (II) with the oxygen ligands in tetrahedral symmetry[255]. The boarded peak centered at 447.1 nm is corresponding to Co (III) octahedral site, where the boarded peak at 720.6 nm can be attributed to the presence of Co (II) octahedral site[354]. No significant Co (II) tetrahedral site shown up which typically utilized as the evidence of atomic dispersing of Co[354, 355]. The Co-DeAl-BEA-100 exhibits characteristic bands at 236.3, 365.4, 661.9, and 734.8 nm, indicating the presenting of mixed Co (II, III) nano particles based on the following band assignment: The band at 236.3 nm refers to charge transferring of Co (II) and oxygen ligands[255]. The band centered at 365.4 nm can be attributed to Co (III) species[255, 356]. The band centered 661.9 correspond to Co (II) tetrahedral site, and the 734.8 nm as the Co (II) octahedral site. The Co-SBA-300 behaved very similar to Co-DABEA samples, as it can be seen the features in the range of 400 -550 nm, indicating

the present of Co (III) species. The Co (II) feature of Co-SBA-300 can be found at near 700 nm, which indicating the solely presenting of Co (II) in Co-SBA-300. The H-DeAl-BEA contains no features related to Co, indicating the above features are exclusively belong to Co_3O_4.

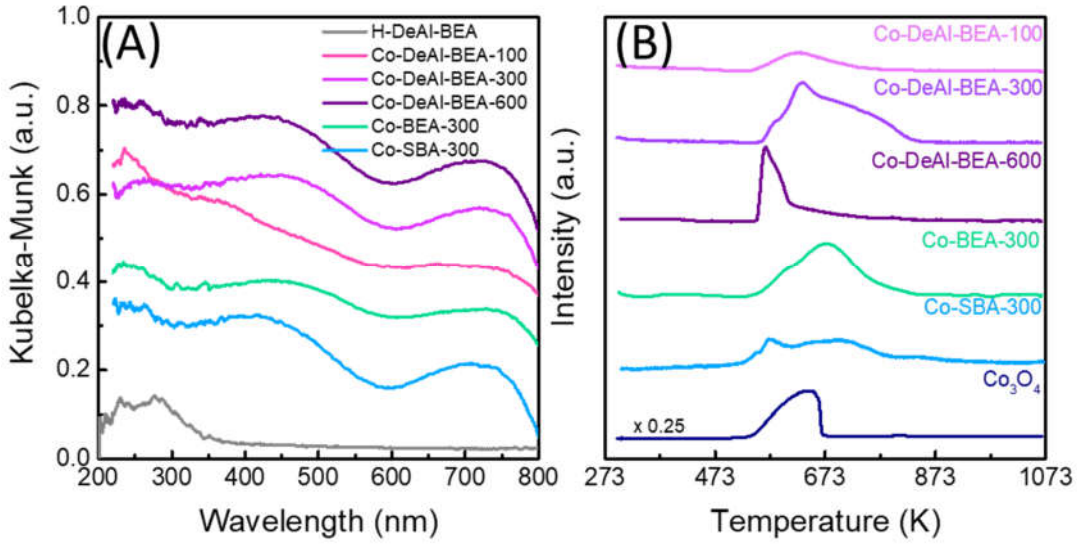

Figure 5.2 Coordination environment and status of Co catalysts sites characterized by UV-vis DRS (A), and H_2-TPR profile of Co-DeAl-BEA catalysts.

5.4.3 Reducibility of Co-particles in Co-DeAl-BEA catalysts

The reducibility of Co-DeAl-BEA catalysts were examined by H_2-TPR showing the profiles in **Figure 5.2 (B)**. The Co-DeAl-BEA-300 exhibits three reduction events at 588.9 K, 630.7 K, and 742.8 K, which can be attributed to the reduction of Co (III) to Co (II), Co (II) reduced to Co (0), and small Co (II) in tetrahedral site reduced to Co (0). The splitting of the peak and shifting to higher temperature indicates some portions of Co are strongly coordinated with the support, which should be the

contribution of silanol cage in H-DeAl-BEA created by dealumination. However, The TPR profile of Co-BEA-300 showing a boarded peak centered at 679.4 K, which can be deconvoluted to reduction of Co (III) to Co (II), and Co (II) to Co (0). Although the deconvolution of this peak is challenge, the large particle of Co_3O_4 often reduced in single step. The overall peak shifted to higher temperature could be the formation of $CoAl_2O_4$ in Co-BEA-300. In Co-DeAl-BEA-100, a board peak centered at 625.1 K can be deconvoluted to two reduction events: Co (III) reduced to Co (II), and Co (II) reduce to Co (0). The peak position well overlapping with the bulk Co_3O_4, indicates the surface Co spices are nano particles. In Co-DeAl-BEA-600, the higher loading yields more Co oxide nanoparticles, evidenced by the peak centered at 564.1 K. and 591.2 K, which can be attributed to the reduction of Co (III) to Co (II), and Co (II) reduced to Co (0), respectively. Co-DeAl-BEA-600 has much larger Co oxide nano particles as the reduction peak shifted to lower temperature, hints that less interaction between Co and DABEA support, agreed by the results of UV-vis and Raman.

5.4.4 Catalytic performance of Co-DeAl-BEA in methane decomposition

Figure 5.3A shows time on stream methane decomposition performance over Co-DeAl-BEA catalysts at 773 K. Typically, the catalysts exhibit around 1 hours of induction period then reach stable performance. For comparison purpose, the non-loaded H-DABEA support did not exhibit any methane activation, indicating the methane decomposition is exclusively resulted from Co species. For the DeAl-BEA supported samples, the Co-DeAl-BEA -300 exhibited high and stable methane conversion around 15.3 % for 8 hours without significant deactivation. For the Co-

DeAl-BEA -600, the methane conversion started from 14.6 % and eventually reached 19.5 %. This can be understood by the increase of Co particles in DeAl-BEA support provide more catalytic sites for methane decomposition. However, the Co-DABEA-100 shows much lower methane conversion around stable at 3.5 % for 8 hours of reaction. Such low methane decomposition activity can be attributed to the insufficient of Co sites for methane decomposition. Distinctly, Co-DeAl-BEA-300, Co-BEA-300, and Co-SBA-300 exhibited different catalytic performance under methane decomposition condition. For Co-BEA-300, maximum conversion around 8.6 % was reached at the then rapidly deactivated and lose activity within 4 hours. The trend follows typical deactivation profile of supported metallic catalyst under methane condition. The Co-SBA-300 also exhibited deactivation. After exposure to methane condition, the Co-SBA-300 reach methane conversion as high as 18.3 %, then start deactivating after 2 hours of reaction. Only Co-DABEA-300 and Co-DABEA-600 able to exhibit stable performance without deactivation for 8 hours, hints that the high stability and activity contributed by the silanol caging effect by the dealuminated site.

In terms of product formation, only hydrogen was detected by the GC TCD, no other hydrocarbons products (except methane) were detected in both TCD and FID detector, indicating the reaction is a typical catalytic derived methane decomposition. Based on this, a time on stream of hydrogen production was showing in **Figure 5.3 (B)**. The stable hydrogen formation rate around 137 $\mu mol \cdot min^{-1} \cdot g^{-1}$ was reached by Co-DeAl-BEA-600 within 8 hours of continues reaction, higher than 119 $\mu mol \cdot min^{-1} \cdot g^{-1}$ by Co-DeAl-BEA-300. The difference of hydrogen formation rate between Co-DeAl-BEA-300 and Co-DeAl-BEA-600 corresponding to the methane conversion in **Figure 5.3**

(B). The zoomed in figure in **Figure 5.3 (B)** demonstrated Co-DeAl-BEA-100 only reached 2.1 $\mu mol \cdot min^{-1} \cdot g^{-1}$, then rapidly deactivated. This is because the low loading did not form sufficient Co sites, as it can be verified in DR UV-vis data in **Figure 5.2 (A)** with low intensity at 400-500 nm region and 700-750 nm indicating the low concentration Co (III) and Co-O-Co frameworks. For the deactivation of Co-BEA-300 and Co-SBA-300. Their initial hydrogen formation rate can reach high around 59.2 $\mu mol \cdot min^{-1} \cdot g^{-1}$ and 158.3 $\mu mol \cdot min^{-1} \cdot g^{-1}$, respectively, then followed by rapidly deactivation. The high hydrogen production rate by Co-SBA-300 can be attributed by its high surface area. However, both catalysts deactivated because no caging effect provided by the silanol groups to stable Co sites on BEA and SBA.

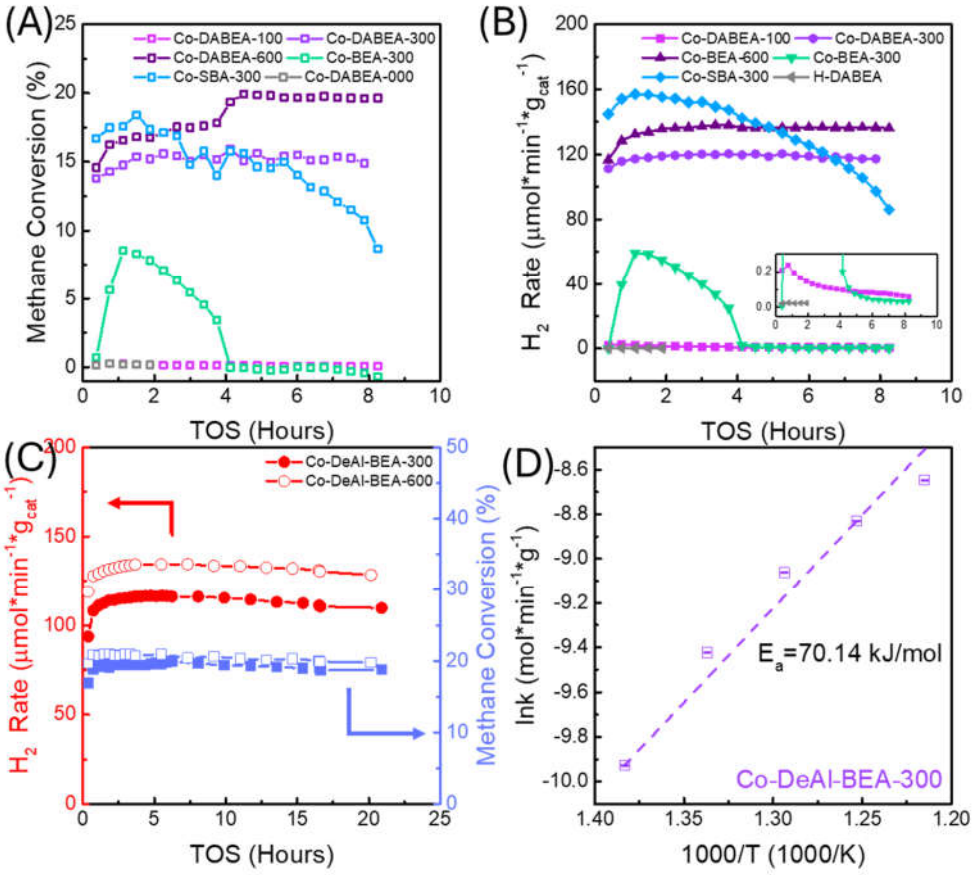

Figure 5.3. Catalytic performance of Co-DeAl-BEA under NMD conditions demonstrated methane conversion (A), H_2 formation rate (B), long term stability (C), and reaction activation energy measured from 723 K to 823 K (D). (NMD reaction conditions: 0.375 g catalyst, 773 K, WHSV=6400 h^{-1}, 10 mL/min 50 % CH_4 balanced in Ar as internal standard).

Regarding the stability of Co-DeAl-BEA-300 and Co-DeAl-BEA-600, the long-term stability test in the same condition (773 K, WHSV=6400 h^{-1}) was performed for 20 hours showing in **Figure 5.3 (C).** With in 20 hours of continuous reaction, Co-DeAl-BEA-300 exhibit stable conversion around 18.9 % for Co-DeAl-BEA-300 and

20.64 % for Co-DeAl-BEA-600. The hydrogen formation rate is corresponding to their methane conversion, indicating no additional byproducts were formed. The overall methane decomposition performance shows high stability for 20 hours without obvious deactivation. Although the Co loading in Co-DeAl-BEA-600 double times than Co-DeAl-BEA-300, the activity only improved for 8.4 %. To understand the activation energy of methane decomposition over Co catalysts, the Co-DeAl-BEA-300 was examined from 723 K to 823 K under typical flow conditions. The rate of hydrogen formation was determined and plot with Arrhenius equation to determines overall reaction activation energy as 70.14 kJ/mol, much smaller than thermal methane decomposition and liquid catalysts[357].

5.4.5 Spent catalysts characterization and analysis.

Microstructure of spent Co-DeAl-BEA catalysts after 8 hours of methane decomposition were visualized by SEM and TEM, presented in **Figure 5.4** (A-O). Distinct CNTs formed on the spent catalysts exhibit different quantity, morphology, and configuration. For Co-DeAl-BEA-100, 300, and 600 catalysts, different amount of CNTs can be visible in proportion to the Co loading (**Figures 5.4 (A, D,** and **G)**). A notable difference between **Figure 5.4 (A)** contrasts with **Figures 5.4 (D)** and **(G)** that almost no CNTs formed for spent Co-DeAl-BEA-100, where the spent Co-DeAl-BEA-300 and 600 formed lavish CNTs between catalyst particles. This can be attributed to the low catalytic activity in Co-DeAl-BEA-100 evidenced in **Figures 5.3 (A-B)**. For spent Co-BEA-300 and Co-SBA-300 in **Figures 5.4 (J)** and **(M)** the CNTs were barely able to be found, primarily because of their low catalytic activity and rapidly

deactivation so the reaction did not accumulate CNTs. With carefully examination of **Figures 5.4 (J)** and **(M)**, the spent Co-SBA-300 exhibited more CNTs than Co-BEA-300, which should be attributed to the higher activity and less deactivation rate of Co-SBA-300 than Co-BEA-300 as evidenced in **Figures 5.3 (A-B)**.

Besides the quantity of CNTs, the morphology of CNTs and grown mechanism can be revealed from the microstructure of spent catalyst. The TEM image in **Figures 5.4 (B-C**, **E-F**, **H-I, K-L**, and **N-O)** demonstrated multiwall configured CNTs (MWCNTs) generated with different diameters and wall thicknesses. In spent Co-DeAl-BEA-100, the TEM image in **Figure 5.4 (B)** shows two type MWCNTs with diameters approximately 21 nm with wall thickness 5 nm, and 8 nm diameter with wall thickness around 2 nm, respectively. Two dark dots marked in a yellow circle are reacted Co nanoparticles (NPs), which have been pulled out from the catalyst surface, indicating the typical tip-grown mechanism of MWCNTs. **Figure 5.4 (C)** snapshot of a tip grown just cause the reacted Co-NPs (marked in yellow circle) leaving the support, the particles covered by few layers of CNTs forming a capsule convert the reacted Co-NPs leaving the surface. The reacted Co-NPs remaining in the support can also be visualized from the catalysts marked in blue circles, around 17-20 nm in size. In spent Co-DeAl-BEA-300, the SEM image (**Figure 5.4 (D)**) shows visible CNTs grown from the catalyst surface, which should be identified as base-grown (violet circles). The tip growth is also visible in **Figure 5.4 (D)**, identified by the light dots on the CNTs (Green circles). From the image, it can be concluded that the base grown is more dominant than the tip grown in **Figure 5.4 (D)**, thanks to the dealumination created by the silanol caging, which can be used to enhance the Co site with support. The zoomed-in

configuration of spent Co-DeAl-BEA-300 and CNTs in **Figure 5.4 (E)** and (F) indicate much smaller Co-NPs distributed on the H-DeAl-BEA matrix with 10-15 nm size since the silanol cage has limited ability to withhold Co-NPs. The morphology of CNTs indicating primarily MWCNTs with 17-20 nm outer diameter and wall thickness 7-8 nm. As for Co-DeAl-BEA-600, the SEM image revealed more tip grow (**Figure 5.4 (G)**) than base grow cases. The morphology of CNTs in **Figures 5.4 (H-I)** indicates that MWCNTs were presented with outer diameter around 36-38 nm, much higher than the Co-DeAl-BEA-100 and 300. This can be attributed to the size of the reacted Co NPs on tip. A snapshot of tip grows in **Figure 5.4 (I)** demonstrated a pear-shaped reacted Co-NP at the tip of MWCNT, has diameter close correlated to the out diameter of MWCNTs. The thicker MWCNTs mainly caused by larger particles, and its more likely from tip grown due to larger particle size cannot fit into the silanol cage to be stabilized. Back to Co-BEA-300 and Co-SBA-300, although the insufficient CNTs did not provide distinct tip or base grown of CNTs in **Figures 5.4 (J)** and **(M)**. The TEM image in **Figures 5.4 (K-L)** and **(N-O)** exhibited morphology MWCNTs and a snapshot of tip growth for the two spent catalysts, has a much larger out diameter 25-40 nm with corresponding wall thickness 12-16 nm. The snapshot of reacted Co-NPs on MWCNT tip (**Figures 5.4 (L)** and **(O)**) showing pear shaped, reacted Co NPs on the tips to enable MWCNTs gown. A notable strong shape changing of reacted Co NPs can be found in **Figure 5.4 (L)**, where the nanoparticle has been pulled to a reversal cone shape by the MWCNTs. Due to no silanol caging the Co particles in Co-dabea-300 and Co-SBA-300, the contraction force of CNTs can significantly change the

geometry of nanoparticles and make it much easy to release from the surface, as evidence by literatures[358, 359].

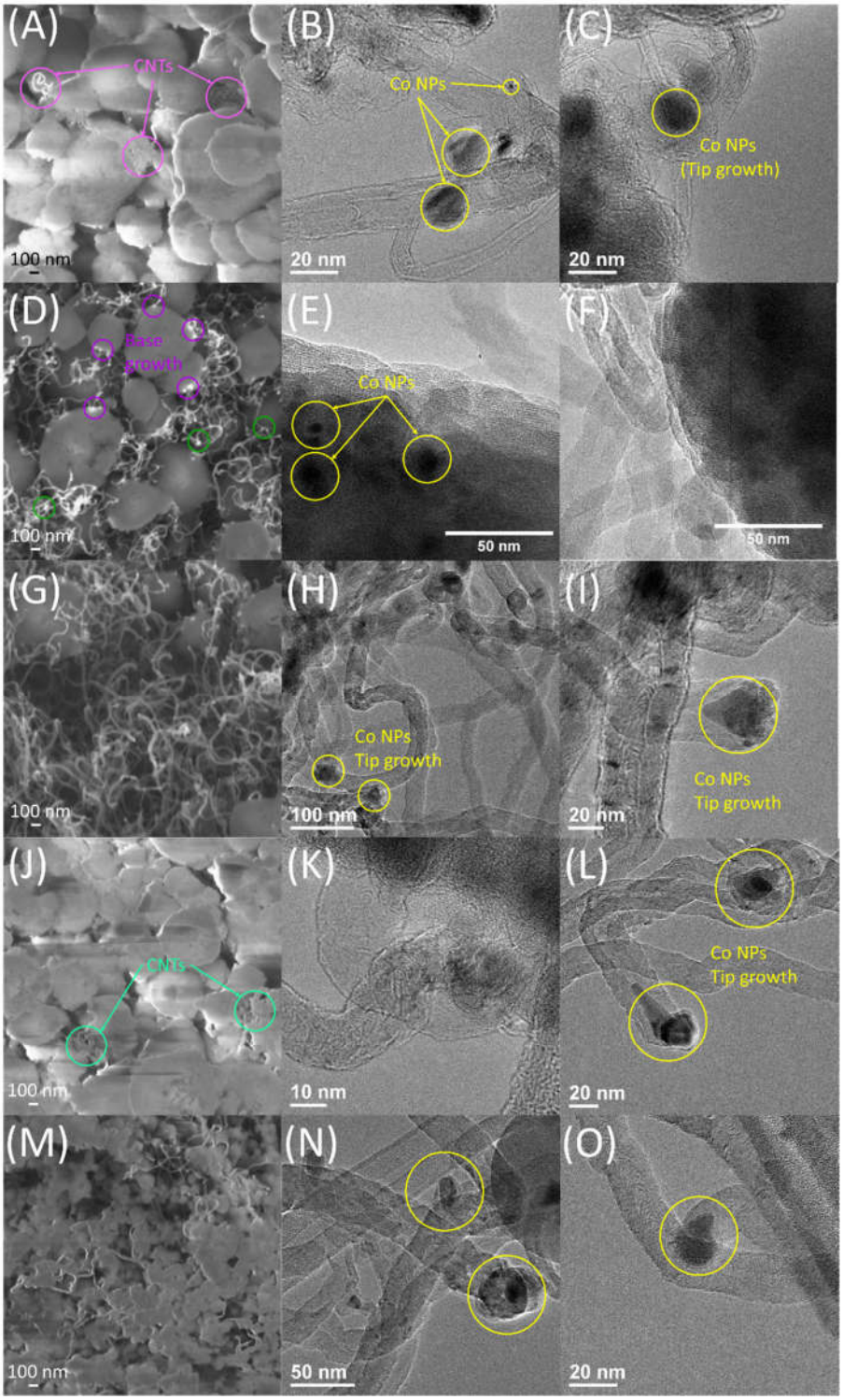
(A)
CNTs
100 nm
(B)
Co NPs
20 nm
(C)
Co NPs
(Tip growth)
20 nm
(D)
Base
growth
100 nm
(E)
Co NPs
50 nm
(F)
50 nm
(G)
100 nm
(H)
Co NPs
Tip growth
100 nm
(I)
Co NPs
Tip growth
20 nm
(J)
CNTs
100 nm
(K)
10 nm
(L)
Co NPs
Tip growth
20 nm
(M)
100 nm
(N)
50 nm
(O)
20 nm

Figure 5.4. Microstructure and morphology of spent Co-DeAl-BEA catalysts after 8 hours of NMD. SEM images of CNTs distributions (A), (D), (G), (J), and (M), TEM image of CNTs morphology (B-C), (E-F), (H-I), (K-L), and (N-O).

Although carbon formation characterized by SEM and TEM provides morphology and growth mechanism. More physicochemical properties can be examined by TGA and TPO methods. In TGA analysis, spent catalysts under 8 hours of continues methane decomposition are presented in **Figure 5.5 A**. From the weight loss curve, Co-DABEA-600 accumulated the highest weight loss as 70.3 %, then followed by Co-SBA-300 (47.4 %), Co-DeAl-BEA-300 (35.2 %), Co-BEA-300 (9.5 %), and Co-DeAl-BEA-100 (1.3 %). In the details of the weight loss curve, Co-DABEA-300 started weight loss at 581 K, much lower than the Co-BEA-300 (638.3 K) and Co-SG-300 (660 K). Such low weight loss temperature often indicates higher activation of carbon species generated in the reaction. The weight loss starting temperature for these catalysts hits different activity of carbon was formed. Typically, sharper and lower weigh loss temperature refers to the carbon with higher activity.

The CNTs deposits on the spent catalysts were probed by the TPO after 8 h TOS under catalytic methane decomposition reaction. **Figures 5.5 (B-D)** shows the important species of CO_2, CO, and O_2 evolution. One notable difference which used to describe the different activity of CNTs can be explained by the peak revolution event at different temperatures. The CO_2 trend shows peak temperature has Co-DeAl-BEA-100 (731.7 K) < Co-DeAl-BEA-300 (753.81 K) < Co-DeAl-BEA-600 (782.3 K) ≈ Co-

BEA-300 (783 K) < Co-SBA-300 (788.7 K). Although the Co-DeAl-BEA-100 has highest activity CNTs, the low activity of methane decomposition did not make it as an effective catalyst. Back to its microstructure in **Figures 5.4 (B)** and **(C)**, the existing of thin MWCNTs indicating it growth from smaller Co active site, thus the MWCNTs could exhibited higher activity in TPO due to less thickness. Similar, more active CNTs in Co-DeAl-BEA-300 than 600 can be also evidenced in **Figures 5.4 (D)** and **(G)**. The similar active CNTs found in Co-BEA-300 with Co-DeAl-BEA-600 can be ascribed to their similar morphology. The lowest activity found in spent Co-SBA-300 due to its high thickness of CNTs in **Figures 5.4 (N)** and **(O)**. Besides, the peak shape and geometry such as asymmetry in the CO_2, CO and O_2 peaks also corresponding to different carbon configuration such as crystalline, ordering, hybridization, although they are all MWCNTs. Spectra for each spent catalyst sample can be deconvoluted into three peaks - low, medium, and high temperature peaks - as reported previously. In this case, the low temperature peak can be thin, low wall thicknessed carbon nano tube contains high density of defects. The medium peak temperature represents the intermediate thick and number of walled MWCNTs. The high peak temperature represents ridged, ordered, and thick MWCNTs or even carbon nanofibers. Based on this, the MWCNTs formed in Co-DeAl-BEA-100 and 300 are very active, low thicknesses with structural defects. The MWCNTs in Co-DeAl-BEA-600 and Co-BEA-300 are intermediated thickness, much more robust than the MWCNTs from Co-DeAl-BEA-100 and 300. The hardest MWCNTs have high thicknesses due to the absence of silanol have no control over the particle size of Co species, and generate MWCNTs with the highest wall thickness (**Figures 5.4 (N-O)**), which are more robust

than the previously spent catalysts. A notable TPO feature in spent Co-DeAl-BEA-300, 600, and Co-SBA-300, an additionally peak can be found right after their major peak. This secondary peak could be the oxidation of the carburized Co-NPs or carbon deposits which is not CNTs configuration. Based on the size of the peak, Co-SBA-300 has highest intensity than Co-DeAl-BEA-300 and 600, hints that the peak contains possible low active coke, with the carbon dissolved in the Co-NPs. Interestingly, the spent Co-BEA-300 only present a mini, highly symmetry peak, which can be ascribed to its low activation of Co did not function due to the strongly bonding with the aluminate in H-BEA.

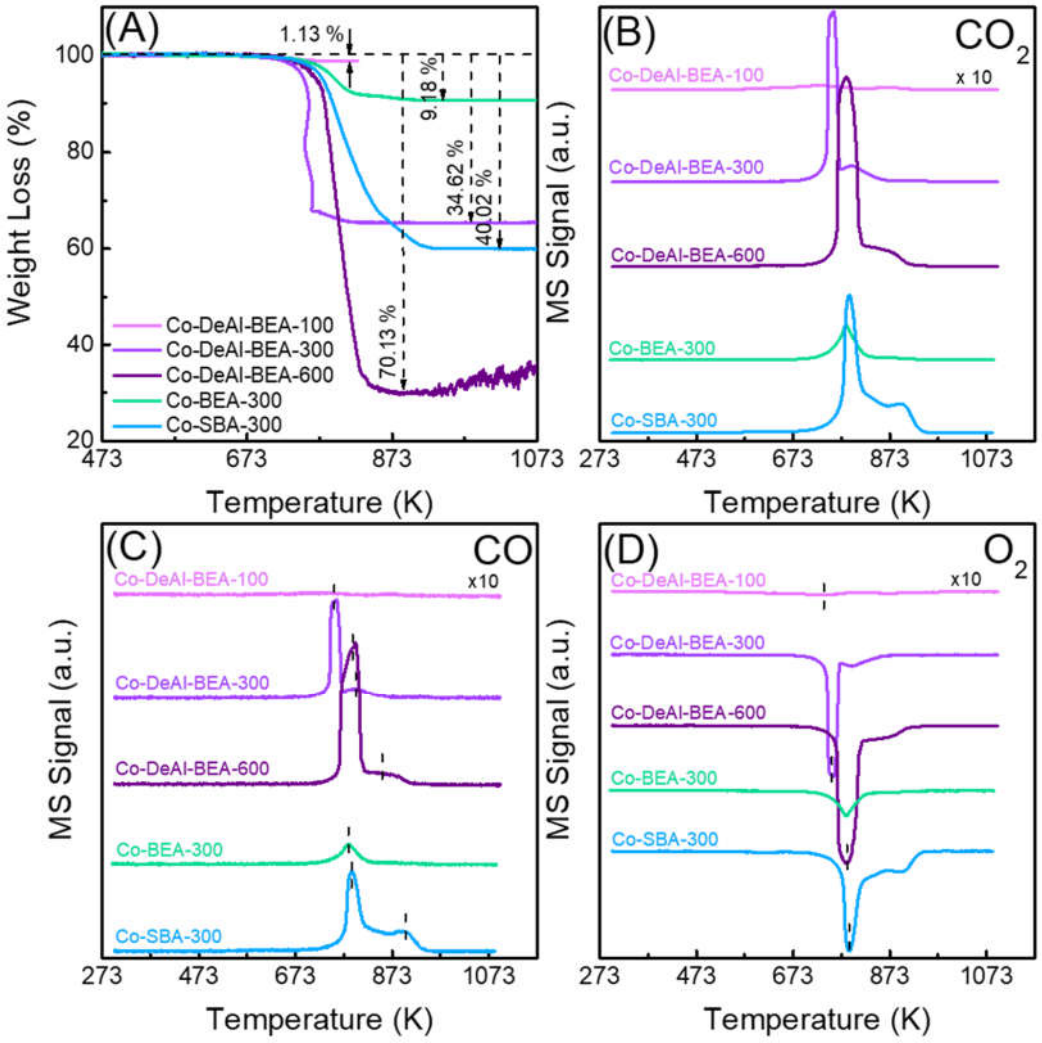

Figure 5.5 Spent catalysts analysis after 8 hours NMD reaction at 773 K by TGA (A), and TPO profile of CO_2 evolution signal (B), CO evolution signal (C), and O_2 consumption signal (D).

5.5. Summary

The developed Co-DeAl-BEA catalyst demonstrated stable methane decomposition activity toward hydrogen and MWCNTs production at relative low temperature at 773 K. The results show dealumination BEA zeolite could stably

supported Co species with NPs configuration by its silanol group caging the Co species to prevent deactivation. At 773 K, both Co-DeAl-BEA-300 and Co-DeAl-BEA-600 exhibited stable NMD performance over 20 hours without deactivation. The characterization shows different morphology of CNTs, that can be ascribed to the dealumination of support. Without silanol caging effect in the support, Co speices tend to be grown higher thickness CNTs and with tip growth process, resulting Co speices leave the support, such as Co-DeAl-BEA-600, Co-BEA-300, and CoSBA-300. However, with the silanol caging effect, the Co-DeAl-BEA-300 exhibits majority base growth due to the silanol can stabilize Co-NPs. Besides, the loading of Co species could also result in different activity and performance depending on the Co site configuration. Although both Co-DeAl-BEA-300 and 600 exhibited high activity of NMD, the Co-DeAl-BEA-300 has much uniform, relatively smaller spent Co NPs than Co-DeAl-BEA-600 catalysts, which nits that at least a portion of Co speices were not confined by silanol cage in Co-DeAl-BEA-600. When reducing the loading to 1 wt. %, the Co-DeAl-BEA-100 exhibits low catalytic activity, probably because of insufficient sites and the majority of them are confined by the silanol groups.

Chapter 6. Conclusions, Limitations, Recommendations, and Contributions

6.1. Conclusions of the Thesis Study

Methane upgrading is an essential technology system produces key products such as hydrocarbons, syngas, methanol, chloride, and sulfide. The current, conventional methane upgrading process cannot satisfy the goal of net-zero emission of CO_2 by 2050 due to irreducible emissions. When carbon pricing increases, non-oxidative methane upgrading can become the crucial technology for economically obtaining hydrogen and essential chemicals. Engineeringly, there are still some challenges that need to be resolved, such as processing study to reach a profitable production rate for commercialization. From this aspect of science, the challenge remaining is the high energy penalty to active C-H bonds in methane molecules. The reaction is strongly limited by thermodynamics and kinetic, which require effective catalysts to break through kinetic limitation. Besides, the spontaneous coke formation can strongly cause deactivation under non-oxidative methane upgrading, which needs to be addressed to move forward and develop this technology. This dissertation primarily focused on designing robust and active catalysts with strong coking tolerance for non-oxidative methane upgrading. Towards hydrocarbon production via NMC, the dissertation targeted understanding and developing methane-active, coking tolerance catalysts to be continuously operated under high temperatures. For converting methane into hydrogen and carbons, the dissertation proposed stable, zeolite-supported Co

catalysts functioning at much lower temperatures around 773 K. The brief conclusions of the dissertation studies are listed below.

Chapter 2 introduced the novel vitreous silica supported Fe/SiO_2 catalysts prepared via oxyhydrogen flame fusion method. Thanks to the rapid melting and quenching of the flame fusion enable phase transition from quartz to vitreous status amorphous silica. The characterization revealed that high density of defects created by the flame fusion which existed in the vitreous silica structure can significantly enhance the stability of Fe isolated sites, and maintain high methane activation at 1273 K. The developed vitreous Fe/SiO_2 also exhibiting lower coke selectivity than cristobalite supported Fe catalysts, indicating the vitreous Fe/SiO_2 is an effective catalyst for NMC. Chapter 3 provide detail discussion of silica catalyst development for NMC and investigated the alternative catalyst screened by NMC. Given by the 4d transition metals are active catalysts for methane activation, different CH_4 interaction over these catalysts as the specific electronic structures. Using vitreous silica support, Mn, Fe, Co, Ni, and Cu species supported by vitreous silica were evaluated and exhibiting a volcano shaped trend. The detail of characterization indicated that only Mn, Fe, and Co species supported by silica has isolated site configuration, where Ni and Cu species stay as surface nano particles configuration. This difference of configuration resulting controversy performance under NMC conditions. The Co/SiO_2 received lowest coke formation and highest C_2 formations, where Mn has highest activity to response NMC, but favors coke formation. Cu/SiO_2 and Ni/SiO_2 are not possible to be fabricated with a single site in this way: Both Cu and Ni are easy to be reduced, and they do not have stable silicate precursors such as Mn, Fe, and Co.

To explore the high conversion and continued reaction, vitreous silica supported Fe/SiO_2 in Chapter 4 was configured to a 13 cm long catalytic wall reactor and studied the performance that demonstrated 60 % methane conversion and reached equilibrium. The overall CWR exhibited better thermal efficiency than conventional fixed bed reactor, due to its thermal conductivity dominated by conductivity, much more efficient than convection and radiation. Besides, the CWR design uses fewer catalysts than fixed the bed design. In terms of products olefins, aromatics, and collectible carbon nanospheres (with a diameter around 150-200 nm) were obtained. The product distribution can also be shifted between hydrogen or hydrocarbon-dominated parts and aromatics by adjusting the reaction conditions. The unique design of the catalytic wall reactor can continue the reaction without degradation, as proven by long-term stability with 140 hours of continuous testing.

In Chapter 5, we demonstrated a dealuminated zeolite BEA-supported catalyst for methane upgrade to hydrogen and solid carbon at lower temperatures. With dealumination removed Al^{3+} ions, the dealuminated BEA exhibits no more Brønsted acid, which is known as the key active site of hydrocarbon oligomerization in zeolite chemistry. The “left-over” silanol group can provide a confinement effect to stabilize the nano sized Co spices, which is critical to the catalyst stability during carbon nanotube growth. The Co-DeAl-BEA-300 exhibits a majority base gown of MWCNTs grown, with continuous hydrogen production over 20 hours without obvious degradation.

6.2. Limitations and Recommendations

The thesis has overviewed and addressed challenges in non-oxidative methane upgrading technologies by developing effective and robust catalysts, which has great potential towards commercial scale development. However, there are still enigma and challenges remain in the overall technology which cannot be fully resolve by this thesis. Given by this, we recommend future research focused on below directions.

6.2.1 Distinct the Surface Reaction and Gas Phase Reactions for Fe/SiO_2 System

The study has revealed that of surface reaction combined with gas phase reaction co-existed. To fully understand the surface catalytic contribution and mechanisms of Fe/SiO_2 based catalysts, it is recommended to establish the control space velocity and temperature of reactor to reduce the effect the gas phase reaction. Using the spices MS probing as advanced characterization techniques is expected to distinguish the contributions of gas phase and surface catalytic reactions, which might further answer critical spices evolution from in-situ viewpoint with better understanding of non-oxidative methane chemistry over Fe/SiO_2.

6.2.2. Innovation in Catalysts Development for NMC with Control Environment

Although we developed flame fused vitreous silica supported single site Fe, Mn, and Co/SiO_2 catalysts, the open flame and natural of precursors has some possible chemical status changes which was beyond our control. Given that the rapidly heating

and melting is critical to the catalyst's development, which could also be carried out under controlled environments. We proposed using ultra-fast, sparks plasma sintering of precursor with the silica could control the oxidation of metal, maintain high dispersing, and expand to more metals. Given that the stability and availability of silica precursor is very limited, this technique compactable with alternative precursors and can tolerate rapidly cooling and heating under controllable of atmospheric.

6.2.3. Requires More Processing Stimulation and Reaction Engineering Studies

More engagement of process simulation from the aspect of reaction engineering or economy is required to provide more scope, viewpoint, and valuable information to understand the overall technology. Reaction engineering is also required to understand how NMC and NMD operate. Based on the previous discussion in Section 1.5 that the NMC is strongly limited by pressure, removing hydrogen using a durable, efficient proton conductive membrane is a promising technology. The materials and membrane study can greatly promote NMC. We truly wish the recent membrane development could be combined with NMC as a membrane reactor to break through the current equilibrium limitation. Besides the membrane reactor, develop auto auto-thermal reactor from NMC as an efficient reactor system suitable for commercial-scaled development will be useful. However, this requires more process control study, especially for our developed high conversion reactor, which requires a more comprehensive process condition study to produce hydrogen or hydrocarbons depending on the demand.

6.2.4. Tailoring Catalyst Configuration for NMD and Discovering Spent Catalyst Utilizations

Co-DeAl-BEA catalyst exhibited different activity of NMD and CNTs products by its loading and the silanol caging effect of Co NPs. However, we still do not understand the detailed confinement effect and the geometry of Co NPs based on current results. A study to reveal the Co-DeAl-BEA system from processing parameters to control the size and distribution of NPs, which can potentially change the particle size and interact with the silanol groups, is much needed. Besides, the bimetallic design can also change the activity and interaction with the silanol, such as alloying Co with Mo, Fe, and Sn, which has not yet been discovered in the DeAl-BEA system.

6.3. Contributions

The contribution provided by this dissertation not only to the catalysts development for non-oxidative methane upgrading toward hydrocarbons and hydrogen production to indirectly reduce CO_2 emissions. It also systematically demonstrated creating defects sites in the support are critical strategies to improve robustness and activity of catalyst. For different type and properties of support, defects creation dependent on treatment condition to tailoring defects formation using removal, phase transformation, and incorporation method. The dissertation also practiced and demonstrated systematic approaches of testing and characterize these defects formation to build strong interactions with the catalytic active phase using simple and complex instruments. The dissertation also established an approach from catalyst fundamental to actual reaction engineering, such as the catalytic wall reactor, which demonstrated

possible ways of continuous NMC reaction operation with carbon removal. The byproducts are solid carbon spheres with a diameter 150-200 nm, which is very ideal cathode material for fuel cells. The dissertation also investigated low-temperature NMD to hydrogen process. The proposed catalysts (Co-DABEA-300) were validated for methane upgrade to hydrogen and MWCNTs with increases the long-term stability. The byproduct of MWCNTs is more value-added than the amorphous carbon form conventional methane pyrolysis, which is a promising process to improve overall profits for NMD.

Achievements

Published Work

1) **Liu, Z**., Cheng, S., Schulman, E., Chen, W., Vlachos, D.G., Shu, Y., Tran, D.T. and Liu, D., 2023. Direct non-oxidative methane coupling on vitreous silica-supported iron catalysts. Catalysis Today, 416, p.113873.
2) Pan Y, Bhowmick A, Wu W, Zhang Y, Diao Y, Zheng A, Zhang C, Xie R, **Liu Z**, Meng J, Liu D. Titanium silicalite-1 nanosheet-supported platinum for non-oxidative ethane dehydrogenation. ACS Catalysis. 2021 Jul 27;11(15):9970-85.
3) Ali Kamali; Yuan Zahng; **Zixiao Liu**; Emily Schulman; Mohammed Almafrachi; Sheng Zhang; Tong Wang; Lorelis Gonzalez-Lopez; Xinpeng Zhao; Wenfei Zhang; Qulan Zhou; Mohamad Al-Sheikhly; Liangbing Hu, Defective Ceria Created by Oxhydrogen Flame and Its Influences on Pt Dispersion, Pt-Ceria Interaction and Catalytic Hydrogenation, Accepted by Molecular Catalysis, Sept. 2023.

Working Papers

1) **Liu, Zixiao**, et al. "Direct, non-oxidative conversion of methane to olefins and aromatics over vitreous silica-supported metal catalysts." Manuscript Submitted to Chemical Engineering Journal (2024).

2) **Liu, Zixiao**, et al. "Direct, non-oxidative conversion of methane in Fe/SiO2 catalytic wall reactor." Manuscript preparation in progress (2022).
3) **Liu, Zixiao**, et al. “Stable Co-BEA Zeolite Catalyst via Dealumination Treatment for Catalytic Methane Decomposition." Manuscript under preparation (2024).
4) **Liu, Zixiao**, et al. “Immobilized Molten Salt for Selective Ammonia Separation under Joule Heating Reactor” Manuscript under preparation (2024).
5) Emily Schulman; Su Cheun Oh; **Zixiao Liu**; Limei Qiu; Aiguo Zheng; Yuxia Diao; Guangtong Xu; Asher C Leff; Dat T Tran; Dongxia Liu, Manuscrpit submitted to ChemCatChem, Aug. 2023.
6) Antara Bhowmick, Lu Liu**, Zixiao Liu**, Chen Zhang, Dongxia Liu, Protocol for preparation of electrifiable carbon membrane reactor for non-oxidative alkane dehydrogenation, Star Protocols, under revision (2024).

Bibliography

1. Shi, Y.; Ni, R.; Zhao, Y., Review on multidimensional adsorbents for CO_2 capture from ambient air: recent advances and future perspectives. *Energy & Fuels* **2023,** *37* (9), 6365-6381.
2. Yoro, K. O.; Daramola, M. O., CO_2 emission sources, greenhouse gases, and the global warming effect. In *Advances in carbon capture*, Elsevier: 2020; pp 3-28.
3. Doney, S. C.; Fabry, V. J.; Feely, R. A.; Kleypas, J. A., Ocean acidification: the other CO_2 problem. *Annual review of marine science* **2009,** *1*, 169-192.
4. Feely, R. A.; Doney, S. C.; Cooley, S. R., Ocean acidification: Present conditions and future changes in a high-CO_2 world. *Oceanography* **2009,** *22* (4), 36-47.
5. Cao, L.; Caldeira, K., Atmospheric CO_2 stabilization and ocean acidification. *Geophysical Research Letters* **2008,** *35* (19).
6. Ewing, M.; Israel, B.; Jutt, T.; Talebian, H.; Stepanik, L., Hydrogen on the path to net-zero emissions. *PEMBINA Institute: Calgary, AB, Canada* **2020**.
7. Davis, S. J.; Lewis, N. S.; Shaner, M.; Aggarwal, S.; Arent, D.; Azevedo, I. L.; Benson, S. M.; Bradley, T.; Brouwer, J.; Chiang, Y.-M., Net-zero emissions energy systems. *Science* **2018,** *360* (6396), eaas9793.
8. Falkus, M. E., The early development of the British Gas Industry, 1790-1815. *Economic History Review* **1982**, 217-234.
9. Murkin, C.; Brightling, J., Eighty years of steam reforming. *Johnson Matthey Technology Review* **2016,** *60* (4), 263-269.
10. Ajanovic, A.; Haas, R., Economic and environmental prospects for battery electric‐and fuel cell vehicles: a review. *Fuel cells* **2019,** *19* (5), 515-529.
11. Oni, A.; Anaya, K.; Giwa, T.; Di Lullo, G.; Kumar, A., Comparative assessment of blue hydrogen from steam methane reforming, autothermal reforming, and natural gas decomposition technologies for natural gas-producing regions. *Energy Conversion and Management* **2022,** *254*, 115245.
12. Sheldon, D., Methanol production‐a technical history. *Johnson Matthey Technology Review* **2017,** *61* (3), 172-182.
13. Kajaste-Rudnitskaja, R.; Hurme, M.; Oinas, P., Methanol-Managing greenhouse gas emissions in the production chain by optimizing the resource base. *Aims Energy* **2018,** *6* (6), 1074-1102.
14. Dry, M. E., The fischer–tropsch process: 1950–2000. *Catalysis today* **2002,** *71* (3-4), 227-241.
15. Stranges, A. N., A history of the fischer-tropsch synthesis in Germany 1926-45. *Studies in surface science and catalysis* **2007**, 1-27.
16. Evans, M., Unconventional hydrocarbons and the US technology revolution. *Risks, Rewards and Regulation of Unconventional Gas: A Global Perspective* **2016**, 59-91.
17. Menon, R. R., Exploration and production issues in South Asia. *Journal of Unconventional Oil and Gas Resources* **2014,** *6*, 39-47.

18. Han, D.; Jung, J.; Kwon, S., Comparative study on supervised learning models for productivity forecasting of shale reservoirs based on a data-driven approach. *Applied Sciences* **2020,** *10* (4), 1267.
19. Deublein, D.; Steinhauser, A., *Biogas from waste and renewable resources: an introduction*. John Wiley & Sons: 2011.
20. Weiland, P., Biogas production: current state and perspectives. *Applied microbiology and biotechnology* **2010,** *85*, 849-860.
21. Raboni, M.; Viotti, P.; Capodaglio, A. G., A comprehensive analysis of the current and future role of biofuels for transport in the European Union (EU). *Revista ambiente & agua* **2015,** *10*, 9-21.
22. Murray, B. C.; Galik, C. S.; Vegh, T., Biogas in the United States: estimating future production and learning from international experiences. *Mitigation and adaptation strategies for global change* **2017,** *22*, 485-501.
23. Dinh, H. N. *Overview of Clean Hydrogen Program at NREL*; National Renewable Energy Laboratory (NREL), Golden, CO (United States): 2023.
24. Chen, L.; Qi, Z.; Zhang, S.; Su, J.; Somorjai, G. A., Catalytic hydrogen production from methane: A review on recent progress and prospect. *Catalysts* **2020,** *10* (8), 858.
25. Lutz, A. E.; Bradshaw, R. W.; Keller, J. O.; Witmer, D. E., Thermodynamic analysis of hydrogen production by steam reforming. *International Journal of Hydrogen Energy* **2003,** *28* (2), 159-167.
26. Wang, S.; Nabavi, S. A.; Clough, P. T., A review on bi/polymetallic catalysts for steam methane reforming. *international journal of hydrogen energy* **2023**.
27. Zhang, H.; Sun, Z.; Hu, Y. H., Steam reforming of methane: Current states of catalyst design and process upgrading. *Renewable and Sustainable Energy Reviews* **2021,** *149*, 111330.
28. Velazquez Abad, A.; Dodds, P., Production of hydrogen. **2017**.
29. Rojas, J.; Zhai, S.; Sun, E.; Haribal, V.; Marin-Quiros, S.; Sarkar, A.; Gupta, R.; Cargnello, M.; Chueh, W.; Majumdar, A., Technoeconomics and carbon footprint of hydrogen production. *International Journal of Hydrogen Energy* **2024,** *49*, 59-74.
30. Arora, S.; Prasad, R., An overview on dry reforming of methane: strategies to reduce carbonaceous deactivation of catalysts. *RSC advances* **2016,** *6* (110), 108668-108688.
31. Pakhare, D.; Spivey, J., A review of dry (CO_2) reforming of methane over noble metal catalysts. *Chemical Society Reviews* **2014,** *43* (22), 7813-7837.
32. Yu, J.; Le, T.; Jing, D.; Stavitski, E.; Hunter, N.; Lalit, K.; Leshchev, D.; Resasco, D. E.; Sargent, E. H.; Wang, B., Balancing elementary steps enables coke-free dry reforming of methane. *Nature Communications* **2023,** *14* (1), 7514.
33. Wittich, K.; Krämer, M.; Bottke, N.; Schunk, S. A., Catalytic dry reforming of methane: insights from model systems. *ChemCatChem* **2020,** *12* (8), 2130-2147.
34. ST C, T.; Neumann, P.; Von Linde, F., The Calcor standard and Calcor economy processes. *Oil Gas European Magazine* **2001,** *45*.
35. Rostrup-Nielsen, J., Sulfur-passivated nickel catalysts for carbon-free steam reforming of methane. *Journal of Catalysis* **1984,** *85* (1), 31-43.

36. Jafarbegloo, M.; Tarlani, A.; Mesbah, A. W.; Sahebdelfar, S., Thermodynamic analysis of carbon dioxide reforming of methane and its practical relevance. *International Journal of Hydrogen Energy* **2015,** *40* (6), 2445-2451.
37. Tanios, C.; Labaki, M., Catalytic reforming: a sustainable technology for hydrogen production. In *Recent advances in renewable energy technologies*, Elsevier: 2022; pp 199-247.
38. Rahmatmand, B.; Rahimpour, M. R.; Keshavarz, P., Introducing a novel process to enhance the syngas conversion to methanol over $Cu/ZnO/Al_2O_3$ catalyst. *Fuel processing technology* **2019,** *193*, 159-179.
39. York, A. P.; Xiao, T.; Green, M. L., Brief overview of the partial oxidation of methane to synthesis gas. *Topics in Catalysis* **2003,** *22*, 345-358.
40. Vozniuk, O.; Tanchoux, N.; Millet, J.-M.; Albonetti, S.; Di Renzo, F.; Cavani, F., Spinel mixed oxides for chemical-loop reforming: from solid state to potential application. In *Studies in surface science and catalysis*, Elsevier: 2019; Vol. 178, pp 281-302.
41. Chen, Z.; Elnashaie, S. S., Development of a novel autothermal reforming process and its economics for clean hydrogen production. *Asia‐Pacific Journal of Chemical Engineering* **2006,** *1* (12), 5-12.
42. Kim, J.; Park, J.; Qi, M.; Lee, I.; Moon, I., Process integration of an autothermal reforming hydrogen production system with cryogenic air separation and carbon dioxide capture using liquefied natural gas cold energy. *Industrial & Engineering Chemistry Research* **2021,** *60* (19), 7257-7274.
43. Cloete, S.; Khan, M. N.; Amini, S., Economic assessment of membrane-assisted autothermal reforming for cost effective hydrogen production with CO_2 capture. *International Journal of Hydrogen Energy* **2019,** *44* (7), 3492-3510.
44. Chae, H. J.; Kim, J.-H.; Lee, S. C.; Kim, H.-S.; Jo, S. B.; Ryu, J.-H.; Kim, T. Y.; Lee, C. H.; Kim, S. J.; Kang, S.-H., Catalytic technologies for CO hydrogenation for the production of light hydrocarbons and middle distillates. *Catalysts* **2020,** *10* (1), 99.
45. Yu, J.; Yang, M.; Zhang, J.; Ge, Q.; Zimina, A.; Pruessmann, T.; Zheng, L.; Grunwaldt, J.-D.; Sun, J., Stabilizing Cu+ in Cu/SiO_2 catalysts with a shattuckite-like structure boosts CO_2 hydrogenation into methanol. *ACS Catalysis* **2020,** *10* (24), 14694-14706.
46. Guil-López, R.; Mota, N.; Llorente, J.; Millán, E.; Pawelec, B.; Fierro, J.; Navarro, R., Methanol synthesis from CO_2: a review of the latest developments in heterogeneous catalysis. *Materials* **2019,** *12* (23), 3902.
47. Deka, T. J.; Osman, A. I.; Baruah, D. C.; Rooney, D. W., Methanol fuel production, utilization, and techno-economy: A review. *Environmental Chemistry Letters* **2022,** *20* (6), 3525-3554.
48. Schorn, F.; Breuer, J. L.; Samsun, R. C.; Schnorbus, T.; Heuser, B.; Peters, R.; Stolten, D., Methanol as a renewable energy carrier: An assessment of production and transportation costs for selected global locations. *Advances in Applied Energy* **2021,** *3*, 100050.
49. Hamelinck, C.; Bunse, M., Carbon footprint of methanol. *Gear Up* **2022,** *67*.

50. Li, X.; Nisa, M. U.; Chen, Y.; Li, Z., Co-based catalysts supported on silica and carbon materials: effect of support property on cobalt species and Fischer–Tropsch synthesis performance. *Industrial & Engineering Chemistry Research* **2019,** *58* (8), 3459-3467.
51. Okoye-Chine, C.; Mbuya, C.; Ntelane, T.; Moyo, M.; Hildebrandt, D., The effect of silanol groups on the metal-support interactions in silica-supported cobalt Fischer-Tropsch catalysts. A temperature programmed surface reaction. *Journal of Catalysis* **2020,** *381*, 121-129.
52. Iglesia, E., Design, synthesis, and use of cobalt-based Fischer-Tropsch synthesis catalysts. *Applied Catalysis A: General* **1997,** *161* (1-2), 59-78.
53. Somorjai, G. A., Surface science and catalysis. *Science* **1985,** *227* (4689), 902-908.
54. Xu, H.; Li, M.; Nawaz, M. A.; Liu, D., Doping of K and Zn elements in FeZr-Ni/ZSM-5: Highly selective catalyst for syngas to aromatics. *Catalysis Communications* **2019,** *121*, 95-99.
55. Suib, S. L., *New and future developments in catalysis: Catalysis for remediation and environmental concerns*. Newnes: 2013.
56. Liu, B.; Li, W.; Zheng, J.; Lin, Q.; Zhang, X.; Zhang, J.; Jiang, F.; Xu, Y.; Liu, X., CO_2 formation mechanism in Fischer–Tropsch synthesis over iron-based catalysts: a combined experimental and theoretical study. *Catalysis Science & Technology* **2018,** *8* (20), 5288-5301.
57. Cheng, Y.; Lin, J.; Xu, K.; Wang, H.; Yao, X.; Pei, Y.; Yan, S.; Qiao, M.; Zong, B., Fischer–Tropsch synthesis to lower olefins over potassium-promoted reduced graphene oxide supported iron catalysts. *ACS catalysis* **2016,** *6* (1), 389-399.
58. Amenomiya, Y.; Birss, V. I.; Goledzinowski, M.; Galuszka, J.; Sanger, A. R., Conversion of methane by oxidative coupling. *Catalysis Reviews—Science and Engineering* **1990,** *32* (3), 163-227.
59. Keller, G.; Bhasin, M., Synthesis of ethylene via oxidative coupling of methane: I. Determination of active catalysts. *Journal of Catalysis* **1982,** *73* (1), 9-19.
60. Tiyatha, W.; Chukeaw, T.; Sringam, S.; Witoon, T.; Chareonpanich, M.; Rupprechter, G.; Seubsai, A., Oxidative coupling of methane: comparisons of $MnTiO_3$–Na_2WO_4 and $MnOx$–TiO_2–Na_2WO_4 catalysts on different silica supports. *Scientific Reports* **2022,** *12* (1), 2595.
61. Farrell, B. L.; Linic, S., Oxidative coupling of methane over mixed oxide catalysts designed for solid oxide membrane reactors. *Catalysis Science & Technology* **2016,** *6* (12), 4370-4376.
62. Gambo, Y.; Jalil, A.; Triwahyono, S.; Abdulrasheed, A., Recent advances and future prospect in catalysts for oxidative coupling of methane to ethylene: A review. *Journal of industrial and engineering chemistry* **2018,** *59*, 218-229.
63. Godini, H. R.; Azadi, M.; Khadivi, M.; Gharibi, A.; Jazayeri, S. M.; Salerno, D.; Penteado, A.; Mokhtarani, B.; Orjuela, A.; Karsten, T., Conceptual Process Design and Economic Analysis of Oxidative Coupling of Methane. In *Computer Aided Chemical Engineering*, Elsevier: 2018; Vol. 44, pp 361-366.

64. Karakaya, C.; Zhu, H.; Loebick, C.; Weissman, J. G.; Kee, R. J., A detailed reaction mechanism for oxidative coupling of methane over $Mn/Na_2WO_4/SiO_2$ catalyst for non-isothermal conditions. *Catalysis Today* **2018,** *312*, 10-22.
65. Smith, K. J.; Galuszka, J., Effect of carbon dioxide on methane oxidative coupling kinetics. *Industrial & engineering chemistry research* **1994,** *33* (1), 14-20.
66. Wang, H.; Shao, C.; Gascon, J.; Takanabe, K.; Sarathy, S. M., Noncatalytic oxidative coupling of methane (OCM): Gas-phase reactions in a jet stirred reactor (JSR). *ACS omega* **2021,** *6* (49), 33757-33768.
67. Liu, S.; Udyavara, S.; Zhang, C.; Peter, M.; Lohr, T. L.; Dravid, V. P.; Neurock, M.; Marks, T. J., "Soft" oxidative coupling of methane to ethylene: Mechanistic insights from combined experiment and theory. *Proceedings of the National Academy of Sciences* **2021,** *118* (23), e2012666118.
68. Lunsford, J. H., Catalytic conversion of methane to more useful chemicals and fuels: a challenge for the 21st century. *Catalysis today* **2000,** *63* (2-4), 165-174.
69. Wolf, E. E., *Methane conversion by oxidative processes: fundamental and engineering aspects*. Springer: 1992; Vol. 85.
70. Zavyalova, U.; Holena, M.; Schlögl, R.; Baerns, M., Statistical analysis of past catalytic data on oxidative methane coupling for new insights into the composition of high‐performance catalysts. *ChemCatChem* **2011,** *3* (12), 1935-1947.
71. Cruellas, A.; Bakker, J.; van Sint Annaland, M.; Medrano, J.; Gallucci, F., Techno-economic analysis of oxidative coupling of methane: Current state of the art and future perspectives. *Energy Conversion and Management* **2019,** *198*, 111789.
72. Zhang, K.; Sun, S.; Huang, K., Oxidative coupling of methane (OCM) conversion into C_2 products through a CO_2/O_2 co-transport membrane reactor. *Journal of Membrane Science* **2022,** *661*, 120915.
73. Matus, E.; Sukhova, O.; Ismagilov, I.; Zaikovskii, V.; Kerzhentsev, M.; Ismagilov, Z.; Dosumov, K.; Mustafin, A., Deactivation and regeneration of Mo/ZSM-5 catalysts for methane dehydroaromatization. *Eurasian Chemico-Technological Journal* **2010,** *12* (1), 1-8.
74. Tempelman, C. H.; Hensen, E. J., On the deactivation of Mo/HZSM-5 in the methane dehydroaromatization reaction. *Applied Catalysis B: Environmental* **2015,** *176*, 731-739.
75. Lua, A. C.; Wang, H. Y., Decomposition of methane over unsupported porous nickel and alloy catalyst. *Applied Catalysis B: Environmental* **2013,** *132*, 469-478.
76. Zeng, J. Catalytic Methane Pyrolysis in Complex Liquid and Gas Phase Systems. University of California, Santa Barbara, 2021.
77. Hamdani, I. R.; Ahmad, A.; Chulliyil, H. M.; Srinivasakannan, C.; Shoaibi, A. A.; Hossain, M. M., Thermocatalytic decomposition of methane: a review on carbon-based catalysts. *ACS omega* **2023,** *8* (32), 28945-28967.
78. Keipi, T.; Tolvanen, H.; Konttinen, J., Economic analysis of hydrogen production by methane thermal decomposition: Comparison to competing technologies. *Energy Conversion and Management* **2018,** *159*, 264-273.

79. Kosinov, N.; Hensen, E. J., Reactivity, selectivity, and stability of zeolite‐based catalysts for methane dehydroaromatization. *Advanced Materials* **2020,** *32* (44), 2002565.
80. Linstorm, P., NIST chemistry webbook, NIST standard reference database number 69. *J. Phys. Chem. Ref. Data, Monograph* **1998,** *9*, 1-1951.
81. Zhang, Z.-G., Process, reactor and catalyst design: Towards application of direct conversion of methane to aromatics under nonoxidative conditions. *Carbon Resources Conversion* **2019,** *2* (3), 157-174.
82. Cheng, S.; Oh, S. C.; Sakbodin, M.; Qiu, L.; Diao, Y.; Liu, D., Understanding the impact of hydrogen activation by SrCe0. 8Zr0. 2O3− δ perovskite membrane material on direct non-oxidative methane conversion. *Frontiers in Chemistry* **2022,** *9*, 806464.
83. Oh, S. C.; Sakbodin, M.; Liu, D., Direct non-oxidative methane conversion in membrane reactor. In *Catalysis*, 2019; pp 127-165.
84. Sakbodin, M.; Schulman, E.; Cheng, S.; Huang, Y. L.; Pan, Y.; Albertus, P.; Wachsman, E. D.; Liu, D., Direct Nonoxidative Methane Conversion in an Autothermal Hydrogen‐Permeable Membrane Reactor. *Advanced Energy Materials* **2021,** *11* (46), 2102782.
85. Sakbodin, M.; Wu, Y.; Oh, S. C.; Wachsman, E. D.; Liu, D., Hydrogen‐permeable tubular membrane reactor: Promoting conversion and product selectivity for non‐oxidative activation of methane over an Fe©SiO_2 catalyst. *Angewandte Chemie* **2016,** *128* (52), 16383-16386.
86. Guo, X.; Fang, G.; Li, G.; Ma, H.; Fan, H.; Yu, L.; Ma, C.; Wu, X.; Deng, D.; Wei, M., Direct, nonoxidative conversion of methane to ethylene, aromatics, and hydrogen. *science* **2014,** *344* (6184), 616-619.
87. Lin, T.; An, Y.; Yu, F.; Gong, K.; Yu, H.; Wang, C.; Sun, Y.; Zhong, L., Advances in selectivity control for Fischer–Tropsch synthesis to fuels and chemicals with high carbon efficiency. *ACS Catalysis* **2022,** *12* (19), 12092-12112.
88. Pérez, B. J. L.; Jiménez, J. A. M.; Bhardwaj, R.; Goetheer, E.; van Sint Annaland, M.; Gallucci, F., Methane pyrolysis in a molten gallium bubble column reactor for sustainable hydrogen production: Proof of concept & techno-economic assessment. *international journal of hydrogen energy* **2021,** *46* (7), 4917-4935.
89. Bone, W. A.; Coward, H. F., CXVII.—The thermal decomposition of hydrocarbons. Part I.[Methane, ethane, ethylene, and acetylene.]. *Journal of the Chemical Society, Transactions* **1908,** *93*, 1197-1225.
90. Jones, C. W. H., LXI.—The decomposition of methane. Part I. *Journal of the Chemical Society (Resumed)* **1929**, 419-422.
91. Kassel, L. S., The thermal decomposition of methane1. *Journal of the American Chemical Society* **1932,** *54* (10), 3949-3961.
92. Stanley, H.; Nash, A., Higher Hydrocarbons from Methane. *Nature* **1928,** *122* (3080), 725-725.
93. Wheeler, R., Higher hydrocarbons from methane. *Nature* **1928,** *122* (3081), 773-773.

94. Slater, W. E., XV.—The influence of different surfaces on the decomposition of methane. *Journal of the Chemical Society, Transactions* **1916,** *109*, 160-164.
95. Yamaguti, B., THE CATALYSIS OF NICKEL ON THE THERMAL DECOMPOSITION OF METHANE. *Bulletin of the Chemical Society of Japan* **1927,** *2* (11), 289-294.
96. Holliday, G.; Exell, H., CXLI.—The thermal decomposition of methane. Part I. Decomposition in silica bulbs. *Journal of the Chemical Society (Resumed)* **1929**, 1066-1074.
97. Cantelo, R., The thermal decomposition of methane. *The Journal of Physical Chemistry* **2002,** *28* (10), 1036-1048.
98. Wang, Z.; Navarrete, J., production of carbon nanotubes and hydrogen catalyzed with Ni/MCM-41 catalysts. *Green and Sustainable Chemistry* **2012,** *2* (3), 91-96.
99. Awadallah, A. E.; El-Desouki, D. S.; Aboul-Gheit, N. A.; Ibrahim, A. H.; Aboul-Gheit, A. K., Effect of crystalline structure and pore geometry of silica based supported materials on the catalytic behavior of metallic nickel particles during methane decomposition to COx-free hydrogen and carbon nanomaterials. *International Journal of Hydrogen Energy* **2016,** *41* (38), 16890-16902.
100. García-Sancho, C.; Guil-López, R.; Pascual, L.; Maireles-Torres, P.; Navarro, R.; Fierro, J., Optimization of nickel loading of mixed oxide catalyst ex-hydrotalcite for H2 production by methane decomposition. *Applied Catalysis A: General* **2017,** *548*, 71-82.
101. Bai, Z.; Chen, H.; Li, B.; Li, W., Methane decomposition over Ni loaded activated carbon for hydrogen production and the formation of filamentous carbon. *International journal of hydrogen energy* **2007,** *32* (1), 32-37.
102. Pudukudy, M.; Yaakob, Z.; Kadier, A.; Takriff, M. S.; Hassan, N. S. M., One-pot sol–gel synthesis of Ni/TiO_2 catalysts for methane decomposition into COx free hydrogen and multiwalled carbon nanotubes. *international journal of hydrogen energy* **2017,** *42* (26), 16495-16513.
103. Pudukudy, M.; Yaakob, Z.; Jia, Q.; Takriff, M. S., Catalytic decomposition of undiluted methane into hydrogen and carbon nanotubes over Pt promoted Ni/CeO_2 catalysts. *New Journal of Chemistry* **2018,** *42* (18), 14843-14856.
104. Abdullahi, I.; Sakulchaicharoen, N.; Herrera, J. E., A mechanistic study on the growth of multi-walled carbon nanotubes by methane decomposition over nickel–alumina catalyst. *Diamond and Related Materials* **2012,** *23*, 76-82.
105. Wen, Y.; Wei, C.; JIANG, C.; Jie, W.; Wenjing, S., Cerium oxide promoted Ni/MgO catalyst for the synthesis of multi-walled carbon nanotubes. *Chinese Journal of Catalysis* **2011,** *32* (6-8), 1323-1328.
106. Awadallah, A. E.; Mostafa, M. S.; Aboul-Enein, A. A.; Hanafi, S. A., Hydrogen production via methane decomposition over Al_2O_3–TiO_2 binary oxides supported Ni catalysts: Effect of Ti content on the catalytic efficiency. *Fuel* **2014,** *129*, 68-77.
107. Pudukudy, M.; Yaakob, Z., Methane decomposition over Ni, Co and Fe based monometallic catalysts supported on sol gel derived SiO_2 microflakes. *Chemical Engineering Journal* **2015,** *262*, 1009-1021.

108. Choudhary, V. R.; Banerjee, S.; Rajput, A. M., Continuous production of H2 at low temperature from methane decomposition over Ni-containing catalyst followed by gasification by steam of the carbon on the catalyst in two parallel reactors operated in cyclic manner. *Journal of catalysis* **2001,** *198* (1), 136-141.
109. Reshetenko, T.; Avdeeva, L.; Ismagilov, Z.; Chuvilin, A.; Fenelonov, V., Catalytic filamentous carbons-supported Ni for low-temperature methane decomposition. *Catalysis Today* **2005,** *102*, 115-120.
110. Yang, H.; Whitten, J. L., Dissociative chemisorption of CH_4 on Ni (111). *The Journal of chemical physics* **1992,** *96* (7), 5529-5537.
111. Zhou, L.; Enakonda, L. R.; Harb, M.; Saih, Y.; Aguilar-Tapia, A.; Ould-Chikh, S.; Hazemann, J.-l.; Li, J.; Wei, N.; Gary, D., Fe catalysts for methane decomposition to produce hydrogen and carbon nano materials. *Applied catalysis B: environmental* **2017,** *208*, 44-59.
112. Zhou, L.; Enakonda, L. R.; Saih, Y.; Loptain, S.; Gary, D.; Del‐Gallo, P.; Basset, J. M., Catalytic methane decomposition over Fe‐Al_2O_3. *ChemSusChem* **2016,** *9* (11), 1243-1248.
113. Takenaka, S.; Serizawa, M.; Otsuka, K., Formation of filamentous carbons over supported Fe catalysts through methane decomposition. *Journal of Catalysis* **2004,** *222* (2), 520-531.
114. Silva, R. R.; Oliveira, H. A.; Guarino, A. C.; Toledo, B. B.; Moura, M. B.; Oliveira, B. T.; Passos, F. B., Effect of support on methane decomposition for hydrogen production over cobalt catalysts. *International Journal of Hydrogen Energy* **2016,** *41* (16), 6763-6772.
115. Al Mesfer, M. K.; Danish, M.; Shah, M., Synthesis, evaluation, and kinetic assessment of Co‐based catalyst for enhanced methane decomposition reaction for hydrogen production. *International Journal of Chemical Kinetics* **2022,** *54* (2), 90-103.
116. Takenaka, S.; Ishida, M.; Serizawa, M.; Tanabe, E.; Otsuka, K., Formation of carbon nanofibers and carbon nanotubes through methane decomposition over supported cobalt catalysts. *The Journal of Physical Chemistry B* **2004,** *108* (31), 11464-11472.
117. Ogihara, H.; Takenaka, S.; Yamanaka, I.; Tanabe, E.; Genseki, A.; Otsuka, K., Formation of highly concentrated hydrogen through methane decomposition over Pd-based alloy catalysts. *Journal of Catalysis* **2006,** *238* (2), 353-360.
118. Takenaka, S.; Shigeta, Y.; Tanabe, E.; Otsuka, K., Methane decomposition into hydrogen and carbon nanofibers over supported Pd–Ni catalysts. *Journal of Catalysis* **2003,** *220* (2), 468-477.
119. Pudukudy, M.; Yaakob, Z.; Akmal, Z. S., Direct decomposition of methane over Pd promoted Ni/SBA-15 catalysts. *Applied Surface Science* **2015,** *353*, 127-136.
120. Nuernberg, G. D. B.; Fajardo, H. V.; Foletto, E. L.; Hickel-Probst, S. M.; Carreño, N. L.; Probst, L. F.; Barrault, J., Methane conversion to hydrogen and nanotubes on Pt/Ni catalysts supported over spinel MgAl2O4. *Catalysis today* **2011,** *176* (1), 465-469.
121. Khalifeh, O.; Taghvaei, H.; Mosallanejad, A.; Rahimpour, M. R.; Shariati, A., Extra pure hydrogen production through methane decomposition using

nanosecond pulsed plasma and Pt–Re catalyst. *Chemical Engineering Journal* **2016,** *294*, 132-145.
122. Kutteri, D. A.; Wang, I.-W.; Samanta, A.; Li, L.; Hu, J., Methane decomposition to tip and base grown carbon nanotubes and CO x-free H 2 over mono-and bimetallic 3d transition metal catalysts. *Catalysis Science & Technology* **2018,** *8* (3), 858-869.
123. 浅井宏太; 永易圭行; 高根孝仁; 岩本伸司; 矢ヶ崎えり子; 石井憲一; 井上正志, 高温領域における Ni 触媒上でのメタン分解反応の機構. *Journal of the Japan Petroleum Institute* **2008,** *51* (1), 42-49.
124. Qian, J. X.; Chen, T. W.; Enakonda, L. R.; Liu, D. B.; Mignani, G.; Basset, J.-M.; Zhou, L., Methane decomposition to produce COx-free hydrogen and nano-carbon over metal catalysts: A review. *International Journal of Hydrogen Energy* **2020,** *45* (15), 7981-8001.
125. Li, Y.; Li, D.; Wang, G., Methane decomposition to COx-free hydrogen and nano-carbon material on group 8–10 base metal catalysts: a review. *Catalysis today* **2011,** *162* (1), 1-48.
126. Wang, P.; Zhu, H.; Huang, M.; Wan, C.; Li, D.; Jiang, L., Catalytic methane decomposition to hydrogen and carbon over hydrotalcite‐derivative composition‐uniform and sintering‐resistant Ni‐Fe/Al2O3 alloy catalysts. *International Journal of Energy Research* **2022,** *46* (12), 16810-16822.
127. Takenaka, S.; Ogihara, H.; Yamanaka, I.; Otsuka, K., Decomposition of methane over supported-Ni catalysts: effects of the supports on the catalytic lifetime. *Applied Catalysis A: General* **2001,** *217* (1-2), 101-110.
128. Liang, W.; Yan, H.; Chen, C.; Lin, D.; Tan, K.; Feng, X.; Liu, Y.; Chen, X.; Yang, C.; Shan, H., Revealing the effect of nickel particle size on carbon formation type in the methane decomposition reaction. *Catalysts* **2020,** *10* (8), 890.
129. Chen, D.; Christensen, K. O.; Ochoa-Fernández, E.; Yu, Z.; Tøtdal, B.; Latorre, N.; Monzón, A.; Holmen, A., Synthesis of carbon nanofibers: effects of Ni crystal size during methane decomposition. *Journal of Catalysis* **2005,** *229* (1), 82-96.
130. Al-Fatesh, A. S.; Kasim, S. O.; Ibrahim, A. A.; Al-Awadi, A. S.; Abasaeed, A. E.; Fakeeha, A. H.; Awadallah, A. E., Catalytic methane decomposition over ZrO2 supported iron catalysts: Effect of WO3 and La2O3 addition on catalytic activity and stability. *Renewable Energy* **2020,** *155*, 969-978.
131. Serban, M.; Lewis, M. A.; Marshall, C. L.; Doctor, R. D., Hydrogen production by direct contact pyrolysis of natural gas. *Energy & fuels* **2003,** *17* (3), 705-713.
132. Plevan, M.; Geißler, T.; Abánades, A.; Mehravaran, K.; Rathnam, R. K.; Rubbia, C.; Salmieri, D.; Stoppel, L.; Stückrad, S.; Wetzel, T., Thermal cracking of methane in a liquid metal bubble column reactor: Experiments and kinetic analysis. *International Journal of Hydrogen Energy* **2015,** *40* (25), 8020-8033.
133. Geißler, T.; Plevan, M.; Abánades, A.; Heinzel, A.; Mehravaran, K.; Rathnam, R. K.; Rubbia, C.; Salmieri, D.; Stoppel, L.; Stückrad, S., Experimental investigation and thermo-chemical modeling of methane pyrolysis in a liquid

metal bubble column reactor with a packed bed. *International Journal of Hydrogen Energy* **2015,** *40* (41), 14134-14146.
134. Wang, K.; Li, W.; Zhou, X., Hydrogen generation by direct decomposition of hydrocarbons over molten magnesium. *Journal of Molecular Catalysis A: Chemical* **2008,** *283* (1-2), 153-157.
135. Upham, D. C.; Agarwal, V.; Khechfe, A.; Snodgrass, Z. R.; Gordon, M. J.; Metiu, H.; McFarland, E. W., Catalytic molten metals for the direct conversion of methane to hydrogen and separable carbon. *Science* **2017,** *358* (6365), 917-921.
136. Kim, J.; Oh, C.; Oh, H.; Lee, Y.; Seo, H.; Kim, Y. K., Catalytic methane pyrolysis for simultaneous production of hydrogen and graphitic carbon using a ceramic sparger in a molten NiSn alloy. *Carbon* **2023,** *207*, 1-12.
137. Zaghloul, N.; Kodama, S.; Sekiguchi, H., Hydrogen Production by Methane Pyrolysis in a Molten‐Metal Bubble Column. *Chemical Engineering & Technology* **2021,** *44* (11), 1986-1993.
138. Chen, L.; Song, Z.; Zhang, S.; Chang, C.-K.; Chuang, Y.-C.; Peng, X.; Dun, C.; Urban, J. J.; Guo, J.; Chen, J.-L., Ternary NiMo-Bi liquid alloy catalyst for efficient hydrogen production from methane pyrolysis. *Science* **2023,** *381* (6660), 857-861.
139. Palmer, C.; Tarazkar, M.; Kristoffersen, H. H.; Gelinas, J.; Gordon, M. J.; McFarland, E. W.; Metiu, H., Methane pyrolysis with a molten Cu–Bi alloy catalyst. *Acs Catalysis* **2019,** *9* (9), 8337-8345.
140. Kang, D.; Rahimi, N.; Gordon, M. J.; Metiu, H.; McFarland, E. W., Catalytic methane pyrolysis in molten MnCl2-KCl. *Applied Catalysis B: Environmental* **2019,** *254*, 659-666.
141. Kang, D.; Palmer, C.; Mannini, D.; Rahimi, N.; Gordon, M. J.; Metiu, H.; McFarland, E. W., Catalytic methane pyrolysis in molten alkali chloride salts containing iron. *Acs Catalysis* **2020,** *10* (13), 7032-7042.
142. Zeng, J.; Tarazkar, M.; Pennebaker, T.; Gordon, M. J.; Metiu, H.; McFarland, E. W., Catalytic methane pyrolysis with liquid and vapor phase tellurium. *Acs Catalysis* **2020,** *10* (15), 8223-8230.
143. Rahimi, N.; Kang, D.; Gelinas, J.; Menon, A.; Gordon, M. J.; Metiu, H.; McFarland, E. W., Solid carbon production and recovery from high temperature methane pyrolysis in bubble columns containing molten metals and molten salts. *Carbon* **2019,** *151*, 181-191.
144. Kubokawa, M., The decomposition of methane on the surface of platinum [I]. *The Review of Physical Chemistry of Japan* **1937,** *11* (2), 82-106.
145. Belchetz, L.; Rideal, E. K., The Primary Decomposition of Hydrocarbon Vapors on Carbon Filaments. *Journal of the American Chemical Society* **1935,** *57* (7), 1168-1174.
146. Storch, H., The thermal decomposition of methane by a carbon filament1. *Journal of the American Chemical Society* **1932,** *54* (11), 4188-4198.
147. Kubokawa, M., The decomposition of methane on reduced nickel. *The Review of Physical Chemistry of Japan* **1938,** *12* (2), 90-104.

148. Belgued, M.; Pareja, P.; Amariglio, A.; Amariglio, H., Conversion of methane into higher hydrocarbons on platinum. *Nature* **1991,** *352* (6338), 789-790.
149. Gerceker, D.; Motagamwala, A. H.; Rivera-Dones, K. R.; Miller, J. B.; Huber, G. W.; Mavrikakis, M.; Dumesic, J. A., Methane conversion to ethylene and aromatics on PtSn catalysts. *ACS Catalysis* **2017,** *7* (3), 2088-2100.
150. Xiao, Y.; Varma, A., Highly selective nonoxidative coupling of methane over Pt-Bi bimetallic catalysts. *ACS Catalysis* **2018,** *8* (4), 2735-2740.
151. Dipu, A. L.; Ohbuchi, S.; Nishikawa, Y.; Iguchi, S.; Ogihara, H.; Yamanaka, I., Direct nonoxidative conversion of methane to higher hydrocarbons over silica-supported nickel phosphide catalyst. *ACS Catalysis* **2019,** *10* (1), 375-379.
152. Dutta, K.; Li, L.; Gupta, P.; Gutierrez, D. P.; Kopyscinski, J., Direct non-oxidative methane aromatization over gallium nitride catalyst in a continuous flow reactor. *Catalysis Communications* **2018,** *106*, 16-19.
153. Li, Z.; Xiao, Y.; Chowdhury, P. R.; Wu, Z.; Ma, T.; Chen, J. Z.; Wan, G.; Kim, T.-H.; Jing, D.; He, P., Direct methane activation by atomically thin platinum nanolayers on two-dimensional metal carbides. *Nature Catalysis* **2021,** *4* (10), 882-891.
154. Wang, L.; Tao, L.; Xie, M.; Xu, G.; Huang, J.; Xu, Y., Dehydrogenation and aromatization of methane under non-oxidizing conditions. *Catalysis Letters* **1993,** *21*, 35-41.
155. Wang, L.; Xu, Y.; Xie, M.; Liu, S.; Tao, L.; Xu, G., Activation and aromatization of methane and ethane overMo (VI)/HZSM-5 and W (VI)/HZSM-5 zeolites catalysts. In *Studies in Surface Science and Catalysis*, Elsevier: 1995; Vol. 94, pp 495-500.
156. Wang, D.; Lunsford, J. H.; Rosynek, M. P., Characterization of a Mo/ZSM-5 catalyst for the conversion of methane to benzene. *Journal of Catalysis* **1997,** *169* (1), 347-358.
157. Weckhuysen, B. M.; Wang, D.; Rosynek, M. P.; Lunsford, J. H., Conversion of methane to benzene over transition metal ion ZSM-5 zeolites: I. Catalytic characterization. *Journal of catalysis* **1998,** *175* (2), 338-346.
158. Kosinov, N.; Wijpkema, A. S.; Uslamin, E.; Rohling, R.; Coumans, F. J.; Mezari, B.; Parastaev, A.; Poryvaev, A. S.; Fedin, M. V.; Pidko, E. A., Confined carbon mediating dehydroaromatization of methane over Mo/ZSM‐5. *Angewandte Chemie International Edition* **2018,** *57* (4), 1016-1020.
159. Razdan, N. K.; Bhan, A., Carbidic Mo is the sole kinetically-relevant active site for catalytic methane dehydroaromatization on Mo/H-ZSM-5. *Journal of Catalysis* **2020,** *389*, 667-676.
160. López-Martín, A.; Sini, M.; Cutrufello, M.; Caballero, A.; Colón, G., Characterization of Re-Mo/ZSM-5 catalysts: How Re improves the performance of Mo in the methane dehydroaromatization reaction. *Applied Catalysis B: Environmental* **2022,** *304*, 120960.
161. Gu, Y.; Chen, P.; Yan, H.; Wang, X.; Lyu, Y.; Tian, Y.; Liu, W.; Yan, Z.; Liu, X., Coking mechanism of Mo/ZSM-5 catalyst in methane dehydroaromatization. *Applied Catalysis A: General* **2021,** *613*, 118019.

162. Rahman, M.; Infantes-Molina, A.; Hoffman, A. S.; Bare, S. R.; Emerson, K. L.; Khatib, S. J., Effect of Si/Al ratio of ZSM-5 support on structure and activity of Mo species in methane dehydroaromatization. *Fuel* **2020,** *278*, 118290.
163. Liu, Y.; Coza, M.; Drozhzhin, V.; van den Bosch, Y.; Meng, L.; van de Poll, R.; Hensen, E. J.; Kosinov, N., Transition-metal catalysts for methane dehydroaromatization (Mo, Re, Fe): activity, stability, active sites, and carbon deposits. *ACS Catalysis* **2022,** *13* (1), 1-10.
164. Lai, Y.; Veser, G., Zn‐HZSM‐5 catalysts for methane dehydroaromatization. *Environmental Progress & Sustainable Energy* **2016,** *35* (2), 334-344.
165. Abdelsayed, V.; Smith, M. W.; Shekhawat, D., Investigation of the stability of Zn-based HZSM-5 catalysts for methane dehydroaromatization. *Applied Catalysis A: General* **2015,** *505*, 365-374.
166. Tan, P., Active phase, catalytic activity, and induction period of Fe/zeolite material in nonoxidative aromatization of methane. *Journal of Catalysis* **2016,** *338*, 21-29.
167. Zeng, J. L.; Xiong, Z. T.; Zhang, H. B.; Lin, G. D.; Tsai, K., Nonoxidative dehydrogenation and aromatization of methane over W/HZSM‐5‐based catalysts. *Catalysis letters* **1998,** *53*, 119-124.
168. Liu, Y.; Zhang, H.; Wijpkema, A. S.; Coumans, F. J.; Meng, L.; Uslamin, E. A.; Longo, A.; Hensen, E. J.; Kosinov, N., Understanding the Preparation and Reactivity of Mo/ZSM‐5 Methane Dehydroaromatization Catalysts. *Chemistry‐A European Journal* **2022,** *28* (5), e202103894.
169. Lezcano‐González, I.; Oord, R.; Rovezzi, M.; Glatzel, P.; Botchway, S. W.; Weckhuysen, B. M.; Beale, A. M., Molybdenum speciation and its impact on catalytic activity during methane dehydroaromatization in zeolite ZSM‐5 as revealed by operando X‐ray methods. *Angewandte Chemie* **2016,** *128* (17), 5301-5305.
170. Xie, P.; Pu, T.; Nie, A.; Hwang, S.; Purdy, S. C.; Yu, W.; Su, D.; Miller, J. T.; Wang, C., Nanoceria-supported single-atom platinum catalysts for direct methane conversion. *Acs Catalysis* **2018,** *8* (5), 4044-4048.
171. Soulivong, D.; Norsic, S.; Taoufik, M.; Coperet, C.; Thivolle-Cazat, J.; Chakka, S.; Basset, J.-M., Non-Oxidative Coupling Reaction of Methane to Ethane and Hydrogen Catalyzed by the Silica-Supported Tantalum Hydride:(· SiO) 2Ta− H. *Journal of the American Chemical Society* **2008,** *130* (15), 5044-5045.
172. Šot, P.; Newton, M. A.; Baabe, D.; Walter, M. D.; van Bavel, A. P.; Horton, A. D.; Copéret, C.; van Bokhoven, J. A., Non‐oxidative methane coupling over silica versus silica‐supported iron (II) single sites. *Chemistry‐A European Journal* **2020,** *26* (36), 8012-8016.
173. Huang, X.; Eggart, D.; Qin, G.; Sarma, B. B.; Gaur, A.; Yang, J.; Pan, Y.; Li, M.; Hao, J.; Yu, H., Methyl radical chemistry in non-oxidative methane activation over metal single sites. *Nature Communications* **2023,** *14* (1), 5716.

174. Gao, J.; Zheng, Y.; Jehng, J.-M.; Tang, Y.; Wachs, I. E.; Podkolzin, S. G., Identification of molybdenum oxide nanostructures on zeolites for natural gas conversion. *Science* **2015,** *348* (6235), 686-690.
175. Li, T.-H.; Yan, M.; Liu, Y.; Huang, Z.-Q.; Chang, C.-R.; Li, J., Cooperative Catalysis by Multiple Active Centers in Nonoxidative Conversion of Methane. *The Journal of Physical Chemistry C* **2020,** *124* (25), 13656-13663.
176. Liu, Y.; Liu, J. C.; Li, T. H.; Duan, Z. H.; Zhang, T. Y.; Yan, M.; Li, W. L.; Xiao, H.; Wang, Y. G.; Chang, C. R., Unravelling the enigma of nonoxidative conversion of methane on iron single‐atom catalysts. *Angewandte Chemie* **2020,** *132* (42), 18745-18749.
177. Kim, S. K.; Kim, H. W.; Han, S. J.; Lee, S. W.; Shin, J.; Kim, Y. T., Mechanistic and microkinetic study of non-oxidative methane coupling on a single-atom iron catalyst. *Communications Chemistry* **2020,** *3* (1), 58.
178. Postma, R. S.; Lefferts, L., Effect of ethane and ethylene on catalytic non oxidative coupling of methane. *Reaction Chemistry & Engineering* **2021,** *6* (12), 2425-2433.
179. Hao, J.; Schwach, P.; Li, L.; Guo, X.; Weng, J.; Zhang, H.; Shen, H.; Fang, G.; Huang, X.; Pan, X., Direct experimental detection of hydrogen radicals in non-oxidative methane catalytic reaction. *Journal of Energy Chemistry* **2021,** *52*, 372-376.
180. Postma, R. S.; Lefferts, L., Influence of axial temperature profiles on Fe/SiO2 catalyzed non‐oxidative coupling of methane. *ChemCatChem* **2021,** *13* (4), 1157-1160.
181. Puente‐Urbina, A.; Pan, Z.; Paunović, V.; Šot, P.; Hemberger, P.; van Bokhoven, J. A., Direct Evidence on the Mechanism of Methane Conversion under Non‐oxidative Conditions over Iron‐modified Silica: The Role of Propargyl Radicals Unveiled. *Angewandte Chemie* **2021,** *133* (45), 24204-24209.
182. Postma, R.; Mendes, P.; Pirro, L.; Banerjee, A.; Thybaut, J.; Lefferts, L., Modelling of the catalytic initiation of methane coupling under non-oxidative conditions. *Chemical Engineering Journal* **2023,** *454*, 140273.
183. Oh, S. C.; Cheng, S.; Pan, Y.; Schulman, E.; Liu, D., Multifunctional Reactors for Direct Nonoxidative Methane Conversion. In *Direct Natural Gas Conversion to Value-Added Chemicals*, CRC Press: 2020; pp 305-330.
184. Oh, S. C.; Schulman, E.; Zhang, J.; Fan, J.; Pan, Y.; Meng, J.; Liu, D., Direct non‐oxidative methane conversion in a millisecond catalytic wall reactor. *Angewandte Chemie International Edition* **2019,** *58* (21), 7083-7086.
185. Huang, K.; Miller, J. B.; Huber, G. W.; Dumesic, J. A.; Maravelias, C. T., A general framework for the evaluation of direct nonoxidative methane conversion strategies. *Joule* **2018,** *2* (2), 349-365.
186. Huang, K.; Maravelias, C. T., Synthesis and analysis of nonoxidative methane aromatization strategies. *Energy Technology* **2020,** *8* (8), 1900650.
187. Kim, H. W.; Lee, S. W.; Na, G. S.; Han, S. J.; Kim, S. K.; Shin, J. H.; Chang, H.; Kim, Y. T., Reaction condition optimization for non-oxidative conversion of

methane using artificial intelligence. *Reaction Chemistry & Engineering* **2021,** *6* (2), 235-243.
188. Han, S. J.; Lee, S. W.; Kim, H. W.; Kim, S. K.; Kim, Y. T., Nonoxidative direct conversion of methane on silica-based iron catalysts: effect of catalytic surface. *ACS Catalysis* **2019,** *9* (9), 7984-7997.
189. Han, S. J.; Gebreyohannes, T. G.; Kim, S. K.; Kim, H. W.; Shin, J.; Kim, Y. T., Methane direct conversion to olefins, aromatics, and hydrogen over silica entrapped bimetallic MeFe-SiO2 (Me= Co, Ni, Pd, Pt) catalysts. *Molecular Catalysis* **2023,** *535*, 112864.
190. Liu, H.-X.; Ban, T.; Yu, X.-Y.; Huang, Z.-Q.; Chang, C.-R., Silica-Confined Two-Atom Single-Cluster Catalyst for Direct Nonoxidative Conversion of Methane: A DFT Study. *The Journal of Physical Chemistry C* **2021,** *125* (42), 23212-23218.
191. He, S.-Y.; Li, T.-H.; Huang, Z.-Q.; Liu, Y.; Li, J.; Chang, C.-R., Screening silica-confined single-atom catalysts for nonoxidative conversion of methane. *The Journal of Chemical Physics* **2021,** *154* (17).
192. Natural Gas Weekly Update. U.S. Energy Information Administration: United States of America 2024.
193. Borry, R. W.; Lu, E. C.; Kim, Y.-H.; Iglesia, E., Non-oxidative catalytic conversion of methane with continuous hydrogen removal. *Stud. Surf. Sci. Catal* **1998,** *119*, 403-410.
194. Musyoka, N. M.; Petrik, L. F.; Hums, E.; Kuhnt, A.; Schwieger, W., Thermal stability studies of zeolites A and X synthesized from South African coal fly ash. *Research on Chemical Intermediates* **2015,** *41*, 575-582.
195. Buchholz, A.; Wang, W.; Xu, M.; Arnold, A.; Hunger, M., Thermal stability and dehydroxylation of Brønsted acid sites in silicoaluminophosphates H-SAPO-11, H-SAPO-18, H-SAPO-31, and H-SAPO-34 investigated by multi-nuclear solid-state NMR spectroscopy. *Microporous and mesoporous materials* **2002,** *56* (3), 267-278.
196. Liu, S.-b.; Wu, J.-F.; Ma, L.-J.; Tsai, T.-C.; Wang, I., On the thermal stability of zeolite beta. *Journal of Catalysis* **1991,** *132* (2), 432-439.
197. Hondo, E.; Gani, T. Z.; Kosari, M.; Xi, S.; Bella; Ashok, J.; Tan, J. Y.; Wang, T.; Bian, H.; Lim, K. H., Unveiling the Roles of Precursor Structure and Controlled Sintering on Ni-Phyllosilicate-Derived Catalysts for Low-Temperature Methane Decomposition. *ACS Sustainable Chemistry & Engineering* **2023**.
198. Lin, X.; Huang, M.; Zhu, H.; Wan, C.; Li, D.; Jiang, L., Hydrotalcite-derived nickel–gallium alloy catalysts with enhanced resistance against metal sintering for methane decomposition. *International Journal of Hydrogen Energy* **2023,** *48* (27), 10016-10031.
199. Beck, A.; Frey, H.; Huang, X.; Clark, A. H.; Goodman, E. D.; Cargnello, M.; Willinger, M.; van Bokhoven, J. A., Controlling the Strong Metal‐Support Interaction Overlayer Structure in Pt/TiO2 Catalysts Prevents Particle Evaporation. *Angewandte Chemie International Edition* **2023,** *62* (27), e202301468.

200. Zafeiratos, S.; Piccinin, S.; Teschner, D., Alloys in catalysis: phase separation and surface segregation phenomena in response to the reactive environment. *Catalysis Science & Technology* **2012,** *2* (9), 1787-1801.
201. Cuenya, B. R.; Behafarid, F., Nanocatalysis: size-and shape-dependent chemisorption and catalytic reactivity. *Surface Science Reports* **2015,** *70* (2), 135-187.
202. Niu, J.; Chen, S.; Zheng, X.; Liu, H.; Jin, Y.; Zhang, R., Understanding the effect of Ni cluster size on methane activation and dehydrogenation. *International Journal of Hydrogen Energy* **2023,** *48* (29), 10903-10910.
203. van Teijlingen, A.; Davis, S. A.; Hall, S. R., Size-dependent melting point depression of nickel nanoparticles. *Nanoscale Advances* **2020,** *2* (6), 2347-2351.
204. Gardiner Jr, W.; Owen, J.; Clark, T.; Dove, J.; Bauer, S.; Miller, J.; McLean, W. In *Rate and mechanism of methane pyrolysis from 2000o to 2700oK*, Symposium (International) on Combustion, Elsevier: 1975; pp 857-868.
205. Belchetz, L., The thermal catalytic decomposition of methane. *Transactions of the Faraday Society* **1934,** *30*, 170-176.
206. Fang, T.; Yeh, C. T., Catalytic pyrolysis of methane. *Journal of the Chinese Chemical Society* **1982,** *29* (4), 265-273.
207. Devries, L.; Ryason, P. *Conversions of low molecular weight hydrocarbons to higher molecular weight hydrocarbons using a metal-containing catalyst*; 1986.
208. Van Der Zwet, G.; Hendriks, P.; Van Santen, R., Pyrolysis of methane and the role of surface area. *Catalysis today* **1989,** *4* (3-4), 365-369.
209. Menon, U.; Rahman, M.; Khatib, S. J., A critical literature review of the advances in methane dehydroaromatization over multifunctional metal-promoted zeolite catalysts. *Applied Catalysis A: General* **2020,** *608*, 117870.
210. Zhang, T., Recent advances in heterogeneous catalysis for the nonoxidative conversion of methane. *Chemical Science* **2021,** *12* (38), 12529-12545.
211. Impeng, S.; Khongpracha, P.; Sirijaraensre, J.; Jansang, B.; Ehara, M.; Limtrakul, J., Methane activation on Fe-and FeO-embedded graphene and boron nitride sheet: role of atomic defects in catalytic activities. *RSC advances* **2015,** *5* (119), 97918-97927.
212. Ismagilov, Z. R.; Matus, E. V.; Tsikoza, L. T., Direct conversion of methane on Mo/ZSM-5 catalysts to produce benzene and hydrogen: achievements and perspectives. *Energy & Environmental Science* **2008,** *1* (5), 526-541.
213. Dixit, G. K.; Kumar, M.; Katiyar, A.; Jansen, A. P.; van Bavel, A. P.; Agrawal, R.; Shenai, P. M.; Srinivasan, V., Unraveling the activity of iron carbide clusters embedded in silica for thermocatalytic conversion of methane. *Catalysis Science & Technology* **2021,** *11* (22), 7398-7411.
214. Görlich, E., The structure of SiO2—Current views. *Ceramics International* **1982,** *8* (1), 3-16.
215. DeAngelis, M. T.; Rondinone, A. J.; Pawel, M. D.; Labotka, T. C.; Anovitz, L. M., Sol-gel synthesis of nanocrystalline fayalite (Fe2SiO4). *American Mineralogist* **2012,** *97* (4), 653-656.
216. Cresko, J.; Rightor, E.; Carpenter, A.; Peretti, K.; Elliott, N.; Nimbalkar, S.; Morrow III, W. R.; Hasanbeigi, A.; Hedman, B.; Supekar, S. *DOE Industrial*

Decarbonization Roadmap; USDOE Office of Energy Efficiency and Renewable Energy (EERE): 2022.
217. Gamal, A.; Eid, K.; El-Naas, M. H.; Kumar, D.; Kumar, A., Catalytic methane decomposition to carbon nanostructures and COx-free hydrogen: A mini-review. *Nanomaterials* **2021,** *11* (5), 1226.
218. Ahmed, I.; Rehan, M.; Basit, A.; Hong, K.-S., Greenhouse gases emission reduction for electric power generation sector by efficient dispatching of thermal plants integrated with renewable systems. *Scientific Reports* **2022,** *12* (1), 12380.
219. Rivera, A.; Movalia, S.; Pit, H.; Larsen, K., Global Greenhouse Gas Emissions: 1990-2020 and Preliminary 2021 Estimates. *Rhodium Group* **2022,** *19*.
220. Ramasubramanian, V., *Direct and Non-oxidative Conversion of Methane to Valuable Products*. The University of Tulsa: 2020.
221. Song, Y.; Xu, Y. B.; Suzuki, Y.; Nakagome, H.; Zhang, Z. G., A clue to exploration of the pathway of coke formation on Mo/HZSM-5 catalyst in the non-oxidative methane dehydroaromatization at 1073 K. *Applied Catalysis a-General* **2014,** *482*, 387-396.
222. Huang, X.; Jiao, X.; Lin, M.; Wang, K.; Jia, L.; Hou, B.; Li, D., Coke distribution determines the lifespan of a hollow Mo/HZSM-5 capsule catalyst in CH 4 dehydroaromatization. *Catalysis Science & Technology* **2018,** *8* (22), 5740-5749.
223. Toraman, H. E.; Alexopoulos, K.; Oh, S. C.; Cheng, S.; Liu, D.; Vlachos, D. G., Ethylene production by direct conversion of methane over isolated single active centers. *Chemical Engineering Journal* **2021,** *420*, 130493.
224. Fujimoto, Y.; Ohba, T., Size-dependent catalytic hydrogen production via methane decomposition and aromatization at a low-temperature using Co, Ni, Cu, Mo, and Ru nanometals. *Physical Chemistry Chemical Physics* **2022,** *24* (47), 28794-28803.
225. Huang, M.; Li, J.; Liu, Q.; Zhang, M.; Liu, Z.; Gao, B., Enhanced catalytic performance of the hollow Mo/HZSM-5 nanocrystal for methane dehydroaromatization. *Fuel* **2023,** *334*, 126765.
226. Liu, Z.; Cheng, S.; Schulman, E.; Chen, W.; Vlachos, D. G.; Shu, Y.; Tran, D. T.; Liu, D., Direct non-oxidative methane coupling on vitreous silica supported iron catalysts. *Catalysis Today* **2023,** *416*, 113873.
227. Chen, G.; Liang, T.; Yoo, P.; Fadaeerayeni, S.; Sarnello, E.; Li, T.; Liao, P.; Xiang, Y., Catalytic Light Alkanes Conversion through Anaerobic Ammodehydrogenation. *ACS Catalysis* **2021,** *11* (13), 7987-7995.
228. Lee, S.-J.; Titus, C. J.; Alonso Mori, R.; Baker, M. L.; Bennett, D. A.; Cho, H.-M.; Doriese, W. B.; Fowler, J. W.; Gaffney, K. J.; Gallo, A., Soft X-ray spectroscopy with transition-edge sensors at Stanford Synchrotron Radiation Lightsource beamline 10-1. *Review of Scientific Instruments* **2019,** *90* (11).
229. Ravel, B.; Newville, M., ATHENA, ARTEMIS, HEPHAESTUS: data analysis for X-ray absorption spectroscopy using IFEFFIT. *Journal of synchrotron radiation* **2005,** *12* (4), 537-541.
230. Seabold, S.; Perktold, J., Statsmodels: econometric and statistical modeling with python. *SciPy* **2010,** *7*, 1.

231. Wilke, M.; Farges, F.; Petit, P.-E.; Brown Jr, G. E.; Martin, F., Oxidation state and coordination of Fe in minerals: An Fe K-XANES spectroscopic study. *American Mineralogist* **2001,** *86* (5-6), 714-730.
232. Wilke, M.; Partzsch, G. M.; Bernhardt, R.; Lattard, D., Determination of the iron oxidation state in basaltic glasses using XANES at the K-edge. *Chemical Geology* **2004,** *213* (1-3), 71-87.
233. Jahrman, E. P.; Weaver, J. L.; Govind, N.; Perestjuk, M.; Seidler, G. T., Iron redox analysis of silicate-based minerals and glasses using synchrotron X-ray absorption and laboratory X-ray emission spectroscopy. *Journal of Non-Crystalline Solids* **2022,** *577*, 121326.
234. Kraft, S.; Stümpel, J.; Becker, P.; Kuetgens, U., High resolution x‐ray absorption spectroscopy with absolute energy calibration for the determination of absorption edge energies. *Review of scientific instruments* **1996,** *67* (3), 681-687.
235. Jahrman, E. P.; Masias, K. L. S.; Peck, T. C.; Roberts, C. A., X‐ray absorption fine structure characterization of a multicomponent spinel catalyst. *X‐Ray Spectrometry* **2023,** *52* (2), 90-101.
236. Newville, M. In *Larch: an analysis package for XAFS and related spectroscopies*, Journal of Physics: Conference Series, IOP Publishing: 2013; p 012007.
237. Calvin, S., *XAFS for Everyone*. CRC press: 2013.
238. Henderson, G. S.; Neuville, D. R.; Cochain, B.; Cormier, L., The structure of GeO_2–SiO_2 glasses and melts: A Raman spectroscopy study. *Journal of Non-Crystalline Solids* **2009,** *355* (8), 468-474.
239. Chligui, M.; Guimbretiere, G.; Canizares, A.; Matzen, G.; Simon, P., New features in the raman spectrum of silica: Key-points in the improvement on structure knowledge. **2010**.
240. Pasquarello, A.; Car, R., Identification of Raman defect lines as signatures of ring structures in vitreous silica. *Physical Review Letters* **1998,** *80* (23), 5145.
241. Little, D. J.; Ams, M.; Dekker, P.; Marshall, G. D.; Dawes, J. M.; Withford, M. J., Femtosecond laser modification of fused silica: the effect of writing polarization on Si-O ring structure. *Optics express* **2008,** *16* (24), 20029-20037.
242. Mishchik, K. Ultrafast laser-induced modification of optical glasses: a spectroscopy insight into the microscopic mechanisms. Université Jean Monnet-Saint-Etienne, 2012.
243. Visuvamithiran, P.; Shanthi, K.; Palanichamy, M.; Murugesan, V., Direct synthesis of Mn-Ti-SBA-15 catalyst for the oxidation of ethylbenzene. *Catalysis Science & Technology* **2013,** *3* (9), 2340-2348.
244. He, Z.; Wu, J.; Gao, B.; He, H., Hydrothermal synthesis and characterization of aluminum-free Mn-β zeolite: a catalyst for phenol hydroxylation. *ACS Applied Materials & Interfaces* **2015,** *7* (4), 2424-2432.
245. Meng, Y.; Genuino, H. C.; Kuo, C.-H.; Huang, H.; Chen, S.-Y.; Zhang, L.; Rossi, A.; Suib, S. L., One-step hydrothermal synthesis of manganese-containing MFI-type zeolite, Mn–ZSM-5, characterization, and catalytic oxidation of hydrocarbons. *Journal of the American Chemical Society* **2013,** *135* (23), 8594-8605.

246. Baran, R.; Valentin, L.; Dzwigaj, S., Incorporation of Mn into the vacant T-atom sites of a BEA zeolite as isolated, mononuclear Mn: FTIR, XPS, EPR and DR UV-Vis studies. *Physical Chemistry Chemical Physics* **2016,** *18* (17), 12050-12057.
247. Pan, Z.; Wang, R.; Nie, Z.; Chen, J., Effect of a second metal (Co, Fe, Mo and W) on performance of Ni_2P/SiO_2 for hydrodeoxygenation of methyl laurate. *Journal of Energy Chemistry* **2016,** *25* (3), 418-426.
248. Palčić, A.; Bruzzese, P. C.; Pyra, K.; Bertmer, M.; Góra-Marek, K.; Poppitz, D.; Pöppl, A.; Gläser, R.; Jabłońska, M., Nanosized Cu-SSZ-13 and its application in NH3-SCR. *Catalysts* **2020,** *10* (5), 506.
249. Suharbiansah, R. S.; Pyra, K.; Liebau, M.; Poppitz, D.; Gora-Marek, K.; Gläser, R.; Jabłońska, M., Micro-/mesoporous copper-containing zeolite Y applied in NH3-SCR, DeNOx. *Microporous and Mesoporous Materials* **2022,** *334*, 111793.
250. Yu, Y.; Zhang, L.; Wang, J.; Yang, Z.; Long, M.; Hu, N.; Zhang, Y., Preparation of hollow porous Cu_2O microspheres and photocatalytic activity under visible light irradiation. *Nanoscale Research Letters* **2012,** *7*, 1-6.
251. Umegaki, T.; Takei, C.; Watanuki, Y.; Xu, Q.; Kojima, Y., Fabrication of hollow nickel-silica composite spheres using L (+)-arginine and their catalytic performance for hydrolytic dehydrogenation of ammonia borane. *Journal of Molecular Catalysis A: Chemical* **2013,** *371*, 1-7.
252. Martínez-Sánchez, C.; Regmi, C.; Lee, S.; Rodríguez-González, V., Effects of Ce doping on the photocatalytic and electrochemical performance of nickel hydroxide nanostructures. *Topics in Catalysis* **2021,** *64*, 73-83.
253. Aronson, B. J.; Blanford, C. F.; Stein, A., Synthesis, characterization, and ion-exchange properties of zinc and magnesium manganese oxides confined within MCM-41 channels. *The Journal of Physical Chemistry B* **2000,** *104* (3), 449-459.
254. Lomate, S.; Sultana, A.; Fujitani, T., Vapor phase catalytic transfer hydrogenation (CTH) of levulinic acid to γ-valerolactone over copper supported catalysts using formic acid as hydrogen source. *Catalysis Letters* **2018,** *148*, 348-358.
255. Zhang, Q.; Chen, C.; Wang, M.; Cai, J.; Xu, J.; Xia, C., Facile preparation of highly-dispersed cobalt-silicon mixed oxide nanosphere and its catalytic application in cyclohexane selective oxidation. *Nanoscale research letters* **2011,** *6*, 1-7.
256. Vaschetto, E. G.; Sicardi, M. I.; Elías, V. R.; Ferrero, G. O.; Carraro, P. M.; Casuscelli, S. G.; Eimer, G. A., Metal modified silica for catalytic wet air oxidation (CWAO) of glyphosate under atmospheric conditions. *Adsorption* **2019,** *25* (7), 1299-1306.
257. Zheng, S.; Song, L.; Tang, S.; Liu, C.; Yue, H.; Liang, B., Insight into the synergism between MnO_2 and acid sites over Mn–SiO_2@ TiO_2 nano-cups for low-temperature selective catalytic reduction of NO with NH 3. *RSC advances* **2018,** *8* (4), 1979-1986.

258. Silva, P. H.; Oliveira, H. S.; Batista, M. S., Redox effects in Cu, Co or Fe in oxides nanocrystals with high catalytic activity for the acetonitrile combustion. *SN Applied Sciences* **2020,** *2*, 1-9.
259. Song, W.; Poyraz, A. S.; Meng, Y.; Ren, Z.; Chen, S.-Y.; Suib, S. L., Mesoporous Co_3O_4 with controlled porosity: inverse micelle synthesis and high-performance catalytic CO oxidation at− 60° C. *Chemistry of Materials* **2014,** *26* (15), 4629-4639.
260. Stanciulescu, M.; Caravaggio, G.; Dobri, A.; Moir, J.; Burich, R.; Charland, J.-P.; Bulsink, P., Low-temperature selective catalytic reduction of NO_x with NH_3 over Mn-containing catalysts. *Applied Catalysis B: Environmental* **2012,** *123*, 229-240.
261. Liu, X.; Gao, S.; Yang, F.; Zhou, S.; Kong, Y., High promoting of selective oxidation of ethylbenzene by Mn-ZSM-5 synthesized without organic template and calcination. *Research on Chemical Intermediates* **2020,** *46*, 2817-2832.
262. Kubin, M.; Guo, M.; Kroll, T.; Löchel, H.; Källman, E.; Baker, M. L.; Mitzner, R.; Gul, S.; Kern, J.; Föhlisch, A., Probing the oxidation state of transition metal complexes: a case study on how charge and spin densities determine Mn L-edge X-ray absorption energies. *Chemical science* **2018,** *9* (33), 6813-6829.
263. Mitzner, R.; Rehanek, J.; Kern, J.; Gul, S.; Hattne, J.; Taguchi, T.; Alonso-Mori, R.; Tran, R.; Weniger, C.; Schröder, H., L-edge x-ray absorption spectroscopy of dilute systems relevant to metalloproteins using an x-ray free-electron laser. *The journal of physical chemistry letters* **2013,** *4* (21), 3641-3647.
264. Meng, L.; Chan, Y.; Wang, H.; Dai, Y.; Wang, X.; Zou, J., Recycling of iron and silicon from drinking water treatment sludge for synthesis of magnetic iron oxide@ SiO_2 composites. *Environmental Science and Pollution Research* **2016,** *23*, 5122-5133.
265. Gil-Horán, R. H.; Chavarría-Hernández, J. C.; Quintana-Owen, P.; Gutiérrez-Alejandre, A., Ethanol conversion to short-chain olefins over ZSM-5 zeolite catalysts enhanced with P, Fe, and Ni. *Topics in Catalysis* **2020,** *63* (5-6), 414-427.
266. Mitsunobu, S.; Zhu, M.; Takeichi, Y.; Ohigashi, T.; Suga, H.; Jinno, M.; Makita, H.; Sakata, M.; Ono, K.; Mase, K., Direct detection of Fe (II) in extracellular polymeric substances (EPS) at the mineral-microbe interface in bacterial pyrite leaching. *Microbes and Environments* **2016,** *31* (1), 63-69.
267. Wang, W.; Wu, Y.; Liu, T.; Zhao, Y.; Qu, Y.; Yang, R.; Xue, Z.; Wang, Z.; Zhou, F.; Long, J., Single Co sites in ordered SiO2 channels for boosting nonoxidative propane dehydrogenation. *ACS Catalysis* **2022,** *12* (4), 2632-2638.
268. Khabra, A.; Cohen, H.; Pinhasi, G. A.; Querol, X.; Córdoba Sola, P.; Zidki, T., Synthesis of a $SiO_2/Co(OH)_2$ Nanocomposite Catalyst for SO_X/NO_X Oxidation in Flue Gas. *Catalysts* **2022,** *13* (1), 29.
269. Istomin, S. Y.; Tyablikov, O.; Kazakov, S.; Antipov, E.; Kurbakov, A.; Tsirlin, A.; Hollmann, N.; Chin, Y.; Lin, H.-J.; Chen, C., An unusual high-spin ground state of Co 3+ in octahedral coordination in brownmillerite-type cobalt oxide. *Dalton Transactions* **2015,** *44* (23), 10708-10713.

270. Ye, R.-P.; Gong, W.; Sun, Z.; Sheng, Q.; Shi, X.; Wang, T.; Yao, Y.; Razink, J. J.; Lin, L.; Zhou, Z., Enhanced stability of Ni/SiO2 catalyst for CO_2 methanation: Derived from nickel phyllosilicate with strong metal-support interactions. *Energy* **2019,** *188*, 116059.
271. Amin, M. H., Relationship between the pore structure of mesoporous silica supports and the activity of nickel nanocatalysts in the CO_2 reforming of methane. *Catalysts* **2020,** *10* (1), 51.
272. Huang, W.; Ding, S.; Chen, Y.; Hao, W.; Lai, X.; Peng, J.; Tu, J.; Cao, Y.; Li, X., 3D NiO hollow sphere/reduced graphene oxide composite for high-performance glucose biosensor. *Scientific reports* **2017,** *7* (1), 5220.
273. Yin, Z.; Xiao, Y.; Wan, X.; Jiang, Y.; Chen, G.; Shi, Q.; Cao, S., High photocatalytic activity of Cu 2 O embedded in hierarchically hollow SiO $_2$ for efficient chemoselective hydrogenation of nitroarenes. *Journal of Materials Science* **2021,** *56*, 3874-3886.
274. Sivkov, D. V.; Petrova, O. V.; Nekipelov, S. V.; Vinogradov, A. S.; Skandakov, R. N.; Isaenko, S. I.; Ob'edkov, A. M.; Kaverin, B. S.; Vilkov, I. V.; Korolev, R. I., The identification of Cu–O–C bond in Cu/MWCNTs hybrid nanocomposite by XPS and NEXAFS spectroscopy. *Nanomaterials* **2021,** *11* (11), 2993.
275. Kaur, A.; Chahal, P.; Hogan, T., Selective fabrication of SiC/Si diodes by excimer laser under ambient conditions. *IEEE Electron Device Letters* **2015,** *37* (2), 142-145.
276. Zheng, G.; Xiang, Y.; Xu, L.; Luo, H.; Wang, B.; Liu, Y.; Han, X.; Zhao, W.; Chen, S.; Chen, H., Controlling surface oxides in Si/C nanocomposite anodes for high‐performance Li‐ion batteries. *Advanced Energy Materials* **2018,** *8* (29), 1801718.
277. Wang, T.-H.; Gole, J. L.; White, M. G.; Watkins, C.; Street, S. C.; Fang, Z.; Dixon, D. A., The surprising oxidation state of fumed silica and the nature of water binding to silicon oxides and hydroxides. *Chemical Physics Letters* **2011,** *501* (4-6), 159-165.
278. Bancroft, G.; Nesbitt, H.; Ho, R.; Shaw, D.; Tse, J.; Biesinger, M., Toward a comprehensive understanding of solid-state core-level XPS linewidths: Experimental and theoretical studies on the Si 2 p and O 1 s linewidths in silicates. *Physical review B* **2009,** *80* (7), 075405.
279. Alam, A.; Howlader, M.; Deen, M., Oxygen plasma and humidity dependent surface analysis of silicon, silicon dioxide and glass for direct wafer bonding. *ECS Journal of Solid State Science and Technology* **2013,** *2* (12), P515.
280. Hashemi, A.; Bahari, A., Structural and dielectric characteristic of povidone–silica nanocomposite films on the Si (n) substrate. *Applied Physics A* **2017,** *123*, 1-7.
281. Calaway, M.; Fries, M. In *Adventitious Carbon on Primary Sample Containment Metal Surfaces*, Lunar and Planetary Science Conference, 2015.
282. Bourlier, Y.; Bouttemy, M.; Patard, O.; Gamarra, P.; Piotrowicz, S.; Vigneron, J.; Aubry, R.; Delage, S.; Etcheberry, A., Investigation of InAlN layers surface reactivity after thermal annealings: a complete XPS study for HEMT. *ECS Journal of Solid State Science and Technology* **2018,** *7* (6), P329.

283. Greczynski, G.; Hultman, L., The same chemical state of carbon gives rise to two peaks in X-ray photoelectron spectroscopy. *Scientific reports* **2021,** *11* (1), 11195.
284. Graff, M. J.; Albright, L. F., Coke deposition from acetylene, butadiene and benzene decompositions at 500–900° C on solid surfaces. *Carbon* **1982,** *20* (4), 319-330.
285. Das, K.; Waiba, S.; Jana, A.; Maji, B., Manganese-catalyzed hydrogenation, dehydrogenation, and hydroelementation reactions. *Chemical Society Reviews* **2022,** *51* (11), 4386-4464.
286. Ma, D.; Wang, D. Z.; Su, L. L.; Shu, Y. Y.; Xu, Y.; Bao, X. H., Carbonaceous deposition on Mo/HMCM-22 catalysts for methane aromatization: A TP technique investigation. *Journal of Catalysis* **2002,** *208* (2), 260-269.
287. Liu, H. M.; Su, L. L.; Wang, H. X.; Shen, W. J.; Bao, X. H.; Xu, Y. D., The chemical nature of carbonaceous deposits and their role in methane dehydro-aromatization on Mo/MCM-22 catalysts. *Appl Catal a-Gen* **2002,** *236* (1-2), 263-280.
288. Abedin, M. A.; Kanitkar, S.; Bhattar, S.; Spivey, J. J., Sulfated hafnia as a support for Mo oxide: A novel catalyst for methane dehydroaromatization. *Catalysis Today* **2019**.
289. Kanitkar, S.; Abedin, M. A.; Bhattar, S.; Spivey, J. J., Methane dehydroaromatization over molybdenum supported on sulfated zirconia catalysts. *Appl Catal a-Gen* **2019,** *575*, 25-37.
290. Abedin, M. A.; Kanitkar, S.; Bhattar, S.; Spivey, J. J., Promotional Effect of Cr in Sulfated Zirconia-Based Mo Catalyst for Methane Dehydroaromatization. *Energy Technol-Ger* **2019**.
291. Gueret, C.; Billaud, F.; Fixari, B.; Leperchec, P., Thermal Coupling of Methane, Experimental Investigations on Coke Deposits. *Carbon* **1995,** *33* (2), 159-170.
292. Wang, S.; Lee, W. J.; Li, C. E.; Kuan, B.; Burke, N.; Patel, J., The pyrolysis of natural gas: A study of carbon deposition and the suitability of reactor materials. *Aiche J* **2019,** *65* (3), 1035-1046.
293. Vander Wal, R.; Sengupta, A.; Musselman, E.; Skoptsov, G., Microwave-Driven Plasma-Mediated Methane Cracking: Product Carbon Characterization. *C-J Carbon Res* **2018,** *4* (4).
294. Singh, M.; Sengupta, A.; Zeller, K.; Skoptsov, G.; Vander Wal, R. L., Effect of hydrogen concentration on graphene synthesis using microwave-driven plasma-mediated methane cracking. *Carbon* **2019,** *143*, 802-813.
295. Chalmin, E.; Farges, F.; Brown, G. E., A pre-edge analysis of Mn K-edge XANES spectra to help determine the speciation of manganese in minerals and glasses. *Contributions to Mineralogy and Petrology* **2009,** *157*, 111-126.
296. Gaur, A.; Shrivastava, B., Speciation using X-ray absorption fine structure (XAFS). *Review Journal of Chemistry* **2015,** *5*, 361-398.
297. Phillips, B.; Hutta, J.; Warshaw, I., Phase equilibria in the system NiO–Al_2O_3–SiO2. *Journal of the American Ceramic Society* **1963,** *46* (12), 579-583.

298. Wu, P.; Eriksson, G.; Pelton, A. D.; Blander, M., Prediction of the thermodynamic properties and phase diagrams of silicate systems–evaluation of the FeO-MgO-SiO2 system. *ISIJ international* **1993,** *33* (1), 26-35.
299. Eriksson, G.; Wu, P.; Blander, M.; Pelton, A. D., Critical evaluation and optimization of the thermodynamic properties and phase diagrams of the MnO–SiO_2 and CaO–SiO_2 systems. *Canadian Metallurgical Quarterly* **1994,** *33* (1), 13-21.
300. Jung, I.-H.; Decterov, S. A.; Pelton, A. D., Thermodynamic modeling of the CoO–SiO2 and CoO–FeO–Fe_2O_3–SiO_2 systems. *International journal of materials research* **2007,** *98* (9), 816-825.
301. Breuer, K.-H.; Eysel, W., Structural and chemical varieties of dioptase, Cu_6 $[Si_6O_{18}]\cdot$ 6 H_2O* I. Thermal properties. *Zeitschrift für Kristallographie* **1988,** *184* (1-2), 1-11.
302. Breuer, K.-H.; Eysel, W.; Müller, R., Structural and chemical varieties of dioptase, Cu6 $[Si_6O_{18}]\cdot$ $6H_2O$: II. Structural properties. *Zeitschrift für Kristallographie* **1989,** *187* (1-2), 15-23.
303. Fujino, K.; Sasaki, S.; Takeuchi, Y.; Sadanaga, R., X-ray determination of electron distributions in forsterite, fayalite and tephroite. *Acta Crystallographica Section B: Structural Crystallography and Crystal Chemistry* **1981,** *37* (3), 513-518.
304. Smyth, J. R., High temperature crystal chemistry of fayalite. *American Mineralogist: Journal of Earth and Planetary Materials* **1975,** *60* (11-12), 1092-1097.
305. Tamada, O.; Fujino, K.; Sasaki, S., Structures and electron distributions of α-Co2SiO4 and α-Ni_2SiO_4 (olivine structure). *Acta Crystallographica Section B: Structural Science* **1983,** *39* (6), 692-697.
306. Otto, H.; Meibohm, M., Crystal structure of copper polysilicate, Cu $[SiO_3]$. *Zeitschrift für Kristallographie-Crystalline Materials* **1999,** *214* (9), 558-565.
307. Huang, Z.-Q.; Chen, Y.-T.; Chang, C.-R.; Li, J., Theoretical insights into dual-metal-site catalysts for the nonoxidative coupling of methane. *ACS Catalysis* **2021,** *11* (21), 13149-13159.
308. Guo, X.; Fang, G.; Li, G.; Ma, H.; Fan, H.; Yu, L.; Ma, C.; Wu, X.; Deng, D.; Wei, M.; Tan, D.; Si, R.; Zhang, S.; Li, J.; Sun, L.; Tang, Z.; Pan, X.; Bao, X., Direct, Nonoxidative Conversion of Methane to Ethylene, Aromatics, and Hydrogen. *Science* **2014,** *344* (6184), 616-619.
309. Schröder, A.; Klüppel, M.; Schuster, R. H., Characterisation of Surface Activity of Carbon Black and its Relation to Polymer‐Filler Interaction. *Macromolecular Materials and Engineering* **2007,** *292* (8), 885-916.
310. Singh, M.; Vander Wal, R. L., Nanostructure Quantification of Carbon Blacks. *C* **2019,** *5* (1), 2.
311. Ferrari, A. C.; Robertson, J., Interpretation of Raman spectra of disordered and amorphous carbon. *Physical Review B* **2000,** *61* (20), 14095-14107.
312. Freihofer, G.; Raghavan, S.; Gosztola, D., Investigation of temperature dependent multi-walled nanotube G and D doublet using pseudo-voigt functions. *Applied Spectroscopy* **2013,** *67* (3), 321-328.

313. Bokobza, L.; Bruneel, J.-L.; Couzi, M., Raman Spectra of Carbon-Based Materials (from Graphite to Carbon Black) and of Some Silicone Composites. *C* **2015,** *1* (1), 77-94.
314. Pimenta, M.; Dresselhaus, G.; Dresselhaus, M. S.; Cancado, L.; Jorio, A.; Saito, R., Studying disorder in graphite-based systems by Raman spectroscopy. *Physical chemistry chemical physics* **2007,** *9* (11), 1276-1290.
315. El-Shafie, M., Kambara, S. and Hayakawa, Y., Hydrogen Production Technologies Overview. *Journal of Power and Energy Engineering* **2019,** *7*, 107-154.
316. Hefner, R. A., The Age of Energy Gases (Fig. 1). China's Opportunity for Global Energy Leadership, Oklahoma City. *GHK Company* **2007**, 1-32.
317. National Academies of Sciences, E.; Medicine, *Accelerating Decarbonization of the U.S. Energy System*. The National Academies Press: Washington, DC, 2021; p 268.
318. Iulianelli, A.; Liguori, S.; Wilcox, J.; Basile, A., Advances on methane steam reforming to produce hydrogen through membrane reactors technology: A review. *Catalysis Reviews* **2016,** *58* (1), 1-35.
319. Acar, C.; Dincer, I., Review and evaluation of hydrogen production options for better environment. *Journal of Cleaner Production* **2019,** *218*, 835-849.
320. Abbas, H. F.; Wan Daud, W. M. A., Hydrogen production by methane decomposition: A review. *International Journal of Hydrogen Energy* **2010,** *35* (3), 1160-1190.
321. Xu, Y.; Bao, X.; Lin, L., Direct conversion of methane under nonoxidative conditions. *Journal of Catalysis* **2003,** *216*, 386-395.
322. Dagle, R. A.; Dagle, V.; Bearden, M. D.; Holladay, J. D.; Krause, T. R.; Ahmed, S. *An Overview of Natural Gas Conversion Technologies for Co-Production of Hydrogen and Value-Added Solid Carbon Products*; United States, 2017; p Medium: ED; Size: 74 p.
323. Yousefi, M.; Donne, S., Technical challenges for developing thermal methane cracking in small or medium scales to produce pure hydrogen - A review. *International Journal of Hydrogen Energy* **2022,** *47* (2), 699-727.
324. Naikoo, G. A.; Arshad, F.; Hassan, I. U.; Tabook, M. A.; Pedram, M. Z.; Mustaqeem, M.; Tabassum, H.; Ahmed, W.; Rezakazemi, M., Thermocatalytic Hydrogen Production Through Decomposition of Methane-A Review. *Frontiers in Chemistry* **2021,** *9*.
325. Sánchez-Bastardo, N.; Schlögl, R.; Ruland, H., Methane Pyrolysis for CO2-Free H2 Production: A Green Process to Overcome Renewable Energies Unsteadiness. *Chemie Ingenieur Technik* **2020,** *92* (10), 1596-1609.
326. Qian, J.; Chen, T.; Linga Reddy, D.; Liu, D.; Basset, J.; Zhou, L., Methane decomposition to pure hydrogen and carbon nano materials: State-of-the-art and future perspectives. *International Journal of Hydrogen Energy* **2020,** *45*.
327. Ibrahim, A.; Alfatesh, A.; Khan, W.; Soliman, M.; Al-otaibi, R.; Fakeeha, A., Thermo-catalytic methane decomposition: A review of state of the art of catalysts. *Journal- Chemical Society of Pakistan* **2015,** *37*, 1280-1308.

328. Muradov, N., Catalysis of methane decomposition over elemental carbon. *Catalysis communications* **2001,** *2* (3-4), 89-94.
329. Abuseada, M.; Wei, C.; Spearrin, R. M.; Fisher, T. S., Solar–thermal production of graphitic carbon and hydrogen via methane decomposition. *Energy & Fuels* **2022,** *36* (7), 3920-3928.
330. Guil-Lopez, R.; Botas, J.; Fierro, J.; Serrano, D., Comparison of metal and carbon catalysts for hydrogen production by methane decomposition. *Applied Catalysis A: General* **2011,** *396* (1-2), 40-51.
331. Avdeeva, L.; Kochubey, D.; Shaikhutdinov, S. K., Cobalt catalysts of methane decomposition: accumulation of the filamentous carbon. *Applied Catalysis A: General* **1999,** *177* (1), 43-51.
332. Al-Fatesh, A.; Fakeeha, A.; Khan, W.; Ibrahim, A.; He, S.; Seshan, K., Production of hydrogen by catalytic methane decomposition over alumina supported mono-, bi-and tri-metallic catalysts. *International Journal of Hydrogen Energy* **2016,** *41* (48), 22932-22940.
333. Al-Fatesh, A. S.; Abdelkader, A.; Osman, A. I.; Lanre, M. S.; Fakeeha, A. H.; Alhoshan, M.; Alanazi, Y. M.; Awadallah, A. E.; Rooney, D. W., Non-supported bimetallic catalysts of Fe and Co for methane decomposition into H2 and a mixture of graphene nanosheets and carbon nanotubes. *international journal of hydrogen energy* **2023,** *48* (68), 26506-26517.
334. Ashik, U.; Daud, W. W.; Abbas, H. F., Methane decomposition kinetics and reaction rate over Ni/SiO_2 nanocatalyst produced through co-precipitation cum modified Stöber method. *International Journal of Hydrogen Energy* **2017,** *42* (2), 938-952.
335. Pudukudy, M.; Yaakob, Z.; Akmal, Z. S., Direct decomposition of methane over SBA-15 supported Ni, Co and Fe based bimetallic catalysts. *Applied Surface Science* **2015,** *330*, 418-430.
336. Alstrup, I.; Teresa Tavares, M., The kinetics of carbon formation from CH_4 + H_2 on a silica-supported nickel catalyst. *Journal of Catalysis* **1992,** *135* (1), 147-155.
337. Grabke, H. J., Evidence on the surface concentration of carbon on gamma iron from the kinetics of the carburization in CH_4–H_2. *Metallurgical Transactions* **1970,** *1* (10), 2972-2975.
338. Hofmann, S.; Csányi, G.; Ferrari, A. C.; Payne, M. C.; Robertson, J., Surface Diffusion: The Low Activation Energy Path for Nanotube Growth. *Physical Review Letters* **2005,** *95* (3), 036101.
339. Baker, R. T. K.; Barber, M. A.; Harris, P. S.; Feates, F. S.; Waite, R. J., Nucleation and growth of carbon deposits from the nickel catalyzed decomposition of acetylene. *Journal of Catalysis* **1972,** *26* (1), 51-62.
340. Awadallah, A.; Aboul-Enein, A.; Yonis, M.; Aboul-Gheit, A., Effect of structural promoters on the catalytic performance of cobalt-based catalysts during natural gas decomposition to hydrogen and carbon nanotubes. *Fullerenes, Nanotubes and Carbon Nanostructures* **2016,** *24* (3), 181-189.
341. Mei, I. L. S.; Lock, S.; Vo, D.-V. N.; Abdullah, B., Thermo-catalytic methane decomposition for hydrogen production: Effect of palladium promoter on Ni-

based catalysts. *Bulletin of Chemical Reaction Engineering & Catalysis* **2016,** *11* (2), 191-199.
342. Hamdan, M.; Halawy, L.; Hijazi, A.; Aouad, S.; Zeaiter, J., Highly-stable Ni–Zn catalyst on USY zeolite support for low temperature methane pyrolysis. *International Journal of Hydrogen Energy* **2024,** *61*, 840-850.
343. Saraswat, S. K.; Pant, K., Synthesis of carbon nanotubes by thermo catalytic decomposition of methane over Cu and Zn promoted Ni/MCM-22 catalyst. *Journal of Environmental Chemical Engineering* **2013,** *1* (4), 746-754.
344. Sun, H.; Ren, S.; Ji, X.; Song, W.; Guo, Q.; Shen, B., Doping Fe and Zn to modulate Ni nanoparticles on IM-5 for methane decomposition to form hydrogen and CNTs. *International Journal of Hydrogen Energy* **2023,** *48* (35), 13081-13096.
345. Majewska, J.; Michalkiewicz, B., Production of hydrogen and carbon nanomaterials from methane using Co/ZSM-5 catalyst. *International journal of hydrogen energy* **2016,** *41* (20), 8668-8678.
346. Song, G.; Li, C.; Zhou, W.; Wu, L.; Lim, K. H.; Hu, F.; Wang, T.; Liu, S.; Ren, Z.; Kawi, S., Catalytic decomposition of methane for controllable production of carbon nanotubes and high purity H2 over LTA zeolite-derived Ni-based yolk-shell catalysts. *Chemical Engineering Journal* **2023,** *474*, 145643.
347. Al-Nayili, A.; Albdiry, M.; Salman, N., Dealumination of zeolite frameworks and Lewis acid catalyst activation for transfer hydrogenation. *Arabian Journal for Science and Engineering* **2021,** *46*, 5709-5716.
348. Yang, H.; Liu, Q.; Li, Y.; Sun, K.; Chen, Z.; Peng, Q.; Chen, C., Isolated Single‐Atom Ruthenium Anchored on Beta Zeolite as an Efficient Heterogeneous Catalyst for Styrene Epoxidation. *ChemNanoMat* **2020,** *6* (11), 1647-1651.
349. Hanafi, S.; Gobara, H.; Elmelawy, M.; Abo-El-Enein, S.; Alkahlawy, A., Catalytic behavior of Pt nanoparticles dealuminated Y-zeolite for some n-alkane hydroisomerization. *Egyptian Journal of Petroleum* **2014,** *23* (2), 151-161.
350. Omegna, A.; Vasic, M.; van Bokhoven, J. A.; Pirngruber, G.; Prins, R., Dealumination and realumination of microcrystalline zeolite beta: an XRD, FTIR and quantitative multinuclear (MQ) MAS NMR study. *Physical Chemistry Chemical Physics* **2004,** *6* (2), 447-452.
351. Sobuś, N.; Michorczyk, B.; Piotrowski, M.; Kuterasiński, Ł.; Chlebda, D. K.; Łojewska, J.; Jędrzejczyk, R. J.; Jodłowski, P.; Kuśtrowski, P.; Czekaj, I., Design of Co, Cu and Fe–BEA zeolite catalysts for selective conversion of lactic acid into acrylic acid. *Catalysis Letters* **2019,** *149*, 3349-3360.
352. Bhargava, R.; Khan, S.; Ahmad, N.; Ansari, M. M. N. In *Investigation of structural, optical and electrical properties of Co_3O_4 nanoparticles*, AIP conference proceedings, AIP Publishing: 2018.
353. Fierro, G.; Eberhardt, M. A.; Houalla, M.; Hercules, D. M.; Hall, W. K., Redox chemistry of CoZSM-5 zeolite. *The Journal of Physical Chemistry* **1996,** *100* (20), 8468-8477.

354. Jimenez, J. D.; Wen, C.; Royko, M. M.; Kropf, A. J.; Segre, C.; Lauterbach, J., Influence of coordination environment of anchored single‐site cobalt catalyst on CO2 hydrogenation. *ChemCatChem* **2020,** *12* (3), 846-854.
355. Ahn, H. S.; Yano, J.; Tilley, T. D., Water oxidation by cobalt centers on various oxide surfaces: the effects of oxide surface acidity and oxygen atom affinity on catalysis. *ACS Catalysis* **2015,** *5* (4), 2573-2576.
356. Carvalho, W. A.; Varaldo, P. B.; Wallau, M.; Schuchardt, U., Mesoporous redox molecular sieves analogous to MCM-41. *Zeolites* **1997,** *18* (5-6), 408-416.
357. McConnachie, M.; Konarova, M.; Smart, S., Literature review of the catalytic pyrolysis of methane for hydrogen and carbon production. *International Journal of Hydrogen Energy* **2023**.
358. Huang, X.; Farra, R.; Schlögl, R.; Willinger, M.-G., Growth and termination dynamics of multiwalled carbon nanotubes at near ambient pressure: an in situ transmission electron microscopy study. *Nano letters* **2019,** *19* (8), 5380-5387.
359. Hofmann, S.; Sharma, R.; Ducati, C.; Du, G.; Mattevi, C.; Cepek, C.; Cantoro, M.; Pisana, S.; Parvez, A.; Cervantes-Sodi, F., In situ observations of catalyst dynamics during surface-bound carbon nanotube nucleation. *Nano letters* **2007,** *7* (3), 602-608.